A STUDY ON THE SURFACE ADSORBATES OF AN ENANTIOSELECTIVE, HETEROGENEOUSLY CATALYSED, HYDROGENATION REACTION

A thesis submitted to
Cardiff University
For the degree of
Philosophiae Doctor

By

Robert Jon Taylor B.Sc.

Department of Chemistry
Cardiff University

February 2010

UMI Number: U584417

All rights reserved

INFORMATION TO ALL USERS
The quality of this reproduction is dependent upon the quality of the copy submitted.

In the unlikely event that the author did not send a complete manuscript
and there are missing pages, these will be noted. Also, if material had to be removed,
a note will indicate the deletion.

UMI U584417
Published by ProQuest LLC 2013. Copyright in the Dissertation held by the Author.
Microform Edition © ProQuest LLC.
All rights reserved. This work is protected against
unauthorized copying under Title 17, United States Code.

ProQuest LLC
789 East Eisenhower Parkway
P.O. Box 1346
Ann Arbor, MI 48106-1346

Dedication

With love to my family and friends for all their patience, help and support...

Acknowledgements

I would like to recognise the members of my family for their continued love and support. To Jo whose eternal patience, love and most of all her optimism was my tonic, for Mum and Dad, whose advice, experience and unerring faith in me were always appreciated, two of my best friends James and Helen for the great times we always have, to my Nanna and Grandad whose pride in me was highly valued and a special mention goes to my Mamgu who was always there and I adore. I thank you all.

I would like to thank my friends and colleagues in my own research group and Dr Damien Murphy and the members of his team with whom I had the pleasure to work and socialise with. Most notably, I would like to thank Dr Neil Rees and Dr Yu Xiong Jiang whose exceptional knowledge and experience were key aspects to my development.

I would also like to extend my gratitude to Dr David Willock for his extensive effort, knowledge and guidance in the computational chemistry commissioned for this study.

In particular, I would like to thank Professor Gary Attard for all the help he has provided throughout my time at Cardiff University. His unbounded energy and enthusiasm for science was always a reliable source of motivation for me. From him I have learned the most.

Abstract

Surface Enhanced Raman Spectroscopy (SERS), Cyclic Voltammetry (CV) and Density Functional Theory (DFT) have been used to investigate the Orito reaction – a heterogeneously catalysed enantioselective hydrogenation reaction. Using a spectro-electrochemical flowcell, designed and built in-house, the boundaries for *in situ* measurements have been pushed closer to the real Orito reaction conditions than ever before.

By increasing the surface coverage of adsorbed hydrogen, it was found that the reactants methyl pyruvate (MP), ethyl pyruvate (EP) and ethyl benzoylformate (EBF) all formed a half-hydrogenated state (HHS) on a platinum surface under both gas phase and electrochemical conditions. Through controlled solution concentration experiments on MP and EP under electrochemical conditions, the surface coverage of hydrogen was found to decrease as a function of higher pyruvate concentrations.

By co-adsorbing MP or EP with cinchonidine (CD) – a cinchona alkaloid frequently used to chirally modify the catalyst surface in the Orito reaction, the coverage of adsorbed hydrogen was found to remain high (relative to unmodified surfaces) even at high pyruvate concentrations and the strength of the M-H bond was found to be slightly weaker (as deduced from a red shift in the frequency of the M-H stretching vibration). It was found that the modifier competes with the HHS for adsorption sites and creates a chiral pocket into which hydrogen can also adsorb and interact with the modifier causing the M-H bond to weaken via hydrogen bonding with the tertiary nitrogen atom of the quinuclidine substituent of CD. It is proposed here that the rate enhancement commonly observed for modified catalysts, is due to an increase in the coverage of surface hydrogen and an activation of surface hydrogen towards reaction with the pyruvate reactant.

Adsorption studies of EP on well defined platinum surfaces using CV revealed a trend for adsorption and decarbonylation decreasing in the order {100}>{110}>{111}. The same trend for the equivalent palladium surfaces was also found, but with no evidence of decarbonylation.

Contents

Chapter 2 Theoretical Background

Chapter 3 Experimental

Chapter 6 Adsorption of Cinchona Alkaloids on Platinum Surfaces

Chapter 7 Co-adsorption of α-Ketoesters with Cinchona Modifiers on Platinum Surfaces

List of Symbols

English

Symbol	Description	Units
A	Area	cm^2
b	Path length	cm
c	Speed of light through a vacuum	2.9979×10^{8} m s^{-1}
$\bar{c}$	Concentration of absorbing species	mol dm^{-3}
C_o	Concentration of electroactive species	mol cm^{-3}
D_o	Diffusion co-efficient	cm^2 s^{-1}
D_e	Dissociation energy	kJ mol^{-1}
e^-	Charge on one electron	-1.602×10^{-19} C
E	Energy	eV, J, J mol^{-1}
$\bar{E}$	Electric field	V m^{-1}
E_F	Fermi energy	eV
E_{vac}	Vacuum energy	eV
F	Faraday constant	9.649×10^{4} C mol^{-1}
h	Planck's constant	6.626×10^{-34} J s
i	Current	A
k	Boltzmann constant	1.381×10^{-23} J K^{-1}
l	Bond length	Å, nm
n	Number of electrons	-
N_A	Avogadro's constant	6.022×10^{-23} mol^{-1}
Q	Charge	C
R	Gas constant	8.314 J K^{-1} mol^{-1}
t	Time	s
T	Temperature	K
v	Scan rate	V s^{-1}
V	Potential	V

Greek

Symbol	Description	Units
α	Polarisability	$C \cdot m^2 \cdot V^{-1}$
δ	Charge	V
ε	Absorptivity co-efficient	$M^{-1}cm^{-1}$
λ	Wavelength	m
μ	Dipole moment	Debye
ν	Frequency	s^{-1}
$\tilde{\nu}$	Wavenumber	cm^{-1}
σ	Hammett parameter	-
σ_c	Cross section	cm^2
σ_d	Charge density	$\mu C\ cm^{-2}$
Φ	Work function	eV
Ω	Solid angle	Steradians

Abbreviations

CD	Cinchonidine
CN	Cinchonine
CO	Carbon monoxide
CS-NP	Core-shell nanoparticle
CT	Charge transfer (SERS theory)
CV	Cyclic Voltammetry/cyclic voltammogram
DCM	Dichloromethane
DFT	Density Functional Theory
ee	Enantiomeric excess
EM	Electromagnetic (SERS theory)
EP	Ethyl pyruvate
EL	Ethyl lactate
EtOH	Ethanol
HER	Hydrogen evolution reaction
HHS	Half hydrogenated state
HMMP	High molecular mass product
HPLC	High Performance Liquid Chromatography

HQnClB	Hydroquinine-4-chlorobenzoate
H OPD	Hydrogen overpotential deposition
H UPD	Hydrogen underpotential deposition
KPL	Ketopantolactone
MP	Methyl pyruvate
ML	Methyl lactate
NLE	Non-linear effect
OCP	Open circuit potential
ORC	Oxidation reduction cycle
PA	Pyruvic acid
PL	Pantolactone
PTFE	Polytetrafluoroethylene (Teflon®)
Q	Quinoline
QD	Quinidine
QN	Quinuclidine
QNE	Quinine
SCE	Saturated calomel electrode
SERS	Surface Enhanced Raman Scattering

Chapter 1
Introduction

1.1 Historical perspective

In 1811, Francois Arago discovered that the plane of polarised light could be rotated by passing it through a quartz crystal [1]. In 1835, Jean-Baptiste Biot also found this observation to be true for sugar solutions [2]. But, it was not until 1848 when Louis Pasteur [3] noted subtle differences between the tartaric acid crystals obtained from wine production and those obtained using chemical synthesis that an explanation for this unusual behaviour could be afforded. He noted that the chemically synthesised tartaric acid crystals did not rotate polarised light whereas those obtained from wine lees did. By microscopic inspection of the crystals in the commercial sample, Pasteur was able to discriminate between and separate two different types of crystal. Some of the crystal types were of a "left handed" form whereas the other (its mirror image) was "right handed". Apart from this rare feature of visually different structures, the two crystal types were indistinguishable from one another in almost all physical properties including hardness, solubility, density, boiling point etc. However, there was one difference. Pasteur found that when the "separated" crystals (using visual inspection and a pair of tweezers) were re-dissolved to form two solutions, one solution rotated the plane of polarised light in a clockwise fashion (known as dextrorotatory and given the prefix (+)), whereas the other rotated the light in an anti-clockwise fashion (known as levorotatory, given the prefix (-)). This property was called *optical activity*. Therefore, the crystal formed from synthetic, commercial sources did not rotate polarised light because both crystal types were present *in equal measure*. Pasteur described this observation as an "asymmetry" between the two forms of tartaric acid and that it was extended throughout the two crystal types. This molecular asymmetry was later termed "*chirality*" by Lord Kelvin in 1893. From such observations, van't Hoff was to deduce the basis of such chirality in organic molecules as stemming from tetrahedral arrangements of different chemical substituents around a central carbon atom [4]. Hence the study of molecular and structural shape is a discipline which originated in the 19th century that has developed to become one of the most important topics in modern 21st century science [5]. In the present study, adsorption of chiral and achiral molecules at solid surfaces will be investigated with a view to elucidating a mechanism in heterogeneous enantioselective hydrogenation catalysis.

1.1.1 Chirality

The word chirality is derived from the Greek word *cheir* meaning "hand". An object is described as being "chiral" if it is non-superimposable on the form of its mirror image.

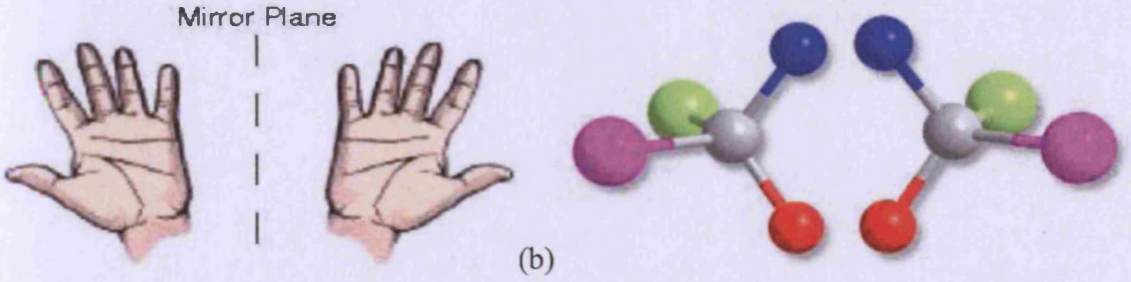

Figure 1.1 Examples of chiral objects: (a) hands and (b) an sp^3 hybridised carbon atom bonded to four different constituents.

That is, one entity cannot be manipulated in three dimensions to match the same spatial arrangement as the other and so may be defined as either left-handed or right-handed.

In molecular terms, such entities constitute a class of stereoisomers called optical isomers and are referred to as enantiomers, each enantiomer being a mirror image of the other. A central carbon atom bonded to four different atoms or distinguishable groups will confer chirality on the molecule. Using the Cahn-Ingold-Prelog system [6], whereby the atoms or groups bonded to the stereocentre are assigned a priority according to their mass and labelled 1-4 in descending order of priority (Figure 1.2), a nomenclature has been developed to label enantiomers. The enantiomer is viewed from above with the fourth atom/group (that of lowest mass) pointing away. If groups 1-3 in preference were noted to run in a clockwise fashion then the enantiomer is given the prefix *R*- (rectus) or *S*- (sinister) if 1-3 runs anti-clockwise.

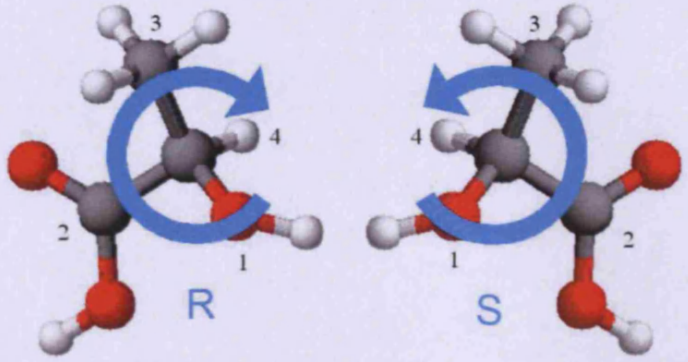

Figure 1.2 Enantiomers being described using the Cahn-Ingold-Prelog system of nomenclature.

Non-superimposable stereoisomers that are not mirror images of one another are termed *diastereoisomers* and often contain more than one stereocentre. Compounds containing two or more stereocentres but in themselves are not chiral are known as *meso-compounds*. A meso-compound is superimposable on its mirror image.

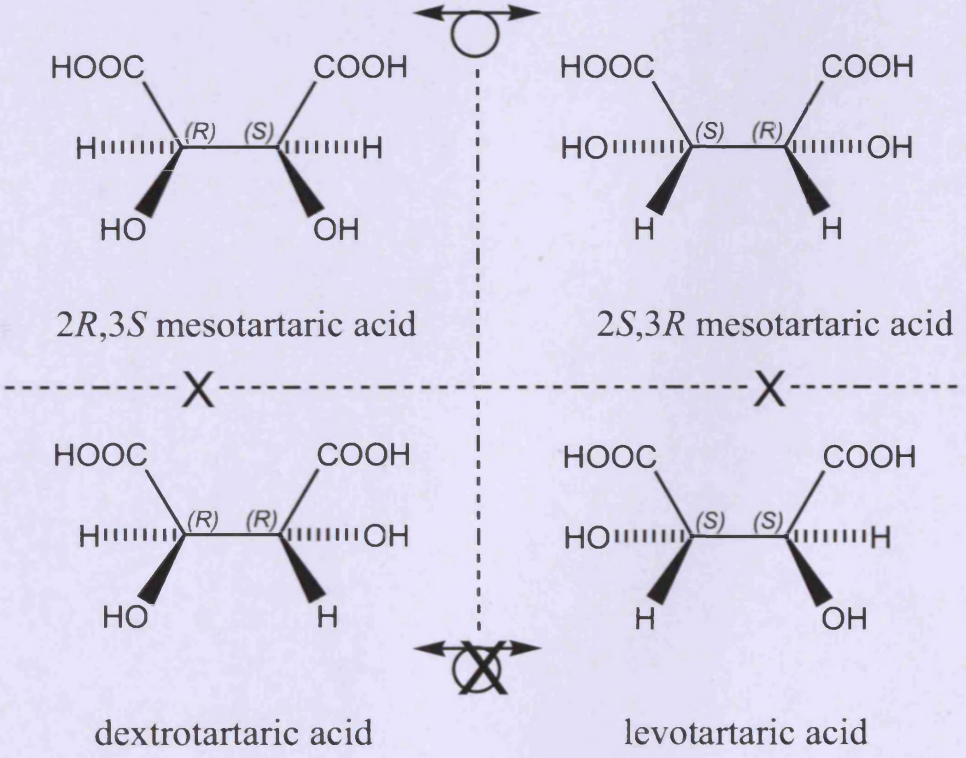

Figure 1.3 The meso-compounds are mirror images and superimposable on each other, so are equivalent. Dextrotartaric acid is the enantiomer of levotartaric acid (non-superimposable mirror images). The meso-compounds are diastereoisomers of dextro- and levotartaric acid (not mirror images).

1.1.2 Importance of Research into Molecular Arrangement

As described earlier, enantiomers are physically identical in every way except for their interaction with molecules or light of left or right handedness. In biochemical surroundings, the chirality of a molecule can be recognised and may lead to a specific physiological response. In the pharmaceutical industry, the most infamous example of this behaviour was found with the use of thalidomide to treat morning sickness in pregnant women in the 1950's [7]. It was later realised that thalidomide had two enantiomeric forms and whilst one enantiomer was found to be therapeutic, the other was teratogenic and led to birth defects [8]. Consequently, there is now unprecedented concern in manufacturing pure enantiomeric compounds that contain exclusively only one type of handedness. The interest in separation of enantiomers extends to all industries that are concerned with biochemical environments and these would include flavours [9], fragrances [10], pharmaceuticals [11] and agrochemicals [12].

1.1.3 Enantiomeric Separation

If both enantiomers are present in a mixture to the same extent, this mixture is termed a *racemate*. If there is an excess of one enantiomer, then the excess can be quantified as a percentage of the total mixture. Equation 1.1 is often used to quantify this parameter and is termed the *enantiomeric excess* (ee).

$$\mathrm{ee} = \frac{[\mathrm{R}]-[\mathrm{S}]}{[\mathrm{R}]+[\mathrm{S}]} \times 100\% \qquad (1.1)$$

[R] is the concentration of the *R*-enantiomer present and [S] the concentration of the *S*-enantiomer. For the *S*-enantiomer percentage, the numerator is changed to [S] – [R]. Ideally the substance should be enantiopure (>99% ee of *R*- or *S*-). To achieve such enantiomeric purity on a bulk scale can often prove extremely expensive ($120 billion worldwide sales per year of pharmaceuticals is testament to this statement) [13].

For a small quantity of racemate, the enantiomers may be separated by chiral chromatography, whereby the mixture, in a gas or liquid state, is eluted through a column containing a material that interacts more strongly with one enantiomer over the other (i.e. the column itself should be a chiral material). Depending on the ability of the column to resolve the racemate, the eluate collected should be either the pure *R*- or *S*-enantiomer differentiated

via their characteristic retention times on the column. Alternatively, an enantioselective reaction could be used to target one enantiomer by producing two chemically different diastereoisomers, which in turn can then be separated since they would have different physical properties. The original *R*- and *S*- compounds may then be recovered via subsequent chemical reaction to re-generate the *R*- or *S*-enantiomer [14]. Another approach to cause separation of enantiomers is to use an enzyme or molecule which itself is chiral and selectively consumes one of the enantiomers leaving behind the isolated enantiomer [14].

It is evident from the above that it is not a simple matter to separate enantiomers. Hence, a more efficient method would be to produce a single, pure enantiomer directly [15]. Enantioselective catalysis can be used to this end and provides an elegant solution to industrial problems of producing enantiopure chemicals. This resulted in a Nobel prize award for Knowles, Noyori and Sharpless in 2001 [16], who pioneered the use of homogeneous catalysts for the enantioselective production of compounds. For all of the enantiopurity obtained ($\geq$ 99% ee), homogeneous catalysts give rise to three major difficulties:

1. Separation from the reaction mixture after use of both catalyst and product.
2. Limited opportunities for re-use.
3. Sensitivity to normal ambient reaction conditions such as oxygen/water vapours.

These problems can be overcome if the reaction is performed with a catalyst in a different phase to the reactant and products, i.e. by using a heterogeneous catalyst.

1.2 Heterogeneous Catalysis

"A catalyst is a substance that increases the rate at which a chemical reaction reaches equilibrium without being consumed in the process" [17,18]. As mentioned above, catalysis is heterogeneous if the reaction rate enhancement takes place at an interface between the catalyst in one phase and the reactant(s) in another phase.

1.2.1 Reaction Rate

The rate is determined by the change in concentration or partial pressure of the reactant(s), *r*, and/or the product(s), *p*, over a unit of elapsed time in a closed system.

$$\text{rate} = \frac{d[r]}{dt} = k(T)[r]^m \qquad (1.2)$$

and is dependent on the concentration of r to the power of its reaction order (denoted by superscript m in this case) and the rate constant, k, at a fixed temperature defined by the Arrhenius equation:

$$k = Ae^{-E_a/RT} \qquad (1.3)$$

where A is the collision frequency of the reactants, E_a is the activation energy for the reaction, R is the universal gas constant and T is the absolute temperature in K. The units of k are dependent on m. At a fixed temperature, a catalyst will increase the rate constant and hence the reaction rate by lowering E_a. Therefore, the amount of catalyst is controlled to optimise the reduction of E_a without diluting the reaction mixture, thereby achieving maximum rate enhancement. Hence the rate values are normalised to the amount of catalyst mol dm^{-3} g^{-1} s^{-1} to give the specific rate, or if the quantity of reaction sites is known, the number of product molecules generated per site per second (turnover frequency, s^{-1}).

For a heterogeneously catalysed reaction, the rate values may be normalised to the surface area of catalyst (mol dm^{-3} m^{-2} s^{-1}). There are other kinetic factors that may impact on the rate of the reaction including: (1) diffusion of the reactant to the catalyst surface; (2) adsorption of the reactant onto the surface; (3) diffusion of the adsorbate across the surface to the active site; (4) reaction of the reactant-catalyst complex; (5) desorption of product from the active site; and (6) diffusion of product away from the surface. Therefore the reaction rate is dependent not only on the catalyst's ability to lower E_a, but also the kinetic factors that control A [17].

1.2.2 Molecular Adsorption on Metal Surfaces

Catalysis at solid surfaces is often explained in terms of the *Sabatier principle*. Here, the highest coverage of surface intermediates possible is postulated as being beneficial to the activation of the reactant molecules and hence their subsequent conversion into useful products. For example, the catalytic processes involving oxidation might include the initial adsorption of oxygen gas molecules followed by dissociation to form adsorbed oxygen atoms. One refers to such atoms as being chemisorbed.

Chemisorption is a process that involves the exchange of electrons between the adsorbate and surface leading to the formation of a chemical bond with adsorption enthalpies in excess of

50 kJ mol^{-1}. The larger the adsorption enthalpy, the greater the extent of interaction (and hence coverage) of the surface with the oxygen atoms. However, if the interaction becomes too great, it is then very difficult for these strongly chemisorbed atoms to go on to react with other molecules, and indeed for other molecules to chemisorb at sites already occupied by, for example, the oxygen atoms discussed above. Therefore the Sabatier principle states that the best heterogeneous catalyst will be one in which the chemisorption of molecular species is sufficient to "activate" these molecules, but not so great that subsequent surface diffusion, surface reaction and surface desorption of products are completely quenched. This means that when different metals are compared (in terms of catalytic rate) versus adsorption enthalpy of a reactant, the plot often exhibits a "volcano curve" trend with optimal activity being exhibited by those surfaces satisfying the Sabatier principle.

The formation of the chemical bond in chemisorption is often directional with respect to a particular molecular orbital and a specific surface site. In general, the less highly co-ordinated surface atoms tend to be occupied initially by an adsorbate. *Non-dissociative* and *dissociative* are two sub-divisions of chemisorption that represent the stability of the adsorbate. In non-dissociative chemisorption the adsorbate is stable and does not break up into smaller molecular fragments. An example of this process includes carbon monoxide adsorption on platinum [19]. Dissociative adsorption involves decomposition of the adsorbate, such as the oxygen example given above or dissociation of H_2 on platinum to form adsorbed hydrogen atoms [20]. The symmetry of the underlying substrate may be translated into the chemisorbed overlayer such that well ordered arrays of the adsorbate exist. Inter-adsorbate interactions may also improve the order of the overlayer. The temperature of the substrate can play a role in symmetry of the overlayer if it is sufficiently high to allow for lateral movement of the adsorbates across the surface. In this situation, any adsorbate-adsorbate interaction can result in the formation of *islands*. These are localised areas of high coverage separated by clean areas or areas of low coverage [21]. Conversely, adsorption can also occur at totally random sites.

Another important interaction is the so-called physisorbed state. Physisorption is characterised by an electrostatic interaction between the surface and an adsorbate where bonding occurs through Van der Waals type forces. That is to say, the electrons are redistributed within the molecule forming a polarised state at the surface and the surface electrons separately. No electrons are exchanged between the surface and the adsorbed

molecule. The adsorption strength is considered to be weaker than in chemisorption with adsorption enthalpies generally < 30 kJ mol^{-1}. These "precursor states" are often important in catalysis because they allow rapid diffusion of a reactant across the surface of the solid until it locates an "active site" [22] and undergoes chemisorption.

For most inert gases or substrates, physisorption may be the only channel for adsorption available and hence the coverage is strongly dependent on substrate temperature. The process is usually reversible, so raising the temperature will cause desorption with no change to the substrate or desorbing molecule. Higher coverages will occur at lower temperatures with universal physisorption occurring at 0 K. Van der Waals interactions can also occur between the physisorbates and can act laterally to give rise to ordered overlayers or islands. There is usually very little adsorption site specificity, if any, with physisorption and so an ordered overlayer will not reciprocate any order of the underlying substrate i.e. the overlayers tend to be incommensurate.

1.2.3 Adsorption Isotherms

The equilibrium at which gas molecules adsorb and desorb from a surface at constant temperature as a function of pressure can be determined from isotherms to give the fractional coverage θ.

$$\theta = \frac{N_A}{N} \tag{1.4}$$

where N_A is the number of adsorbates and N is the total number of adsorption sites. The Langmuir isotherm was the first attempt to describe the equilibrium and is based on the assumption that the number of gaseous molecules impinging on the surface is proportional to the pressure, P [23]. Therefore, the rate of adsorption is proportional to $P(1-\theta)$ and the rate of desorption is proportional to θ such that equilibrium is established when both rates are equal:

$$k_a P(1-\theta) = k_d \theta \tag{1.5}$$

where k_a and k_d are the rate constants for the adsorption and desorption processes, respectively. The coverage is then found with the following equation:

$$\theta = \frac{KP}{1+KP} \tag{1.6}$$

where

$$K = \frac{k_a}{k_d} \tag{1.7}$$

Figure 1.4 shows a plot of the fractional adsorbate coverage against pressure for a Langmuir type equilibrium.

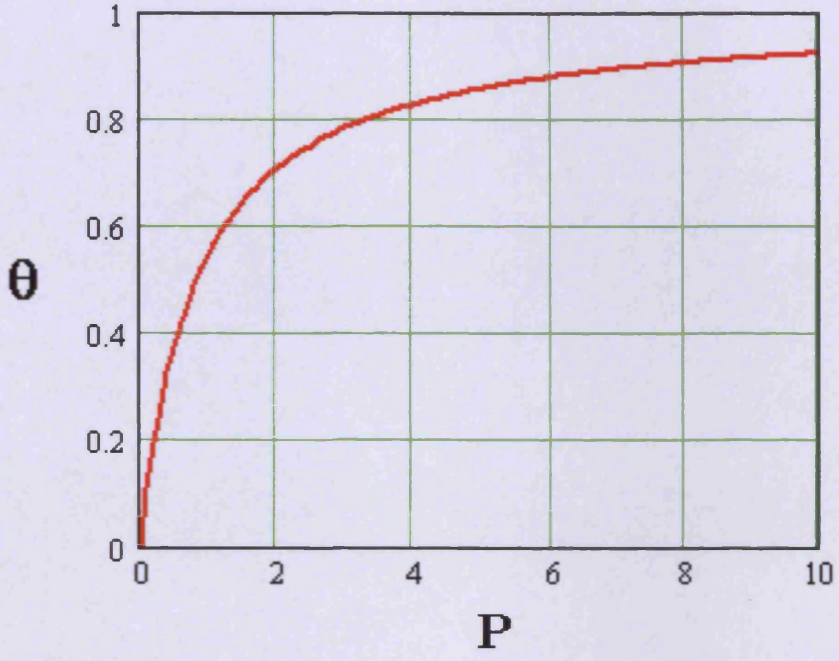

Figure 1.4 The Langmuir isotherm

Although this model is ubiquitous in assessments of reaction kinetics, it falls short in the evaluation of the adsorbate interactions. In order to work, the following assumptions are made:

1. The solid surface is uniform and contains a number of equivalent sites which each support one adsorbate molecule.
2. A collision of a gas phase molecule with a vacant site on the surface will result in adsorption, but will be elastic with an occupied site i.e. the molecule will desorb back into the gas phase.
3. The heat of adsorption is independent of coverage.

This last assumption is particularly erroneous as it is commonly observed that the heat of adsorption decreases (i.e. becomes less exothermic) as coverage increases. This can be ascribed to: 1) the repulsive forces of inter-adsorbate interactions; 2) a change in bonding

type of the adsorbate at different coverages; 3) an increase in the work function (energy required to remove an electron from the substrate) of the substrate; 4) heterogeneity of the surface (the antithesis of assumption # 1, above) [17].

The Langmuir isotherm is concerned with coverages up to one monolayer primarily and is based on chemisorptive processes. A variation on this isotherm that includes multilayer adsorption was devised by Brunauer, Emmett and Teller (BET) and is primarily based on physisorptive processes. It describes the multilayers as being adsorbed consecutively such that second layer adsorption commences after the first layer is fully covered and each adsorbate provides a site of adsorption for successive layers.

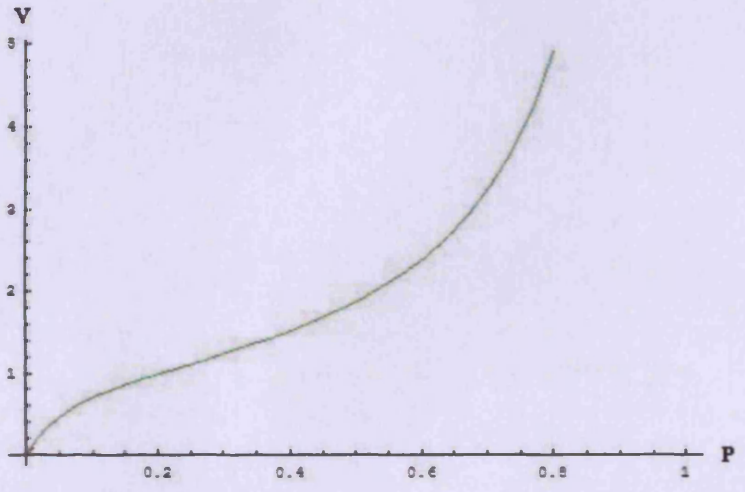

Figure 1.5. The BET isotherm

The BET isotherm successfully portrays the volume adsorbed against pressure as being an s-shaped curve (Figure 1.5) due to multilayer adsorption. However, the assumptions by Langmuir on the absence of lateral adsorbate interactions and surface homogeneity are also assumed. Furthermore, the heat of adsorption in the second layer and subsequent layers are assumed to be equal to the heat of liquefaction of the gas phase molecule (i.e. is independent of the substrate). The heat of adsorption of the first layer is commonly greater than the heat of liquefaction. Based on these assumptions, the BET equation is formulated as follows:

$$V = \frac{V_m c P}{(P_0 - P)\left\{1 + \frac{(c-1)P}{P_0}\right\}} \qquad (1.8)$$

where V is volume, V_m is the maximum volume, P is pressure, P_0 is the saturated vapour pressure and $c \approx e^{(Q_a - Q_l)/RT)}$ with $Q_a - Q_l$ being the difference between heat of adsorption on the first layer and heat of liquefaction of the gas phase molecule. This can be rearranged to:

$$\frac{P}{V(P_0 - P)} = \frac{1}{V_m c} + \frac{(c-1)}{V_m c}\frac{P}{P_0} \qquad (1.9)$$

which should yield a straight line if $P/V(P_0-P)$ is plotted against P/P_0. The intercept on the y-axis is given by $1/V_m c$ and should give the monolayer volume and hence the surface area of the substrate.

1.3 The Context of the Present Study – a Literature Review

Heterogeneously catalysed enantioselective reactions can be dated back to 1932 with a report by Schwab *et al* of the dehydrogenation of 2-butanol to butanone over copper, nickel, palladium and platinum supported on quartz cleaved to produce a chiral template [24]. Other naturally occurring chiral materials have been used to support catalysed hydrogenations of C=N and C=C bonds including cellulose [25], polysaccharides [26] and silk [27].

In 1939 Lipkin *et al* reported the hydrogenation of cinnamic acid over chirally modified platinum [28]. The concept of chirally modifying a catalyst with naturally occurring chiral products has been extended to various hydrogenation reactions including ephedrine modified palladium for hydrogenation of the C=N bond of pyruvic acid oxime [29] and rhodium catalysed hydrogenation of ortho-toluic acid modified with N-ethyldicyclohexylamine [30]. However, the highest reaction performances are achieved with the hydrogenation of β-ketoesters over tartaric acid modified Raney-nickel discovered by Izumi [31] and the hydrogenation of α-ketoesters over cinchonidine modified platinum discovered by Orito and co-workers [32].

Both Izumi- and Orito-type reactions are considered to be model systems for understanding enantioselectivity in heterogeneous catalysis. Much progress has been made in the understanding of the Orito reaction, but the true nature of the mechanism for enantioselectivity is still a subject of active debate. The potential advantages in elucidating this mechanism include an optimisation for existing reaction schemes and diversification to

other reaction schemes, which under heterogeneous conditions can reduce the cost of industrial processes where homogeneous reactions are currently used. The Orito reaction will now be discussed in detail.

1.3.1 The Orito Reaction

The enantioselective hydrogenation of a prochiral activated ketone to the corresponding alcohol heterogeneously catalysed with chirally modified platinum, was first observed by Orito *et al* in the late 1970's [32]. Orito had shown that using the chiral alkaloid cinchonidine (CD) to modify a carbon supported platinum catalyst, methyl pyruvate (MP) dissolved in dichloromethane was converted to *R*-methyl lactate (ML) under 30 bar hydrogen pressure to a high ee. When using cinchonine (CN) (an epimer of CD) as modifier, the selectivity was reversed to give *S*-ML to a similar ee.

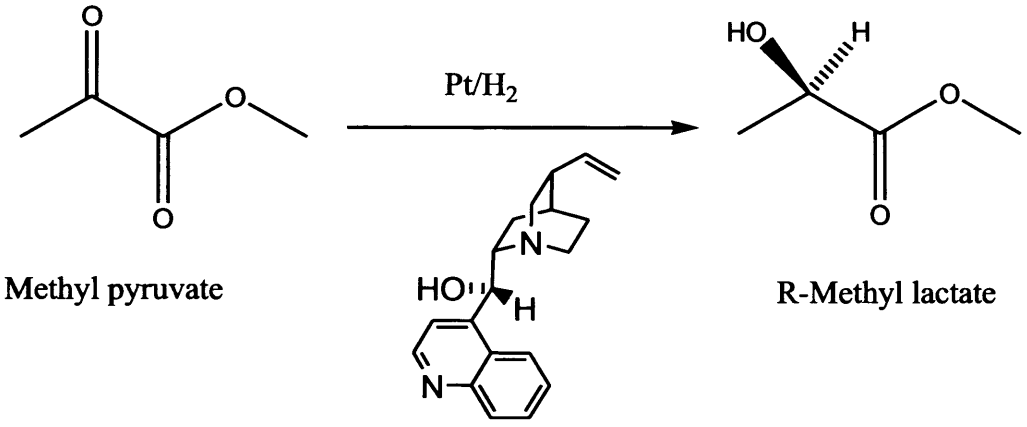

Figure 1.6 Orito's reaction scheme for the enantioselective hydrogenation of MP.

1.3.2 Surface Science Studies of the Reactants Methyl Pyruvate and Ethyl Pyruvate

In the Orito reaction, the carbonyl group to be hydrogenated is activated by an electron withdrawing group in the alpha position [32]. In Figure 1.6, it is seen for MP that it is the ester group withdrawing electrons from the ketone. The stability of the ketone is therefore reduced and is subsequently prone to reaction, in this case with hydrogen to form a chiral alcohol. Enantiopure methyl and ethyl lactate (EL) has very little commercial use although the racemate can be used as a polar solvent in cleaners, degreasers and product ingredients in such industries as electronics manufacturing, adhesives, paints and other coatings, printing, de-inking, and textile manufacturing [33]. MP is structurally similar to ethyl pyruvate (EP)

only differing by one carbon in the length of the ester alkyl chain. Both MP and EP give a high reaction performance with regard to final ee and rate and therefore their interaction with the metal surface is considered important in the understanding of the mechanism of the Orito reaction.

EP has received a great deal of attention in reaction studies. However, as an adsorbate the spectroscopic information regarding orientation of this and related molecules adsorbed on a platinum surface is sparse. Earlier studies of simpler carbonyl compounds such as acetone adsorbed on transition metals including platinum{111} using Electron Energy Loss Spectroscopy (EELS) identified two different adsorption modes involving σ-bonds to the surface:

- An η^1 lone pair bond from the oxygen of the carbonyl to the platinum surface in an end-on mode (Figure 1.7 b).
- An η^2 mode involving both a metal-oxygen and metal-carbon bond derived from the keto carbonyl [34,35] (Figure 1.7 c).

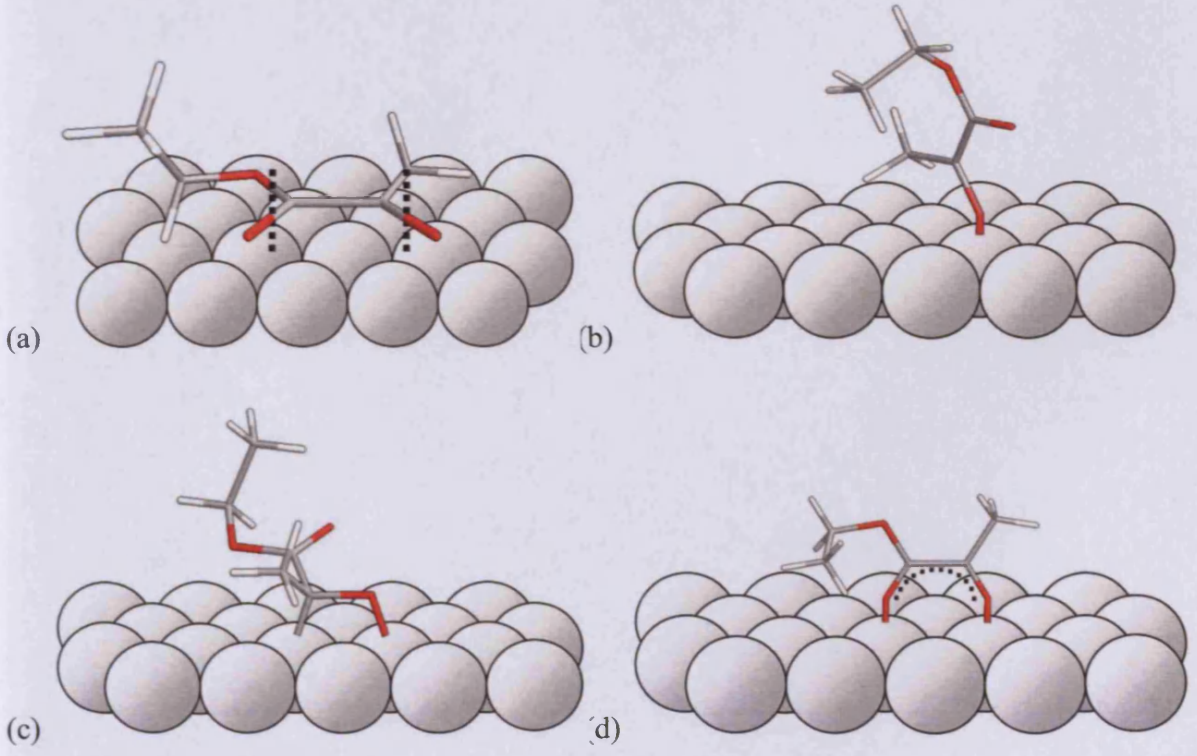

Figure 1.7. EP adsorption modes; (a) π-bonded, (b) η^1, (c) η^2 and (d) enediolate.

X-ray Absorption Near Edge Structure (XANES) was later employed for a study of EP on platinum{111} [36]. An adsorption mode related to the η^1 configuration was identified via an oxygen lone pair bond from the keto carbonyl, but no evidence for an η^2 type configuration could be obtained. However, a flat orientation of EP with the molecular plane lying parallel to the surface plane was proposed (Figure 1.7 a), involving an interaction of the π-orbitals of the two carbonyl groups with the platinum surface. Both adsorption modes were seen to co-exist on the surface, but admission of hydrogen gas was found to cause the molecular plane of the η^1 type mode to be tilted at an angle closer to that of the surface plane. This species was postulated to be a precursor to the flat orientation, which correlated with theories produced from catalytic studies involving the mechanism of hydrogenation [37]. Another publication by the same authors utilised X-ray Photoelectron Spectroscopy (XPS) and Ultra-violet Photoelectron Spectroscopy (UPS) to probe the binding energy of core shell and valence shell electrons [38]. A stabilisation of the highest occupied molecular orbital (HOMO) upon adsorption was interpreted as a lone-pair donation to unoccupied platinum d-states with a back-donation to the lowest unoccupied molecular orbital (LUMO) as described by the Blyholder model for carbon monoxide (CO) adsorption [39] in an η^1 type configuration (in this case, bonding was from the oxygen and not the carbon). The η^2 configuration was discarded, as this would involve charge transfer from the π-orbital. It was concluded that the keto carbonyl was involved in chemisorption to the surface and possibly the ester carbonyl too. What was not entirely clear was the orientation of the molecule. Nonetheless, through analysis of analogous molecular adsorption and surface area occupation an upright or tilted orientation with respect to the surface plane was strongly favoured.

When the study of EP on platinum{111} was extended to MP using Density Functional Theory (DFT) the most energetically stable mode was found to be the η^2 configuration over the η^1 [40]. The π-bond of the carbonyl was shown to rehybridise to have more σ-bond character (confirmed by an extension of the C-O bond length in the η^2 configuration compared to the free molecule and the η^1 configuration). This was regarded as being the basis of a faster reaction rate of hydrogenation of the η^2 mode, therefore, it was proposed that the rate of hydrogenation may be dependent on the ratio of the η^1 and η^2 states at the surface.

Reflection-Absorption Infra-Red Spectroscopy (RAIRS) was another technique used to study MP on platinum as a function of temperature and confirmed the η^1 and η^2 adsorption

geometries. It also introduced another adsorption mode whereby both keto and ester carbonyls were oxygen lone pair bonded to the surface with a delocalised π system existing between the O-C-C-O bonds, known as an enediolate configuration [41] (Figure 1.7 d). However, this configuration was only stable at very low temperatures (110 K) and at higher ambient temperatures (230 K), MP was believed to polymerise. Only in the presence of a modifier ((1-napthyl)ethylamine) was an η^1 bound MP stabilised at higher ambient temperatures (up to 300 K) and was therefore postulated as the enantioselective adsorption mode.

The adsorption of MP on other transition metals has been the subject of investigation using nickel{111} and copper{111}. Adsorption on copper{111} showed a predominant η^2 configuration, which was consistent with the results for MP adsorbed on platinum and hence copper was postulated as a possible alternative for the catalytic hydrogenation reaction [42]. However, copper does not dissociate hydrogen readily and therefore should be precluded as acting as a hydrogenation catalyst. Nickel{111} was found to stabilise a cis-bidentate type adsorption of MP, which is much like the enediolate configuration but with no delocalisation as described for platinum [43]. Theoretical studies of this system revealed an η^1 type adsorption of lone pair bonding from the keto oxygen to the nickel surface [44] to be favourable. However, these theoretical calculations were carried out using only a single nickel atom as substrate and not an extended plane. The relevance of these studies on nickel is questionable as nickel is known to be inactive in the hydrogenation of α-ketoesters [45,46] and indeed nickel is understood to yield different decomposition fragments from dissociative adsorption compared to platinum [44].

1.3.3 Other Activated Ketones

Enantiopure EL may not be a commercially desired compound, but other optically active alcohols are useful organic synthons [47] such as *R*-pantolactone in vitamin B5 and co-enzyme A synthesis [48]. The cyclic nature of the reactant ketopantolactone (KPL) affects the degree of enantioselectivity generated from the reaction with reported ee's of 79% compared to the linear EP (ee >95%). However, the sense of enantioselectivity is not changed as Pt/Al_2O_3 modified by CD gives rise to an excess of *R*-pantolactone [48].

Altering the functionality of other α-ketoesters has so far been found not to lead to a change in the sense of enantioselectivity [49,50]. The substitution of different groups on the α-ketoester can lead to steric effects between the reactant and the modifier and electronic effects within the reactant, which could feasibly either help or hinder the enantioselective step. The evidence so far suggests steric repulsion has a deleterious effect. This was demonstrated in several studies concerned with increasing the mass of the aliphatic group on both the keto and ester side of the molecule. Such modifications resulted in a minor loss in ee and hence the requirement of lower ambient temperatures and higher hydrogen pressure to maintain reaction performance [51,50,52]. Electron withdrawing/releasing properties of different substituents (as dictated by the Hammett Parameters [53]) can be used to augment or reduce the activation of the reactant ketone. It was clear that without the electron withdrawal by groups alpha to the ketone, the performance of the reaction was reduced [49,54]. It is the electrophilicity of the ketone that drives the reaction to a faster rate than for conventional ketones. The variety of different electron withdrawing groups has now been extended to include α-ketoacids [55], α-ketoamides [56], KPL [57], pyrrolidine-2,3-5-triones [58], α-ketoacetals [59] and α-diketones [60, 61] all of which produce the *R*-enantiomer as the major product on CD modified platinum.

1.3.4 Catalyst

The hydrogenation of ketones to the secondary alcohol is not heterogeneously catalysed exclusively with platinum. In the context of homogenous catalysis, rhodium [62] and ruthenium [63] homonuclear complexes have been used with remarkable success. For the heterogeneous enantioselective hydrogenation of β-functionalised ketones, nickel [64] and copper [65] are the metals of choice as seen in Izumi type reactions. For the Orito reaction, platinum was the original choice and remains as the highest performing metal in terms of rate, enantioselectivity and applicability to a wide range of substrates. Furthermore, with platinum the reaction rate of EP on an unmodified surface is relatively high at 57 mmol L^{-1} min^{-1} g^{-1} [66], but is curiously higher when modified with a cinchona alkaloid (200 mmol L^{-1} min^{-1} g^{-1}). Expectations would be for a lower rate due to fewer reaction sites being available as a result of modifier adsorption [67] as will be discussed further in section 1.3.11.

Iridium is next to platinum in the periodic table and does give rise to similar catalytic traits in hydrogenation reactions [68]. The racemic reaction is observed to be significantly higher on

iridium than on platinum (Ir: 1430 mmol h^{-1} g^{-1}, Pt: 50 mmol h^{-1} g^{-1}), but the extent of rate enhancement on modified iridium is less than that of platinum. The enantioselectivity also suffers using iridium with reported ee's of only 39% [69, 70], but like platinum, it favours the *R*-enantiomer in the presence of CD. The range of metals suitable for this reaction has been further demonstrated with a report on rhodium catalysed hydrogenation of hydroxy-phenones to an ee of 80% and a conversion of 89% surpassing the results achieved with platinum [71] under optimised reaction conditions.

Palladium, like iridium, gives a fast racemic reaction but no observed rate enhancement (and sometimes even a rate deceleration) when modified with CD [72]. More interestingly, the selectivity was reversed on palladium, i.e. CD gave the *S*-lactate product and initial attempts with EP only produced excesses of 4% [45]. Later experiments with MP using CN as modifier and optimising the reaction conditions, enabled an ee of 14% *R*-ML to be generated [72]. Palladium is renowned for being an excellent catalyst for the hydrogenation of C=C bonds. With the reversal of selectivity, it was postulated that an enolic species was favoured on palladium and it was the C=C bond that was hydrogenated requiring a change from *keto*- to the *enol*-tautomer for adsorbed MP [46]. Use of deuterium confirmed the formation of the *enol*-form on palladium [72]. Pertaining to the two carbonyls in the *keto*-pyruvate ester, a *trans* configuration is more energetically favourable [46], which was assumed to direct the 2^{nd} hydrogen to the *Si*-face with a CD modified surface and hence give the *R*-enantiomer. Upon enolisation, steric repulsion caused by a shift in electron density, would stabilise the *cis* configuration leaving the *Re*-face to be protonated (Figure 1.8).

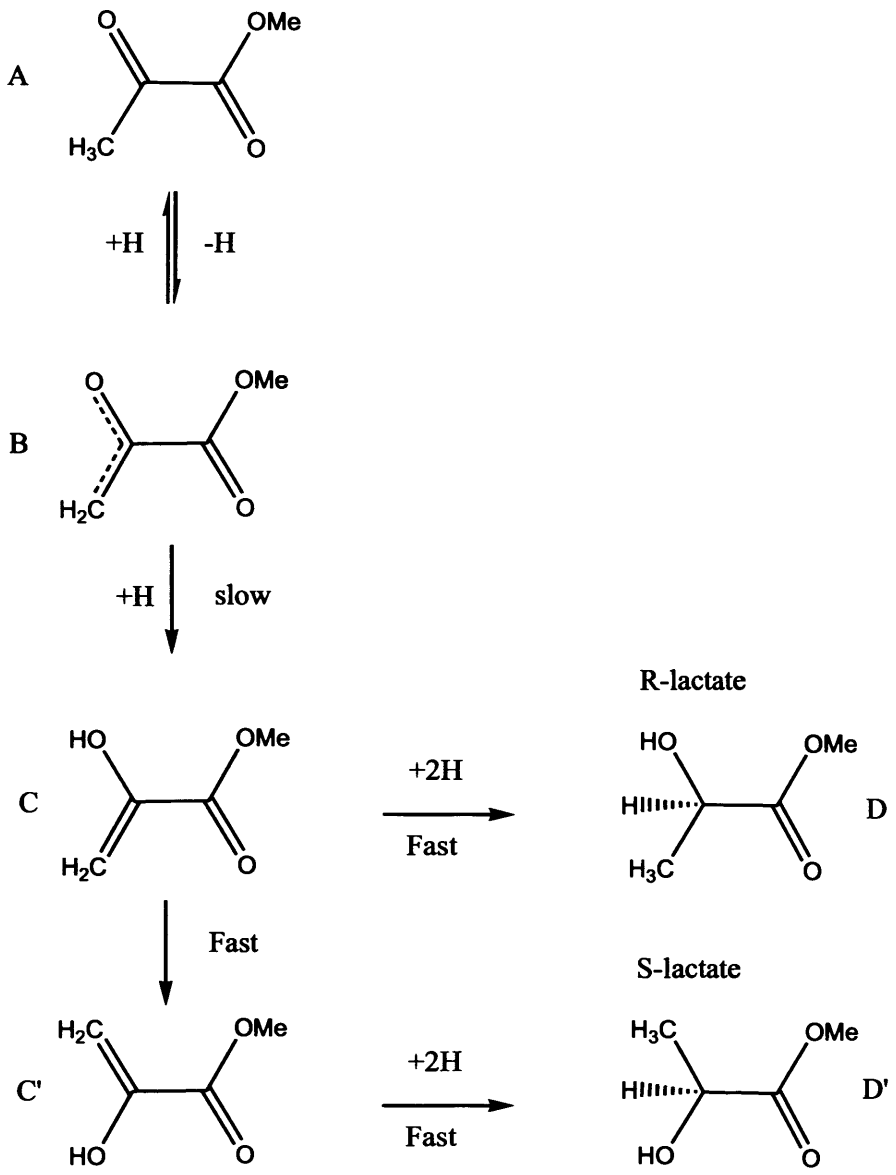

Figure 1.8 Tautomerism of MP; (A) *trans-keto*-MP, (B) delocalized π electrons, (C) *trans-enol*-MP, (C') *cis-enol*-MP. Reprinted from [46].

What was also understood through the work of Wells and co-workers, was that under aerobic pre-modification conditions of the palladium catalyst, the reversal of enantioselectivity holds true. But, under anaerobic conditions, the enantioselectivity was the same as platinum indicating that palladium oxide was responsible for the preferential formation of the *enol*-tautomer (32% *R*-EL with CD) [73]. The majority of the literature for palladium catalysed Orito type reactions involves unsaturated carboxylic acids demonstrating a degree of versatility towards other desirable products [74].

1.3.5 Support

The chemical characteristics of the metal are not the only aspect to consider in heterogeneous catalysis. Physical properties such as metal particle size, dispersion and surface area are also key aspects to achieving the optimum reaction performance. The material on which the metal is supported helps to control these features and to a lesser extent can affect the chemical environment too. The materials used successfully to support the platinum catalyst in the Orito reaction include alumina, silica, titania, carbon, clays and zeolites at varying platinum metal percentage weights [75]. 5% platinum on alumina support was recognised as the best performing combination with two commercial catalysts emerging as standards for this reaction; E4759 from Englehard and JMC 94 from Johnson Matthey [76], both of which have a platinum dispersion between 0.2-0.3 corresponding to a mean platinum particle size of 4.5 nm. A high pore volume was also considered necessary to reduce intraparticle mass transfer restrictions and so improve performance [77]. The alumina support in combination with acetic acid as solvent has been proven to react to form an oxonium cation, which was postulated to contribute to the high enantioselectivities achieved with this support [78]. The explanation for improved performance was based on an electrostatic model [79].

A further physical attribute to a support is its bearing on the symmetry of the catalyst particle. The elimination of the support can allow greater control of the particle morphology if colloid preparation methods are used ($\leq \pm$ 0.5 nm particles size distribution compared to the broader $\pm$ 0.9 nm of a standard supported catalyst). Using a polymer stabilised platinum colloid, Liu and co-workers were able to induce a 97.6% ee [80]. In contrast to the traditional supported catalysts, this quasi homogeneous catalyst gave rise to better enantioselectivity even with a smaller metal particle size (1.4 nm average diameter). Moreover, varying the size of both the cluster (up to 4 nm) and the reactant side chain (up to 4 carbons) did not result in a significant loss of ee [81]. Particle sizes that were too small (< 1 nm) to adsorb modifier and an adjacent reactant are unable to catalyse the enantioselective reaction, but will catalyse the racemic and other side reactions [82].

1.3.6 Morphology

As discussed above, the enantioselectivity was impaired on smaller platinum particles for supported catalysts where the size of low index terrace sites decrease proportionally. A mean particle size of <3 nm resulted in a loss of enantioselectivity [77], but at 2 nm polymer stabilised colloidal catalysts were at their optimum [81]. Nonetheless, this phenomenon strongly indicated a specificity for the morphology of the surface and was well illustrated with a study involving selective blocking of step or terrace sites with bismuth or sulphur adatoms, respectively [83]. Step sites were shown to be integral to enantiodiscrimination as signified by loss of enantioselectivity on a bismuthated catalyst. This study also suggested an inhibition of undesirable side reactions leading to the observed increase in rate. Furthermore, sintering the catalyst at elevated temperatures caused an increase in particle size and crystallinity (large {111} terraces, straight steps). The enantioselectivity consequently improved, but was accompanied by a loss of reaction rate [45]. For 5% platinum/graphite catalysts, ee was proportional to sintering temperature up to 700 K with a maximum reported ee of 63% [84]. Above this temperature the sintering was deleterious to both enantioselectivity and rate. The new crystalline structures at 700 K were noted to be hexagonal in shape (Figure 1.9) and the intrinsic chirality at the kink sites was postulated as being the adsorption site of the modifier and where the enantiodiscriminatory step took place. The decrease of the ee above 700 K was also related to this model whereby the density of these "corner" sites was lowered throughout the catalyst.

Catalyst restructuring has also been found to be induced by adsorption of the modifier (CD) when stirred in toluene in a pre-treatment of the catalyst [85] and was thought to be beneficial to the enantioselectivity. The average particle size was reduced from 4.4 nm to 3.8 nm when modifier was added to the pre-treatment mix. This resulted in an increase in ee from 52% to 66%. The achiral quinoline moiety of CD was also tested in the pre-treatment step and was found to have similar effects as CD indicating that the restructuring of the catalyst promotes selectivity but is not itself a chiral process.

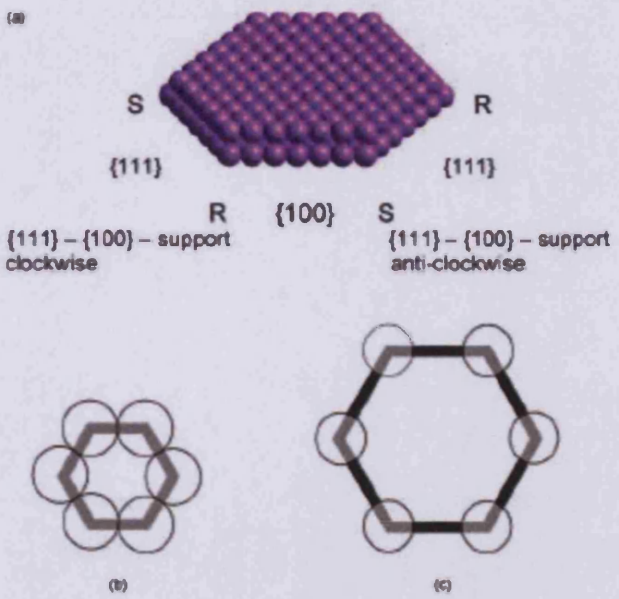

Figure 1.9 (a) A schematic presentation of an hexagonal bi-layer of platinum atoms on a support surface, showing the edge structures which define chirality at the kink sites; (b) optimum arrangement of diastereoisomeric enantioselective sites (open circles) formed by alkaloid adsorption at the chiral kink sites around an hexagonal platinum particle; (c) non-optimum arrangement of such sites around a larger platinum particle. Reprinted from [84].

1.3.7 Modifier

The enantioselectivity of the Orito reaction was derived from the modification of the catalyst surface with cinchona alkaloids, so called as they are extracted from the bark of *Cinchona Ledgeriana*. The most recognised of the cinchona alkaloid series is quinine (QNE) which has commercial uses for its anti-malarial properties and as flavour additive in some beverages and is also used as a modifier in the Orito reaction.

CD and its near enantiomer CN (Figure 1.10) were the original choice of alkaloids for chirally modifying the supported platinum catalyst surface and are still yet to be surpassed in terms of enantioselectivity and rate by any other modifier. The cinchona alkaloid can be divided into three sections; the aromatic quinoline (Q) ring system thought to be responsible for anchoring the alkaloid to the metallic surface, quinuclidine (QN); an aliphatic ring system containing a tertiary nitrogen believed to have a leading role in facilitating complexation with the reactant and a stereogenic centre directing the sense of chirality of the product.

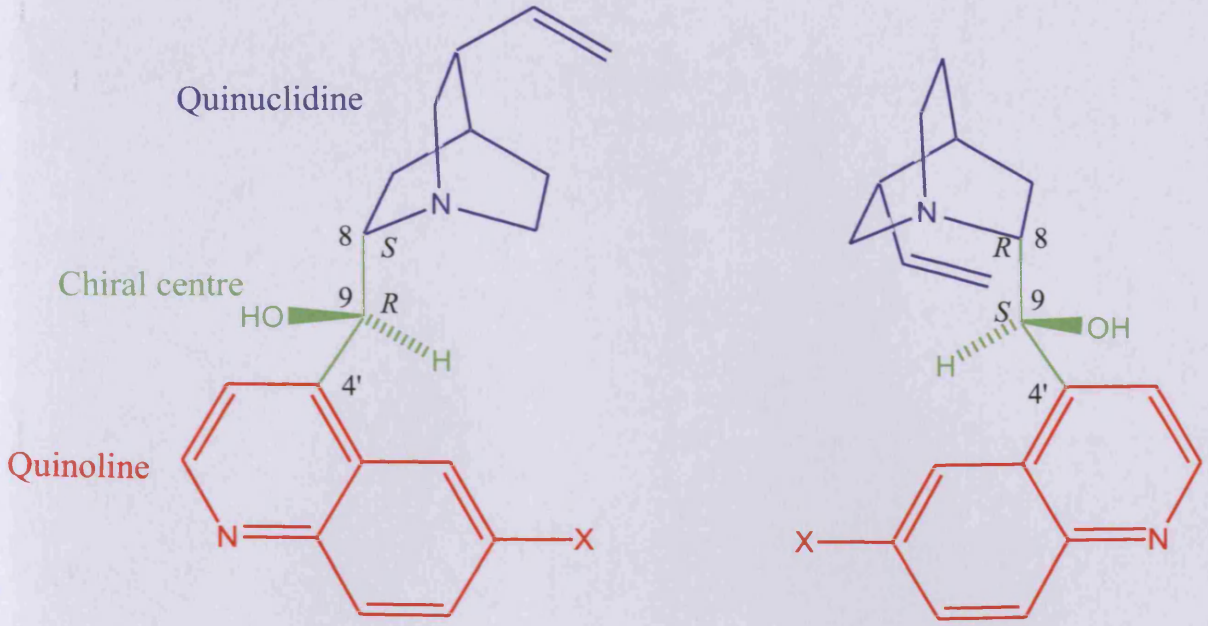

Cinchonidine Cinchonine

Figure 1.10 Structures of the cinchona alkaloids used in the Orito reaction. The functional group X is a hydrogen for CD and CN and a methoxy group for quinine and quinidine respectively.

A rotation about the C8-C9 bond can result in the tertiary nitrogen of the QN moiety pointing down towards the Q ring, known as 'closed', or pointing to the surface (away from the aromatic ring electrons), known as 'open' conformation. In addition, a rotation about the C4′-C9 bond results in the benzene ring of the Q moiety being behind the QN ring. This leads to four possible conformations of the alkaloid in the liquid phase. Deuterium exchange experiments performed on CD adsorbed on a platinum surface by Wells and colleagues has revealed that the Q ring does indeed interact with the surface [86]. This can now be considered when addressing the possible conformations of the adsorbed modifier. Baiker and co-workers used a first-principles calculation to establish eight different surface adsorbed conformations [87].

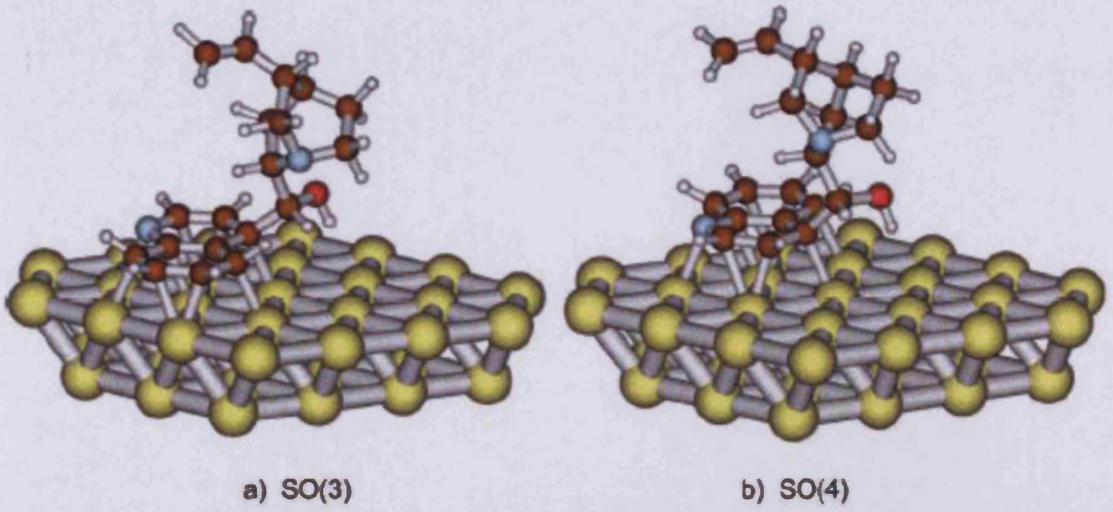

Figure 1.11 (a) Surface Open(3) (SO(3)) and (b) Surface Open(4) (SO(4)) conformations of CD on a platinum surface. Reprinted from [87].

The conformation that was thought to be prevalent on the surface is that depicted by Figure 1.11 (a) – 'open 3', which through theoretical calculations was shown to have the lowest minimum energy structure of all postulated conformers [88]. In this configuration, the Q ring was suggested as lying flat on the plane of the surface. This calculation corroborated several spectral analyses performed on CD adsorbed onto a platinum surface, the majority of which have used the various applications of Infra-Red spectroscopy and surface sensitive Raman [89,90]. The flat orientation was evidenced to occur at solution concentrations below a certain value. Above this value, the Q ring tilted away from the plane parallel to the surface and was thought to be the result of close packing of the modifier to accommodate more molecules on the surface [91]. This concentration also coincided with a drop in the rate and selectivity of the reaction [76]. Scanning Tunnelling Microscopy (STM) has also been employed to add further evidence for the 'open 3' adsorption geometry [92]. Although in reference 92 the STM images were not clear enough to determine the adsorption geometry, a clear mode was favoured through its lack of mobility across the surface. This was related to a stronger interaction with the surface and led to the assignment of this species to a flat adsorbed 'open 3' configuration.

Another curiosity to the Orito reaction is the non-linear effect (NLE) seen with different modifiers [93]. This was likened to the phenomenon in homogeneous catalysis whereby a different strength of interaction with a racemic mixture of chiral auxiliaries still led to an

enantiomeric excess of the product [94]. It was thought that the main reason for NLE in Orito type chemistry was from different adsorption strengths for different modifiers [95], but may be further directed by the adsorption mode [96]. A study with CD and quinidine (QD) found that CD preferentially modified the surface because it was more strongly adsorbed on account of CD adopting a flat (strong) adsorption geometry and QD adopting a more tilted (weak) adsorption geometry [96]. The NLE in the hydrogenation of EP was tested with several modifiers, the trend for the adsorption strength was found to decrease in the order CD>CN>QNE>QD in toluene and CD>QNE>CN>QD in acetic acid [97,98]. With the use of ATR-IR, Zaera *et al* determined that the adsorption strength decreased as follows CN>QD>CD>QNE [99]. However, these experiments were not conducted at reaction conditions, with particular reference to the low hydrogen coverage, which may be the source of disparity between the two trends. Further differences were seen in the NLE with different reactants [100]. In terms of the adsorption strength, it was found that QNE>CN in the hydrogenation of EP, but CN>QNE in the hydrogenation of KPL. Acetic acid as solvent was also found to be favourable to QNE, but toluene was found to be favourable to CN. The differences seen for the choice of solvent was thought to be a function of modifier solubility [97] (QNE is more soluble in acetic acid [103]). The differences seen with the choice of reactant was thought to be due to a specific interaction between the reactant and the modifier, such as the ease of desorption of the reactant-modifier complex [100].

1.3.8 Solvents

Choosing the correct solvent is paramount to achieving the best performance from the Orito reaction. It has been previously recognised that the hydrogenation of α-ketoesters was best using solvents of a dielectric constant between 2 and 10. The same could not be said of α-ketoacids where the results were more sporadic [55].

The population of the 'open 3' conformation of CD was thought to play a key role in enantioselection as a function of dielectric constant [101,102]. Zaera *et al* published data on the solubility of the modifier in a variety of solvents and established a correlation between solvent polarity/dielectric constant with the cinchona solubility [103] (Figure 1.12). Further to this, the lifetime of the modifier on the surface was lower with solvents of high cinchona solubility through ease of desorption, which led to the proposed explanation for NLE as discussed above. This statement was illustrated from a study using multiple cinchona

modifiers in the reaction slurry [96]. The enantioselectivity was found to be directed by the modifier that was least soluble leading to a greater lifetime on the surface. When applying this postulate of the lifetime of the modifier on the surface to the choice of solvent, it should be noted that the lifetime needs to be long enough to induce enantiodiscrimination, but not too long so as to poison the catalyst surface by blocking reaction sites [103] as described by the Sabatier principle.

An exception to this trend occurred with acetic acid where it can be seen that the solubility of CD is the highest in the range of solvents examined by Zaera *et al* (data point #32, Figure 1.12), yet it was acetic acid where the best selectivities were achieved [80]. The pH of the solvent may contribute to the reaction performance of acetic acid as an NMR study revealed a protonation of the basic tertiary nitrogen, which allowed the opportunity for hydrogen bonding to occur between the modifier and a carbonyl group on the reactant [104].

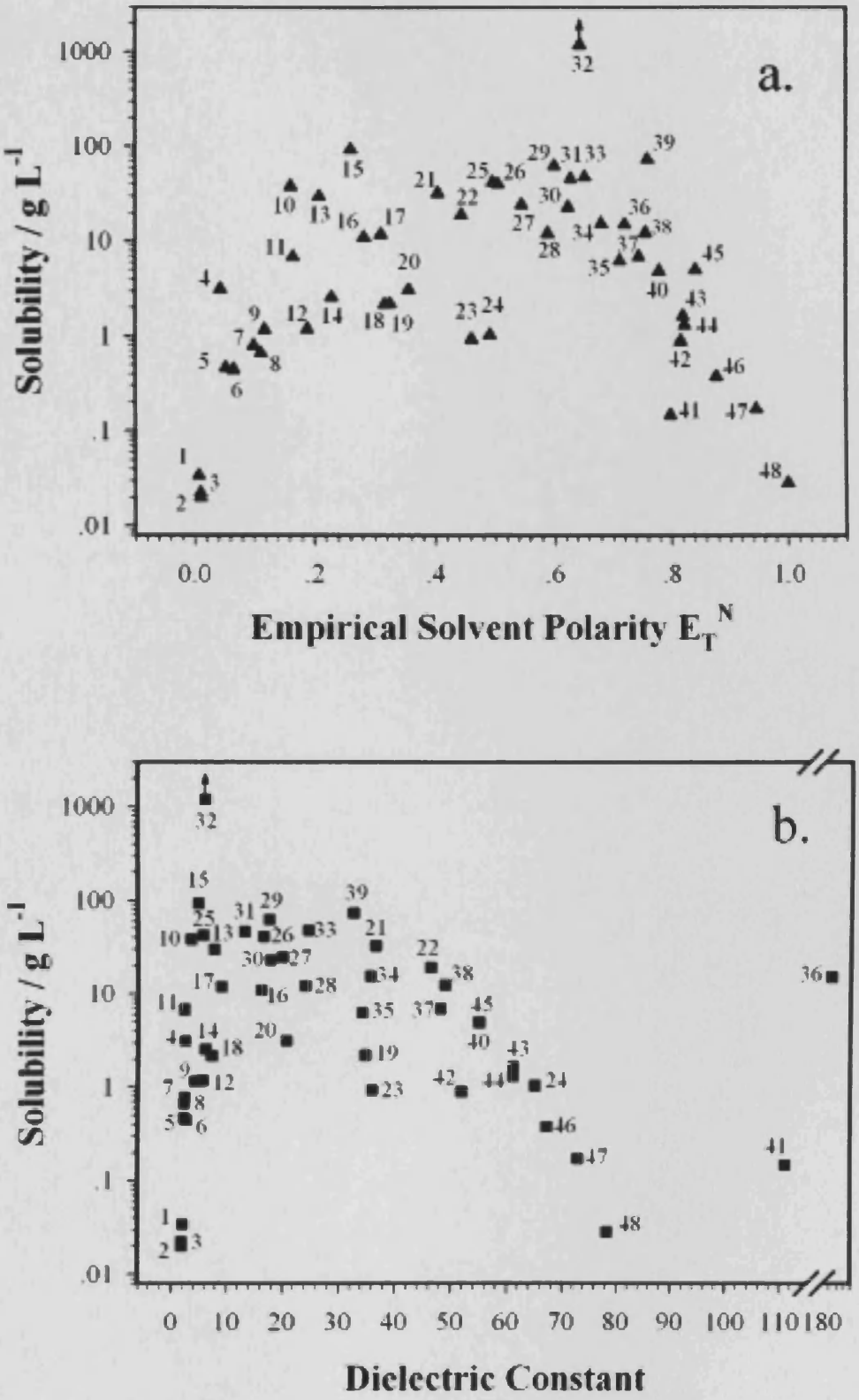

Figure 1.12 (a.) Polarity of 48 different solvents *vs.* solubility of CD, (b.) Dielectric constant *vs.* solubility of CD. Each number referred to a different solvent used to dissolve the modifier. Reprinted from [103].

Solvent effects on the reactant have not been explored very much. A study involving alcoholic solvents identified the formation of a hemiketal by reaction of an α-ketoester with an alcohol (Figure 1.13) [110]. Formation of high molecular mass products (HMMPs) like the hemiketal was postulated to be detrimental to the reaction as was reflected in the reaction performance in alcoholic solvents. This side reaction was determined to occur on alumina supported platinum and was thought to be sensitive to the acidic nature of the support and also the basic nature of the tertiary nitrogen on the QN moiety of CD.

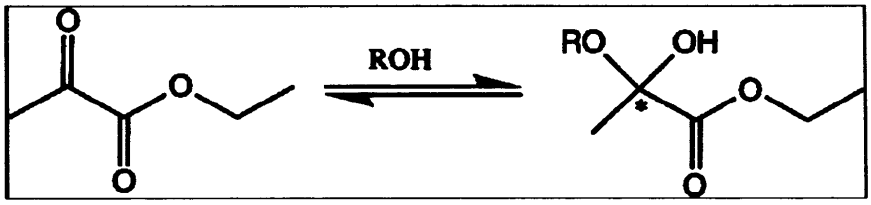

Figure 1.13 Reaction of EP with an alcoholic solvent to produce a hemiketal. Reprinted from [110].

The two solvents found to be most successful for the Orito reaction were toluene and acetic acid. However, despite the fact that properties such as the dielectric constant, modifier solubility and hydrogen solubility favour toluene, it was acetic acid that provided the best performance with good rates and high ee's at low modifier loading [105].

It was not only in the liquid phase where the Orito reaction was reported to proceed. Supercritical ethane is a medium that has been successfully implemented for this reaction with high reaction rates and ee up to 75% being observed [106]. Gas phase experiments of EP hydrogenation on CD modified platinum have yielded an ee of 51%, but, the rate was decelerated by modification in contrast to the liquid phase reaction [107]. However, both of these media are only applicable to those reactants that exhibit a high vapour pressure.

1.3.9 Side Reactions

As well as the main hydrogenation reaction to form a chiral alcohol, other less significant side reactions are known to occur during the Orito reaction most of which are detrimental to the reaction performance. The activated ketone and alcoholic solvents will decompose on platinum to form carbon monoxide (CO) - a known catalytic poison. CO formation was found to be suppressed and even removed by the action of the modifier and dissolved hydrogen [108, 66, 151]. As well as decomposition, short chain alcohols may also form hemiketals with

an activated ketone, which may also undergo hydrogenation [109]. Hemiketal formation can be catalysed by both the basic cinchona modifier and the acidic alumina catalyst support. The hydrogenation of hemiketals was thought to be insignificant compared to the main hydrogenation reaction, as reaction calorimetry and hydrogen uptake data were unable to detect the hydrogenated hemiketal product. However, there was a possibility that in reference [110], the study of the heats and rates of reaction were identical for both ketone and hemiketal hydrogenation.

Enolisable compounds are capable of undergoing aldol condensation to form HMMPs which could feasibly poison active sites on the catalyst. EP and MP are enolisable compounds that have been shown to condense into oligomers and extensive polymer chains on low index platinum surfaces in the absence of hydrogen and modifier under high vacuum [111, 112], and at more ambient conditions on the alumina support [115]. Polymerisation was shown to be reversible (addition of hydrogen reversed the reaction to generate the monomer) and therefore was thought not to pose a significant threat to the reaction performance [113]. The aldol reaction has also been shown to develop in solution of non-acidic solvents, catalysed by CD. This behaviour can sometimes have a beneficial effect as the *enol* of the aldol product potentially could protonate the QN nitrogen of the modifier CD, which was known to have a positive influence on the reaction performance as mentioned earlier [114]. However, in acidic media the aldol condensation should be inhibited (as should the decomposition of EP on alumina) [115] since the nucleophilic tertiary nitrogen on CD will be protonated.

Not only was the hydrogenation of ketones catalysed by platinum, but also the protonation of the quinoline (Q) ring of the modifier [116]. The Q ring moiety was responsible for tethering the modifier to the surface and upon hydrogenation of the aromatic system this was no longer the case and led to a loss in enantioselectivity [150]. This was most pronounced after 70% conversion when dihydrocinchonidine (DHCD) was used [117]. Stopping the reaction at this point was found to preserve the activity of the catalyst more effectively which resulted in it being available for re-use [118].

1.3.10 Proposed models for Enantio-Induction

The ultimate question to be answered concerning the Orito reaction, is how does it work? Or more specifically, what is the mechanism for enantioselectivity? Three mechanisms have been proposed. These are referred to as the "template model", the "shielding model" and the "1:1 interaction model".

1.3.10.1 The Template Model

The first attempt to explain the enantiodifferentiation step was based on ordered arrays of the modifier adsorbed on the platinum surface forming "exposed" chiral ensembles of platinum atoms. If CD was the choice of modifier, the α-ketoester reactant in the energetically favoured *s-trans* conformation would then be favoured to adsorb *si*-face down and thereby react to form an *R*-hydroxyester [67]. Similarly, CN would only expose platinum ensembles of opposite chirality leading to formation of an *S*-hydroxyester. The originators of the template model later discounted their model on the basis of surface science experiments including XPS, LEED and NEXAFS that showed no evidence of ordered arrays of CD on a platinum{111} surface [119]. In addition, kinetic studies predicted a different behaviour to models based on the template model [86].

1.3.10.2 The Shielding Model

Proposed by the Margitfalvi group, the shielding model was centred around interactions of the modifier with the reactant in the solution phase prior to adsorption [120]. Upon interaction with the reactant, the modifier is proposed to change to the 'closed' conformation. π-π orbital overlap between the delocalised π system of the Q ring and the conjugated double bond(s) of the carbonyl on the pyruvate molecule occurred together with interaction with the tertiary nitrogen of the QN ring to give rise to the required enantioselective step. It was further suggested that the π-π interaction can have a shielding effect that orientates the reactant in the enantiodifferentiating step on the platinum surface [120]. The model was based on observations made concerning the transient period at the start of the reaction where ee increased monotonically with time. This increase in ee with time was reported as being proportional to the concentration of the modifier. However, the Margitfalvi shielding model lacks a coherent explanation for the observed enantioselectivities at very low modifier concentrations unless the reactant-modifier complex is more strongly adsorbed than the modifier alone [121]. In addition, modifiers fixed in the "open" configuration were

subsequently found to give rates and ee's comparable with CD [125]. Hence, the shielding model has also been discounted.

1.3.10.3 The 1:1 Interaction Model

Wells *et al* first postulated a model involving a hydrogen bond between the tertiary nitrogen from the QN moiety of CD to the alcohol group of a half-hydrogenated intermediate state of the reactant [122]. This 1:1 interaction was first addressed by Blaser *et al* when they reported that alkylation of the tertiary nitrogen led to complete loss of enantioselectivity [123]. It was proposed that the tertiary nitrogen could either undergo a nucleophilic attack on the carbon of the keto, or when protonated, an electrophilic attack on the keto oxygen [124].

In this model, the modifier was adsorbed on the platinum surface via the Q ring, which was thought to be flat against the plane of the surface and adsorbed with an interaction between the aromatic π states and unoccupied metal valence states. The nitrogen in the QN substituent was assumed to be pointing towards the surface area adjacent to the Q ring – the 'open 3' conformation. What is yet to be determined is the exact interaction with the co-adsorbed reactant that gave rise to enantiodiscrimination. Figure 1.14 shows four proposed models of how this interaction might occur.

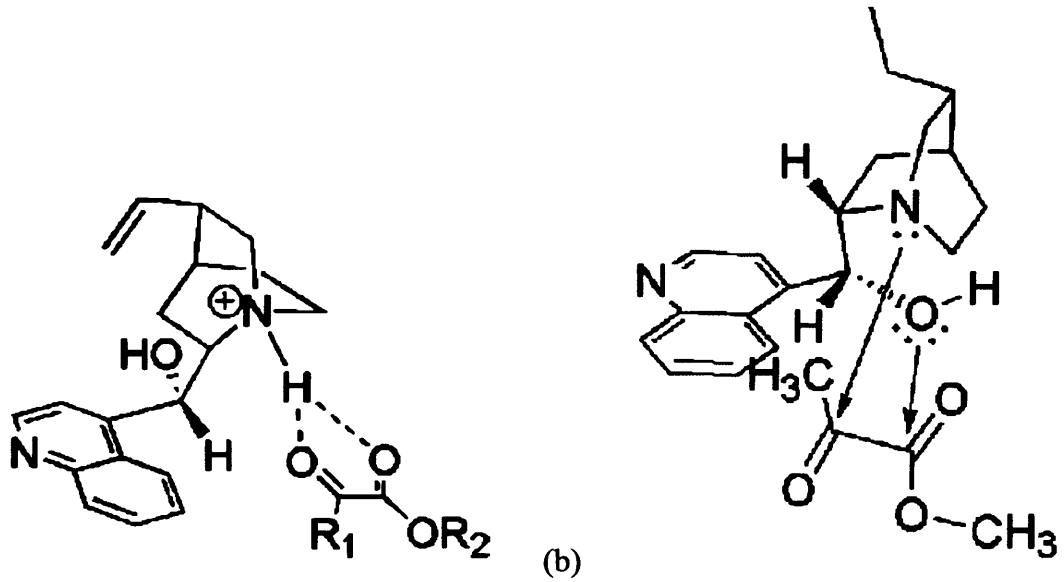

a) (b)

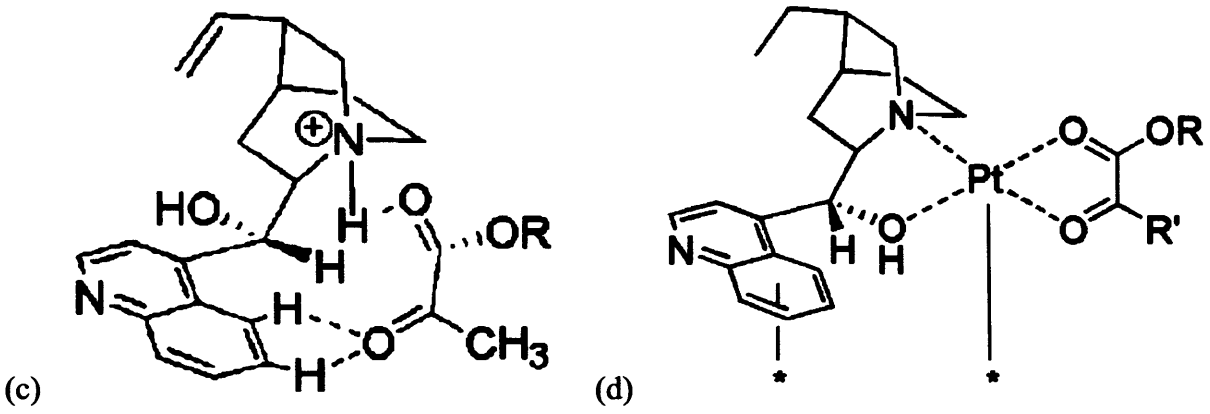

Figure 1.14 Modifier and reactant interactions, (a): Baiker's model, (b): Augustine's model, (c): McBreen's model, (d): Bartok's model. Reprinted from [125].

In Baiker's model, it was suggested that in protic solvents the QN nitrogen was protonated and that this may accept a hydrogen bond from one or both of the carbonyl oxygens on the reactant [126]. In the Augustine model, nucleophilic attack from the QN nitrogen to the electron deficient keto carbon and another nucleophilic attack from the hydroxyl oxygen at C9 on the modifier to the ester carbonyl carbon formed a pseudo six-membered ring [127]. The oxygen of the keto carbonyl is directed towards the surface and is in a favourable position to react and accept hydrogen atoms on the *Si*-face thereby producing *R*-lactate. The McBreen model also proposed two independent links between the modifier and reactant, but suggested that they are hydrogen bonds [128]. In common with Baiker's model, one hydrogen bond occurs between the protonated nitrogen and a carbonyl oxygen. In McBreen's model however, it was the ester carbonyl that was hydrogen bonded to the N-H group. Furthermore, a second hydrogen bond may exist between the keto oxygen and the aromatic C-H groups of the Q ring, activated to accept a hydrogen bond by the platinum surface. The Bartok group, largely agree with Baiker's model that under protic and aprotic solvents, slightly different mechanisms are responsible for the enantiodifferentiation, but also postulated a more significant role of the catalyst with the formation of a ligand complex between the modifier, the reactant and a platinum cluster [105]. However, this model does not describe how enantiodifferentiation occurred.

1.3.11 Rate Enhancement and the Initial Transient Period

One of the most curious experimental observations of the Orito reaction is that there was a marked overall rate enhancement of the hydrogenation reaction on a modified catalyst compared to the racemic reaction on an unmodified catalyst. This effect referred to a macroscopically observed phenomenon and was not a description of the intrinsic rate at modified sites on the molecular level, since the relative number of modified surface sites was unknown. The expected result from adding a relatively large molecule in the form of a cinchona alkaloid to modify the surface was for the rate to decrease due to competitive adsorption and inhibition of the 'free' surface sites.

During the first minutes of the reaction, the observed enantioselectivity and rate gradually increased up to a maximum, after which steady state conditions could be achieved. This is the initial transient period and was seen to occur to a greater or lesser extent in a wide variety of catalytic systems of this type, but was not universal as the effect was absent in other systems. This was well illustrated by Blackmond *et al* in their article on the subject [129]. Kinetically controlled experiments were performed on the EP/CD/Pt system under wide ranging conditions. Not only was the initial transient period unperturbed by changes in reaction conditions, but consistently reached maximum performance at *ca.* 20% EP conversion. They attributed this to an undefined relationship of rate and reaction progress and dismissed the influence of impurities. Although the investigation of EP was thorough, it was not extended to other systems with different magnitudes of rate enhancement. Other authors also questioned the use of alcoholic solvents in such measurements where hemiketal formation with the reactant could distort the results [109]. Therein lies the basis for two theories on this effect. Firstly, those that advocate an inherent relationship between rate enhancement and enantioselectivity, with a faster rate at modified sites. Secondly, those that suggest a suppression of the catalyst deactivation caused by the products of side reactions with the pyruvate ester reactants.

1.3.11.1 Suppression of Catalyst Deactivation

As discussed earlier, it was known that pyruvate esters can undergo side reactions including ester condensation [111], aldol oligomerisation/polymerisation [130] and decarbonylation [108], the products of which can act as catalyst poisons. CO is one such poison and was a product of decarbonylation of EP on platinum and was proposed to strongly adsorb in the

highly coordinated sites that were considered to be favourable for the reaction [108]. Co-adsorption with the modifier not only dramatically decreased the rate of decarbonylation, but also displaced pre-adsorbed CO. Self-condensation of alkyl pyruvates was known to occur and has been shown with MP on platinum{111} using STM and XPS [130]. In the absence of hydrogen, surface adsorbed MP polymerised to form HMMPs that extended across the surface. However, with hydrogen present, this process was reported as being completely suppressed. Although some articles have suggested that the basic nature of the tertiary nitrogen on CD could catalyse this process in aprotic solvents [114], other articles suggest the modifier retards the aldol reaction [83]. Furthermore, in protic solvents the base catalysed reaction that produced the HMMPs was believed to be prevented by protonation of the basic nitrogen [131]. The enantioselectivity has also been decoupled from the rate enhancement by Murzin and colleagues with experiments on silylated CD derivatives [132]. The modifiers were able to enantiodiscriminate to produce the product but were found to decelerate the reaction rate compared to the racemic reaction.

The QN moiety of the modifier was thought to be involved in the rate enhancement observed in the enantioselective reaction, through a ligand type interaction. Through addition of QN to the reaction slurry, the rate improved in both the racemic and enantioselective reaction [86], and was beneficial to ee at low modifier concentrations in the enantioselective reaction. This was accounted for by the suppression of catalyst deactivation [133]. Addition of other achiral tertiary amines was also found to have this "catalyst reactivation" effect [134] and in non-alcoholic solvents, this effect was attributed to suppression of CD dimerisation, which led to the observed increase in rate and ee [135].

No rate enhancement was seen in the gas phase hydrogenation of MP [136]. Analogous reactions in the liquid phase were performed by the authors who found that rate enhancement did occur. Therefore, they speculated that the related effect was due to a difference in the liquid/solid and gas/solid interface behaviour.

1.3.11.2 Ligand Acceleration

The term 'ligand acceleration' was first used to describe this phenomenon because of its similarity with the homogeneous catalytic effects of cinchona alkaloids [137,138]. There was much evidence to show a relationship between rate and ee in the Orito reaction [139,140,141]. Here, it was proposed that a faster rate occurred at the modified sites. In this theory, the interaction between the modifier, reactant and perhaps the surface altered the energetics of the activated ketone of the reactant making it more susceptible to hydrogenation. This was well illustrated by the correlation between the π-orbital stability (ΔE_{orb}) of the reactant carbonyl in acetophenones versus the rate of their hydrogenation (Figure 1.15) [142]. On a modified surface, the rate was thought to increase because of a further stabilisation of the carbonyl π-orbitals in the diastereomeric complex of the reactant and modifier through a hydrogen bond interaction.

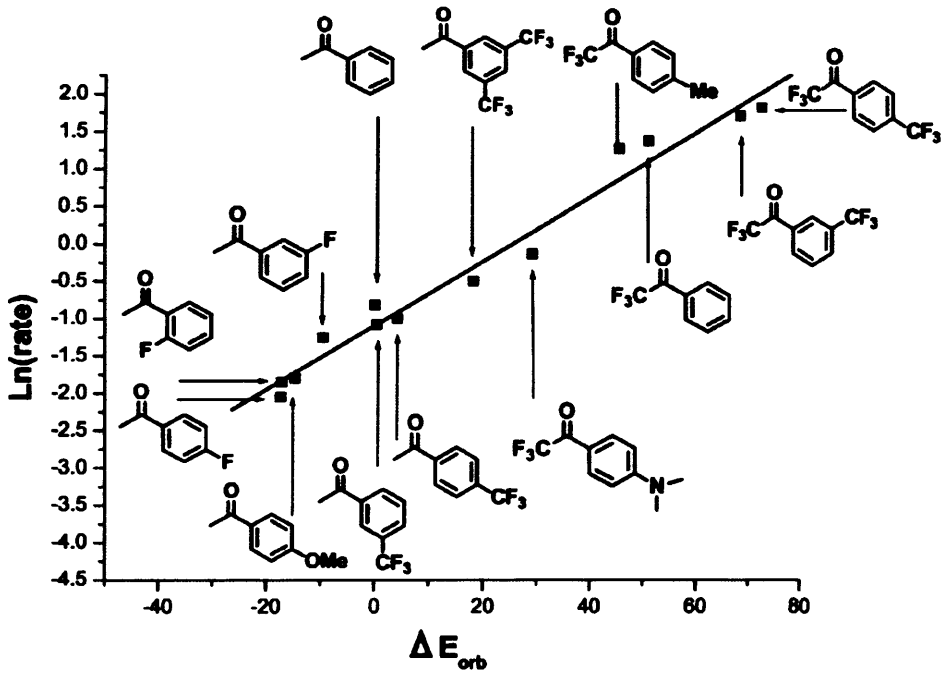

Figure 1.15 π-orbital stability of the carbonyl group in acetophenones *vs.* the observed racemic reaction rate. Reprinted from [142].

Evidence against catalyst deactivation could be seen through the hydrogenation of ketopantolactone (KPL) on platinum. KPL is a cyclic α-ketoester that can not partake in the aldol oligomerisation, and was effected much less by decarbonylation [143], however it did exhibit a hydrogenation rate enhancement in the presence of a variety of modifiers on platinum [48,144] (although it was relatively minimal (≈ ×6 compared to ×10 – ×30)). Thus,

the rate constant for the modified site was deemed to be greater than the rate constant of the unmodified site leading to quantitative kinetic analyses based on the ratio of modified to unmodified sites [145]. In reference 145, the experimentally observed enantioselective rate, *l*, was thought of as a ratio of the enantioselective rate to the racemic rate.

$$l = \frac{k_{mod}\theta_S^e\theta_M + k_u\theta_S^e}{k_u\theta_S} \qquad (1.10)$$

The enantioselective rate was the modified rate constant k_{mod}multiplied by the enantioselective reactant coverage θ_S^e and modifier coverage θ_M plus the racemic rate constant k_u multiplied by θ_S^e. The racemic rate was k_u multiplied by the racemic reactant coverage θ_S.

1.3.12 Kinetic Aspects on Reaction Performance

By altering the reaction conditions (such as concentration of reactant/modifier, amount of catalyst, stirring speed/flow rates, temperature, H_2 pressure etc) in a stepwise fashion, the reaction performance can be optimised and the reaction kinetics may be better understood including reaction mechanism, rate laws, equilibria, activation energy, residence time and possibly the rate enhancement and initial transient period phenomena.

The model reaction using EP as reactant, CD as modifier, platinum as catalyst and an organic solvent was conducted in a batch reactor. A more suitable reactor for industrial manufacture is the fixed bed continuous flow reactor as steady state conditions can be maintained for extended periods unlike the batch reactor where adsorption/desorption equilibria are constantly changing leading to non-linear reaction rates and enantioselectivities.

1.3.12.1 Substrate Concentration

In batch reactors the rate of the racemic reaction was reported to increase with concentration of the substrate, EP, up to 0.1 M where a rate of 57 mmol L^{-1} min^{-1} g^{-1} was reached [66]. In contrast, the rate of the enantioselective reaction continued to increase with concentration up to 2 M of EP reaching a value of 200 mmol L^{-1} min^{-1} g^{-1} with a constant ee [66]. Below a concentration of 0.1 M, no rate enhancement was observed as the racemic and enantioselective rates were similar [66]. This finding was attributed to catalyst deactivation at high reactant concentrations, therefore the rate would be enhanced by the addition of a

modifier. At low concentrations no such deactivation had occurred, therefore rate enhancement would also not occur. The rate enhancement seen at high reactant concentrations with the addition of QN, was also not seen at low reactant concentrations [66] and was again attributed to suppression of catalyst deactivation. Similar to the batch reactor, increasing substrate concentration also increased reaction rate in a fixed bed continuous flow reactor [155], but the ee was shown to slightly decrease at higher concentrations.

1.3.12.2 Modifier Concentration

Using CD as modifier, enantioselectivity was induced at modifier concentrations as low as 1×10^{-7} M in toluene [146]. Both rate and ee increased with CD concentration up to 1×10^{-4} M, above which the ee began to plateau and the rate began to diminish. This was attributed to site blocking by high modifier coverage [146]. The same behaviour was reported to occur using DCM as solvent, although the ee was noted to actually decrease above a certain concentration of CD [61]. Measured under identical conditions, it was found that the concentration of CD was optimal at an order of magnitude lower in acetic acid than in toluene [105]. Reaction performance could be maintained in a fixed bed reactor only when the modifier flux was also maintained [147]. Similar to the batch reactor, by increasing the modifier : reactant ratio, the rate decreased above a certain value, but the ee was maintained [160].

The catalyst could be pre-modified *in situ* by stirring the reaction slurry at a low hydrogen pressure before the reaction was initiated. It could also be performed *ex situ* by mixing the catalyst in a CD solution for 2 hours under anhydrous conditions [148]. Better results were achieved under aerobic conditions [148] where dissolved oxygen was thought to be the source of improved reaction rate [149] and the maintenance of a 90% ee [150]. This was shown not to affect the adsorption of CD [151], but could have been due to restructuring of the catalyst [76]. Other procedures reported to improve catalyst performance included ultra-sonication in the pre-modification process [152] and the addition of a small quantity of water in the reaction medium [153]. The latter method was thought to be a result of improved stability of the open 3 conformer of CD by the presence of pyruvic acid formed via hydrolysis of EP.

1.3.12.3 Hydrogen Pressure, Temperature and Mass Transport Aspects

By increasing the pressure of hydrogen, the rate also continued to increase up to 100 bar, above which the effect on rate was less pronounced [45]. The ee was also affected in a positive way. This was interpreted as being due to a more flat adsorption geometry of the modifier in the presence of hydrogen as observed in spectroscopic studies [91]. However, pressure effects can only be correlated to reaction performance when the rate of diffusion of hydrogen from the gas phase to the liquid phase was high enough to maintain a surface hydrogen equilibrium coverage as described by Blackmond and colleagues [154]. The effect of increasing hydrogen pressure was the same in both reactor types where the rate and ee increases up to 100 bar, above which, both rate and ee plateau [155]. However, by controlling the hydrogen pressure before the introduction of the reaction medium in fixed bed reactors, the initial transient period was found to be prolonged as the pressure increased [156].

Access of the substrate(s) to the catalytic metal particles and the product moving away from the active site is of critical importance to maintaining a high reaction rate. Increasing the stirring speed of the slurry in a batch reactor from 400 to 1000 rpm increased the reaction rate until the diffusion limitations were overcome and the rate levelled off [157]. The hydrogen pressure at which these reactions were performed was considered to be low (548 kPa) and at slow stirring speeds the reaction rate was zero order with respect to the concentration of the reactant EP [158], but was found to be first order for the concentration of solution phase hydrogen. However, the effect was less pronounced at fast stirring speeds and/or high hydrogen pressures [159]. Both ee and rate increased in the fixed bed reactor when the liquid flow rate through the reactor and was optimised at 4.3 mL/min [160].

Increasing the temperature also improved reaction rate for EP hydrogenation, but above 40°C a loss of ee was observed [67]. Thermal desorption of the modifier and/or a reorientation of the surface modifier was thought to be the cause of this behaviour [159].

It is clear that the various models of rate enhancement and enantiodiscrimination are still far from understood. Spectroscopic methods of identifying surface intermediates therefore may lead to elucidation of phenomenon directly related to these fundamental aspects of the Orito reaction.

1.4 Project Aims

Using Surface Enhanced Raman Scattering (SERS) and Cyclic Voltammetry (CV) – highly surface sensitive analytical techniques, the Orito reaction is investigated with the following aims:

- To develop a spectro-electrochemical flowcell that will house a working electrode capable of SERS activity.
- To generate SERS activity from a platinum and palladium working electrode.
- To investigate the interaction of EP and other α-ketoesters on platinum and palladium and co-adsorbed with hydrogen.
- To investigate the interaction of CD and other chiral modifiers on platinum and palladium and co-adsorbed with hydrogen.
- To investigate the interaction of EP co-adsorbed with CD on platinum and co-adsorbed with hydrogen.
- To investigate the adsorption behaviour of EP on well defined platinum and palladium surfaces.
- To add further information on the rate enhancement, initial transient period and the enantiodiscriminatory step.

1.5 References

[1] L.M. Dougherty, A. Dollfus, *Journal of the British Astronomical Association*, 99, 4, 183-186, **1989**.

[2] J.B. Biot, *Bull. Soc. Philomath.*, Paris, (**1815**) 190.

[3] L. Pasteur, *C. R. Acad. Sci.*, 26 (**1848**) 535.

[4] J.H. van't Hoff, *Arch. Neerl. Sci. Exacts. Nat.*, 9 (**1874**) 445.

[5] E.L. Eliel, S.H. Wilen, *Stereochemistry of Organic Compounds*, Wiley, **1994**.

[6] R.T. Morrison, R.N. Boyd, *Organic Chemistry*, **1973**, Allyn and Bacon.

[7] W. G. Mcbride, *The Lancet*, Vol. 278, Issue 7216, **1961**, 1358.

[8] H-J. Schmahl, W. Heger, H. Nau, *Toxicol. Lett.*, 45 (**1989**) 23-33.

[9] R.G. Berger, Flavours and Fragrances: Chemistry, Bioprocessing and Sustainability, **2007**, Springer.

[10] A.M. Stalcup, K.H. Ekborg, M.P. Gasper, D.W. Armstrong *J. Agric. Food Chem.* 41 **(1993)**, p. 1684.

[11] J.J. Partridge, B.L. Bray, *Enantioselective Synthesis: The Optimum Solution*, Ed. K.G. Gadasmasetti, *Process Chemistry in the Pharmaceutical Industry*, Marcel Dekker, New York, N.Y., **1999**.

[12] P. Wang, S. Jiang, D. Liu, H. Zhang, Z. Zhou, *J. Agric. Food Chem.*, **2006**, 54 (5), pp 1577–1583.

[13] G. Rothenberg, Catalysis, Wiley-VCH, **2008**.

[14] G. Quinkert, E. Egert, C. Griesinger, Aspects of Organic Chemistry, Helvetica Chimica Acta, **1996**.

[15] Hans-Ulrich Blaser, ***Chem. Commun.***, **2003**, 293 – 296.

[16] Nobel Lectures, *Angew. Chem., Int. Ed.*, **2002**, 41, 998–2022.

[17] J.M. Thomas, W.J. Thomas, *Introduction to the Principles of Heterogeneous Catalysis*, **1967**, Academic Press Inc.

[18] E.K. Rideal, H.S. Taylor, *Catalysis in Theory and Practice*, **1926**, Macmillan.

[19] A. I. Boronin, P. A. Zhdan, V. P. Khruschev, *React. Kinet. Catal. Lett.*, Vol. 18, No. 1-2, 181-185 **(1981)**.

[20] A.F. Innocentea, A.C.D. Angelo, *J. Power Sources*, 162 **(2006)** 151–159.

[21] K. W. Kolasinski, *Surface Science*, **2002**, Wiley.

[22] A.W. Gauger, H.S. Taylor, *J. Am. Chem. Soc.*, 45 **(1923)** 920.

[23] I. Langmuir, *J. Am. Chem. Soc.* 40, 1361 **(1918)**.

[24] G.M. Schwab, L. Rudolph, *Naturwiss*, 20 **(1932)** 362.

[25] K. Harada, T. Yoshika, *Naturwiss.*, 57 **(1970)** 131.

[26] A.A. Balandin, E.I. Klabunovskii, Y.I. Petrov, *Dokl. Akad. Nauk. SSSR*, 127 **(1959)** 557.

[27] S. Akabori, S. Sakurai, Y. Izumi and Y. Fujii, *Nature*, 178 **(1956)** 323.

[28] D. Lipkin, T.D. Stewart, *J. Am. Chem. Soc.*, 61 **(1939)** 3295.

[29] T. Yoshida, K. Harada, *Bull. Chim. Soc. Japan*, 44 **(1971)** 1062.

[30] M. Besson, P. Gallezot, C. Pinel, S. Neto, Paper O29, *Abstracts of the 4th International Symposium on Heterogeneous catalysis and Fine Chemicals* (New Swiss Chemical Society, **1996**) 84.

[31] Y. Izumi, *Adv. Catal.*, 32 **(1983)** 215.

[32] Y. Orito, S. Imai, S.J. Niwa, *Chem. Soc. Jpn.*, **1979**, 8, 1118.

[33] http://www.anl.gov/Media_Center/Argonne_News/news98/an980316.html

[34] N.R. Avery, W.H. Weinberg, A.B. Anton, B.H. Toby, *Phys. Rev. Lett.*, 51 (**1983**) 682.

[35] N.R. Avery, *Surf. Sci.*, 125 (**1983**) 771.

[36] T. Burgi, F. Atamny, A. Knop-Gericke, M. Havecker, T. Schedel-Niedrig, R. Schlogl, A. Baiker, *Catal. Lett.*, 66 (**2000**) 109-112.

[37] O. Schwalm, B. Minder, J. Weber, A. Baiker, *Catal. Lett.*, 23 (**1994**) 271.

[38] T. Burgi, F. Atamny, R. Schlogl, A. Baiker, *J. Phys. Chem. B*, **2000**, 104, 5953-5960.

[39] G. Blyholder, *J. Phys. Chem.* **1964**, 68, 2772.

[40] A. Vargas, T. Bürgi, A. Baiker, *J. Catal.*, 222 (**2004**) 439–449.

[41] S. Lavoie, M.A. Laliberte, P.H. McBreen, *J. Am. Chem. Soc.*, **2003**, 125, 15756-15757.

[42] C. Fleming, J. Johnston, M. Kadodwala, *Surf. Sci.*, 601 (**2007**) 5485–5491.

[43] M. Castonguay, J.R. Roy, A. Rochefort, P.H. McBreen, *J. Am. Chem. Soc.*, **2000**, 122, 518-524.

[44] A. Rochefort, P. McBreen, *J. Phys. Chem. A*, **2001**, 105, 1320-1325.

[45] H.U. Blaser, H.P. Jalett, Wiehl, D.M. Monti, J.F. Reber, Wehrli, *Stud. Surf. Sci. Catal.*, **1988**, 41, 153.

[46] P. B. Wells, A. G. Wilkinson, *Top. Catal.*, 5 (**1998**) 39–50.

[47] S. Hanessian, *Total Synthesis of Natural Products: The Chiron Approach*, Pergamon Press, New York, **1983** (Chapter 2).

[48] E. Orglmeister, T. Mallat, A. Baiker, *Adv. Synth. Catal.*, **2005**, 347, 78–86.

[49] A. Vargas, F. Hoxha, N. Bonalumi, T. Mallat, A. Baiker, *J. Catal.*, 240 (**2006**) 203–212.

[50] S. Diezi, S. Reimann, N. Bonalumi, T. Mallat, A. Baiker, *J. Catal.*, 239 (**2006**) 255–262.

[51] K. Szöri, M. Sutyinszki, K. Felföldi, M. Bartók, *Appl. Catal. A: Gen.*, 237(**2002**) 275.

[52] M. Sutyinszki, K. Szöri, K. Felföldi, M. Bartók, *Catal. Lett.*, Vol 81, no. 3-4, August **2002**.

[53] N. Issacs, *Physical Organic Chemistry*, 2nd edition, chapter 4 (**1995**).

[54] R. Hess, T. Mallat, A. Baiker, *J. Catal.*, 218 (**2003**) 453–456.

[55] H.U. Blaser, H.P. Jalett, *Stud. Surf. Sci. Catal.*, 78 (**1993**) 139.

[56] G.-Z.Wang, T. Mallat, A. Baiker, *Tetrahedron: Asymmetry*, 8 (**1997**) 2133.

[57] M. Schürch, N. Künzle, T. Mallat, A. Baiker, *J. Catal.* 176 (**1998**) 569.

[58] A. Szabo, N. Künzle, T. Mallat, A. Baiker, *Tetrahedron: Asymmetry*, 10 (**1999**) 61.

[59] B. Török, K. Felföldi, K. Balàzsik, M. Bartók, *Chem. Commun.* (**1999**) 1725.

[60] W.A.H. Vermeer, A. Fulford, P. Johnston, P.B.Wells, *J. Chem. Soc. Chem. Commun.* (**1993**) 1053.

[61] X. Li, N. Dummer, R. Jenkins, R. P.K. Wells, P. B. Wells, D. J. Willock, S. H. Taylor, P. Johnston, G. J. Hutchings, *Catal. Lett.*, Vol. 96, Nos. 3–4, **2004.**

[62] N.B. Johnson, I.C. Lennon, P.H. Moran, J.A. Ramsden, *Acc. Chem. Res.* 40 (**2007**) 12 1291-1299.

[63] M. Jahjah, M. Alame, S. Pellet-Rostaing, M. Lemaire, *Tetrahedron: Asymmetry.* 18 (**2007**) 2305-2312.

[64] T. Osawa, T. Harada, A. Tai, *Catal. Today*, 37, 4 (**1997**) 465-480.

[65] H.J. Yan, D. Wang, M.J. Han, L.J. Wan, C.L. Bai, *Langmuir*, 20, 18, **2004**, 7360-7364.

[66] E. Toukoniitty, D. Y. Murzin, *J. Catal.* 241 (**2006**) 96–102.

[67] I.M. Sutherland, A. Ibbotson, R.B. Moyes, P.B. Wells, *J. Catal.* 125, 77 (**1990**).

[68] G.C. Bond, J.J. Phillipson, P.B. Wells, J.M. Winterbottom, *Trans. Faraday Soc.*, 60 (**1964**) 1847.

[69] K.E. Simons, A. Ibbotson, P. Johnston, H. Plum, P.G. Wells, *J. Catal.*, 150, 321-328 (**1994**).

[70] T. Marzialetti, M. Oportus, D. Ruiz, J.L.G. Fierro, P. Reyes, *Catal. Today* 133–135 (**2008**) 711–719.

[71] O. J. Sonderegger, G. M.-W. Ho, T. Bürgi, A. Baiker, *J. Catal.*, 230 (**2005**) 499–506.

[72] T.J. Hall, P. Johnston, W.A.H. Vermeer, S.R. Watson, P.B. Wells, *Stud. Surf. Sci. Catal.*, 101 (**1996**) 221.

[73] P.J. Collier, T.J. Hall, J.A. Iggo, P. Johnston, J.A. Slipszenko, P.B. Wells, R. Whyman, *Chem. Commun.*, 14, 1451-1452, **1998**.

[74] G. Szollosi, B. Herman, K. Felfoldi, F. Fulop, M. Bartok, *J. Mol. Cat. A: Chem.* 290 (**2008**) 54–59.

[75] K. Balazsik, B. Torok, G. Szakonyic, M. Bartok, *App. Catal. A: General*, 182 (**1999**) 53±63.

[76] M. Studer, H-U. Blaser, C. Exner, *Adv. Synth. Catal.*, **2003**, 345, No. 1+2.

[77] A. Baiker, *J. Mol. Cat. A.: chemical*, 115 (**1997**) 473-493.

[78] M. Bartok, K. Balazsik, G. Szollosi, T. Bartok, *Catal. Commun.*, 2 (**2001**) 269-272.

[79] M. Bartok, T. Bartok, G. Szollosi, K. Felfoldi, *Catal. Lett.*, 61 (**1999**) 57.

[80] X. Zuo, H. Liu, M. Liu, *Tetrahedron Lett.*, 39 (**1998**) 1941-1944.

[81] X. Zuo, H. Liu, D. Guo, X. Yang, *Tetrahedron*, **1999**, 55, 7787–7804.

[82] T.J. Hall, J.E. Halder, G.J. Hutchings, R.L. Jenkins, P. Johnston, P. McMorn, P.B. Wells, R.P.K. Wells, *Top. Catal.*, 11/12 (**2000**) 351–357.

[83] D.J. Jenkins, A.M.S. Alabdulrahman, G.A. Attard, K.G. Griffin, P. Johnston, P.B. Wells, *J. Catal.*, 234 (**2005**) 230–239.

[84] G.A. Attard, K.G. Griffin, D.J. Jenkins, P. Johnston, P.B. Wells, *Catal. Today*, 114 (**2006**) 346–352.

[85] R. Hess, F. Krumeich, T. Mallat, A. Baiker, *Catal. Lett.*, 92 (**2004**) 141.

[86] G. Bond, P.A. Meheux, A. Ibbotson, P.B. Wells, *Catal. Today*, 10 (**1991**) 371.

[87] A. Vargas, A. Baiker, *J. Catal.*, 239 (**2006**) 220–226.

[88] A. Vargas, T. Bürgi, A. Baiker, *J. Catal.*, 226 (**2004**) 69–82.

[89] R. J. LeBlanc, C. T. Williams, *J. Mol. Cat. A: Chem.*, 220 (**2004**) 207–214.

[90] A. Vargas, D. Ferri, A. Baiker, *J. Catal.* 236 (**2005**) 1–8.

[91] R. J. LeBlanc, W. Chu, C. T. Williams, *J. Mol. Cat. A: Chem.*, 212 (**2004**) 277–289.

[92] M. von Arx, M. Wahl, T. A. Jung, A Baiker, *Phys . Chem. Chem. Phys.*, **2005**, 7 , 273–277.

[93] K.E. Simons, P.A. Meheux, S.P. Griffiths, I.M.Sutherland, P. Johnston, P.B. Wells, A.F. Carley, M.K. Rajumon, M.W.Roberts, A. Ibbotson, *Recl. Trav. Chim. Pays-Bas.*, **1994**, 113, 465.

[94] M. Avalos, R. Babiano, P. Cintas, J.L. Jimenez, J.C. Palacios, *Tetrahedron: Asymmetry* **1997**, 8, 2997.

[95] M. Wahl, M. von Arx, T.A. Jung, A. Baiker, *J. Phys. Chem. B*, **2006**, 110, 21777.

[96] W.R.Huck, T. Mallat, A. Baiker, *Catal. Lett.*, **2003**, 87, 241.

[97] M. Bartok, M Sutyinszki, K. Balazsik, G. Szollsi, *Catal. Lett.*, 100, 3–4, **2005**.

[98] D.M. Meier, D. Ferri, T. Mallat, A. Baiker, *J. Catal.* 248 (**2007**) 68–76.

[99] Z. Ma, I. Lee, F. Zaera, *J. Am. Chem. Soc.*, **2007**, 129, 16083-16090.

[100] K. Balazsik, S. Cserenyi, G. Szollosi, F. Fulop, M. Bartok, *Catal. Lett.*, (**2008**) 125:401–407.

[101] H.U. Blaser, H.P. Jalett, J. Wiehl, *J. Mol. Catal.*, 68 (**1991**) 215.

[102] T. Burgi, A. Baiker, *J. Am. Chem. Soc.*, **1998**, 120, 12920.

[103] Z. Ma, F. Zaera, *J. Phys. Chem. B*, **2005**, 109, 406-414.

[104] B. Minder, T. Mallat, P. Skrabal, A. Baiker, *Catal. Lett.* 29 (**1994**) 115.

[105] M. Bartok, K. Balazsik, T. Bartok, Z. Kele, *Catal. Lett.*, Vol. 87, Nos. 3–4, April **2003**.

[106] R. Wandeler, N. Kunzle, M. S. Schneider, T. Mallat, A. Baiker, *J. Catal.* 200, 377–388 (**2000**).

[107] M. von Arx, N. Dummer, D. J. Willock, S. H. Taylor, R. P. K. Wells, P. B. Wells, G. J. Hutchings, *Chem. Commun.*, **2003**, 1926–1927.

[108] D. Ferri, T. Burgi, A. Baiker, *J. Phys. Chem. B*, **2004**, 108, 14384-14391.

[109] T. Mallat, Z. Bodnar, B. Minder, K. Borszeky, A. Baiker, *J. Catal.* 168, 183–193 (**1997**).

[110] F. M. Bohnen, A. Gamez, D. G. Blackmond, *J. Catal.*, 179, 335–338 (**1998**).

[111] J.M. Bonello, E.C.H. Sykes, R. Lindsay, F.J. Williams, A.K. Santra, R.M Lambert, *Surf. Sci.*, 482-485 (**2001**) 207-214.

[112] J. M. Bonello, R. M. Lambert, N. Kunzle, A. Baiker, *J. Am. Chem. Soc.*, **2000**, 122, 9864-9865.

[113] S. Lavoie, M-A. Laliberte, G. Mahieu, V. Demers-Carpentier, P. McBreen, *J. Am. Chem. Soc.*, **2007**, 129, 11668-11669.

[114] D. Ferri, T. Burgi, K. Borszeky, T. Mallat, A. Baiker, *J. Catal.*, 193, 139–144 (**2000**).

[115] D. Ferri, S. Diezi, M. Maciejewski, A. Baiker, *App. Cat A: General*, 297 (**2006**) 165–173.

[116] H.-U. Blaser, H.P. Jalett, W. Lottenbach, M. Studer, *J. Am.Chem. Soc.*, 122 (**2000**) 12675.

[117] M. Bartok, G. Szollosi, K. Balazsik, T. Bartok, *J. Mol. Catal. A: Chemical*, 177 (**2002**) 299–305.

[118] V. Morawsky, U. Pruße, L. Witte, K.-D. Vorlop, *Catal.Commun.*, 1 (**2000**) 15.

[119] A.F. Carley, M.K. Rajumon, M.W. Roberts, P.B. Wells, *J. Chem. Soc. Faraday Trans.*, 91 (**1995**) 2167.

[120] J.L. Margitfalvi, M. Hegedus, E. Tfirst, *Tetrahedron: Asymmetry*, Vol. 7, No. 2, pp. 571-580, **1996.**

[121] H.-U. Blaser, H.-P. Jalett, M. Muller, M. Studer, *Catal. Today*, 37 (**1997**) 441—463.

[122] G. Webb, P.B. Wells, *Catal. today*, 12, 319, (**1992**)

[123] H.U. Blaser, H.P. Jalett, D.M. Monti, A. Baiker, J.T. Wehrli, *Stud. Surf. Sci. Catal.* 67 (**1991**) 147.

[124] O.Schwalm, J. Weber, J. Margitfalvi, A. Baiker, *J. Mol. Struct.*, 297 (**1993**) 285.

[125] M. Bartok, K. Felfoldi, G. Szollosi, T. Bartok, *Catal. Lett.*, 61 (**1999**) 1–5.

[126] T. Burgi, A. Baiker, *Acc. Chem. Res.* **2004**, 37, 909-917.

[127] R.L. Augustine, S.K. Tanielyan, *J. Mol. Cat. A: Chemical* 112 **(1996)** 93-104.

[128] S. Lavoie, M-A. Laliberte, I. Temprano, P.H. McBreen, *J. Am. Chem. Soc.* **2006**, 128, 7588-7593.

[129] J. Wang, Y. Sun, C. LeBlond, R.N. Landau, D.G. Blackmond, *J. Catal.*, 161, 752–758 **(1996)**.

[130] J.M. Bonello, F.J. Williams, A.K. Santra and R.M. Lambert, *J. Phys. Chem. B* 104 **(2000)** 9696.

[131] A. Kraynov, R. Richards, *Appl. Catal. A Gen.* 314 **(2006)** 1.

[132] I. Busygin, E. Toukoniitty, R. Sillanpää, D. Murzin, R. Leino, *Eur. J. Org. Chem.* **2005**, 13, 2811.

[133] J.L. Margitfalvi, E. Talas, M. Hegedus, *Chem. Commun.* **(1999)** 645.

[134] J.L. Margitfalvi, E. Talas, E. Tfirst, *Top. Catal.*,Vol. 39, Nos. 1–2, **2006.**

[135] J. L. Margitfalvi, E. Talas, F. Zsila, S. Kristyan, *Tetrahedron: Asymmetry*, 18 **(2007)** 750–758.

[136] M. von Arx, G.J. Hutchings, *New J. Chem.*, **2003**, 27, 1367–1370.

[137] M. Garland, H.U. Blaser, *J. Am. Chem. Soc.*, **1990**, 112, 7048.

[138] E.N. Jacobsen, I. Marko, W.S. Mungall, G. Schröder, K.B. Sharpless, *J. Am. Chem. Soc.*, **1988**, 110, 1968–1970.

[139] M. Schürch, T. Heinz, R. Aeschimann, T. Mallat, A. Pfaltz, A. Baiker, *J. Catal.*, **1998** 173, 187.

[140] M. Bartók, K. Felföldi, G. Szöllösi, T. Bartók, *React. Kinet. Catal. Lett.* 68 **(1999)** 371.

[141] S. Cserényi, I. Bucsi, K. Felföldi, *React. Kinet. Catal. Lett.*, **2006,** 87, 395.

[142] A. Vargas, T. Burgi, A. Baiker, *New J. Chem.*, **2002**, 26, 807–810.

[143] N. Bonalumi, T. Burgi, A. Baiker, *J. Am. Chem. Soc.* **2003**, 125, 13342.

[144] M. Schurch, O. Schwalm, T. Mallat, J. Weber, A. Baiker, *J. Catal.* **1997**, 169, 275.

[145] D.Y. Murzin, *J. Mol. Cat. A: Chemical* 289 **(2008)** 91–94.

[146] H.U. Blaser, M. Garland, H.P. Jalett, *J. Catal.*, 144 **(1993)** 569.

[147] N. Kunzle, R. Hess, T. Mallat, A. Baiker, *J. Catal.*, 186, 239–241 **(1999)**.

[148] X. Li, R. P. K. Wells, P. B. Wells, G. J. Hutchings, *Catal. Lett.*,Vol. 89, Nos. 3–4, **2003.**

[149] R. L. Augustine, S. K. Tanielyan, *J. Mol. Cat. A: Chem.* 118 **(1997)** 79-87.

[150] M. Bartok, G. Szollosi, K. Balazsik, T. Bartok, *J. Mol. Cat. A: Chemical*, 177 (**2002**) 299–305.

[151] Z. Ma, J. Kubota, F. Zaera, *J. Catal.* 219 (**2003**) 404–416.

[152] B. Torok, K. Felfoldi, G.Szakonyi, M. Bartok, *Ultrason. Sonochem.* **1997**, 4, 301.

[153] R. P. K. Wells, N. R. McGuire, X. Li, R. L. Jenkins, P. J. Collier, R. Whyman, G. J. Hutchings, *Phys. Chem. Chem. Phys.*, **2002**, 4, 2839–2845.

[154] Y. Sun, R. N. Landau, J. Wang, C. LeBlond, D. G. Blackmond, *J. Am. Chem. Soc.* **1996**, 118, 1348-1353.

[155] N. Künzle, J.-W. Solèr, A. Baiker, *Catal. Today*, 79–80 (**2003**) 503–509.

[156] J.L. Margitfalvi, M. Hegedus, *J. Mol. Catal. A: Chemical*, 107 (**1996**) 281-289.

[157] U.K. Singh, R.N. Landau, Y. Sun, C. Leblond, D.G. Blackmond, S.K. Tanielyan, R.L. Augustine, *J. Catal*, 154, 91-97 (**1995**).

[158] Y. Sun, J. Wang, C. LeBlond, R.N. Landau, D. G. Blackmond, *J. Catal.* 161, 759–765 (**1996**).

[159] R. L. Augustine, S. K. Taoielyaa L. K. Doyle, *Tetrahedron: Asymmetry*, 4, 8, 1803-1827, **1993**.

[160] N. Künzle, J.-W. Solèr, A. Baiker, *Catal. Today*, 79–80 (**2003**) 503–509.

Chapter 2
Theoretical Background

2.1 Surface Structure

2.1.1 Geometrical Structure

The surface of a metal catalyst is a crucial aspect of any heterogeneous catalytic reaction [1]. Hence it is necessary to understand the general physical and structural aspects of metal surfaces. When metals solidify from the molten state, the atoms arrange themselves in a three dimensional, repeating pattern (unit cell) forming a crystal. Typically, the solidified metal will consist of many small crystalline domains (grains) randomly distributed throughout the volume of the metal. As such, it is often referred to at this stage as a polycrystalline material. Since the surface arrangement of atoms must reflect the underlying bulk symmetry, macroscopic measurements on polycrystalline surfaces cannot take into account events occurring at individual sites such as grain boundaries, steps [2] and vacancies [3]. Therefore, any measurement from the surface of such a material is considered an average of all of these sites and the microscopic details are often ignored [4]. The majority of this thesis is concerned with events on polycrystalline surfaces. Where possible, well defined surfaces, derived from cutting single crystals, have been used to extend the understanding of the macroscopic events and isolate particular structural relations between adsorption and surface site.

A single crystal consists of one repeating pattern of atoms extended throughout the material (the unit cell). The pattern is specific to the material. For metals, the most common atom packing arrangement is face-centred cubic (fcc), followed by body-centred cubic (bcc) and hexagonal close-packed (hcp). Platinum and palladium, the transition metals to be studied in the present work, take up the fcc packing arrangement (Figure 2.1).

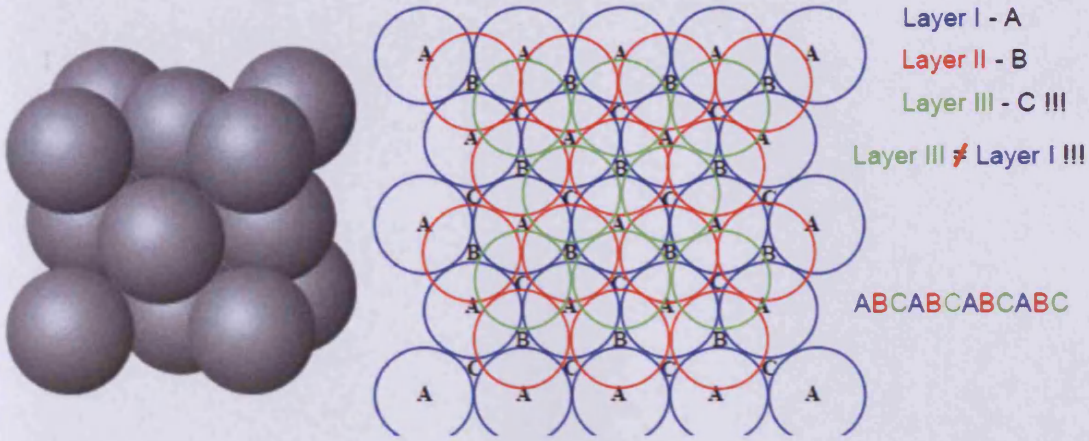

Figure 2.1 Arrangement of atoms in an fcc crystal structure [5].

For fcc metals, the arrangement of the hexagonal layers making up the crystal lattice is repeated every three layers (ABCABC) and is the highest theoretical packing density achievable by packing spheres. The lattice arrangement of hcp metals is very similar but the hexagonal layers are repeated every two rather than every three layers and hence is described as having an ABAB arrangement.

With single crystal surfaces, a surface plane of particular geometrical structure is exposed by cutting through the crystal at a specified angle. The periodicity of the plane is defined using Miller index notation. Miller indices for fcc crystal planes $\{hkl\}$ are defined using three vectors; $\vec{a}$, $\vec{b}$ and $\vec{c}$ (representing the three axes of the unit cell) with the points at which the plane intercepts these axes defined by a, b and c. Where:

$$h = {|\vec{a}|}/{a} \tag{2.1}$$

$$k = {|\vec{b}|}/{b} \tag{2.2}$$

and

$$l = {|\vec{c}|}/{c} \tag{2.3}$$

If *h*, *k* or *l* appear as a fractional value, then all three values of *h*, *k* and *l* are multiplied by a common factor to ensure that all values of *h*, *k* and *l* are integers. For example, if the {*hkl*} values are {1/1,1/2,1/3}, then *h*, *k* and *l* would multiply by 6 to give the Miller index {632}.

The three most commonly investigated single crystals of fcc metal surfaces are the {111}, {110} and {100} surfaces. These are called the "basal" planes, and are depicted schematically in relation to the fcc unit cell in Figure 2.2 [6].

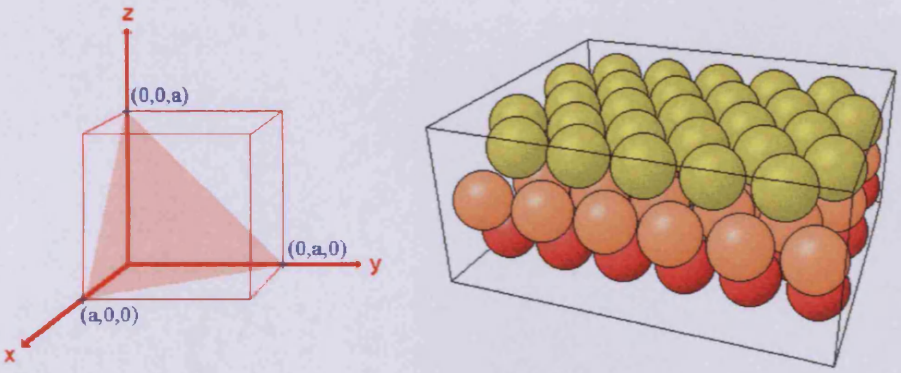

(a). {111}

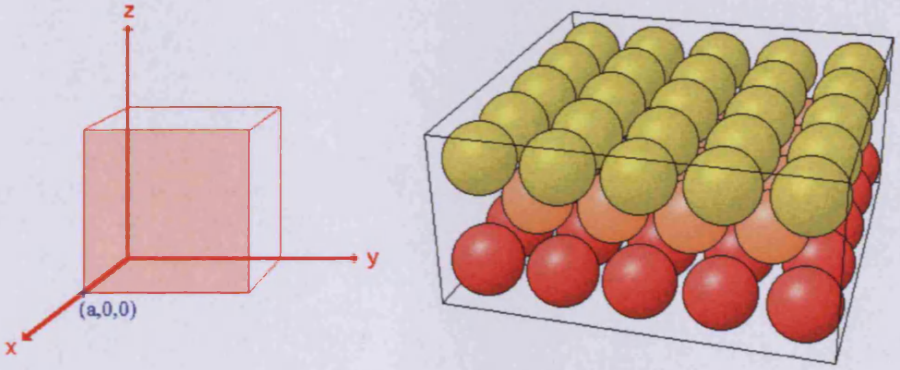

(b). {100}

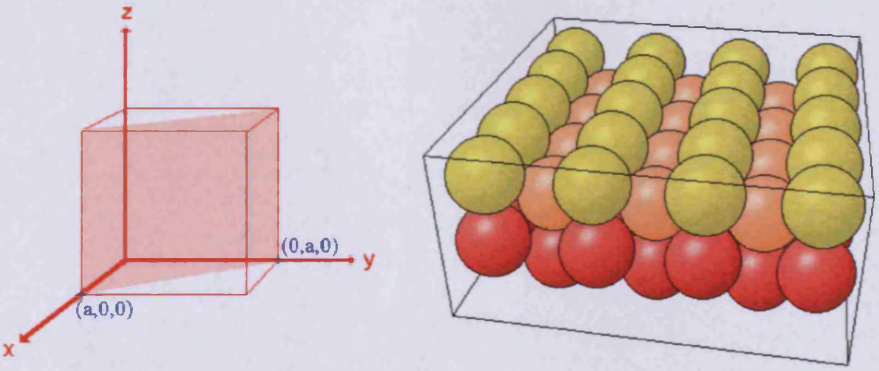

(c). {110}

Figure 2.2 The fcc basal planes and corresponding unit cells reprinted from [7,8].

If the plane of an fcc single crystal intersects any of the three axes at fractional values of the lattice constant, then one of the {*hkl*} values is >1 and the resulting surface is stepped. These surfaces are known as high Miller index surfaces and can be defined by microfacet notation [9]. The stereographic triangle (Figure 2.3) shows the three basal planes at the corners (poles) of the stereographic triangle and each side (zone) represents the range of stepped surfaces associated with sites containing each pole. The equations to convert the microfacet notation to Miller index notation are given within the triangle. Taking the zone between fcc {111} and fcc {100} as an example, a surface which exhibits {100} terraces, n atoms long separated by a monatomic {111} step may be denoted (2n-1,1,1). For example, a surface with a [4{100}×{111}] label in microfacet notation will have a Miller index of {711} [10]. Each zone of the stereographic triangle has a point where *n* in the microfacet notation is 2, i.e. when there is a step (which is two atoms in length) every two atoms of terrace, hence the contributions from each basal plane is effectively equivalent, this point is called the *turning point* of the zone.

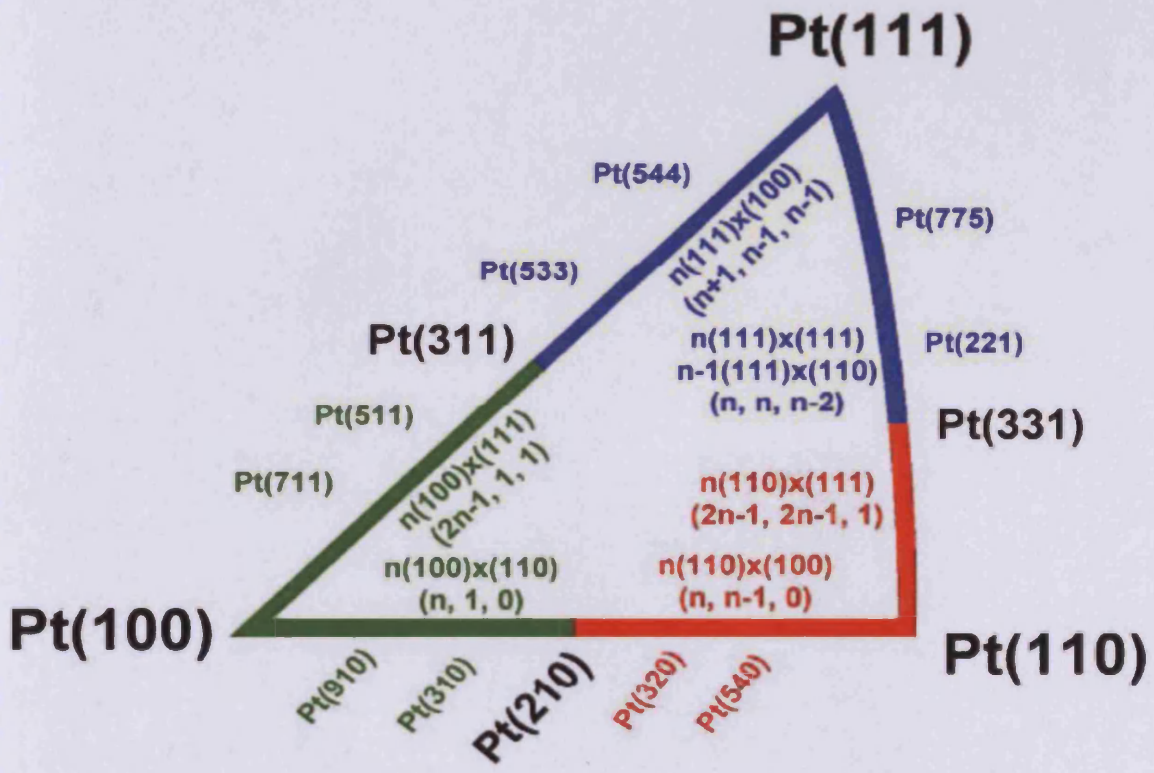

Figure 2.3 The stereographic triangle showing the relative positions and microfacet notations for a range of fcc single crystal surfaces (platinum in this case), reprinted from [6].

2.1.2 Electronic structure

Electronic states in atoms may broadly be classed as either core electrons or valence electrons. The core electrons are strongly bound to the nuclei and do not participate in electrical conduction or chemical bonding. In metals, the valence electrons form continuous bands of overlapping electronic states known as the valence band and the conduction band. It is the ability of the valence electrons to transverse between these two bands that determines electrical properties of the solid including its suitability for catalysis [1]. The density of states at the Fermi energy level is also often invoked to explain variations in catalytic reactions of different metals [11] (Figure 2.4).

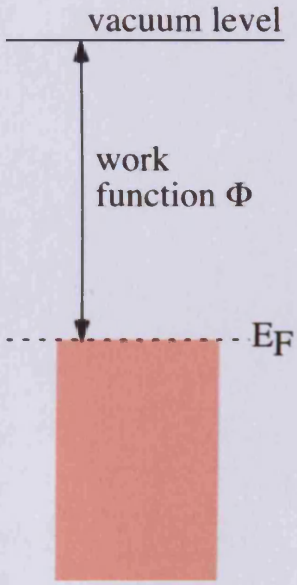

Figure 2.4 Fermi energy E_F, vacuum level E_{vac} and work function Φ of a metal. Shaded region signifies range of electronic states in the solid (valence band) that are filled.

In a metal, the valence band and conduction band are contiguous and so there is no band gap and electrical conductivity is high. Insulators and semi-conductors will have a band gap where no electronic state exists. In Figure 2.4, the valence band is shaded pink and the conduction band is the area directly above the Fermi level. At absolute zero (0 K), the highest occupied electronic state in the conduction band is termed the Fermi energy E_F and is defined as the energy of the highest occupied electronic state where all states below are occupied and above are unoccupied and is related to the *work function* Φ of the metal [1].

$$\Phi = E_{vac} - E_F \qquad (2.4)$$

The work function is the energy required to remove one electron from the material into vacuum and can be described as the ionisation energy of the metal [12]. The surface structure can greatly affect the work function of the metal. This is because when taking into consideration differences in the electrostatic dipole caused by differences in electron density between bulk and surface atoms (due to the lower co-ordination of surface atoms relative to the bulk), the surface structure impinges strongly on the surface distribution of electrons. Hence, the surface dipole contribution D can also enter into equation (2.4.) and therefore the work function is highly dependent on surface properties (including adsorption by gas phase molecules).

The energy of the crystal lattice at the surface is different to that in the bulk [1]. As mentioned earlier, the surface atoms have the full coordination to neighbouring atoms and the electrons that would ordinarily be part of the lattice form delocalised states. This higher energy state can be dissipated with slight changes to bond length and angles between layers in a process known as relaxation. The result for a metal is often a shortening of the distance between the top layer of atoms and the second layer and the effect will be passed down sometimes 5-6 layers deep. This region, distinguishable from the bulk, is known as the *selvedge region* [10].

A more radical way to minimise the surface energy, is to change the periodicity of the surface atoms in a process called reconstruction. In this process the extra valence electrons are directed laterally changing the bond length and angles between adjacent atoms. One of the most studied examples is when platinum{110} reconstructs from a (1 × 1) periodicity to (1 × 2) periodicity, commonly referred to as the missing row reconstruction [10] (Figure 2.5).

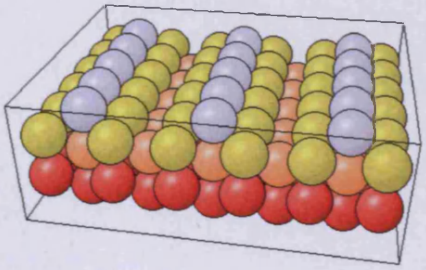

Figure 2.5 The reconstructed (1 × 2) Pt{110} "missing row" clean surface reconstruction.

Reconstruction can also be induced by chemisorption. The ability of a surface site to form a chemical bond with a potential adsorbate is related to the symmetry and energy of the electronic states at the site, which is intimately related to the geometrical structure [13]. At sufficiently strong chemical interactions and high enough adsorbate coverage, the adsorbate can induce a reconstruction of the surface. An example of this phenomenon would be the alkali metal induced (1 × 2) surface reconstruction of palladium{110} [14], similar to the structure in Figure 2.5. Hence, it is evident that metal surfaces are seldom 'static', but are constantly moving to compensate for energy differences between the bulk and surface of the metal.

2.2 Cyclic Voltammetry

Cyclic voltammetry is an important method for characterising electrode surfaces and testing the cleanliness and reproducibility of an electrochemical system [6]. The technique involves sweeping the potential of the working electrode versus a reference electrode between two set potentials (E_1 and E_2) at a fixed rate, v, (V s^{-1}). The current generated, i, is recorded for both the forward scan (anodic current) and the reverse scan (cathodic current). The peaks and troughs of the resulting i-V cycle, are known as a cyclic voltammogram or CV. The general features of the CV may be used to interpret redox processes at the interface [4,15]. Figure 2.6 (a) shows the type of waveform applied in cyclic voltammetry. In this example, the potential is scanned from 0 – 0.8 V with v at 0.05 V s^{-1}, defined by equation 2.5, and is cycled three times.

$$\nu = \frac{dV}{dt} \tag{2.5}$$

Figure 2.6 (b) shows a cyclic voltammogram for a simple reversible redox process of the form:

$$O + ne^- \leftrightarrow R \tag{2.6}$$

where O is the oxidised species, R is the reduced species, and n is the number of electrons involved in the reaction. The process in equation (2.6) is chemically reversible as the product of the forward reaction is the reactant for the reverse reaction and *vice versa*. Provided the system can attain equilibrium within the time taken to complete an electron transfer, the

system will approach thermodynamic equilibrium where an infinitesimal change in the direction of the applied potential will cause a reversal in the process [16].

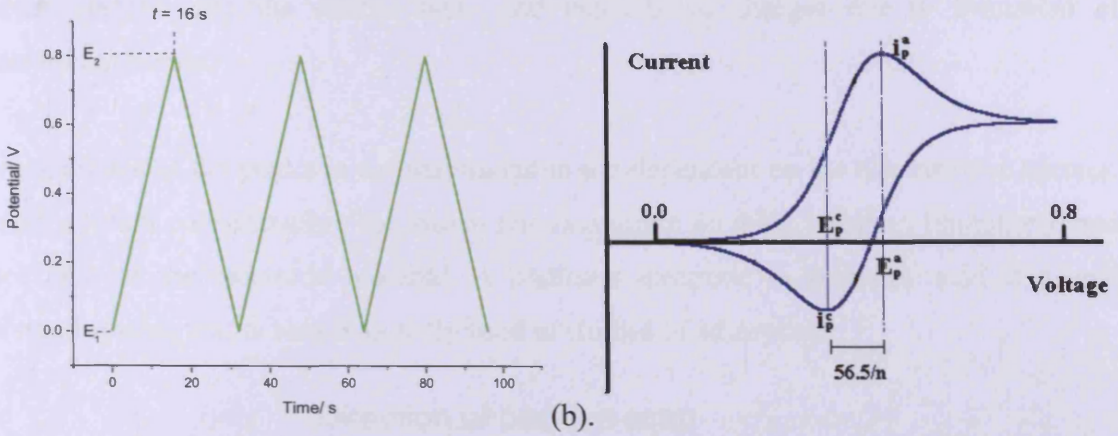

(a). (b).

Figure 2.6 (a). "Saw Tooth" potential waveform applied to a working electrode in cyclic voltammetry. E_1: 0 V, E_2: 0.8 V, v: 0.05 V s^{-1}. (b). The expected CV in a simple reversible redox process. Reprinted from [6].

For a reversible reaction in solution, the position of the voltammetric peaks is independent of v, and the separation of the peaks can be calculated with the equation [16]:

$$\left|E_p^{Ox} - E_P^{Red}\right| = 2.2\frac{RT}{nF} \qquad (2.7)$$

Where R is the gas constant, T is temperature, n is the number of electrons involved in the reaction and F is the Faraday constant. At 298 K the separation is $56.5/n$ mV. Hence the number of electrons involved in the reaction can be calculated from the measured peak separation. The peak current, i_p, for both forward and reverse reactions should be the same under reversible conditions and is calculated with the following equation [16]:

$$i_p = (2.69 \times 10^5)n^{3/2} \cdot A \cdot D_o^{1/2} \cdot \nu^{1/2} \cdot C_o \qquad (2.8)$$

Where A is the area in cm^2, D_o is the diffusion coefficient in cm^2 s^{-1} and C_o is the concentration of the electroactive species in the bulk solution in mol cm^{-3}. Hence, solution redox processes will exhibit a $v^{1/2}$ dependence on sweep rate. In contrast, surface adsorption may be distinguishable from solution processes since $i_p \propto v$, showing a linear dependence of i_p on sweep rate [16]. The peak separation for surface processes at equilibrium is also close to zero mV because bulk diffusion is no longer occurring [17]. The electrical current generated is from charge transferring across the electrode/electrolyte interface and is referred to as a Faradaic process. Adsorption and desorption processes at surfaces can also occur without the

transfer of Faradaic charge and these are known as non-Faradaic processes and can be responsible for electrostatic external currents such as migration of ions to and from the electrode surface into the double layer and capacitative charges due to formation of chemisorption bonds.

The magnitudes of the peaks in a voltammogram are dependent on the electroactive species, the bulk solution concentration, the sweep rate (assuming no mass transport limitations) and surface area of the electrode material. A platinum electrode in sulphuric acid is a well understood system that is also frequently used in studies of adsorption.

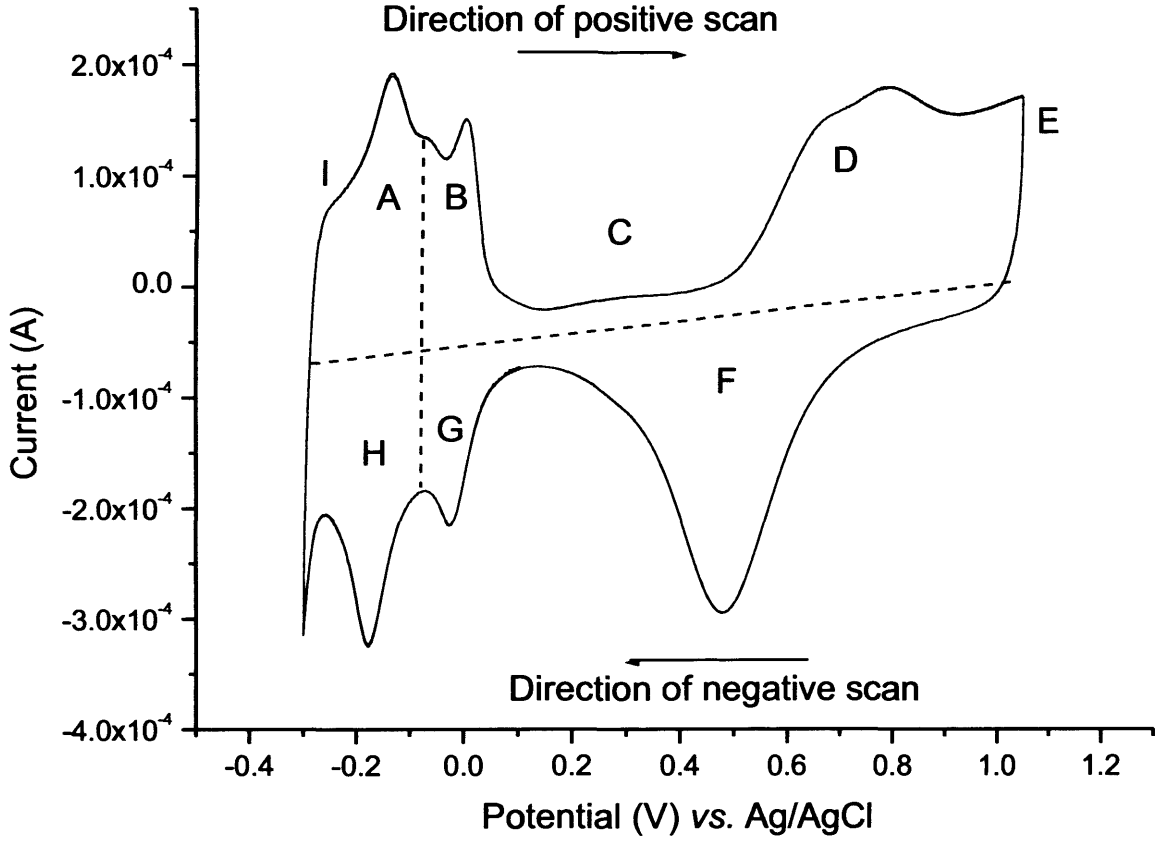

Figure 2.7 Cyclic voltammogram of polycrystalline platinum in 0.1 M H_2SO_4, v: 0.05 V s^{-1}.

Figure 2.7 shows a typical CV generated on a polycrystalline platinum electrode with a gold counter electrode against a silver/silver chloride reference electrode scanning at 0.05 V s^{-1} at room temperature. The CV was taken in a spectro-electrochemical flowcell designed and built in-house. The baseline should be parallel to the potential axis and centred at 0 A on the current axis. The slope to the baseline is indicative of ohmic drop and may be due to distance to the counter electrode through a thin layer configuration.

Each labelled section in Figure 2.7 is the result of an electrochemical process occurring on the working electrode surface. Regions A and B constitute the oxidation of under potentially deposited $H^+_{(aq)}$ ions [18], where electrons from adsorbed hydrogen on the electrode surface transfer into the bulk of the electrode producing a positive electrical current (anodic). The cationic hydrogen ions then desorb into the bulk of the electrolyte:

$$H_{(ads)} \rightarrow H^+_{(aq)} + e^- \qquad (2.9)$$

In region A, hydrogen desorbs from so-called "{110} defect sites", which are more weakly bound than the corresponding "{100} defect sites" that constitute region B [18].

Region C is the double layer region, where the only current flowing is the capacitative charge of the electrochemical double layer [16]. Non-Faradaic processes are occurring in this region where ions of the opposite charge migrate towards the electrode surface as it becomes more positively charged. The "thickness" of the double layer region of the CV is significant as its size is proportional to the capacitance of the electrode, which not only depends on the material, but also the surface area. Hence, for large surface area electrodes the double layer region will be wider than low surface area electrodes. There are numerous models proposed for the distribution of ions at the electrode/electrolyte interface leading to capacitative processes but these will not be discussed further. However, a comprehensive treatment of the double layer may be found in the footnote reference*.

Region D is the oxide forming region, where water in the electrolyte adsorbs on the platinum surface and dissociates into adsorbed hydroxide and solution phase hydrogen cations.

$$H_2O \rightarrow OH_{(ads)} + H^+_{(aq)} + e^- \qquad (2.10)$$

The free electron from the broken O-H bond is transferred into the bulk of the electrode and generates anodic current. Going further positive in potential will break the second O-H bond releasing another electron into the bulk of the electrode, but leaving the surface metal atoms in an oxidised state. These may then decompose to a free platinum site together with oxygen gas (electrolysis occurs).

* The reader is referred to A.J. Bard, L.R. Faulkner, *Electrochemical Methods, Fundamentals and Applications*, Wiley, 1980.

$$2PtOH_{(s)} \rightarrow 2Pt_{(s)} + O_{2\,(g)} + 2H^{+}_{(aq)} + 2e^{-} \qquad (2.11)$$

The reformation of the platinum site will not be geometrically the same as before the oxidation process, but will tend to form clusters. This process is known as place-exchange and can lead to etching, leaving the surface with a rough topography [19]. At Point E, the upper potential limit is reached and the direction of the scan is switched to a negative going sweep. When electrochemically cleaning a thin platinum metal film (as will be performed in the present study), repeated oxidation and reduction of the surface will eventually lead to pinholes in the film. The integrity of the film is lost and undesirable interactions with the underlying base material can occur (the gold core – see section 3.3.2). To minimise this, the upper potential limit is carefully controlled in all experiments.

Region F is the oxide stripping region, where the reverse reaction to that of region D occurs. Electrons are transferred from the bulk of the electrode to form O-H bonds followed by desorption of water molecules in a cathodic current.

$$PtO_x + 2xH^{+} + 2xe^{-} \rightarrow Pt + xH_2O \qquad (2.12)$$

The current generated at regions G and H are from adsorption of $H^{+}_{(aq)}$, where the reverse reaction of that in regions A and B occurs and again a cathodic current is generated. Hence, regions A, B, G and H are collectively known as the hydrogen under-potential deposition region (H UPD) of a platinum CV.

The charge in the H UPD region can be used to estimate the real surface area of the working electrode. It is usually assumed that one electron is transferred per surface platinum atom. The surface atomic density of platinum and relative areas of the three basal planes on polycrystalline platinum are used to estimate the charge density σ_d (210 μC cm^{-2}) expected of the polycrystalline electrode. The charge (Q) generated is then estimated by integrating the area of the H UPD region. The values are entered into equation 2.13 and the area A is found.

$$A = \frac{Q}{\sigma}\ \mathrm{cm}^2 \qquad (2.13)$$

Point I is the lower potential limit set in the waveform, it is the point where the negative potential scan is switched in direction to a positive potential scan. At potentials more negative than -0.35 V *vs.* silver/silver chloride, hydrogen gas is evolved. From equation 2.9:

$$2H_{(ads)} \rightarrow H_{2(g)} \qquad (2.14)$$

2.3 Spectroscopy

Molecular spectroscopic techniques work on the principle that energy is quantised and this can be measured through interaction with electromagnetic (EM) radiation. In classical theory, EM radiation propagates in waves of alternating electric and magnetic field vectors (Figure 2.8). In reality, they also contain particle like character in terms of discrete energy quanta. Einstein's equation relates the frequency, ν (s^{-1}), of the EM wave to the energy of the particle, E (eV), known as a photon [20]:

$$E = \frac{hc}{\lambda} = h\nu \qquad (2.15)$$

where h is Planck's constant (J s), λ is wavelength (m) and c is the speed of light (m s^{-1}) through vacuum.

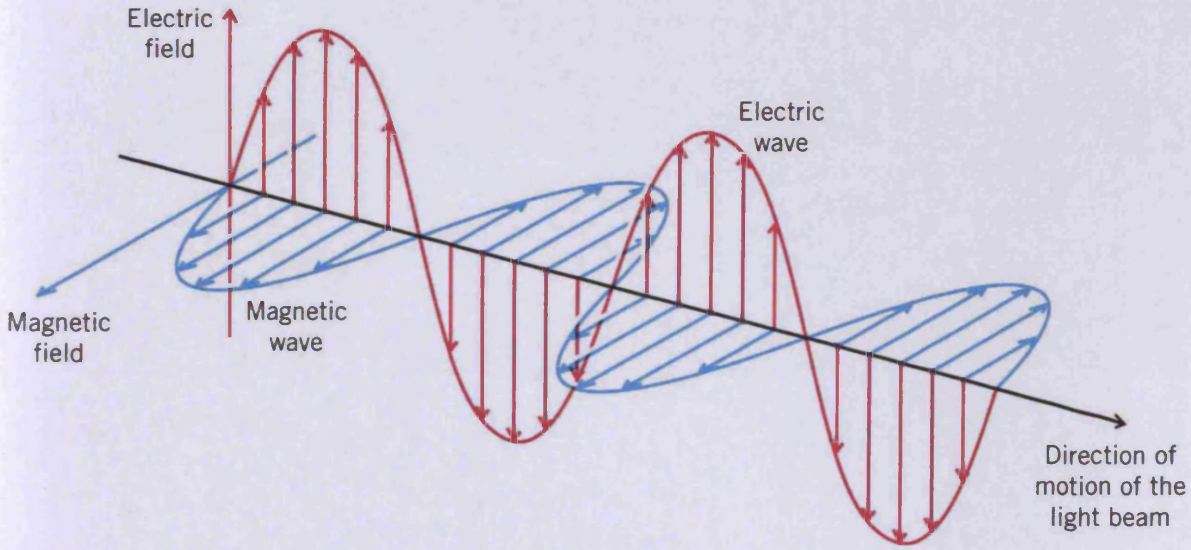

Figure 2.8 An electromagnetic wave propagating in free space, the amplitude of the wave is the magnitude of the field and the distance between the wave peaks is the wavelength (λ).

The strength of the electric field, $\bar{E}$ (V m^{-1}) at a given time (t) may be related to the amplitude of the wave (E_0) and the frequency:

$$\bar{E} = E_0 cos 2\pi\nu t \qquad (2.16)$$

All EM radiation travels at the speed of light through a vacuum and so v is found:

$$\nu = \frac{c}{\lambda} = \tilde{\nu}c \qquad (2.17)$$

often expressed as wavenumbers ($\tilde{\nu}$) in units of m^{-1}[†]. Table 2.1 shows the full frequency range of the EM spectrum used in analytical chemistry with the energy transitions and the associated techniques commonly used to measure them. The present study is concerned with molecular vibrations. The frequencies of which, are found in the Infra-Red (IR) region of the EM spectrum corresponding to wavelengths between 2.5×10^{-6} and 2.5×10^{-5} m.

Table 2.1. Spectroscopic techniques, the general frequency ranges used and the effect studied [46].

Spectroscopy	Range (cm^{-1})	Origin
Gamma-ray	$10^{10} - 10^{8}$	Rearrangement of elementary particles in the nucleus.
X-ray	$10^{8} - 10^{6}$	Transitions between energy levels of inner electrons of atoms and molecules.
UV-visible	$10^{6} - 10^{4}$	Transitions between energy levels of valence electrons of atoms and molecules.
Raman and Infra-Red	$10^{4} - 10^{2}$	Transitions between vibrational levels.
Microwave	$10^{2} - 1$	Transitions between rotational levels.
Electron spin resonance	$1 - 10^{-2}$	Transitions between electron spin levels in magnetic field.
Nuclear magnetic resonance	$10^{-2} - 10^{-4}$	Transitions between nuclear spin levels in magnetic fields.

2.3.1 Molecular vibrations

2.3.1.1 Vibrations of diatomic molecules

The parabolic curve (dashed line) in Figure 2.9 shows the variation of potential energy versus the inter-atomic distances in a diatomic molecule according to the harmonic oscillator model. It represents the extremes of the atomic displacements (internuclear distance) during a vibration at a vibrational energy state (v) where v = 0 is the ground state energy and v = 1 is the first excited state, above which are the subsequent excited energy states. From equation 2.18, the energy of the vibrational state is found from the frequency of the vibration in

[†] Wavenumbers at Infra-Red frequencies are expressed as cm^{-1}.

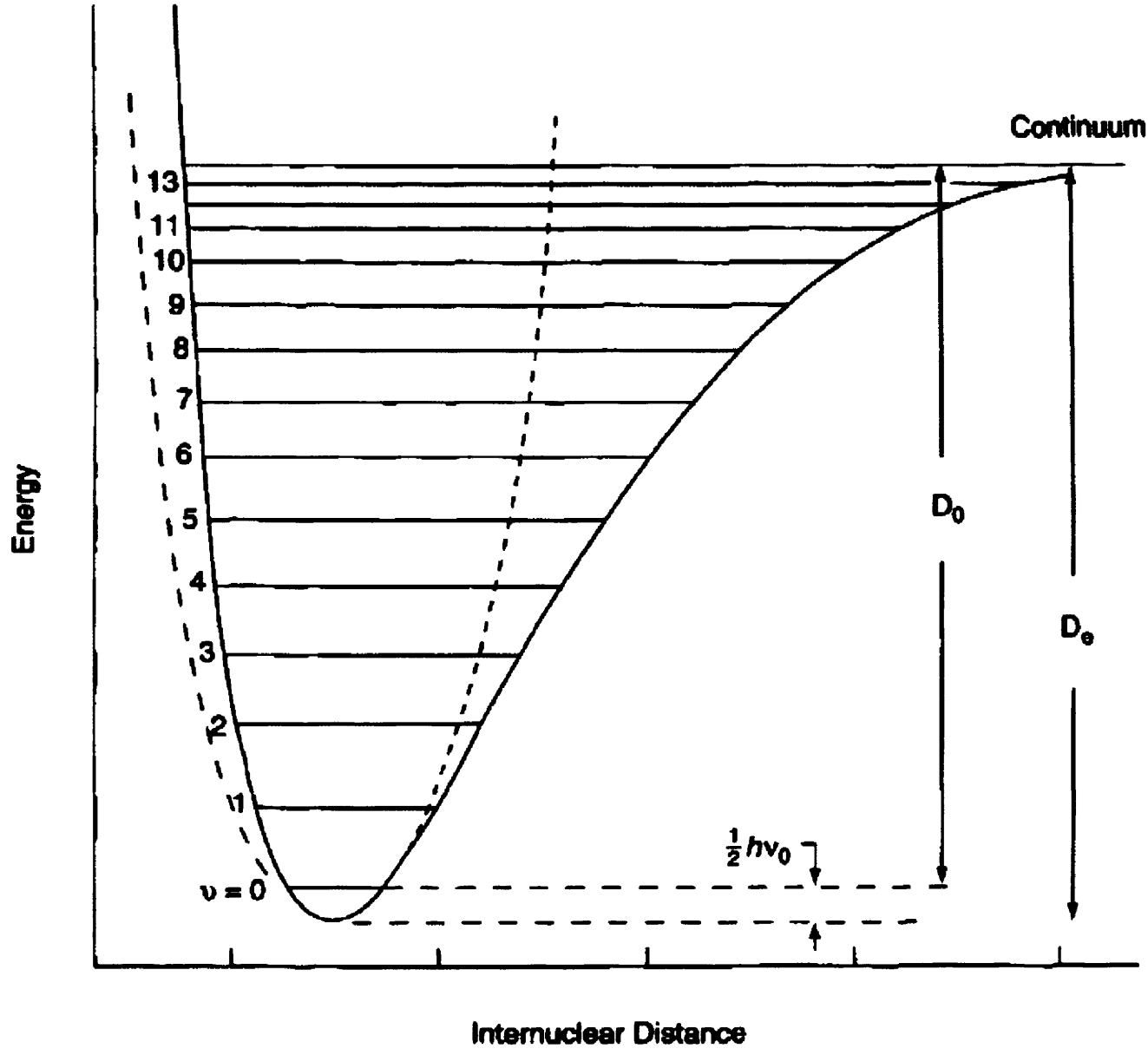

Figure 2.9 Harmonic oscillator model (black dashes) of vibrational energy levels (v) and the Morse cur anharmonic oscillator model (black solid), reprinted from [46].

The maximum internuclear distance is predicted to increase with each successive vibr state and this continues infinitely as described in Hooke's law of elasticity. Ho chemical bonds in real molecules are not infinitely elastic, so at higher energy sta displacement of the atoms is greater than that predicted by the harmonic oscillator mod the energy gap between states becomes progressively smaller. This is closer to the situa real molecules. Hence a more accurate approximation to use would be the anha

oscillator represented by the Morse curve (Figure 2.9, solid line), which predicts that the displacement of the atoms will eventually overcome the recoiling force of the bond and the molecule eventually becomes dissociated. Anharmonicity constants x_e and y_e are included in equation 2.18 to give:

$$E_v = \left(v + {}^1/_2\right) hc\omega_e - \left(v + {}^1/_2\right)^2 hcx_e\omega_e + \left(v + {}^1/_2\right)^3 hcy_e\omega_e + \cdots \quad (2.19)$$

where ω_e is the vibrational frequency corrected for anharmonicity [46]. The strength of the bond is found from the energy at which the atoms dissociate (D_e, Figure 2.9). To calculate the energy at higher vibrational energies, it may be necessary to include further terms for (v + 1/2), but these are less significant at lower energy levels [33].

If the masses of each atom (m_1 and m_2) are known then the reduced mass (μ) of the diatomic molecule is calculated:

$$\mu = \frac{m_1 m_2}{(m_1 + m_2)} \quad (2.20)$$

The equilibrium distance between the atoms is the bond length and the "stiffness" of the bond is the force constant, k:

$$k = 4\pi^2 \nu^2 c^2 \mu \quad (2.21)$$

The magnitude of k is represented by the "steepness" of the potential energy curve; a high value of k will produce a steeper curve. The fundamental frequency of the vibration (ν) may then be calculated in the following expression:

$$\nu = \frac{1}{2\pi}\sqrt{\frac{k}{\mu}} \quad (2.22)$$

2.3.1.2 Vibrations of polyatomic molecules

Ignoring electronic transitions, the energy of a molecule can be described by its translational movement in the x, the y and the z directions in space, its rotational movement along the x, y and z axes and the vibrations in the x, y and z directions of each atom in the molecule. Hence the number of vibrations of a molecule is 3N-6 where N is the number of atoms. However,

linear molecules only have two non-equivalent axes to rotate around so the equation for the number of vibrational modes becomes 3N-5 [22]. The two most common molecules used to demonstrate such relationships are H_2O and CO_2.

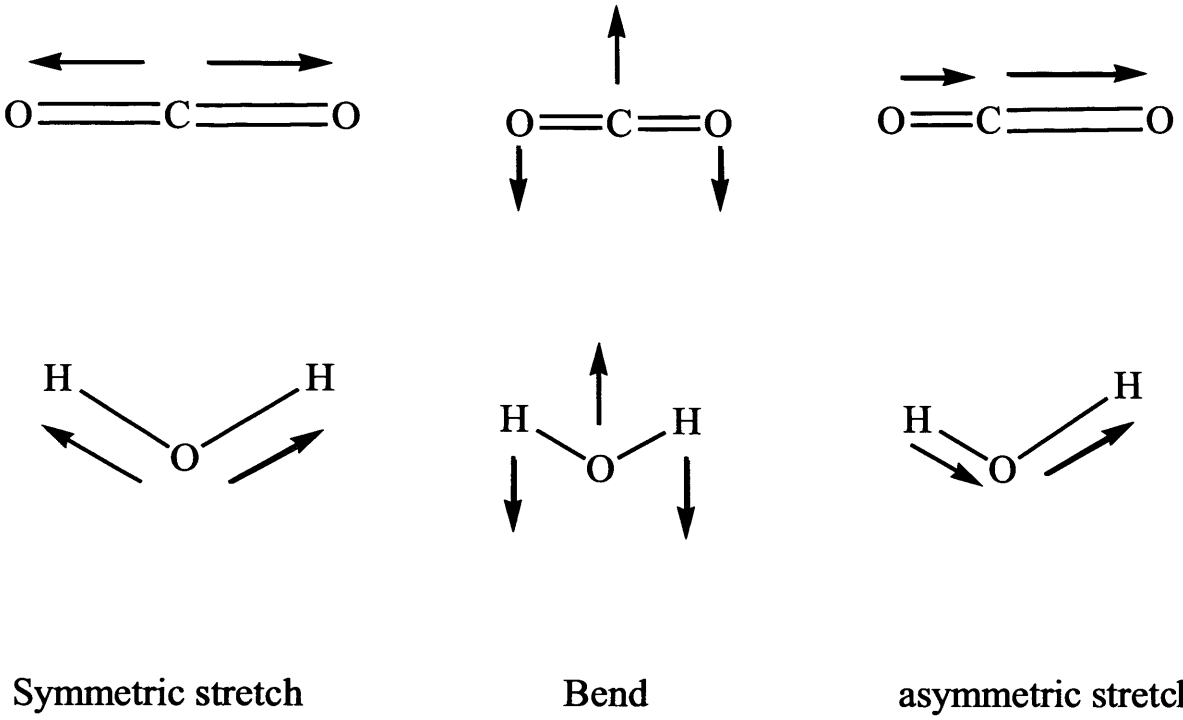

Figure 2.10 Vibrational modes of carbon dioxide and water.

Water is a non-linear molecule and so has 3N-6 = 3 modes of vibration as illustrated in Figure 2.10. Carbon dioxide is a linear molecule and so has 3N-5 = 4 modes of vibration. The fourth mode is another bending mode but orthogonal to the plane of the paper. It has the same energy as the bending mode in the plane of the paper and so these modes are termed degenerate [23].

In more complex molecules, numerous vibrational modes will exist and are often difficult to assign to a peak in a spectrum. When the vibrational spectrum of similar molecules, for example a homologous series of organic compounds are compared, it is found that similar functional groups will give rise to similar bands throughout the series. These are therefore referred to as group frequencies and can be used to help identify an unknown sample. The vibrational modes of two ubiquitous groups in organic chemistry are graphically illustrated in Figure 2.11.

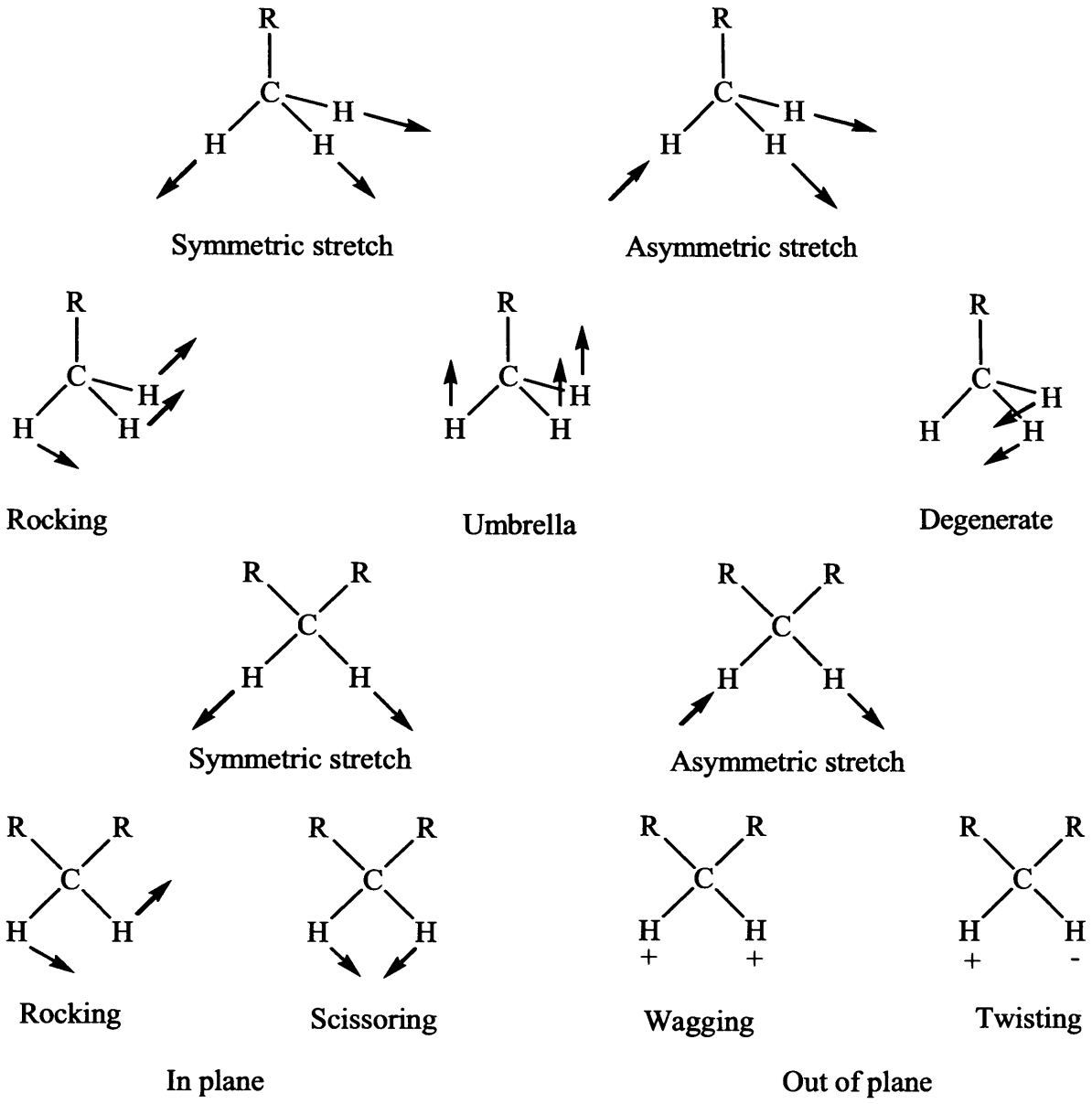

Figure 2.11 Vibrational modes of CH_3 and CH_2 groups.

In this thesis, symmetric stretching modes will be given the symbol νs, anti-symmetric stretching modes νa, rocking modes δr, umbrella modes δu, degenerate bending modes δd, scissoring modes δs, wagging modes δw and twisting modes δt.

The frequency of group vibrations can be found in frequency correlation tables in which a frequency range will be quoted. The exact position of the observed peak will depend on the molecule that the group belongs to and the position of the group in the molecule according to:

1. Vibrational coupling; a fundamental vibrational mode may be described as a mixture of group vibrations coupled together to vibrate at the same frequency [24]. This is seen to occur when the respective groups are in proximity to each other within the molecule and have similar bond force constants. The peak in the spectrum is usually assigned to the most dominant group vibration. An example of coupling is seen with the δ(C-H) vibrations of methylene groups in the n-paraffin series [25]. The δ(C-H) vibration is coupled to the skeletal vibration, which changes in frequency as the carbon chain is increased. Hence, the frequency of the fundamental mode that gives rise to the peak in the spectrum shifts accordingly.
2. Orbital hybridisation; mutual repulsive forces between orbitals hybridised around a central atom are responsible for the angle between the bonds [26], for example, the H-C-H bond angle on methane is 109.5°. However, bond angles may change depending on the relative repulsive forces of the adjacent atom/group. A stronger repulsion will cause the bond angle to close between the other atoms/groups and *vice versa*. The larger the bond angle between sp^3 hybridised orbitals, the higher the percentage of *s* character resulting in a larger force constant and a higher vibrational frequency [27].
3. The electronegativity of the adjacent substituent atom or group can also have an effect on the vibrational frequency by withdrawing or donating electrons from/into a specific bond. In general, electron withdrawal will cause a down-shift (red frequency shift) and electron donation will cause an up-shift (blue frequency shift) to the vibrational frequency of the adjacent bond. The degree to which the substituent does this, can be found in the Hammett parameters (σ). A substituent with a high positive Hammett value will withdraw electrons and a negative value will donate electrons. However, the electronegativity can have marked effects on chemical bonds of functional groups in the α-position to the electronegative/positive group. For example, the ν(C=O) of a carbonyl next to a halogenated methyl group will withdraw electrons from the carbon of the carbonyl group. In this case, the result is a shortening of the π-bond in the carbonyl group leading to an increase in the force constant and an increase in the vibrational frequency [20].

Exchanging a substituent atom for its heavier isotope can aid vibrational analysis. From equation 2.22, the fundamental vibrational frequency is inversely proportional to the reduced mass across the bond. Therefore an increase in the reduced mass will lower the frequency of

vibration. For polyatomic molecules, two (or more) fundamental vibrations of differing symmetry may vibrate at a similar frequency. Spectroscopically, these two vibrational modes only result in one peak and so are degenerate, but due to their differing symmetry are termed "accidental" [28]. The vibrational coupling for accidental degenerate modes may be disrupted by isotopic substitution, leading to frequency shifts to multiple bands including shifts to higher frequency [29]. Furthermore, if H/D exchange is used, then intra-/inter-molecular hydrogen bonds can also be affected as was previously reported in the case of the intermolecular hydrogen bond in heavy water [30]. In general, longer OD···X type bonds are considered to be stronger than OH···X [31]. This will further perturb the vibrational frequency of groups both directly bonded to the H/D and groups coupled to the H/D bonded group.

2.3.2 The Absorption Process

For a molecule to absorb EM radiation, the energy of the radiation $h\nu$ should equal the energy difference between the ground and excited state ΔE. This is known as Bohr's frequency condition based on Einstein's equation (equation 2.15). In vibrational spectroscopy, a fundamental vibrational mode will give rise to a peak in the spectrum at a frequency equal to the energy transition between the ground state (v = 0) and the first excited state (v = 1). The Boltzmann distribution predicts that at room temperature most molecules exist at v = 0:

$$\frac{N_n}{N_m} = \frac{g_n}{g_m} \exp\left[\frac{-(E_n - E_m)}{kT}\right] \qquad (2.23)$$

where N_n is the number of molecules at the excited vibrational state, N_m is the number of molecules at ground state, g is the degeneracies at both states, E is the energy at both states, k is the Boltzmann constant and T is the temperature. Therefore the majority of transitions will be from v = 0. With the harmonic approximation, an energy transition can only occur between adjacent states ($\Delta v = \pm 1$), so the fundamental transition will be prevalent. In the anharmonic approximation $\Delta v = \pm 1, 2, 3\ldots$ is allowed giving rise to the first, second, third... overtone peaks. But these transitions are much less probable leading to weak peak intensities. At elevated temperatures, a higher percentage of molecules will exist at the first excited state so the v = 1 to v = 2 transition will occur more frequently giving rise to a peak at a frequency lower than the fundamental peak since $\Delta E_{v=0}^{v=1} > \Delta E_{v=1}^{v=2}$ according to the anharmonic approximation [46].

Not all vibrations in a covalently bonded molecule will absorb IR radiation. The molecule will have to possess a changing dipole moment, μ during the vibration. A dipole moment is a vector defined as the magnitude of the charge (δ) multiplied by the distance between them (l) and is measured in coulomb-metres and is often quoted in Debyes (1 D = 3.34×10^{-30} Cm).

$$\mu = \delta l \tag{2.24}$$

For a transition between states to be allowed, the transition dipole moment M_{01}, should be non-zero:

$$M_{01} = \int_{-\infty}^{\infty} \psi_1 \mu_x \psi_0 \mathrm{d}x \tag{2.25}$$

where ψ_1 and ψ_0 are the wavefunctions at the excited and ground energy states respectively, μ_x is the dipole moment (a vector) in the x direction (y and z are also evaluated) at any point during the vibration and dx is the change in the vector length. During a vibration, dx will be non-zero, so for M_{01} to be non-zero and absorption to take place, μ_x must also be non-zero [32]:

$$\mu_x = \mu_0 + \left(\frac{\mathrm{d}\mu_x}{\mathrm{d}x}\right) x \tag{2.26}$$

μ_0 is the dipole moment of the molecule at equilibrium vector length, which is not dependent on x and so when equation 2.26 is combined with 2.27 and it is rearranged as such:

$$M_{01} = \mu_0 \int_{-\infty}^{\infty} \psi_1 \psi_0 \mathrm{d}x + \left(\frac{\mathrm{d}\mu_x}{\mathrm{d}x}\right) \int_{-\infty}^{\infty} \psi_1 x \psi_0 \mathrm{d}x \tag{2.27}$$

ψ_1 and ψ_0 are orthogonal to each other, therefore the integration of their product is zero and the first term vanishes. The integrand of the second term is non-zero and $\Delta v = \pm 1$ for a harmonic vibration (forbidding overtone transitions). Hence, M_{01} is non-zero when $\left(\frac{\mathrm{d}\mu_x}{\mathrm{d}x}\right)$ is non-zero. In summary, the vibration is IR-active if there is a change in the dipole moment in the x, y or z direction during the vibration [46].

The intensity of a peak in an absorption spectrum is defined by the absorbance (A), which is inversely proportional to the percentage of light transmitted through the sample and is related to the concentration of the absorbing species ($\bar{c}$) in molarity using the Beer-Lambert law:

$$A = \varepsilon b\bar{c} \qquad (2.28)$$

Where b is the path length in centimetres through which the radiation travels and ε is the molar extinction coefficient. ε can be considered as the probability of a vibrational transition to occur when both Bohr's frequency condition and the selections rules for I.R. absorption are satisfied [33]. A high probability equates to a high ε, and hence a large value for A.

2.3.3 Light Scattering

As previously discussed, for absorption to occur the frequency of the oscillating dipole moment of the molecule must be in resonance with the frequency of the incident light. If the frequency is not the same, the EM field of the incident light can still interact with the electron cloud surrounding the molecule causing the cloud to distort in shape. The distortion is a polarisation of the electron cloud with an induced dipole P:

$$P = E\alpha = E_0\alpha\cos 2\pi\nu_0 t \qquad (2.29)$$

The magnitude of the induced dipole moment is dependent on the electric field E and the propensity of the cloud to polarise, known as the polarisability (α). From equation 2.16, the electric field strength can be combined to give the right hand side of equation 2.29. The induced dipole will oscillate at the same frequency as the incident light and form a short-lived complex known as a virtual state. The excited virtual state will relax by emitting photons of light in random directions, known as scattering and will return back to the original electronic state (Figure 2.12). Like fluorescence, scattering is a two photon process involving an interaction of one photon and emission of another photon. However, Bohr's frequency condition is not met with scattering, so no absorption will take place unlike with the process of fluorescence. The scattering process is faster at 10^{-12} seconds compared to 10^{-8} seconds for fluorescence [34].

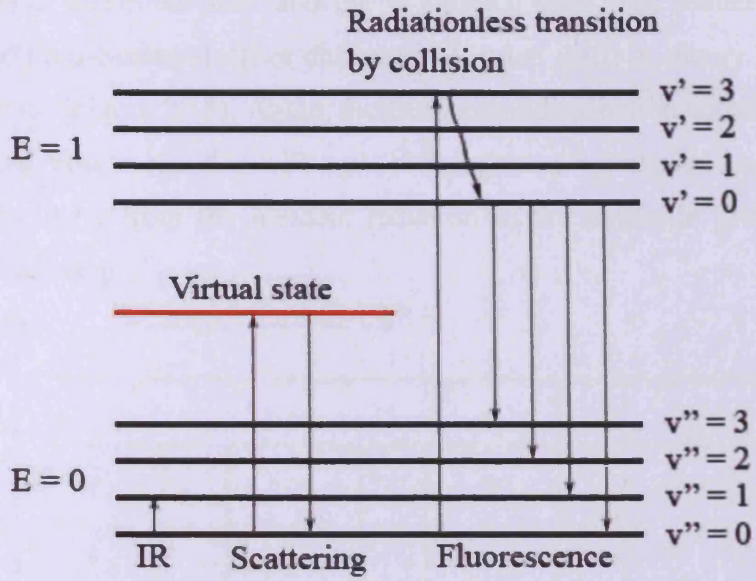

Figure 2.12 Absorption and emission processes for Infra-Red, scattering and fluorescence mechanisms. E=0: electronic ground state, E=1: first electronic excited state, v": vibrational states at electronic ground state, v': vibrational states at first electronic excited state.

The majority of scattering will occur in a time frame too short for the nuclei in the bond to adjust to the energy of the virtual state and so will have no effect on the scattered photons. In this type of scattering the energy of the photons will be close to the frequency of the incident light and is termed elastic or Rayleigh scattering. The energy of the virtual state can be described as the degree of distortion imposed on the electron cloud. The greater the distortion, the higher the energy of the virtual state and the more likely the excess energy will be used in a scattering event [22]. Hence, the intensity of scattered light from a molecule is inversely proportional to the fourth power of the wavelength of the incident light [36].

2.3.4 Raman Spectroscopy

Scattering techniques are not uncommon in spectroscopy with examples in the X-ray region [35]. For vibrational transitions, Raman spectroscopy is the dominant scattering mechanism and was first predicted by Sir Chandrasekhara Venkata Raman in 1928 for whom the Nobel Prize was awarded in 1930.

Raman spectroscopy involves a different type of scattering than the elastic Rayleigh process. In Raman scattering the nuclei in the molecule interact with the complex of the distorted electron cloud and EM wave in the virtual state and so a quantity of the energy is transferred

between the virtual electronic state and the vibrational state. The scattered photon is now either augmented (anti-Stokes shift) or diminished (Stokes shift) in energy by the quantum of the vibrational state (Figure 2.13). Again, the Boltzmann distribution equation predicts that at room temperature most molecules will exist at the ground vibrational state, therefore most energy transfer will be from the incident radiation to the molecule giving rise to Stokes shifted Raman scattering.

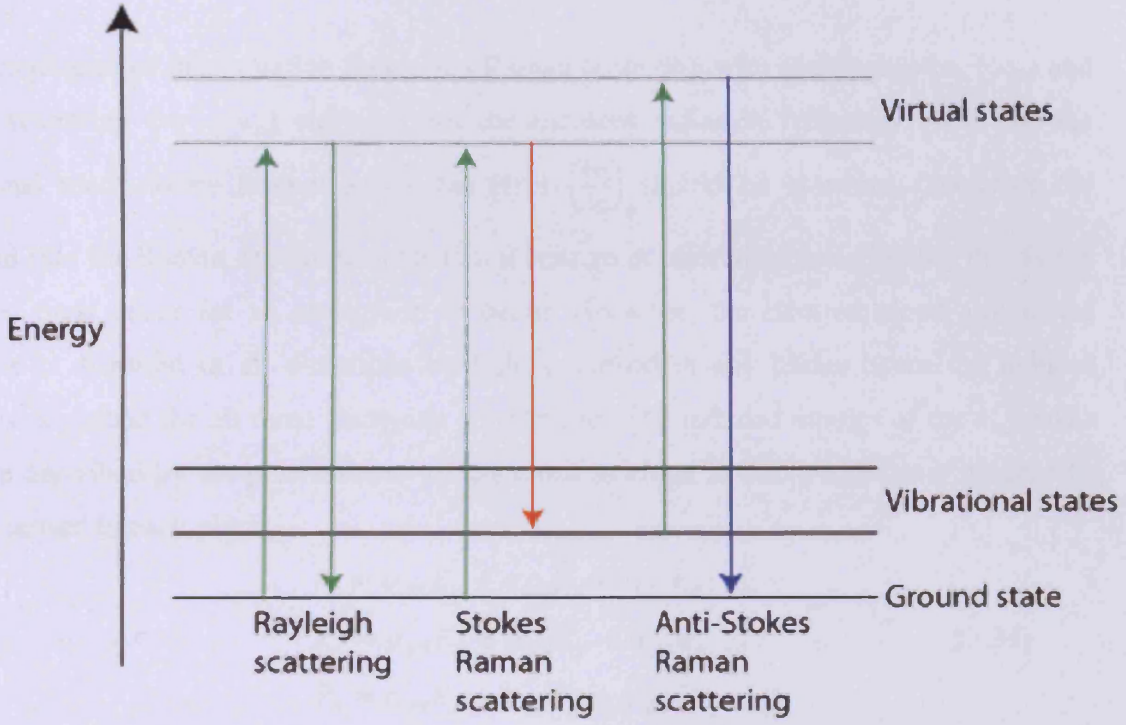

Figure 2.13 Energy states in the scattering process.

As described in section 2.3.3, a dipole P is induced on the molecule by interaction with EM radiation and is proportional to the magnitude of the electric field E and the polarisability of the molecule, α. For small amplitude vibrations, α is dependent on the nuclear displacement q:

$$\alpha = \alpha_0 + \left(\frac{\delta\alpha}{\delta q}\right)_0 q_0 \qquad (2.30)$$

Where α_0 is the polarisability at the equilibrium position of the vibration, $\left(\frac{\delta\alpha}{\delta q}\right)_0$ is the change in polarisability as the nuclei move and q_0 is the vibrational amplitude, evaluated at the equilibrium position. At a vibrational frequency ν_m, the nuclear displacement is found:

$$q = q_0 \cos 2\pi \nu_m t \quad (2.31)$$

By combining equations 2.29 to 2.30 and 2.31 a complete derivation of the induced dipole moment can be found:

$$P = E_0 \alpha_0 \cos 2\pi \nu_0 t + \frac{1}{2}\left(\frac{\delta \alpha}{\delta q}\right)_0 q_0 E_0 [\cos\{2\pi(\nu_0 + \nu_m)t\} + \cos\{2\pi(\nu_0 - \nu_m)t\}] \quad (2.32)$$

The second term of this equation represents Raman scattering with anti-Stokes ($\nu_0 + \nu_m$) and Stokes scattering ($\nu_0 - \nu_m$) shifted from the incident radiation frequency [46]. For the vibrational mode to be Raman active the term $\left(\frac{\delta \alpha}{\delta q}\right)_0$ should be non-zero. Therefore the selection rule for Raman spectroscopy is that a change in molecular polarisability during the vibration must occur for an absorption to occur. However, the electron cloud around the molecule is distorted in all directions by light polarised in any plane, hence the induced dipole is described for all three Cartesian coordinates. The induced dipoles of the *x*, *y* and *z* axes are described by the polarisability of the electron cloud in the specific axis induced by light polarised in each plane:

$$\begin{aligned} P_x &= \alpha_{xx}E_x + \alpha_{xy}E_y + \alpha_{xz}E_z \\ P_y &= \alpha_{yx}E_x + \alpha_{yy}E_y + \alpha_{yz}E_z \\ P_z &= \alpha_{zx}E_x + \alpha_{zy}E_y + \alpha_{zz}E_z \end{aligned} \quad (2.33)$$

This can be represented in matrix form as follows:

$$\begin{bmatrix} P_x \\ P_y \\ P_z \end{bmatrix} = \begin{bmatrix} \alpha_{xx} & \alpha_{xy} & \alpha_{xz} \\ \alpha_{yx} & \alpha_{yy} & \alpha_{yz} \\ \alpha_{zx} & \alpha_{zy} & \alpha_{zz} \end{bmatrix} \begin{bmatrix} E_x \\ E_y \\ E_z \end{bmatrix} \quad (2.34)$$

The 3 × 3 matrix of polarisability values is known as the *polarisability tensor* and represents the polarisability of the molecule in all three coordinates during a vibrational mode. Therefore, the term $\left(\frac{\delta \alpha}{\delta q}\right)_0$ will be non-zero if one of the values in the tensor changes during the vibration [36]. Each value can be assessed in the same integration procedure seen with equations 2.25-2.27.

A change in polarisability can be depicted by polarisability ellipsoids; a three dimensional shape that represents the electron cloud surrounding the molecule. The size, shape and orientation of the ellipsoid is determined by plotting $1/\sqrt{\alpha_i}$ (in the i direction). For a mode to be Raman active the shape, size or orientation should be different at the extremes (+q, -q) of the vibration [46]. Figure 2.14 illustrates the polarisability ellipsoids for three vibrational modes of CO_2. The symmetric stretch (ν_1) shows the size of the ellipsoid at +q to be different to that at –q so the mode is Raman active. However, for both the anti-symmetric stretch (ν_3) and bending mode (ν_2) the ellipsoids at the extremes are the same so they are Raman inactive.

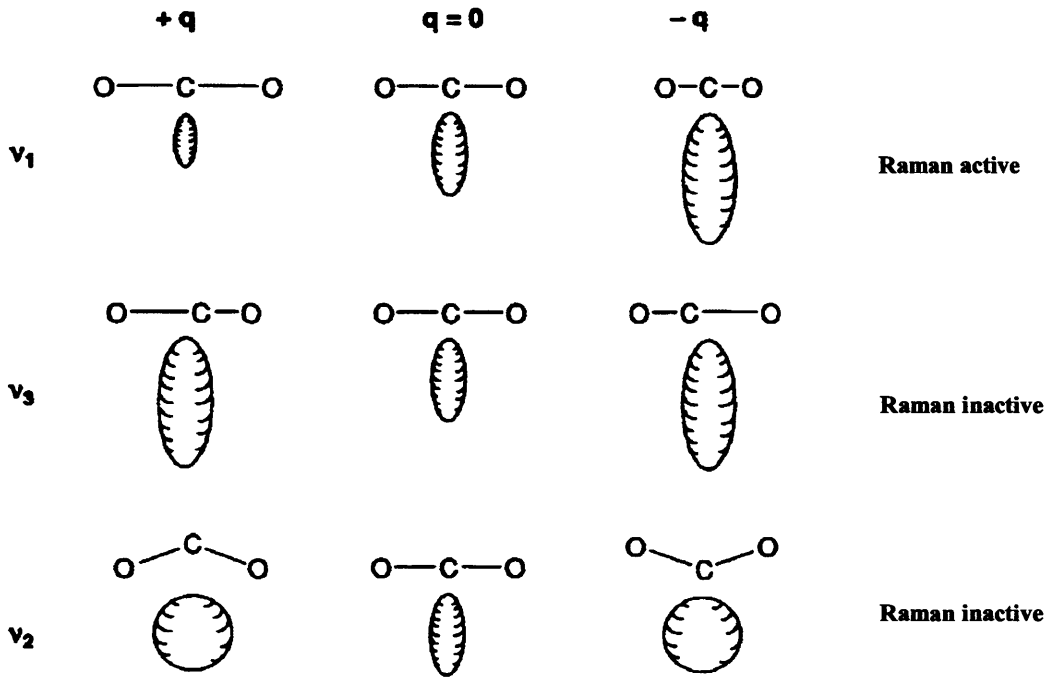

Figure 2.14. Polarisability ellipsoids showing the change in polarisability during a vibration. Reprinted from [46].

For larger molecules, the number and symmetry of vibrational modes may be determined using group theory and which of those modes are Raman active or indeed IR active. In brief, the molecule is classified by the symmetry elements that it possesses (i.e. a rotational axis (*C*), a reflection plane (σ), a centre of inversion (*i*), an improper rotation (*S*) and the identity (*E*)) and the number of operations that can be performed on each element (i.e. $3\sigma_v$ which equates to three vertical reflection planes). The molecule may then be assigned to a class in which all molecules can undergo the same type and number of symmetry operations, known as a *point group*. A basis set may then be used to describe the atomic displacements in a

fundamental vibration, for example, a stretch of a C-H bond would be represented as a vector pointing along the bond in the direction of the atomic displacement (the vectors for all C-H stretches are known as the basis set). The fundamental vibration may then be evaluated by the character of how the basis set transforms under each of the symmetry operations in the point group. The symmetry of the vibration will then correspond to one of the irreducible representations in the character table of the point group.

By consulting the linear functions column (next to the character matrix) in the character table, an x, y or z indicates that a change in the dipole moment along that Cartesian axis is associated with the fundamental vibration, hence the mode is IR-active. Equally, the presence of a quadratic function (x^2, y^2, z^2, xy, xz, yz, $x^2 - y^2$ or $x^2 + y^2$) in the column to the right of the linear functions, indicates a change in polarisability and the vibration is Raman-active. The molecules under investigation in this thesis all possess very low symmetry with the highest symmetry molecules belonging to the C_s point group. Hence, the fundamental vibrations can only be described as being in the molecular plane (A′) or out-of-plane (A″) by group theory, both of which are IR- and Raman-active. For molecules with no symmetry, group theory is unable to describe the symmetry of the vibrations. For a thorough treatment on group theory, the reader is referred to [32].

The propensity of a molecule to undergo Raman scattering can be measured by the cross-section (σ) and is related to the polarisability of the vibrational mode. It is the intensity of Raman scattering measured from a known number of molecules illuminated by an incident monochromatic beam of known wavelength, volume and power. Scattering is assumed to occur homogeneously in all directions and would form a spheroid if the photons travelled a fixed distance from the source. Collection of the scattered photons is generally only through a specified area of the sphere. The size of the collecting area and its distance from the source is used to determine the solid angle (Ω) in steradians (sr), which is proportional to the total area of the sphere (Figure 2.15). Hence, the integrated cross section $d\sigma_c/d\Omega$ of a molecular vibration is traditionally used for comparison and is given in units of cm^2 $molecule^{-1}$ sr^{-1} [37].

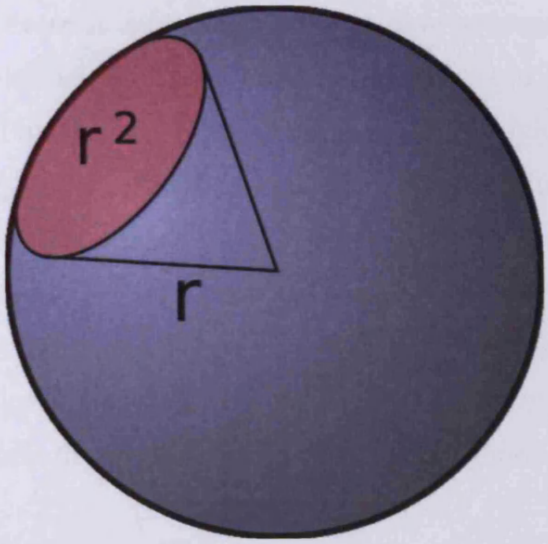

Figure 2.15 Graphic representation of a steradian subtended at distance r from the centre of the sphere. Reprinted from [38].

Knowing the differential cross section of the vibrational mode, the intensity of the Raman scattering (I_R) in photons s^{-1} may be calculated:

$$I_R = \left(\frac{d\sigma}{d\Omega}\right)\Omega\left(\frac{I_L}{A}\right)\rho ALK_e = \left(\frac{d\sigma}{d\Omega}\right)\Omega I_L \rho LK_e \qquad (2.35)$$

Where I_L is the intensity of the incident laser beam (photons s^{-1}), A is the cross sectional area of the laser beam (cm^2), ρ is the molecular density (molecules cm^{-3}), L is the path length of the laser (cm) and K_e is a constant that encompasses instrumental factors such as the quantum efficiency of the detector and the transmission of the optics. The Boltzmann distribution can then be adapted for the relative intensity of anti-Stokes (I_{aS}) and Stokes (I_S) shifted scattering of the Raman shifted frequency (ν_R) of the vibrational mode [47].

$$\frac{I_{aS}}{I_S} = \frac{g_{aS}}{g_S}\exp\left[\frac{-\nu_R}{kT/hc}\right] \qquad (2.36)$$

2.3.5 Surface Enhanced Raman Spectroscopy

In 1974 Fleischmann and colleagues reported unusually high Raman scattering from pyridine adsorbed on a roughened silver electrode [39]. This was first assigned to the high surface area of the electrode enabling more pyridine molecules to adsorb, but was later found by Jeanmarie and Van Duyne [40] and Albrecht and Creighton [41] to be more than just a

surface area factor. The increase in surface area would have accounted for an increase in intensity by a factor of 10 in Fleischmann's work, but the observed increase was closer to 10^6. Since then, the effect of increased intensity from molecules on other metal surfaces have been found on lithium [42], sodium [43] and potassium [44] with the strongest and most reliable activity coming from the coinage metals namely silver, copper and gold [45]. This type of spectroscopy is known as Surface Enhanced Raman Scattering/Spectroscopy (SERS) and is capable of achieving femtomole detection limits [46]. This highly sensitive technique is a useful probe for *in situ* gas-solid, liquid-solid and solid-solid interfaces and is a welcome addition to the plethora of tools to the surface science and heterogeneous catalysis disciplines.

Two theories emerged to explain the SERS effect, but whilst both have their merits, neither can explain the full range of reported phenomena. Empirically, SERS activity is achieved from rough metal surfaces and this physical nature is satisfied in the electromagnetic theory (EM).

2.3.5.1 The Electromagnetic Theory for SERS

The conduction band electrons in a metal are located at a distance from the metal surface, but are bound by positive charge in the sub-surface of the metal. These electrons are able to move laterally across the surface of the metal and when irradiated with an EM field the electrons will oscillate as a group known as a plasmon (a quantised vibration of the electron gas). If the metal is roughened uniformly, the plasmons can resonate with the incident field and absorb the radiation, which increases the electric field on the metal surface. The nanostructures on the surface can also direct the oscillation in a vector normal to the surface plane giving rise to local areas of very high EM field strength (Figure 2.16). Interaction of the electrons in a molecule with the plasmon electrons increases the Raman cross-section of the adsorbate [22].

The plasmon on a flat surface will propagate along the surface plane, but this description is inadequate for the electric field on a roughened surface. For simplicity, the nanostructures that result from a roughened surface are considered to be spherical in shape. The size of the sphere is much smaller than the wavelength of the incident light and so the plasmon will not propagate in a direction along the surface, but will polarise around the sphere as described by the Rayleigh approximation [47]. This induced electric dipole will oscillate at the same frequency as the incident light and the field of the plasmon will be localised on one side of

the spheroid. On a flat surface, the field of the plasmon will propagate along the plane parallel to the surface in a delocalised fashion and the energy will dissipate as heat [48].

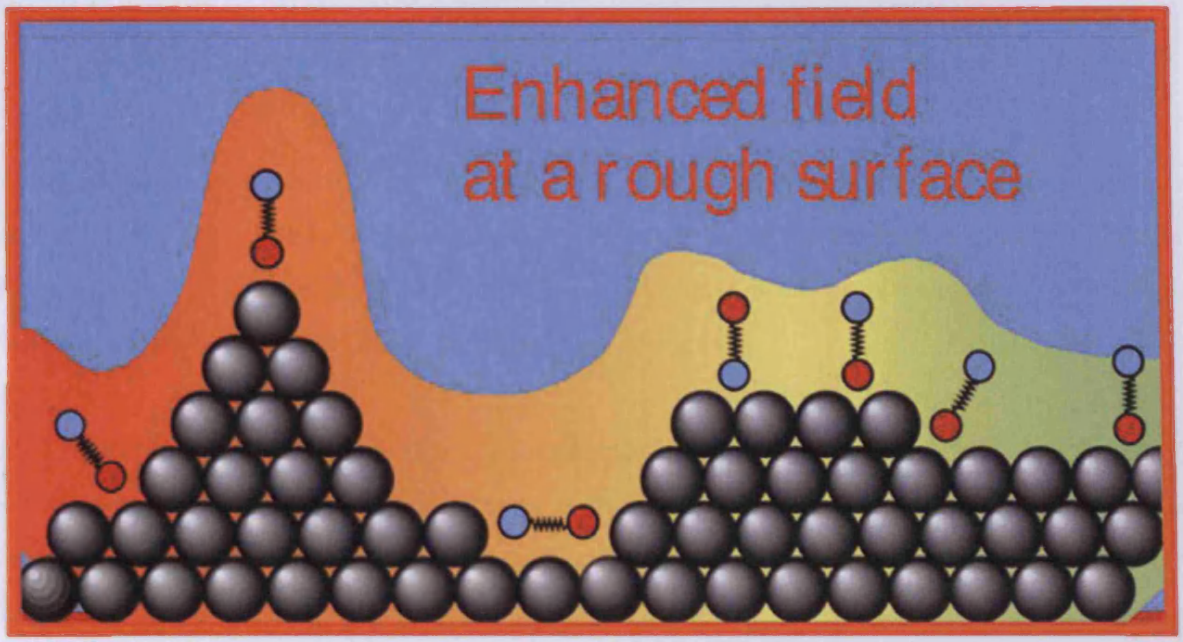

Figure 2.16 EM theory for SERS enhancement. The height of the shaded area above the surface metal atoms indicates a greater EM enhancement.

To describe the electric field E_r at a distance r from the spheroid surface of radius a, the following equation is used [47]:

$$E_r = -E_0 r\cos\theta + g\left(\frac{a^3}{r^3}\right)E_0\cos\theta \qquad (2.37)$$

Where E_0 is the incident field, θ is the angle relative to the direction of the incident field and g is a constant related to the dielectric constants of the metal and surrounding medium at a frequency of the incident radiation:

$$g = [\varepsilon_i(\omega_L) - \varepsilon_0]/[\varepsilon_i(\omega_L) + 2\varepsilon_0] \qquad (2.38)$$

The dielectric constant of the surrounding medium, ε_0, is assumed to be close to unity in the range of frequencies used in Raman spectroscopy. The magnitude of the electric field is proportional to g and is at a maximum when the dielectric constant of the metal, $\varepsilon_i = -2\varepsilon_0$, which would give a denominator of 0 for equation 2.38 and an infinite value of g. ε_i is dependent on the incident frequency of light (ω_L), therefore a maximum value of g can be

achieved by tuning ω_L to meet the resonance condition. However, ε_i can be subdivided into the dielectric constant of the real (ε_1) and imaginary (ε_2) part of the metal as such $\varepsilon_i = \varepsilon_1 + i\varepsilon_2$. Hence g can now be expressed as follows:

$$g = [\{\varepsilon_1(\omega_L) - \varepsilon_0\} + i\varepsilon_2]/[\{\varepsilon_1(\omega_L) + 2\varepsilon_0\} + i\varepsilon_2] \qquad (2.39)$$

Therefore the denominator of g is no longer 0 at the resonance condition and g is not infinite. A large value for g is now dependent on a very small value for the dielectric constant of the imaginary part of the metal, ε_2. Metals with a small contribution from the imaginary dielectric function are said to possess a low dielectric loss factor [49].

As previously mentioned the SERS phenomenon is limited to a few metals with copper, silver and gold providing the best activity with alkali metals showing some activity. This is because a large value for g can be attained with these metals in the frequency range used in Raman spectroscopy [49]. It is not only that the resonance condition is met for these metals at these frequencies; it is also because the dielectric function of the imaginary part is less significant. On that basis it is theoretically possible to generate surface enhanced scattering at different frequencies in the EM spectrum so long as the metal plasmon resonance condition is met and the metal possesses a low dielectric loss factor. However, with the probability of scattering decreasing with the fourth power of frequency, the sensitivity will also decline at lower incident frequencies.

This approximation requires some adjustment as it is known that the nanostructures on a roughened surface are not spherical and it is known that extremely active SERS may originate from the junction between two or more nanoparticles. The enhanced electric field produced in the EM theory means that the analyte does not need to be directly attached to the metal surface. Rather, so long as it is just within the field so that the resonance can be 'felt' by the molecule, the SERS effect would be active. This allows molecules adsorbed in multilayers to be SERS enhanced, but the activity falls away with distance r from the surface as $1/r^3$.

2.3.5.2 Surface Selection Rules

The symmetry of an adsorbed molecule may be lowered by the adjacent surface metal atoms, particularly for chemisorbed complexes [50], which can subsequently change the symmetry of a molecular vibration and its Raman-active status. Therefore, new peaks can emerge and some peaks may disappear.

Interaction of the molecule with the metal surface creates an image charge of the molecular dipole in the sub-surface of the metal [47]. This phenomenon can add to the EM enhancement through the metal acting as an antenna for the emitted Raman scattering [47], but is also related to the "surface selection rules".

If the dipole moment of a molecule and its image are parallel then the molecular dipole moment is screened by the image, there would be no net change in the dipole moment and so absorption of the incident light will not occur. However, if the molecular and image dipole moments are perpendicular, then the molecular dipole moment is augmented by the image and intense absorption can occur. Therefore, not only can the number and position of active modes change, but the relative intensities may also change according to the degree of image screening [51]. For surface Infra-Red spectroscopies, the majority of transition metals are highly reflective for the frequency range used and so the image screening effect is prevalent. For surface Raman techniques, the induced dipole moments may also be screened/augmented by such sub-surface image charges. However, the frequency ranges used are not quite so efficiently reflected by the transition metals in general, so the image charge is less able to screen parallel modes. Added to this, the difference in morphology for SERS active surfaces and the result is a more relaxed set of surface selection rules which follows the general perpendicular *vs.* parallel rule but does not necessarily adhere to it [51].

2.3.5.3 The Charge Transfer Theory for SERS

A second theory dubbed the 'charge transfer' (CT) theory is more focussed on the interaction between the metal and the adsorbate. According to CT, a chemical bond is formed between the adsorbate and the metal atoms enabling charge to resonate between discrete energy states in the molecule and occupied or unoccupied states in the metal depending on the direction of transfer (Figure 2.17). This acts to change the polarisability of the molecules thereby increasing Raman emission [22].

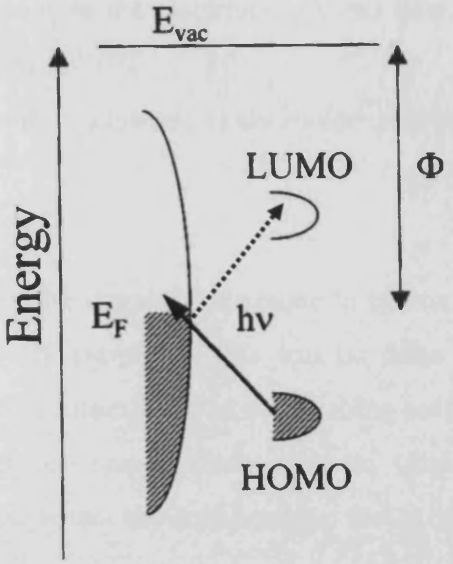

Figure 2.17 Energy levels of the metal states (left) and HOMO and LUMO of the molecule (right), E_F, E_{vac} and Φ are the Fermi energy, vacuum energy and work function of the metal. The solid arrow represents a molecule to metal charge transfer and the dotted arrow represents a metal to molecule transfer [52].

The charge transfer process can be stimulated by the incident light if it is in resonance with the energy gap of the transition. In metal to molecule transitions (Figure 2.17, dotted arrow) the process is described by the following steps:

- A conduction band electron of the metal is excited by absorption of an incident photon, *hv*, to an unoccupied state above the Fermi level leaving a hole below the Fermi level.
- The electron crosses over to an excited electronic state of the molecule via the adsorbate-substrate complex.
- The electron then returns to fill the hole in the metal conduction band leaving the molecule to return to the electronic ground state, but in an excited vibrational state.
- In the second transfer process, a Raman shifted photon is radiated.

For molecule to metal transfers (Figure 2.17, solid arrow):

- An electron in the ground electronic state of the molecule is excited by absorption of a photon, *hv*, to an excited electronic state.
- The electron crosses to the highest unoccupied level in the conduction band of the metal.

- The electron then returns to the electronic ground state but the molecule is left in a vibrationally excited state.
- A Raman shifted photon is scattered as the molecule relaxes back to the ground state.

2.3.5.4 Applications

In its application, SERS is not the simplest technique to master. Attaining SERS activity on the coinage metals is relatively simple as this can be done by mechanical or chemical abrasion of the surface. The difficulties arise in establishing uniform activity across the entire surface. It is often found that on non-uniform surfaces, sites of extremely high intensity known as "hotspots" can misrepresent the enhancement factor of the surface.

It is often required that surface information from a typically non-SERS active metal is the target experiment. In this situation the non-active metal can be deposited in a film on the surface of an active substrate and the activity can extend through the metal film and SERS may be attained from the adsorbate [53]. The nanofilm should cover the underlying substrate completely so as not to have contributions from the analyte adsorbed on that metal. Sites exposing the substrate are known as pinholes. The geometrical growth of the film will vary with the film material and the substrate i.e. islands can form. The technique for achieving pinhole-free surfaces will depend on the two metals used.

The instrumentation required for SERS experiments is the same as that for normal Raman measurements. However, recent developments have enabled the coupling of an STM tip to a Raman spectrometer in Tip Enhanced Raman Scattering (TERS) [54]. The combination of an atomically sharp gold tip and the laser light can be used to enhance the electric field around a single molecule adsorbed on a well defined surface of any material [55,56]. The implementation of this procedure is notoriously difficult to set up, but the sensitivity and information it can provide makes TERS potentially a very powerful surface analytical technique.

2.4 References

[1] K. W. Kolasinski, *Surface Science*, Wiley **2002**.

[2] G.A. Somorjai, *Principles of Surface Chemistry*, Prentice Hall **1972**.

[3] D.M. Kolb, *Surf. Sci.*, 500 **(2002)** 722.

[4] Ph.D. Thesis, D.J. Watson, *The Preparation and Characterisation of Platinum and Palladium Bulk Alloy Single Crystals and A Study of Interactions at Chiral Metal Surfaces*, Cardiff University, **2002**.

[5] http://www.hit.ac.il/staff/Lapsker/50115/04%20Crystal%20structure.pdf

[6] Ph.D. Thesis, S.P. Smale, *A Study of the Hydrogen Evolution Reaction on Platinum and Platinum Group Metal Surfaces*, Cardiff University, **2008**.

[7] http://www.fhi-berlin.mpg.de/~hermann/Balsac/SSDpictures.html

[8] http://www.chem.qmul.ac.uk/surfaces/scc/scat1.htm

[9] B. Lang, R.W. Joyner, G.A. Somorjai, *Surf. Sci.*, 30 **(1972)** 440.

[10] G. Attard, C. Barnes, *Surfaces*, Oxford University Press, New York, **1998**.

[11] P.K. Babu, Y.Y. Tong, H.S. Kim, A. Wieckowski, *J. Electroanal. Chem.*, 524–525 **(2002)** 157–167.

[12] http://rsl.eng.usf.edu/Documents/Tutorials/TutorialsWorkFunction.pdf

[13] K. W. Kolasinski, *Surface Science*, **2002**, Wiley.

[14] C. J. Barnes, M. Lindroos, D. King, *Surf. Sci.*, 201, 1-2 **(1988)** 108-128.

[15] A., M. Dekker, *Interfacial Electrochemistry, Theory, Experiment and Applications*, **1999**.

[16] A.J. Bard, L.R. Faulkner, *Electrochemical Methods, Fundamentals and Applications*, Wiley **1980**.

[17] J. Zhang, *J. Electroanal. Chem.*, **1972**, vol. 331, p. 945.

[18] F. G. Will, C. F. Knorr, *Zeitschrift fur Elektrochemie* **1960**, *64*, 258.

[19] A. Wieckowski, *Interfacial Electrochemistry: Theory, Experiment and Applications*, CRC Press **1999**.

[20] D.L. Pavia, G.M. Lampman, G.S. Kriz, *Introduction to Spectroscopy*, 3rd ed., Brooks/Cole **2001**.

[21] S. Walker, H. Straw, *Spectroscopy*, Vol. 2, Science Papaerbacks **1962**.

[22] E. Smith, G. Dent, *Modern Raman Spectroscopy*, Wiley **2005**.

[23] D.C. Harris, *Quantitative Chemical Analysis*, 6th ed., Freeman **2003**.

[24] G. Socrates, *Infra-red and Raman Characteristic Group Frequencies*, Wiley **2004**.

[25] Schachtschneider, Snyder, *Spectrochim. Acta*, **1963**, 19, 117.

[26] S. Ege, *Organic Chemistry – Structure and Reactivity*, 4th ed., Houghton Mifflin Company, **1999**.

[27] L.J. Bellamy, *The Infra-red Spectra of Complex Molecules*, 2nd ed., **1980**.

[28] P.S. Sindhu, *Fundamentals of Molecular Spectroscopy*, New Age International, **2006**.

[29] J.O. Jensen, *Spectrochimica Acta Part A*, 60 (**2004**) 1895–1905.

[30] A.K. Soper, C.J. Benmore, *Phys. Rev. Lett.*, 101, 065502 (**2008**).

[31] H.D. Lutz, K. Beckenkamp, H. Moller, *J. Mol. Struct.*, 322 (**1994**) 263-266.

[32] D. Willock, *Molecular Symmetry*, Wiley **2009**.

[33] C.N. Banwell, *Fundamentals of Molecular Spectroscopy*, McGraw-Hill **1972**.

[34] M.C. Tobin, *Laser Raman Spectroscopy*, Wiley-Interscience **1971**.

[35] W. Shulke, *Electron Dynamics by Inelastic X-ray Scattering*, Oxford University Press, **2007**.

[36] D.A. Long, *The Raman Effect: A Unified Treament of the Theory of Raman Scattering by Molecules*, **2002**.

[37] R.L. McCreery, *Raman Spectroscopy for Chemical Analysis*, **2000**.

[38] commons.wikimedia.org

[39] M. Fleishman, P.J. Hendra, A.J. McQuillan, *Chem. Phys. Lett.*, 26, 163 (**1974**).

[40] D.C. Jeanmarie, R.P. Van Duyne, *J. Electroanal. Chem.*, 84, 1 (**1977**).

[41] M.G. Albrecht, J.A. Creighton, *J. Am. Chem. Soc.*, 99, 5215, (**1977**).

[42] M. Moskovits, D.P. DiLella, *Surface Enhanced Raman Scattering*, (**1982**) 243-274.

[43] P.A. Lund, D.E. Tevault, R.R. Smardzewski, *J. Phys. Chem.*, 88 (**1984**) 1731.

[44] W. Schulte, B. Breithaupt, K.-P. Charle, U. Kloss, *Ber. Bunsenges. Physik. Chem.*, 88 (**1984**) 308.

[45] A. Kudelski, J. Bukowska, *Vib. Spectrosc.* 10 (**1996**) 335-339

[46] J.R. Ferraro, K. Nakamoto, C.W. Brown, *Introduction to Raman Spectroscopy*, 2nd ed., **1994**.

[47] R.L. Birke, J.R. Lombardi, *Spectroelectrochemistry, Theory and Practice*, ed. R.J. Gale **1988.**

[48] M. Moskovits, *Rev. Mod. Phys.* **1985**, 57, 783.

[49] A. Campion, P. Kambhampati, *Chem. Soc. Rev.*, **1998**, 27, 241.

[50] H. Nicholas, R.M. Hexter, *J. Chem.Phys.* 75, **1981,** 3126-36.

[51] M. Moskovits, *J. Chem. Phys.* 77, **1982**, 4408-4416.

[52] P. Kambhampati, M.C. Foster, A. Campion, *J. Chem. Phys.*, Vol. 110, No. 1, 1 January **1999.**

[53] J-F. Li, Z-L. Yang, B. Ren, G-K. Liu, P-P. Fang, Y-X. Jiang, D-Y. Wu, Z-Q. Tian, *Langmuir* **2006**, 22, 10372-10379.

[54] E. Bailo, V. Deckert, *Chem. Soc. Rev.*, **2008**, 37, 921 – 930.

[55] R.M. Stockle, Y.D. Suh, V. Deckert, R. Zenobi, *Chem. Phys. Lett.*, 318 (**2000**) 131.

[56] M.S. Anderson, *Appl. Phys. Lett.*, 76 (**2000**) 3130.

Chapter 3
Experimental

3.1 Raman Spectrophotometer and Microscope

The apparatus used to run the Raman experiments was a LabRam HR confocal microscope from HORIBA Jobin Yvon Ltd. with the following specifications:

- A 10 mW He-Ne 633 nm laser.
- A ×50 long working distance objective lens with a numerical aperture of 0.55 and a working distance of 8.1 mm producing a spot size of 1.4 μm.
- A ×10 condenser lens with a focal length of 300 mm that focussed the laser into the objective lens.
- A confocal hole with adjustable aperture, set to 200 μm.
- 5 density filters that reduce the power to 50%, 25%, 10%, 1% and 0.1% and a sixth position with no filter i.e. 100% of the power is transmitted in this configuration.
- A notch filter for a 633 nm laser set at an angle to reject this light frequency.
- 1800 grooves/mm diffraction grating.
- 1024 pixel CCD Peltier cooled detector.
- Manually operated X-Y stage.
- Motorised Z-slider.
- Video camera.

The above configuration generated a resolution of 1.539 cm^{-1}, but other components and configurations were available including:

- 30 mW YAG 532 nm laser.
- ×10 and ×100 objective lenses.
- A notch filter for a 532 nm laser.
- 600 gr/mm diffraction grating.

Collection and analysis of the data was performed on the proprietary LabSpec program run on a Dell OPTIPLEX PC. Before running an experiment, the He-Ne laser was allowed 30

minutes after being switched on to warm up to the maximum output power. A shutter was used to prevent the light emission from exiting the laser unit and was always closed until a spectrum was ready to be recorded. The detector was calibrated every time it was switched on and then every two to three days when in constant operation. The detector itself was cooled by a Peltier device to a constant -75 °C and the room was also thermostatically controlled by an air conditioning unit to maintain 20 °C. Nonetheless, minor temperature changes could affect the "zero" coefficient of the detector and ultimately, the position of the spectral peaks. The LabSpec program also needed to be calibrated in frequency against a well defined Raman shift. A silicon single crystal was used for this purpose as the crystal lattice vibration (phonon) occurred reliably at 520.7 cm^{-1}. This would only vary with the zero coefficient so did not need to be checked as often. Parameters used for calibration of the Raman spectrometer were saved every time calibration was performed so a profile of intensity *vs.* time could be viewed. This allowed the operator to assess if the performance of the spectrometer was falling. A fall in performance could be a result of the optics changing position or efficiency, the laser becoming misaligned or loss of power or the detector losing sensitivity.

3.1.1 The Raman Experiment

To run an experiment, the following steps were taken:

1. The sample was secured on the X-Y stage and positioned under the objective lens.
2. An emission guard was placed around the objective lens turret to enclose the laser emission and prevent light contamination when running a spectrum.
3. A white light source was turned on and a beam splitter was set to direct the image from the objective lens to a video camera.
4. The camera icon in the LabSpec program was clicked to open the camera image in a real time display.
5. A joystick connected to the Z-slider was used to move the objective lens up or down to focus the image.
6. Once focussed, the white light source was switched off and the beam splitter was raised to allow the laser light to impinge on the surface and direct the scattering to the detector.
7. The parameters of the spectrum were set. These would include the accumulation time, the number of accumulations, the density filter, the frequency range set by the

position of the grating and the acquisition function (simple, multi-window, depth profile, time profile etc). The correct hardware was then selected i.e. emission source, confocal hole aperture, grating etc.

8. All personnel present would wear the appropriate filter goggles i.e. if the 633 nm (red) laser was used then green or blue coloured goggles would be worn.
9. The laser shutter was opened and the spectrum accumulation icon was clicked.
10. After the run had finished, the laser shutter was closed and the spectrum saved as a .tsf file in the appropriate folder. (The .tsf file would save the parameter settings unlike .txt file which did not).

3.1.2 Data Processing

For display purposes, the data collected could be processed using the LabSpec facilities. Figure 3.1 shows four overlapping spectra (black) collected at different frequency ranges of the diffraction grating to cover the full frequency range (250-3300 cm^{-1})[‡]. The presentation of this data could be improved by subtracting the baseline of each spectrum and combining all four sections to form one full range spectrum (red). A critical eye was required when performing these tasks because processing the data could lead to alterations to the shape or intensity of a peak(s), which could then lead to an incorrect interpretation of a spectrum.

[‡] A grating with fewer gr/mm would provide a much wider frequency range in one spectrum but would sacrifice resolution.

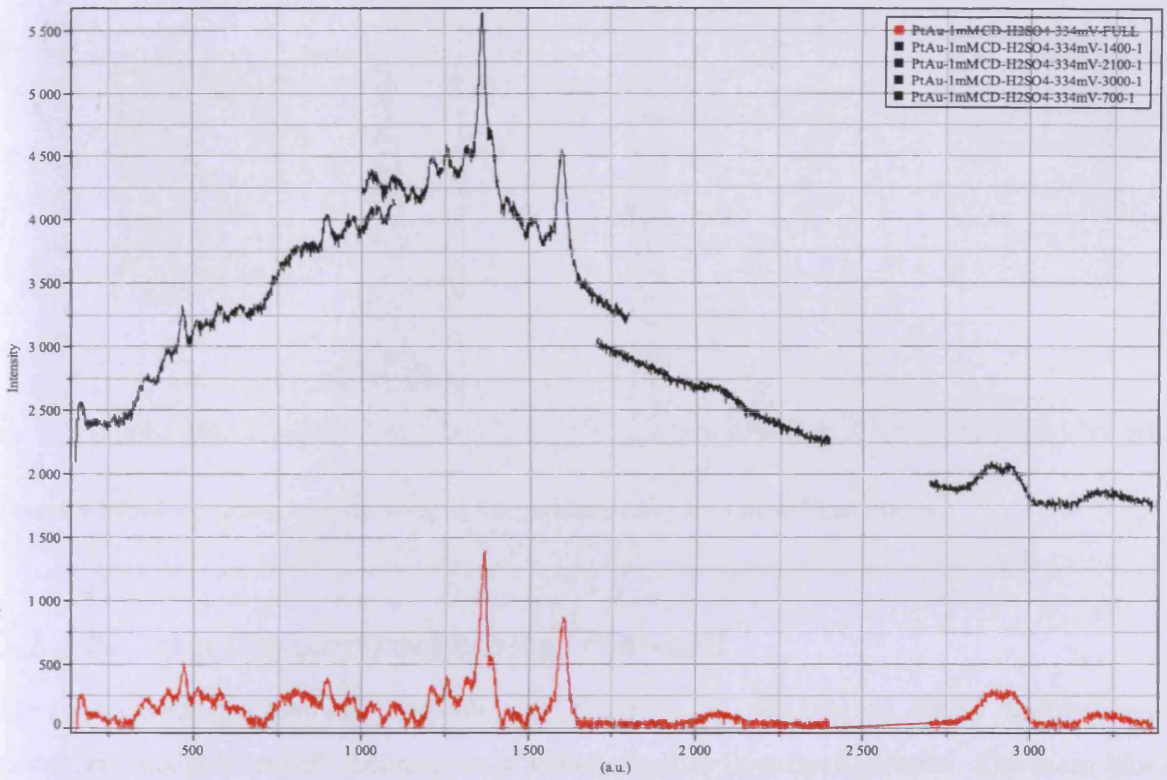

Figure 3.1 An example of typical SERS data before (black line) and after (red line) processing. In this case, the alkaloid cinchonidine adsorbed on platinum is being measured.

The processed data was then saved as a .txt file as this took up less hard disk memory and could be transferred to other graphical programs such as Microsoft Excel or Microcal Origin for more advanced presentation processing. Further analysis on the data could be performed with the LabSpec program, such as peak area integration. Two methods were available; the first was simply highlighting a peak using peak integration cursors which would manually set a baseline (Figure 3.2 a). If there was a shoulder contributing to a peak, then this method was unsuitable as it integrated the whole area under a peak indiscriminately. A second method involved labelling or searching for the peaks and estimating the peak shape and its contribution using a Gaussian and/or Lorentzian peak fitting routine (Figure 3.2 b).

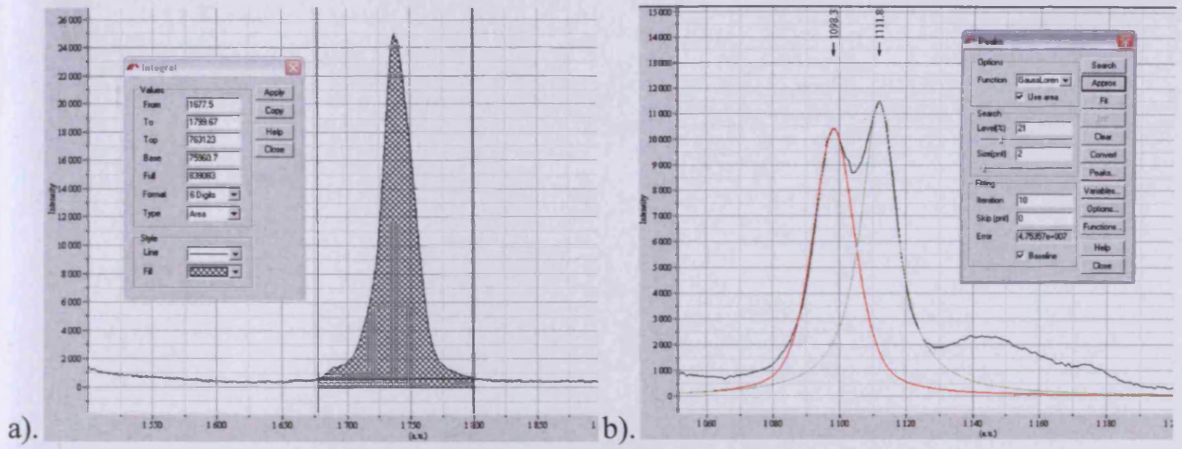

Figure 3.2 Peak area integration methods; a). integration cursors, b). a peak fitting routine.

3.2 The Spectro-electrochemical Flowcell

The spectro-electrochemical flowcell was designed to incorporate SERS spectroscopic measurements with electrochemistry in a sealed channel flow configuration. The main block of the cell was made from PTFE and housed three electrodes in a 12 × 30 × 1 mm channel. A 24 × 50 mm borosilicate glass spectral window (Sigma-Aldrich, cover glass) was sealed on to the channel using Viton® gaskets secured in place with an aluminium top-plate and tube clamps to finger tightness. 1.58 mm O.D. × 0.8 mm I.D. PTFE inlet and outlet tubes were screwed in to the PTFE block with Supelco® HPLC fittings and then sealed with ferrules (Figure 3.3).

Before each experiment, the components of the cell that came into contact with the liquid or gas phase media were cleaned thoroughly. The PTFE cell, the Viton® gaskets and the spectral window were all immersed in a solution of green acid (98% sulphuric acid with potassium permanganate grains added stepwise until a translucent green solution was achieved) for a period of up to one hour. The green acid solution could be re-used or disposed of in an appropriate container with 50% water by volume. All components were thoroughly rinsed, then boiled for 10 minutes, rinsed, boiled and rinsed again with ultra-pure water. During this time, the PTFE inlet and outlet tubes could be cleaned by flowing ethanol for 30 minutes followed by ultra-pure water.

The platinum and palladium polycrystalline working electrodes were flame annealed in a Bunsen burner until cherry red and thus all contaminants were removed as judged by the

colour of the flame. The gold counter electrode was cleaned in the same way only using a smaller flame as the temperature of a standard Bunsen flame exceeded the melting point of gold (1064°C). When the electrode was clean it was cooled in ultra-pure water leaving a droplet over the surface to help keep it clean prior to insertion into the cell. Layers of PTFE tape wrapped around the electrode could be used to ensure the electrode was well sealed into the cell. The height of the electrode above the channel bed could be carefully adjusted such that it was either flush to the surface, thereby reducing turbulence in the stream, or the electrode could be pushed upwards to be closer to the window, thereby reducing solution interference with the backscattered photons. A silver/silver chloride electrode (BASi, RE-6) was used as a potential reference and was upstream of the working electrode to minimise ohmic drop. The gold counter electrode was downstream of the working electrode to minimise the electrochemical products from the counter electrode impinging on the working electrode. Electrical contact was then made to the potentiostat with the supplied crocodile clips (red: counter, white: reference, green: working).

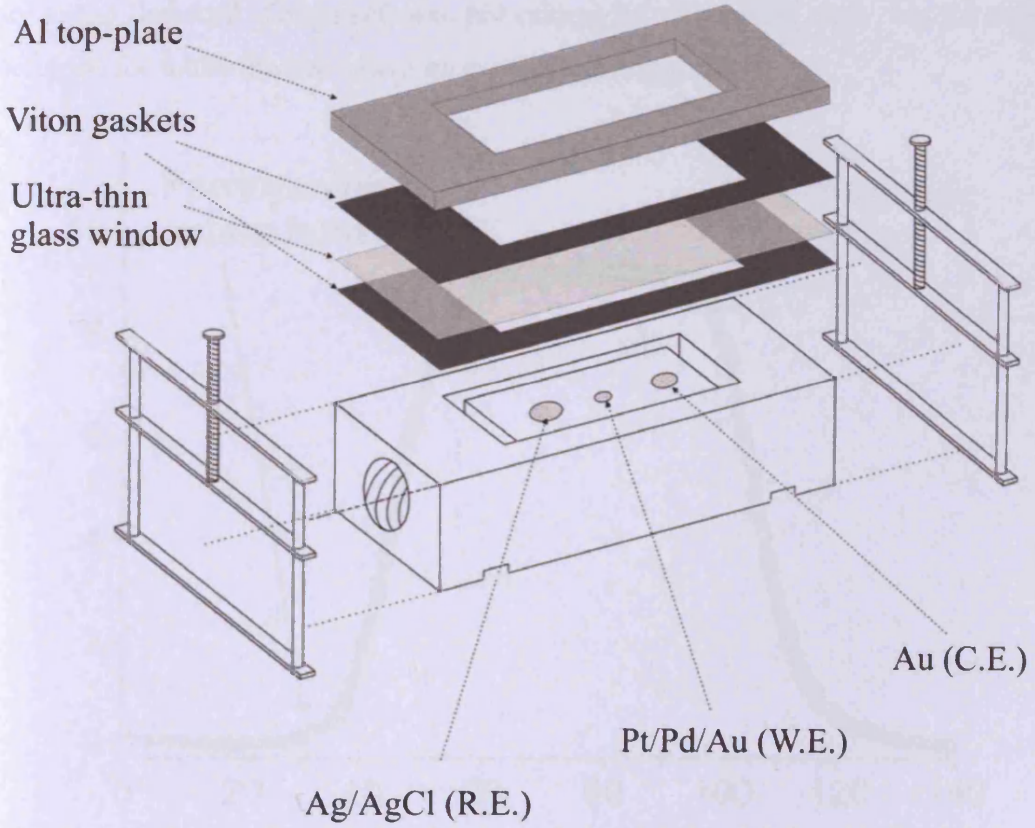

Figure 3.3 Diagram of the spectro-electrochemical flowcell.

Solutions could be degassed at the reservoir in order to minimise the "rogue signals" reported by Etchegoin due to dioxygen interactions with the metal surface [1,2] and then drawn

through the cell and into an appropriate waste container using a single channel peristaltic pump (Cole Parmer, Masterflex C/L) delivering volume flow rates from 1.3 to 7.2 mL min^{-1}. The vacuum created by drawing in the solutions helped to seal the cell and any leaks that existed would result in air bubbles being drawn into the flow. Conversely, by pushing the solution through at gentle pressure, a leak was more likely to occur by positive pressure lifting the gaskets away from the block and this would result in potentially harmful solution spilling onto the microscope stage.

The hydrodynamics of the flow-cell had been tested to ensure analyte delivery and removal was suitably effective. This was achieved by alternating between plugs of solutions of 0.1 M KCl and 10 mM $K_3Fe(CN)_6$ whilst the working electrode was held at a potential at which the ferricyanide would be reduced. Figure 3.4 shows the resulting "concentration transient" for moderate solution flow rates. This indicated that there was some mixing of the solutions, which was due to the depth of the channel and in particular the depth of the trench in the entry to the flow-cell. This result was not critical for the present study, but the cell could be redesigned for future studies where mixing must be minimised.

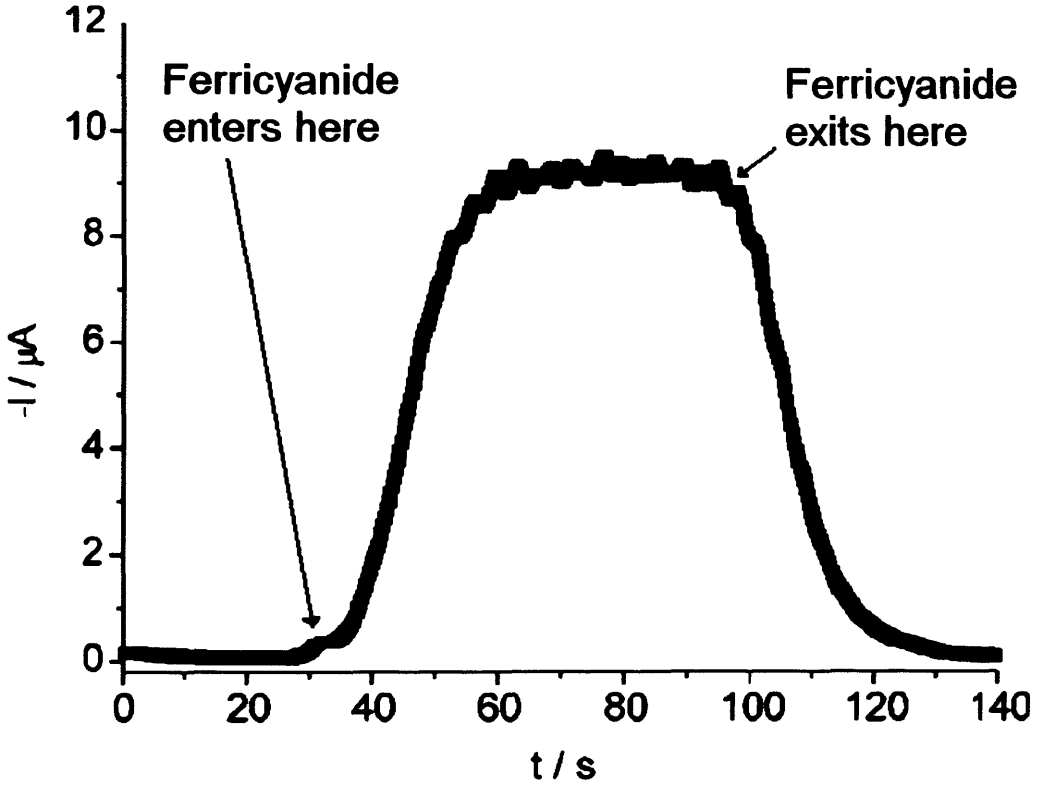

Figure 3.4 A current *vs.* time plot as ferricyanide entered (t = 30s) and left (t = 100s) the cell to ascertain the fluid dynamics of the spectro-electrochemical flowcell at a moderate flow rate.

3.2.1 Gas Phase Studies Using SERS

The cell could be adapted for work in the gas phase by unscrewing the HPLC fittings and removing the inlet and outlet tubes and subsequently screwing in custom made Pyrex® fittings with ground glass joints allowing connection to the gas lines sealed with NESCOFILM®. 3-way splitter valves could be used to control introduction of the analyte and regulate the flow. The flow rate could be monitored by a flow meter on the exit tube of the cell (Figure 3.5). The gases passed through an oxygen and a hydrocarbon trap upstream of the analyte to help remove these two contaminants. Waste gases were directed to the vent above the system.

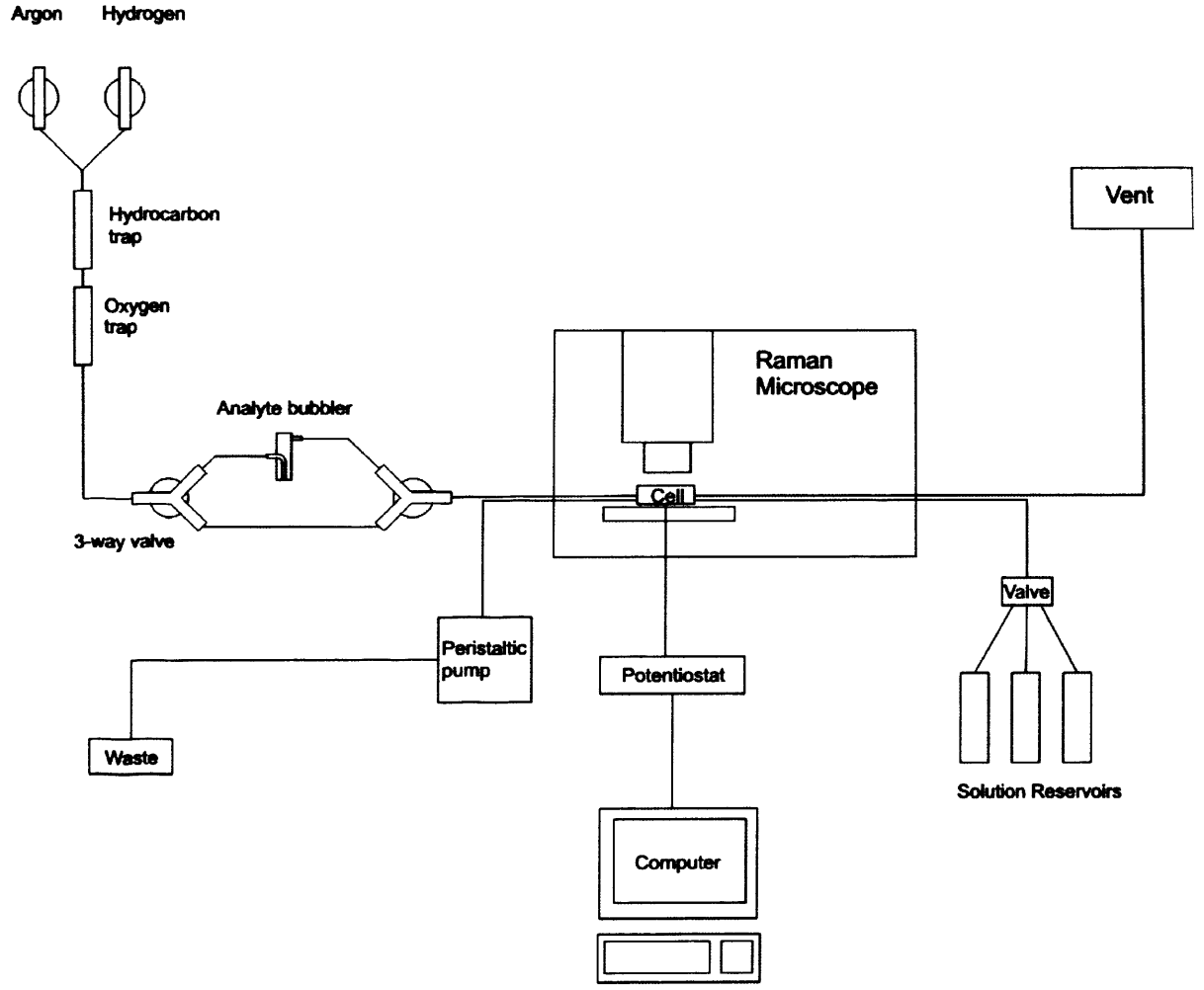

Figure 3.5 Schematic diagram of the EC-SERS system.

The gas phase system was primarily designed for liquid phase analytes that had a gas phase partition. The principle advantage to using gas phase dosing for the investigation of the surface reaction being studied was that the complexity of the interface was reduced by

removing solvent-reactant, solvent-product, solvent-modifier and solvent-catalyst interactions. An advantage for spectroscopic analysis was that the interfering solvent peaks were now absent. The disadvantage was the lack of control over the partial pressure of the analyte. The gas phase analyte would condense on all surfaces between the bubbler and the exit vent including the electrode, which gave rise to backscattered photons from both chemisorbed and physisorbed species. Although a limited level of control could be obtained by altering flow rates with the gas mixtures, the condensed layer could still act like a buffer such that liquid-gas equilibrium would ensure a relatively constant partial pressure of the analyte. The argon flow could be directed around the analyte source, but the analyte would persist for a significant length of time due to the condensed phase on all surfaces upstream of the cell desorbing back into the gas phase. To manage this problem, the length of tubing and pipe-work was made as short as possible. A heating element along that length of the pipe-work could feasibly shift the equilibrium in favour of the gas phase. However, implementing this extra level of control was not expected to yield any further advantages to the current system.

3.3 Preparation of Surfaces for SERS Analysis

The electromagnetic theory for Surface Enhanced Raman Scattering (SERS) dictated that the surface should be rough so that the resonating plasmons from the metal, oscillate in a vector perpendicular to the surface [3]. Due to certain properties of the metal such as plasmon resonance frequency and the dielectric constant of the metal, SERS was limited to a select few metals with the most reliable and strong scatterers being the coinage metals; copper, silver and gold. Platinum and palladium were the two metals required for the present study. Unfortunately, these did not possess the ideal physical properties to generate SERS. Tian, Ren and Wu had reported a high frequency potential waveform that electrochemically etched a platinum surface and produced SERS activity [4]. The waveform was alternated between -0.2 V – +2.4 V *vs.* SCE and depending on the desired roughness factor, the frequency of the waveform was set between 0.5 – 2 kHz, which was at the very limit of the potentiostats available in our laboratory. After many attempts, good SERS activity was not achieved by this method. Voltammetric tests revealed that the potentiostat was not applying the correct upper and lower potentials and even after software and instrument updates as supplied by the manufacturer (CH Instruments), the problem was never overcome. Platinum and palladium

had been reported to give reliable SERS activity through electrodeposition of films of a thickness <1μm [5]. However, this method of surface preparation was not attempted.

A more common method to achieve SERS activity on 'non-active' metals was to deposit a thin layer of the 'non-active' metal over an active substrate. In this way, the SERS activity was 'donated' to the non-active metal surface. The chosen SERS active metal in this study was gold and two methods to activate it were attempted. The first involved electrochemical oxidation-reduction cycles (ORC) to roughen a gold surface and the second involved chemical reduction of a gold solution to form colloidal nanoparticles. Platinum or palladium was subsequently deposited on the roughened gold surface or nanoparticle.

3.3.1 Electrochemical Treatment

The electrochemical waveform used to roughen the surface was devised by Weaver *et al* [6] and is shown in Figure 3.6. In essence, the working electrode was stepped to a high positive potential in a halide electrolyte to oxidise/dissolve the gold and was held at this potential for a short length of time, then scanned at a slow rate to a negative potential and held for a sufficient length of time such that the gold was reduced back to its' zero (metallic) oxidation state. This was followed by a scan at a fast rate back to the positive potential. The cycle was repeated 20-30 times, depending on the desired roughness factor.

Once the SERS active surface was attained, the next step was to plate the surface with platinum or palladium. This could be crudely achieved by adding a few drops of hexachloroplatinic acid solution to 0.1M sulphuric acid (~10^{-3} M pale yellow solution) followed by potential cycling of the gold working electrode in and out of the platinum H UPD potential region. As the platinum was reduced onto the surface, the "{110}" and "{100}" step peaks increased gradually in intensity. One monolayer was achieved when the peaks had stopped growing. Another method of metal deposition was to use a galvanostat (Princeton Applied Research model 273) to pass a current through the working electrode in a 4×10^{-3} M solution of H_2PtCl_6 in 0.7 M Na_2HPO_4 for a specific time, which could give a reproducible coverage in terms of surface area [7]. A CV was then required to check that there were no pinholes in the platinum surface that could allow contributions from the underlying Au surface.

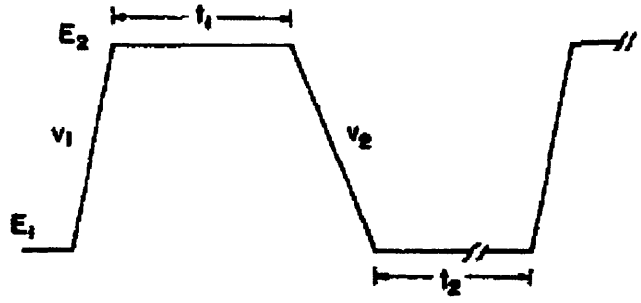

Figure 3.6 The Weaver waveform used to generate a SERS active gold electrode surface [6]. E_1: -300 mV, E_2: 1200 mV, t_1: 1.3 s, t_2: 30 s, v_1: 1000 mVs^{-1}, v_2: 500 mVs^{-1} (SCE).

A successfully roughened surface would give consistently high activity uniformly across the surface with few areas of abnormally high activity known as "hot-spots". In order to achieve this, the gold electrode must first be polished to a flat mirror with no exposed defects and the solutions and cell must be free of contaminants. The activity and stability could be severely retarded by either of these factors being influential prior to roughening.

3.3.2 Core-shell Nanoparticles

The preparation and rigorous cleaning procedures for the electrochemical treatment outlined in the previous section were time consuming and resulted in one SERS active substrate (if carried out correctly). In order to overcome these problems, a new approach was introduced to develop clean and reproducible SERS active electrodes. This method involved preparing colloidal gold nanoparticles coated with platinum or palladium. The Au@Pt or Au@Pd core-shell nanoparticles (CS-NP) were then allowed to 'settle' on a generic working electrode as described by the Zhang method [8] (Figure 3.7). This method could produce multiple SERS active substrates for an extended period of time.

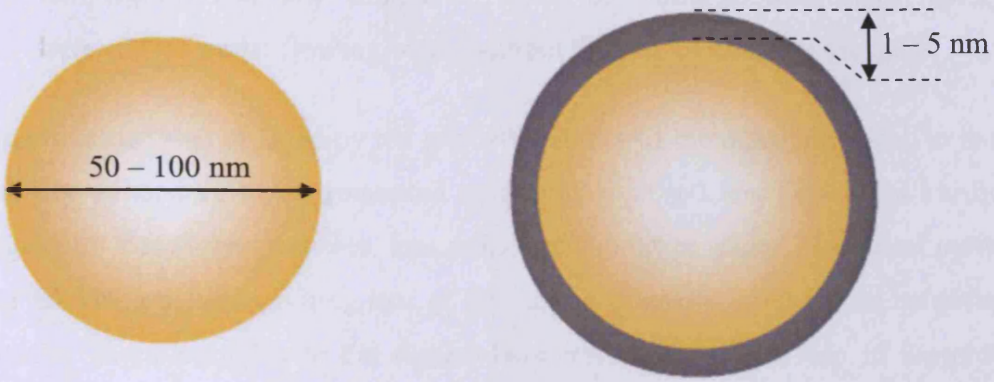

Figure 3.7 Schematic diagram of the gold seed (left) and a metal coated CS-NP (right) used to produce highly SERS active electrodes.

Before any preparation, all glass vessels to be used were cleaned by immersion in *aqua regia* (3 parts 40% hydrochloric acid to 1 part 70% nitric acid by volume) for 30 minutes and rinsed thoroughly with ultra-pure water. Aqua regia is a very toxic and corrosive substance and should only be handled with the appropriate personal protective equipment in a fume cupboard. All solutions were prepared with high purity chemicals and ultra-pure water.

The principle behind using nanoparticles for SERS was that instead of electrochemically roughening the substrate to create the nanostructures, the nanostructures were created in suspension and dropped onto the surface. The method for preparation was as follows:

1. 100 mL of 0.01% by mass chloroauric acid in a 250 mL round bottom flask was refluxed at 110°C until boiling. A silicone oil bath on a hot-plate/stirrer with a temperature probe feedback was used for this step.
2. 0.039 M of sodium citrate was prepared and 600 µL was pipetted directly into the chloroauric acid taking care not to touch the sides (the condenser was briefly removed for this step).
3. Refluxing was continued for 30 minutes. The solution should have changed in colour from light yellow to black and then to red during this period.
4. After 30 minutes, the hot-plate was turned off and the round bottom flask was raised out of the silicone oil bath allowing it to cool. After approximately 15 minutes, the

temperature was low enough to allow the flask to cool more rapidly to room temperature under flowing water without the risk of cracking the glass.

The particle size was dictated by the relative quantity of the reductant added to the amount of metal. The nanoparticle size generated was between 50-60 nm diameter as verified by SEM (Figure 3.8). For larger particles, less reductant should be added. The ideal particle size for SERS activity was approaching that of 100 nm in diameter, so it would be advantageous to synthesise larger particles in the future. However, each time a step in the procedure was changed, the particles needed to be re-examined by SEM and the appropriate quantities of the coating metal and reductant would need to be adjusted.

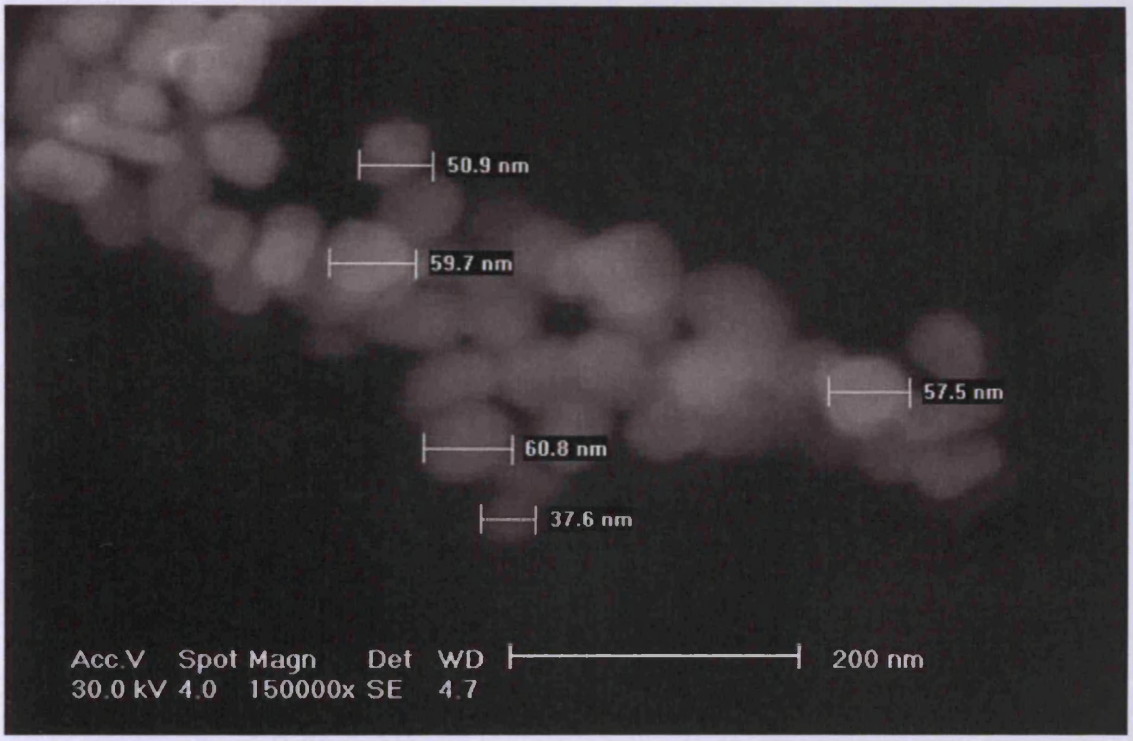

Figure 3.8 SEM image of SERS active gold nanoparticles.

Having prepared the gold seed nanoparticles, the next step was to deposit a thin shell of the desired metal on to the nanoparticles. The quantity of metal required was accurately determined for a coverage of 4-5 monolayers over the gold seed. Sodium citrate was still present in the mixture and could contribute to the reduction of the metal overlayer, so the temperature was set below 100°C in order to avoid this. The procedure continued as follows:

5. 30 mL of the gold seed solution was decanted into a 100 mL round bottom flask.
6. 0.001 M of hexachloroplatinic acid was prepared and 1.47 mL was pipetted into the flask.
7. The solution was refluxed at 80°C on a hot-plate stirrer with temperature feedback. (If a water bath was used, the level of the bath was ensured not to drop below that of the nanoparticle solution).
8. 0.005 M of ascorbic acid was prepared and 1.48 mL was added dropwise directly into the nanoparticle solution.[§]
9. Refluxing was continued for 30 minutes, then the solution was allowed to cool to room temperature.

If the reductant was added too fast, the metal salt could aggregate on the surface of the particle or form particles of its own. For a palladium shell, steps 5-9 were repeated with the following changes:

6. 1.64 mL of 0.001 M tetrachloropalladic acid,
7. At room temperature (no refluxing required),
8. 1.64 mL of 0.005 M ascorbic acid.

The CS-NP colloid was now ready to be separated from the excess solution by centrifugation and dropped onto the electrode surface using the following procedure:

10. Two aliquots (~8 mL) of the CS-NP colloid were decanted into centrifuge tubes (Fisher, 15 mL).
11. The two tubes were placed on opposite sides of the appropriate rotor (balanced) in a centrifuge (Beckman Coulter, Allegra™ 21R Centrifuge).
12. The tubes were then centrifuged at 5000 rpm for 10 minutes.
13. The aqueous layer was removed with a pipette from both tubes, leaving about 0.25 mL of the supernatant in each tube. The supernatants were combined. This would involve adding a small volume of ultra-pure water and sonicating the tubes to ensure that all nanoparticles were in solution (not adhered to the wall of the tube) and could be transferred to one tube.

[§] The peristaltic pump was set to the slowest flow rate (1.3 mL/min, measured periodically) and used to deliver the specified volume.

CARDIFF UNIVERSITY

14. The volume of both tubes was made up to ~5 mL with ultra-pure water and centrifuged again.
15. The aqueous layer was removed from the tube with the nanoparticles leaving about 0.5 mL of the supernatant.

The nanoparticles could remain concentrated up in the centrifuge tube for up to 1 week, after which they may begin to aggregate and would no longer adhere to the electrode in a uniform layer. In the suspension they could last over 2 weeks before any serious aggregation occurred (it was thought that the reductants sodium citrate and ascorbic acid still present in the colloid suspension would stick to the surface of the nanoparticles and act as stabilisers). The nanoparticles were now ready to be dropped onto the surface of the working electrode.

16. The working electrode was inserted into a PTFE collar and polished to a visibly smooth, flat finish using progressive grades of diamond spray and Kemet polishing paper down to 1 μm particle size (rinsed with ultra-pure water between grades).
17. When polished, the electrode was rinsed thoroughly with ultra-pure water, removed from the collar and flame annealed to remove contaminants.
18. The electrode was reinserted into the PTFE collar and placed (polished-end up) in a dessicator with a vacuum connection and tap.
19. Any water present was first removed by vacuum. Subsequently, a droplet of the centrifuged nanoparticles was applied to the electrode surface and the liquid suspension was also removed by vacuum.
20. This could be repeated until a complete coverage of nanoparticles (with a matt gold appearance) was achieved.

When deposited on the electrode surface, the nanoparticles could remain active for 4-5 days. The integrity of the metal overlayer could be determined by CV or by using carbon monoxide as a probe molecule for Raman (platinum group metals will give rise to two peaks around 2000 cm^{-1} illustrating the bridge and on-top adsorption sites while gold only exhibits one peak at ~2100 cm^{-1}). Electrochemical cycling in 0.1 M sulphuric acid followed by 0.1 M sodium hydroxide (see next section) was usually enough to clean the surface of the most persistent adsorbates, enabling full use of the surface when active. Cyclic voltammograms and surface spectra were used to clarify that the surface was clean before analyte

introduction. The nanoparticle preparation was the favoured method for producing SERS active surfaces because the activity was strong, uniform across the surface, reliable and one preparation could enable extended periods of collecting data without disruption. The reproducibility of the surface only necessitated a minimum of three different locations on the surface probed by SERS under specified conditions. Each time a condition was changed, spectra from at least three more spots were taken.

3.4 Cyclic Voltammetry

3.4.1 *In situ* Measurements

The spectro-electrochemical flowcell was designed to take electrochemical measurements for composition surface structure determination, but the primary functions were to clean the electrode surface *in situ* and control the surface environment. A 750 model potentiostat (CH Instruments) was used to run cyclic voltammograms (CV) with the proprietary program on an RM PC.

The cleaning procedure involved a flowing solution of Aristar grade sulphuric acid at a concentration of 0.1 M in ultra-pure water. The platinum working electrode was cycled between -0.3 – 1.1 V *vs.* Ag/AgCl at a scan rate of 0.1 V/s for 20-30 cycles or until the CV was stable (Figure 3.9).

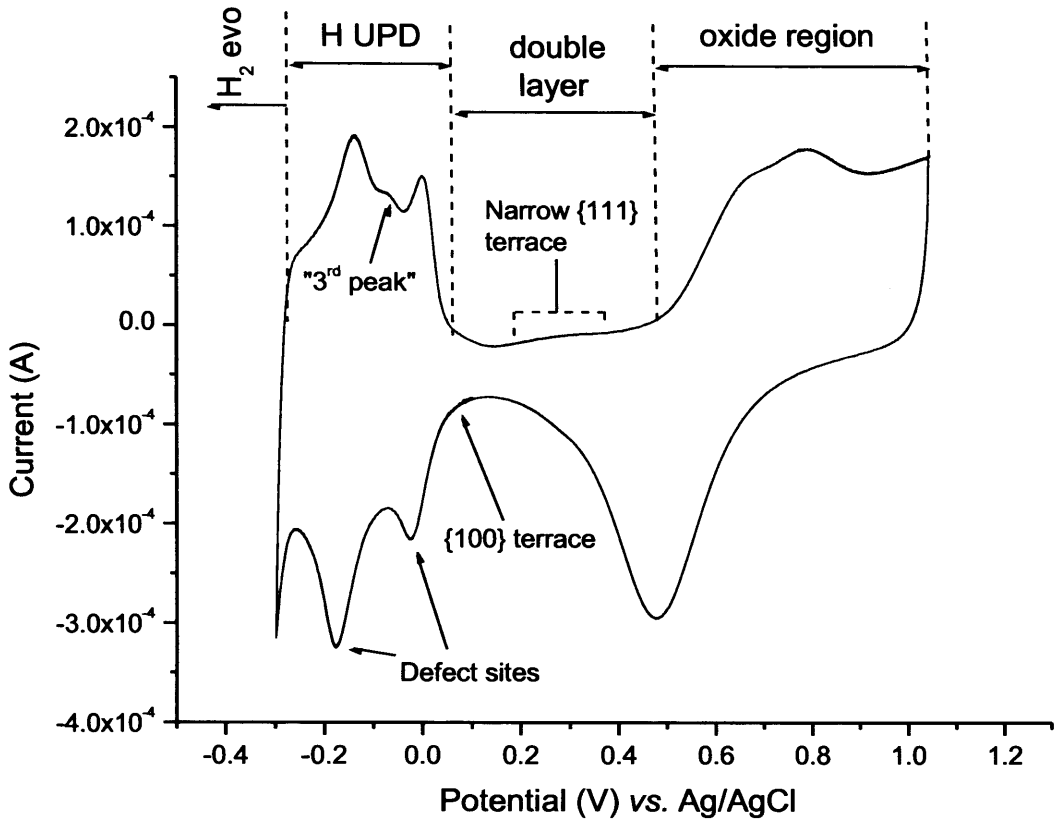

Figure 3.9 CV of Au@Pt core-shell nanoparticles on a platinum electrode in 0.1 M H_2SO_4.

This was followed by further oxidation-reduction cycles (ORCs) in flowing 0.1 M sodium hydroxide with the following parameters: potential range = -0.95 to 0.25 V at a scan rate of 0.1 V/s. The same procedure was applied to palladium producing the CV shown in Figure 3.10 followed by cycling in base solution using the following parameters: potential range = -0.7 to 0.23 V at a scan rate of 0.1 V/s.

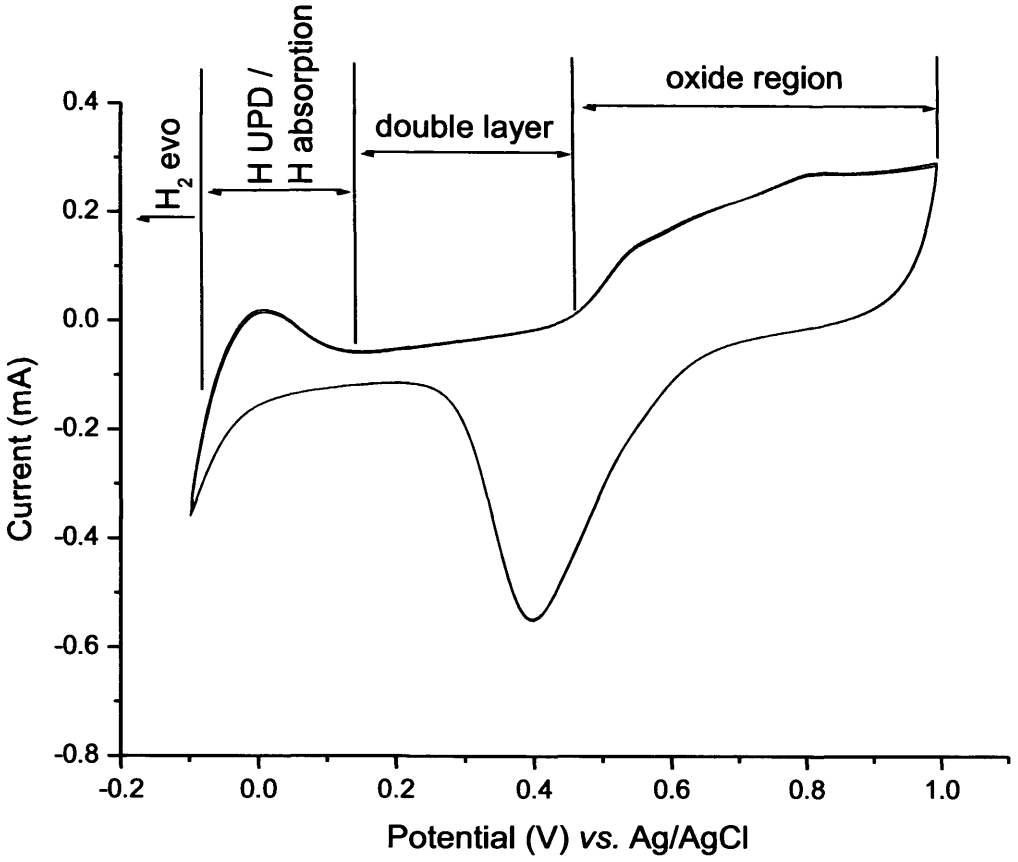

Figure 3.10 CV of palladium electrode in 0.1 M H_2SO_4, E^1: -0.1 V, E^2: 1.05 V, v: 0.1 V/s.

After the ORC cleaning procedure in acid and base solution, degassed ultra-pure water was flowed through the cell for ten minutes to remove all electrolytes. At this point the surface was clean but still in an oxidised state as could be seen by the ν Pt-O peak at 546 cm^{-1} in Figure 3.11. If this presented a problem, such as oxidation of the analyte, the ultra-pure water could be degassed with hydrogen until the surface was fully reduced then switched back to argon.

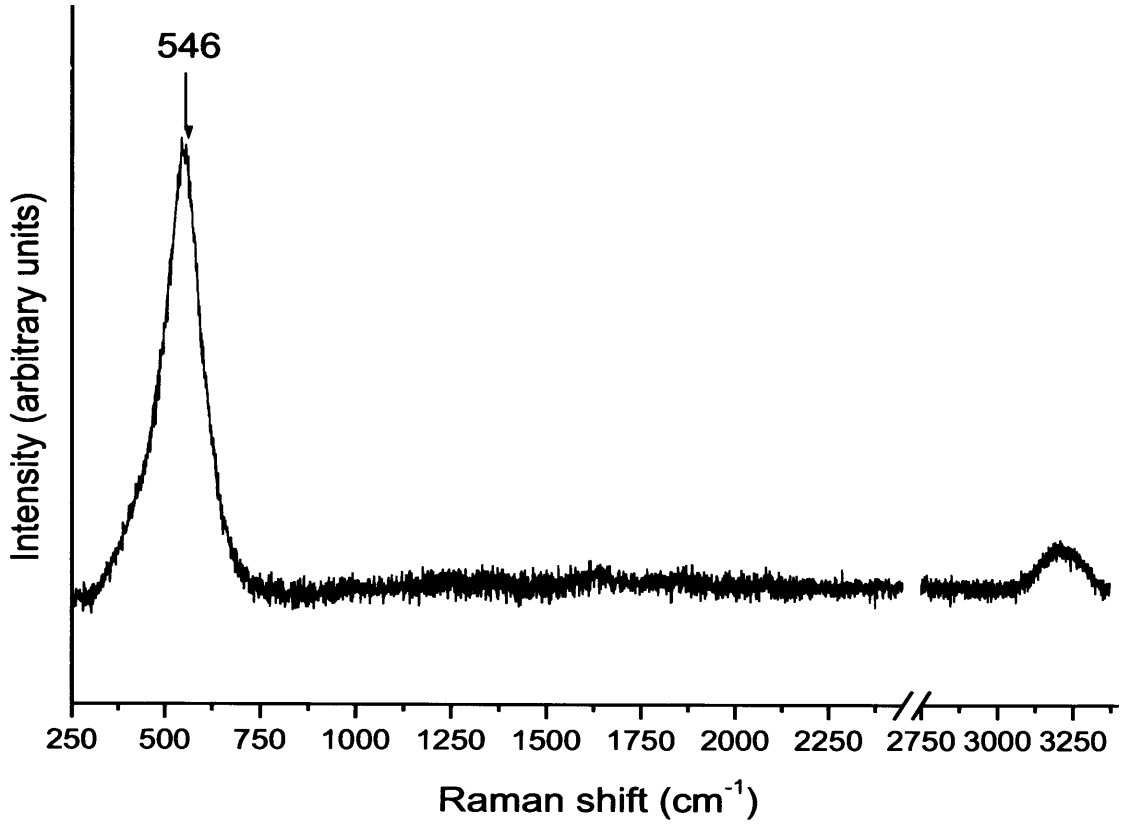

Figure 3.11 Spectrum of a clean platinum surface after rinsing with ultra-pure water.

3.4.2 Single Crystal Measurements

Electrochemical experiments on single crystal electrodes were carried out in a conventional two-compartment, three-electrode cell (Figure 3.12) with a high surface area platinum mesh counter electrode and a high surface area palladium hydride reference (Pd/H) (+60mV *vs.* RHE). A CHi800b electrochemical analyser was used for potentiostatic control.

The cell including all components and solution vessels must be kept clean and contaminant free. All glassware and Teflon® materials could be cleaned by immersion in green acid for at least one hour (often left overnight) ensuring that all internal surfaces were covered. All components were then thoroughly rinsed (20-30 times) with ultra-pure water to ensure all traces of green acid were removed. This was usually enough to clean the materials, but extra steps could be taken by steaming the glass components with ultra-pure water.

The palladium hydride reference electrode was first cleaned of contaminants by heating the palladium wire in a Bunsen flame. This was then charged by partially submerging in water in

the cell with hydrogen gas bubbling through inlet 1 for 30 minutes. By absorbing the hydrogen, the palladium entered an ideally non-polarisable state and would hold its potential for up to 10 hours (β phase of Pd/H). Dissolved oxygen could be removed from the solution by degassing the cell with argon or nitrogen gas through inlet 3 for 30 minutes after which, an overpressure of the inert gas was maintained through inlet 2.

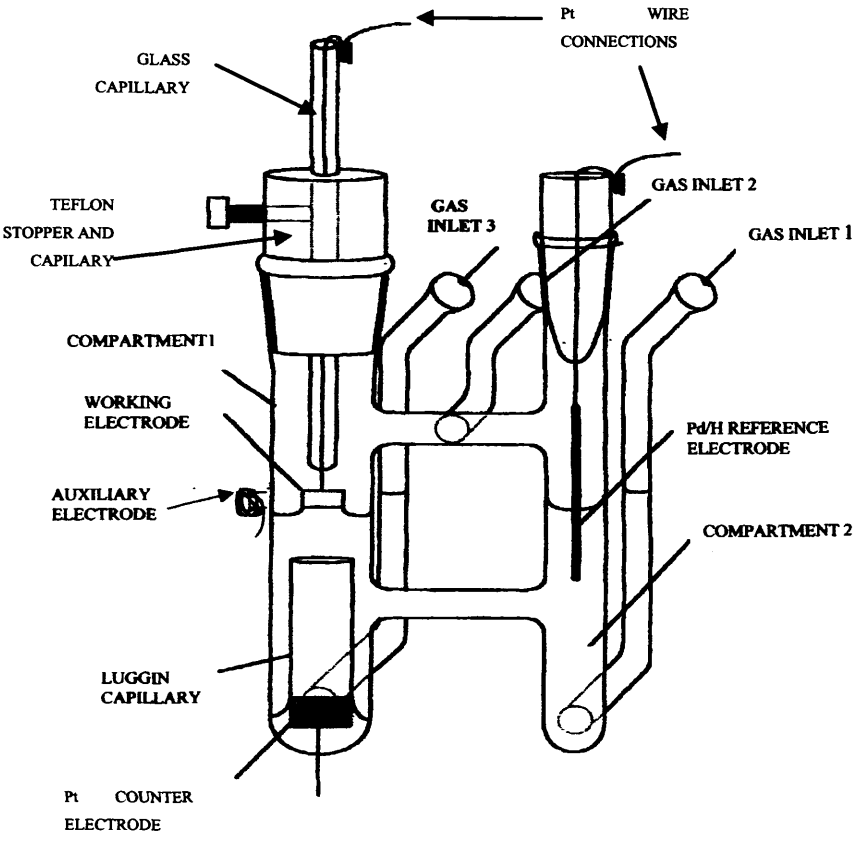

Figure 3.12 Two-compartment, three-electrode electrochemical cell.

The stem of the single crystal electrode was connected to and held on the sample holder by twisting it around an electrical conducting wire (preferably platinum, as this was unaffected by repetitive flame annealing). The connecting wire ran up a glass capillary tube and was securely wrapped around the nub at the top. The glass tube could be raised or lowered such that a meniscus contact was formed between the electrode face and the electrolyte. Without a meniscus, the solution would creep up the side of the electrode and the un-defined surface sites on the outside of the bead would become accessible to electrochemical processing. It was advisable therefore to make the connections to the potentiostat with the supplied crocodile clips before attempting the meniscus formation step as any vibration would disrupt the surface tension of the solution and the meniscus would break. At this point,

electrochemical processes could be measured. Deterioration in the CV indicated the presence of a contaminant, the source of which, needed to be located and remedied – a potentially lengthy process that could require complete overhaul of the system (cleaning followed by reassembly).

Basal plane and high Miller index platinum single crystal electrodes were oriented, cut and polished from small single crystal beads (2.5 mm diameter) as described by Clavilier's method [9]. The microfacet notation for the high Miller index planes of platinum crystals used included:

$$\{11,1,1\} = 6\{100\}\times\{111\}$$
$$\{533\} = 4\{111\}\times\{100\}$$
$$\{755\} = 6\{111\}\times\{100\}$$
$$\{976\}^{R} = 6\{111\}\times 3\{100\}\times\{110\}$$

These electrodes were flame-annealed and cooled in a hydrogen atmosphere prior to each experiment [10], which led to a well-defined surface as measured by CV [11].

Forced deposition was used to create palladium films on the low index platinum crystals [12]. The similarities in the atomic properties between platinum and palladium resulted in epitaxial growth of the palladium films and a structural copy of the underlying platinum (epitaxial pseudomorphic growth). The technique of forced deposition involved flame annealing a platinum single crystal and cooling down in a hydrogen atmosphere (a CV was usually collected at this point to check crystallinity and quality of the surface). The crystal was then rinsed with ultra-pure water and dipped briefly in a small volume of $Pd(NO_3)_2$ solution at a concentration of approximately 1×10^{-2} M and transferred to an atmosphere of high purity hydrogen for 5 seconds. The palladium ions were reduced onto the platinum surface in a uniform layer. The deposition procedure was repeated until a film of sufficient coverage was obtained (typically 10-15 dips equated to approximately 15 monolayers of palladium). After rinsing in ultra-pure water, the platinum/palladium electrode was characterised by CV and was ready for experimentation. Flame annealing the electrode would remove the palladium film and subsequent cooling in hydrogen would return the voltammetric characteristics of the platinum single crystal to those of the nominal platinum $\{hkl\}$ plane.

The purpose of the single crystal electrochemical experiments was to identify any surface structure dependencies of adsorbed ethyl pyruvate (EP). Adsorption was achieved by immersing the working electrode into a sample of distilled EP followed by a rinse in ultra-pure water to remove excess EP. The influence of the hydrogen evolution reaction on the adsorbate was also investigated by holding the working electrode at -0.1 V *vs.* Pd/H (hydrogen evolution range).

3.4.3 Platinum Catalyst Measurements

The same adsorption dependency studies were conducted on a platinum catalyst. A graphite support was used for its electrical conducting properties containing 5% platinum by weight (Johnson Matthey). The catalyst was first sintered at 700K under 5% hydrogen/argon to form well defined nanoparticles [13]. A working electrode was then formed by pressing a sample of the sintered catalyst onto a flame cleaned platinum mesh.

3.5 Running a SERS Experiment

Whether using gas or liquid phase, the system was cleaned and prepared in the same way. When using gas phase dosing, a typical experiment would be run as follows:

1. Argon gas was allowed to flow at 100 mL/min to remove the ultra-pure water left in the cell after the cleaning process and until the system was dry.
2. SER spectra were then recorded to check the cleanliness of the system and establish a baseline.
3. The argon flow was directed through the analyte bubbler and SER spectra were recorded.
4. Hydrogen gas was allowed to flow at 100 mL/min and the argon supply was turned off. The gases could also be mixed to reduce the partial pressure of hydrogen. SER spectra were recorded.

Adsorbates under the gas phase configuration of dosing were susceptible to heat decomposition from the power of the spectrometer laser. Under liquid phase conditions, the dense medium of the solution could absorb some of the power. So for gas phase studies, the power of the laser was reduced and shorter accumulation times were set (compared to measurements under liquid phase conditions).

For studies in aqueous liquid media, the analyte could be introduced immediately after the rinse with ultra-pure water for SERS measurements. A typical experiment involved the following procedure:

1. Sulphuric acid was re-introduced and the potential of the working electrode was held in the double layer region. SER spectra were recorded.
2. The analyte was introduced and SER spectra were recorded.
3. The potential was set to the desired value and SER spectra were recorded.

Typically, the potential was held in either the oxide region or H UPD region to investigate the effect of co-adsorbed oxygen or hydrogen respectively. The potential at which the hydrogen evolution reaction (HER) occurred (-0.33 V *vs.* Ag/AgCl) could also be set to simulate conditions at high hydrogen gas pressure. At potentials more negative than -0.35 V, the volume of hydrogen gas evolved at the surface began to affect the focus of the laser spot on the electrode surface leading to loss of SERS sensitivity. To minimise this interference, the cell could be mounted vertically in an aluminium bracket fixed to the stage, (designed and manufactured in-house). A 90° angle-piece was then used to mount the objective lens 90° from the z-axis. The vertical arrangement of the cell and the ascending flow of the electrolyte facilitated the removal of gas bubbles generated at the electrode surface. Focussing was then controlled by movement along the x-axis.

If organic solvents with low water solubility were to be used, then an aqueous layer on the electrode often leaves the surface hydrophilic in nature preventing access by the organic solvent. Continuing to flow the organic solvent would eventually remove the hydrophilic layer. An intermediary solvent such as ethanol could also be used for this purpose.

3.6 Density Functional Theory

Density functional theory (DFT) was used in reference to the adsorption geometry and vibrational modes of methyl pyruvate (MP) and EP on a platinum{100} surface in Chapter 4.

The calculations presented in Chapter 4 utilised DFT as implemented in the code VASP (Vienna Ab-initio Simulation Package) [14,15]. The exchange and correlation energies are described by the generalised gradient approximation with the revision of the PBE functional [16] due to Hammer *et al* [17]. Projector augmented-wave (PAW) pseudopotentials [18,19]

were used to represent the core states of the atoms. Three-dimensional periodic boundary conditions were applied to the simulation, allowing the use of a plane wave basis set. A relatively high plane wave cut-off energy of 400eV was found to be necessary to ensure accuracy, resulting from the inclusion of carbon and oxygen atoms in the simulation.

A sampling grid of 5 × 5 × 5 *k*-points in reciprocal space was necessary to converge the energy of the fcc bulk metal unit cell. The *k*-points were obtained using the Monkhorst-Pack scheme [20] with convergence of the total energy with respect to *k*-point sampling accelerated using second-order Methfessel-Paxton smearing [21] with a width of 0.1 eV. A bulk calculated equilibrium lattice constant of 3.986 Å was obtained, in good agreement with the experimental value of 3.924Å.

For the simulation of surfaces, a vacuum gap of 10 Å perpendicular to the surface plane was introduced to ensure that interactions between vertically adjacent periodic images are negligible. In order to minimise lateral interactions between periodic images, a $p(4 \times 4)$ slab was necessary due to the relatively large size of the adsorbate used in these calculations. In all surface calculations presented here, cell vectors were kept fixed to preserve the periodicity of the bulk termination. In calculating the optimized surface structures, a five-layer slab of metal atoms, with the lower two layers frozen at the bulk positions, was sufficient to obtain accurate results. The metal slab super-cell is square with dimensions $a = b = 11.9589$ Å, $c = 17.9726$ Å (including vacuum gap) containing 90 Pt atoms. A 3-layer slab was utilized for calculating the vibrational modes with the same dimensions in vectors *a*, *b* and c containing 54 Pt atoms. The surface calculations use a 3×3×1 *k*-point scheme since the *a* and *b* dimensions are greater than the bulk and only 1 *k*-point is required perpendicular to the slab surface.

To obtain the structure of adsorbed molecules, all metal atoms not previously described as frozen, and all adsorbate atoms, were allowed to fully relax and freedom to move. A relaxation of the clean surface was found to result in a reduction of the inter-layer spacing to 1.943 Å, a decrease of -15.6%; this was consistent with the close-packed nature of the platinum{100} surface. This relaxed clean surface was used as the reference for calculations of adsorption energies.

A numerical three-point approach with atomic displacements of 0.04 Å was used to calculate the vibrational modes of the adsorbate molecule which were animated using the Materials Studio® program.

3.7 Water Purification System

The Millipore Milli-Q Plus water system (Millipore, Watford, Hertfordshire) supplied research grade ultra-pure water at a rate of 1.5 litres per minute [22]. Laboratory mains water was initially passed through 5 μm filter (Water Filtration Ltd., Cardiff) before flowing into the Milli-RO 10 Plus purification system. This contained an activated charcoal pre-filtration unit to remove chloride and organic compounds. The water then passed through a semi-permeable reverse osmosis membrane before being stored in a sixty litre reservoir (kept in dark conditions to prevent growth of photosynthetic bacteria). This was an automated process that ran when the volume in the reservoir dropped below a certain level. At the request for ultra-pure water, the Milli-Q system was set to 'cycle' and switched on. Water from the reservoir was pumped into the Milli-Q system where it passed through a mixed bed of purification media and achieved a resistivity of 18.2 MΩ·cm. The Milli-Q system could then be switched to 'production' where the water passed through a 0.22 μm final filter and out of the delivery nozzle.

3.8 Chemical Reagents

Chemical	Formula	Grade	Supplier
Sulphuric acid	H_2SO_4	Aristar	BDH, Poole
Sulphuric acid	H_2SO_4	GPR	Fisons
Argon	Ar	Pureshield	BOC
Hydrogen	H_2	High Purity 99.995%	BOC
Potassium permanganate	$KMnO_4$	GPR	BDH, Poole
Platinum wire, 2 mm diameter	Pt	99.95%	Advent Research Materials Ltd, Eynsham, Oxon. UK
Platinum wire (for single crystal manufacture)	Pt	99.999%	Goodfellows
Platinum/graphite catalyst	Pt/G	5%	Johnson Matthey
Palladium wire, 2 mm diameter	Pd	99.9%	Advent Research Materials Ltd, Eynsham, Oxon.UK
Gold wire, 3 mm	Au	99.95%	Advent Research

diameter.			Materials Ltd, Eynsham, Oxon. UK
Perchloric acid	$HClO_4$	Aristar	BDH, Poole
D-Perchloric acid	$DClO_4$	68 wt. % in D_2O, 99 atom % D	Aldrich
Sodium hydroxide	NaOH	>97%	Fisher Scientific
Chloroauric acid	$HAuCl_4$	41.29%	Johnson Matthey
Hexachloroplatinic acid	H_2PtCl_6	24.95% assay	Johnson Matthey
Tetrachloropalladic acid	H_2PdCl_4	32.19%	Johnson Matthey
Palladium nitrate	$Pd(NO_3)_2 \times H_2O$	41.54%	Johnson Matthey
Sodium citrate	$Na_3C_6H_5O_7$	99+%	Aldrich
Ascorbic acid	$C_6H_8O_6$	99+%	Aldrich
Ethyl Pyruvate	$C_5H_8O_3$	>97%	Fluka
Methyl pyruvate	$C_4H_6O_3$	90%	Aldrich
Keto pantolactone	$C_8H_8O_3$	97%	Aldrich
Ethyl Benzoylformate	$C_{10}H_{10}O_3$	95%	Aldrich
Ethyl Trifluoropyruvate	$C_5H_5Cl_3O_3$	97%	Aldrich
Pyruvaldehyde dimethyl acetal	$C_5H_{10}O_3$	>97%	Aldrich
Hydroquinine 4-chlorobenzoate	$C_{27}H_{29}ClN_2O_3$	98%	Aldrich
Cinchonidine	$C_{19}H_{22}N_2O$	>98%	Fluka
Cinchonine	$C_{19}H_{22}N_2O$	>98%	Fluka
Quinine	$C_{20}H_{24}N_2O$	>98%	Fluka

3.9 References

[1] P. Etchegoin, H. Liem, R.C. Maher, L.F. Cohen, R.J.C. Brown, H. Hartigan, M.J.T. Milton, J.C. Gallop, *Chem. Phys. Lett.* 366 (**2002**) 115.

[2] P. Etchegoin, H. Liem, R.C. Maher, L.F. Cohen, R.J.C. Brown, M.J.T. Milton, J.C. Gallop, *Chem. Phys. Lett.* 367 (**2003**) 223.

[3] E. Smith, G. Dent, *Modern Raman Spectroscopy*, 116-120 **2005**.

[4] Zhong-Qun Tian, Bin Ren, De-Yin Wu, *J. Phys Chem B*, vol 106, no. 37 (**2002**).

[5] E. Mamdouh, Abdelsalam, Sumeet Mahajan, P.N. Bartlett, J.J. Baumberg, A.E. Russell, *J. Am. Chem. Soc.*, **2007**, 129 (23), pp 7399–7406.

[6] P. Gao, D. Gosztola, L.H. Leung, M.J. Weaver, *J. Electroanal. Chem.* **1987**, 233, 211.

[7] S. Zou, M.J. Weaver, *Anal. Chem.* **1998**, 70, 2387-2395.

[8] L.H. Lu, H.S. Wang, S.Q. Xi, H.J. Zhang, *J. Mater. Chem.* **2002**, 12, 156.

[9] J. Clavilier, *J. Electroanal. Chem.* **1980**, 107, 211.

[10] A. Rodes, M.A. Zamakhchari, K.El Achi, J. Clavilier, *J. Electroanal. Chem.* 305 (**1991**) 115.

[11] A. Al-Akl, G.A. Attard, R. Price, B. Timothy, *Phys. Chem. Chem. Phys.* 3 (**2001**) 3261.

[12] F.J. Vidal-Iglesias, A. Al-Akl, D.J. Watson, G.A. Attard, *Electrochem. Commun.* 8 (**2006**) 1147–1150.

[13] G.A. Attard, K.G. Griffin, D.J. Jenkins, P. Johnston, P.B. Wells, *Catal. Today*, 114 (**2006**) 346.

[14] G. Kresse, J. Furthmüller, *J. Phys. Rev. B*, **1996**, 54, 11169-11185.

[15] G. Kresse, J. Furthmüller, *J. Comput. Mater. Sci.*, **1996**, 6, 15-50.

[16] J.P. Perdew, K. Burke, and M. Ernzerhof, *Phys. Rev. Lett.*, **1996**, 77, 3865-3868.

[17] B. Hammer, L. B. Hansen, J. K. Nørskov, *Phys. Rev. B*, 59, 7413 (**1999**).

[18] P.E. Blöchl, *Phys. Rev. B* **1994**, 50, 17953-17959.

[19] G. Kresse, D. Joubert, *Phys. Rev. B* **1999**, 59, 1758-1775.

[20] H.J. Monkhorst, J.D. Pack, *Phys. Rev. B*, **1976**, 13, 5188-5192.

[21] M. Methfessel, A.T. Paxton, *Phys. Rev. B*, **1989**, 40, 3616-3621.

[22] Millipore General Catalogue, Millipore U.K. Ltd., Watford, Hertfordshire.

Chapter 4
Adsorption of Methyl and Ethyl Pyruvate on Platinum and Palladium Surfaces

4.1 Introduction

In the Orito reaction, methyl pyruvate (MP) is converted to *R*-methyl lactate (*R*-ML) over a cinchonidine (CD) modified platinum catalyst in the presence of hydrogen (Figure 4.1). MP was the original choice of reactant made by Orito *et al* when this reaction was first discovered [1]. The structure of MP is very similar to that of the next member of the homologous series ethyl pyruvate (EP) and when conducted under the same conditions, the reaction performances on platinum were almost identical [2]. Hence, both molecules were considered to interact with the surface in the same way and are treated as such in this chapter.

NEXAFS [3] STM [4,5], TPR [5], XANES [6], XPS [7], RAIRS [8] and DFT [9,10] have all been used to study the adsorption behaviour of MP and EP on a platinum{111} surface. Four different adsorption modes (see Chapter 1, section 1.3.2 for adsorption geometries) have been deduced from the experimental findings including:

1) An end-on configuration bound via an oxygen lone pair from the ketone, known as η^1 [9].

2) A Pt-O and Pt-C σ-bonded entity with the C-O bond held horizontal to the surface, known as η^2 [9].

3) A flat orientation with the molecular plane parallel to the surface plane involving π-bound states of one or both carbonyls [7].

4) A Pt-O bond from both carbonyls with a delocalized π-orbital between them known as an enediolate [8].

The general consensus to date being that multiple adsorption modes of the reactant molecule may exist at any one time, but the η^1 mode was thought to dominate and may also be tilted with respect to the surface.

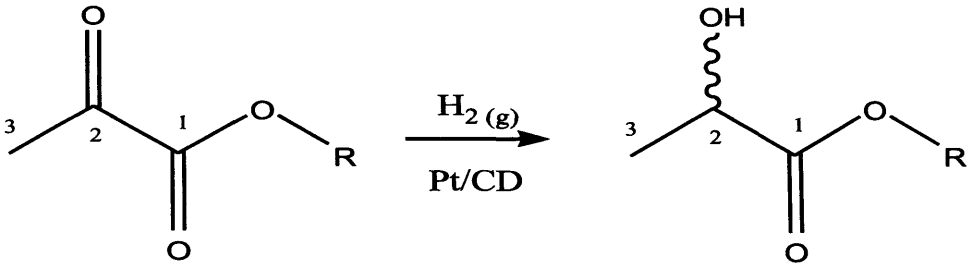

Figure 4.1 Structures of alkyl pyruvate reactants (MP: R = CH_3, EP: R = CH_2CH_3) and the alkyl lactate products (ML and ethyl lactate (EL)).

In this chapter, Surface-Enhanced Raman Scattering (SERS), Density Functional Theory (DFT) and Cyclic Voltammetry (CV) have been used to extract information concerning the adsorption behaviour of MP and EP on polycrystalline and single crystalline platinum and palladium surfaces. Using these techniques it was possible to identify:

1) An adsorption geometry of MP and EP on SERS active polycrystalline platinum and palladium surfaces in the presence of hydrogen.

2) The product of hydrogenation.

3) Products of side reactions derived from dissociative adsorption of the reactant molecule.

4) A preference for selective adsorption at certain single crystal sites.

With regard to the SERS studies, the dosing of the analyte was conducted via both the gas phase and aqueous liquid phases.

4.2 Results

4.2.1 Raman Spectra of the Reactants and Products

Raman spectra of neat liquid MP and EP and the products ML and ethyl lactate (EL) were taken and the peaks were assigned using standard references [11,12] and other reported assignments from related species including EP [13], MP and butadiene [14], ethyl acetate [15], acetylacetone [16], ethyl formate [17], pyruvic acid and propionic acid [18,19].

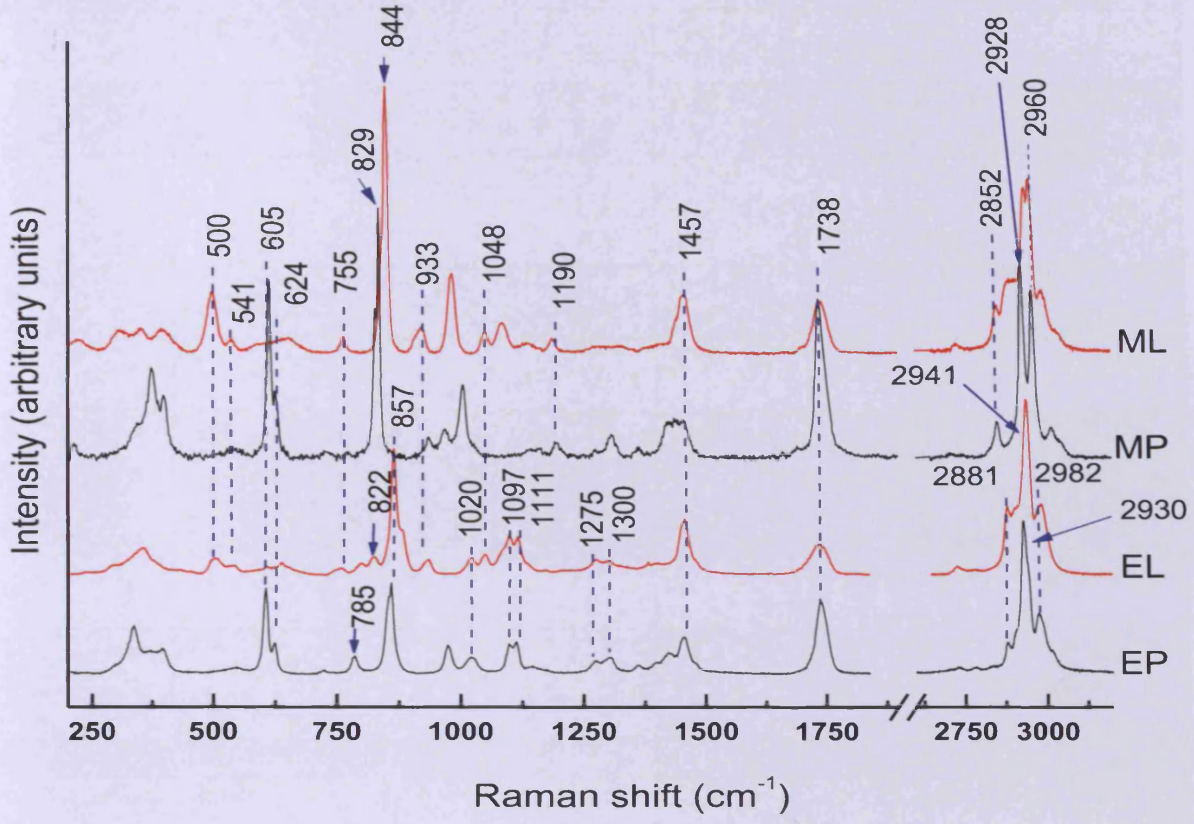

Figure 4.2 Raman spectra of bulk MP, ML, EP and EL.

Table 4.2 Band assignments for bulk Raman spectra of MP and ML (grey) and EP and EL (black).

Band Position (cm^{-1})				Assignment
MP	**ML**	**EP**	**EL**	
3018	2992	3017	2982	va(C^3-H_3) (C^3-H_3)
2961	2958	2977	2977	va(C^5-H_3) (C^4-H_3)
-	-	2944	2941	va(C^4-H_2)
2928	2944	2930	2940	vs(C^3-H_3) (C^3-H_3)
2852	2852	2904	2903	vs(C^5-H_3) (C^4-H_3)
-	-	2881	2881	vs(C^4-H_2)
1738	1738	1738	1738	ν(C=O)
-	-	1470	1470	δ(C^4-H_2)
1457	1457	1457	1455	δd(C^5-H_3)
1423	-	1423	-	δd(C^3-H_3)
-	-	1399	1382	δw(C^4-H_2)
1361	-	1362	-	δs(C^5-H_3)
1306	1306	1304	1300	ν(O-$C^4H_2CH_3$) *anti* ν(O-C^4H_3)
1272	1272	1273	1275	ν(O-$C^4H_2CH_3$) *gauche* ν(O-C^4H_3)
-	-	1111	1114	δr(C^4-C^5H_3) *anti*

-	-	1097	1096	$\delta r(C^4\text{-}C^5H_3)$ *gauche*
-	1083	-	1082	$va(C^1\text{-}C^2\text{-}C^3)$ / δr(O-H)
-	1048	-	1048	$\nu(C^2\text{-}C^3)$ / $\delta r(H_3C^3\text{-}C^2)$ / $\delta r(C^2\text{-}OH)$
1002	979	1020	1019	$\nu(O\text{-}C^4)$ / $\delta r(C^5\text{-}H_3)$ / $\nu(C^1\text{-}C^2)$ / $\nu(C^4\text{-}C^5H_3)$
963		972	-	$va(O\text{-}C^4H_2\text{-}C^5H_3)$ / $\nu(O\text{-}C^4H_3)$ / skeletal
932	917	-	933	ν(C-OH) / $\delta r(C^3\text{-}H_3)$
-	845	-	861	$\nu(O\text{-}C^4)$ / $\delta r(C^5\text{-}H_3)$ / $\delta(C^2\text{-}C^1\text{-}O)$ / $\delta s(C^4\text{-}O\text{-}C^1)$ / $\delta r(C^3\text{-}H_3)$ / skeletal
831	-	857	-	$\nu(O\text{-}C^4)$ / $\delta r(C^5\text{-}H_3)$ / $\delta(C^2\text{-}C^1\text{-}O)$
-	-	-	822	$\nu(C^2\text{-}OH)$ / $\delta r(C^3\text{-}H_3)$ / skeletal
-	-	-	798	$\delta s(C^4\text{-}H_2)$
-	-	785	-	$\delta r(C^4\text{-}H_2)$
-	756	-	755	$\delta s(O\text{-}C^1\text{-}O)$ / $\delta r(C^3\text{-}H_3)$ / skeletal umbrella about C^1
622	649	624	635	δr(C=O)
609	585	605	605	skeletal $(O\text{-}C^1\text{-}C^2)$
	532	-	541	δr(C-O)
	494	-	500	$\delta r(C^2\text{-}C^3)$ / skeletal $(O\text{-}C^1\text{-}C^2)$

4.2.2 Ethyl Pyruvate Dissolved in Dichloromethane

The Orito reaction was originally performed in organic solvents [32] and these still remain the best media to generate optimum performance. Acetic acid and toluene were two such solvents that were most often employed for high reaction performance. Spectroscopically, these were not ideal solvents to use as the peaks resolved from the bulk liquid can interfere with surface peaks from the target molecule. Dichloromethane (DCM) was selected for the solvent as it was a relatively simple molecule and gave rise to fewer Raman peaks, but was also capable of reasonable reaction performance with carbon supported platinum (41% e.e., 850 mmol h^{-1} g^{-1}_{cat} maximum rate) [20].

Attempts to resolve a surface adsorbate from the introduction of EP dissolved in DCM using this system on core-shell nanoparticles (CS-NP) resulted in very low quality spectra. In fact,

the only notable feature to resolve was a broad peak at 1600 cm^{-1} on platinum and 1570 cm^{-1} on palladium. The lack of any other features in the spectra made any interpretation of the peaks difficult. These results were subsequently omitted. However, it was thought that the reason for the poor quality spectra was due to an insufficient quantity of hydrogen on the surface, which in the following sections was shown to be required to observe the reactant intermediates on the surface.

4.2.3 Gas Phase Dosing of Methyl Pyruvate and Ethyl Pyruvate

It has been shown in an article by Hutchings *et al* that the solvent was not integral to the propagation of the reaction and that the Orito reaction could be performed in the gas phase [21]. By introducing the reactant under a high partial pressure of hydrogen, the solvent and related effects could be excluded altogether including the inaccessibility of hydrogen to the surface.

4.2.3.1 Methyl Pyruvate and Ethyl Pyruvate on Au@Pt Core-shell Nanoparticles

It has been proposed that water (present in the electrolyte used for the electrode cleaning procedure (Chapter 3, section 3.4.)) will hydrolyse alkyl pyruvates to form pyruvic acid (PA) and an alcohol [22]. To address this problem, the spectro-electrochemical flowcell was allowed to dry in the gas flow before being opened to the reactant. When the cell was dry, the reactant was first introduced under an atmosphere of the inert gas argon at a flow rate of 200 mL min^{-1} (Figure 4.3, black spectrum) followed by a gas mixture of hydrogen and argon (Figure 4.3, red spectrum).

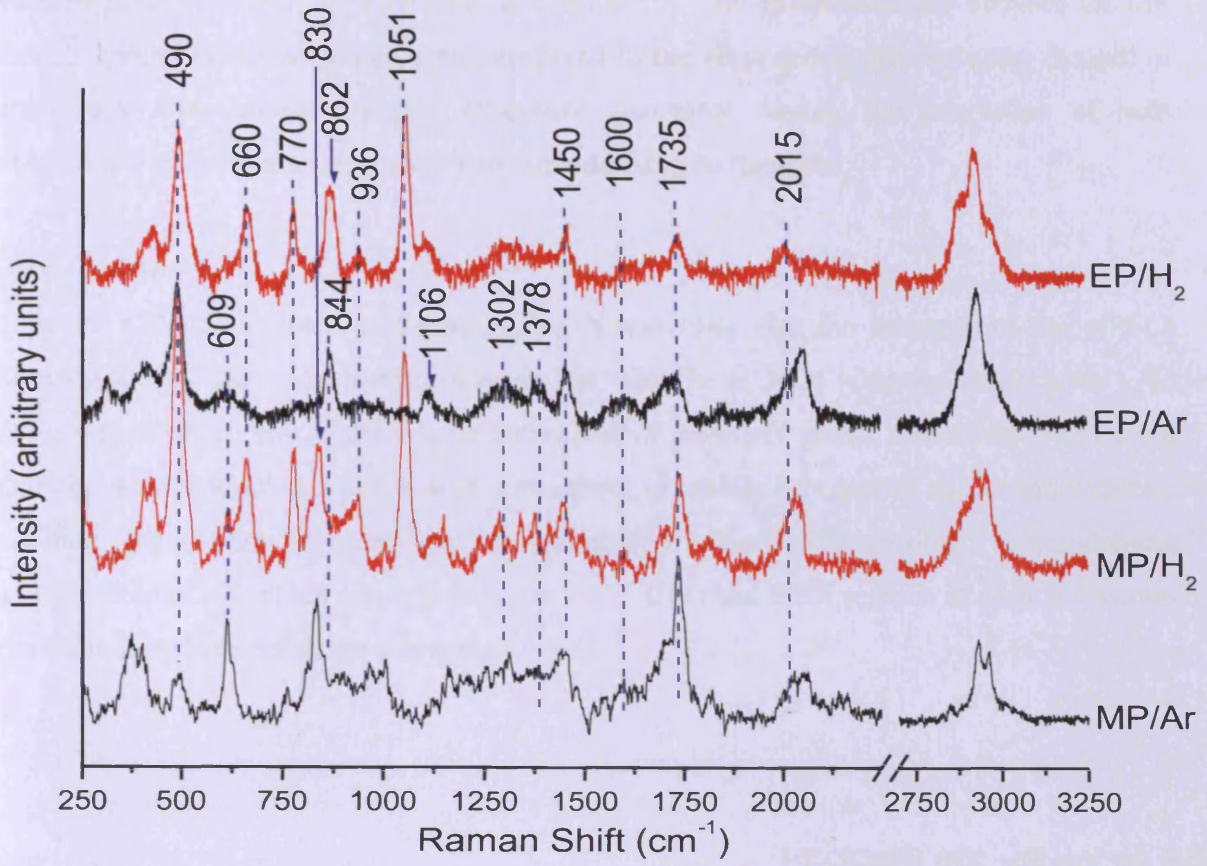

Figure 4.3 SER spectra of gas phase MP and EP on Au@Pt CS-NP under argon and hydrogen atmospheres.

Under argon, there was much more detail to the spectrum than previously seen in DCM including the peaks at 1735, 1450, 1302, 1106 and 609 cm^{-1}, and these could all be assigned to peaks from the bulk Raman spectrum of MP and EP obtained from a condensed layer of the reactant on the platinum surface. Surface enhanced peaks included a peak at 1600 cm^{-1} similar to that seen in DCM, two peaks at ~2015 and 490 cm^{-1}, which were assigned to adsorbed carbon monoxide (CO) (a known product of pyruvate decomposition on platinum [23]) and two peaks resolved at 1378 and 844 cm^{-1}, which will be commented on in sections 4.2.3.3 and 4.2.4.1.

Significant changes were seen when hydrogen was admitted into the cell. The peaks at 1378 and 844cm^{-1} were removed, the peak at 1600 cm^{-1} narrowed and decreased in intensity. The contribution from the condensed layer was reduced as signified by the loss in intensity of the liquid Raman peaks at 1735 and 609 cm^{-1}. The peak at 2015 cm^{-1} from $\nu(C{\equiv}O)$ had also decreased in intensity for EP and six new peaks at lower frequencies emerged from both MP

and EP (1051, 936, 862, 830, 770, 660 and 640 cm^{-1}). The differences seen between the MP and EP spectra under hydrogen were attributed to the alkyl group, but were not thought to result in a significantly different adsorption geometry. Hence, the interaction of both molecules with the platinum surface was considered to be the same.

Carbon Monoxide

Although CO was present under hydrogen, it was clear that the intensity of the ν(Pt-C) vibration at 490 cm^{-1} was significantly greater than the ν(C≡O) vibration at 2015 cm^{-1}. To obtain an understanding of the relative intensities of these two peaks, a short study of CO on platinum was conducted. Formic acid was known to readily decompose to CO and water on platinum [24] and for this purpose it was dissolved to a concentration of 0.1 M in sulphuric acid and held at potentials corresponding to the H UPD and HER regions of platinum versus a palladium hydride reference electrode.

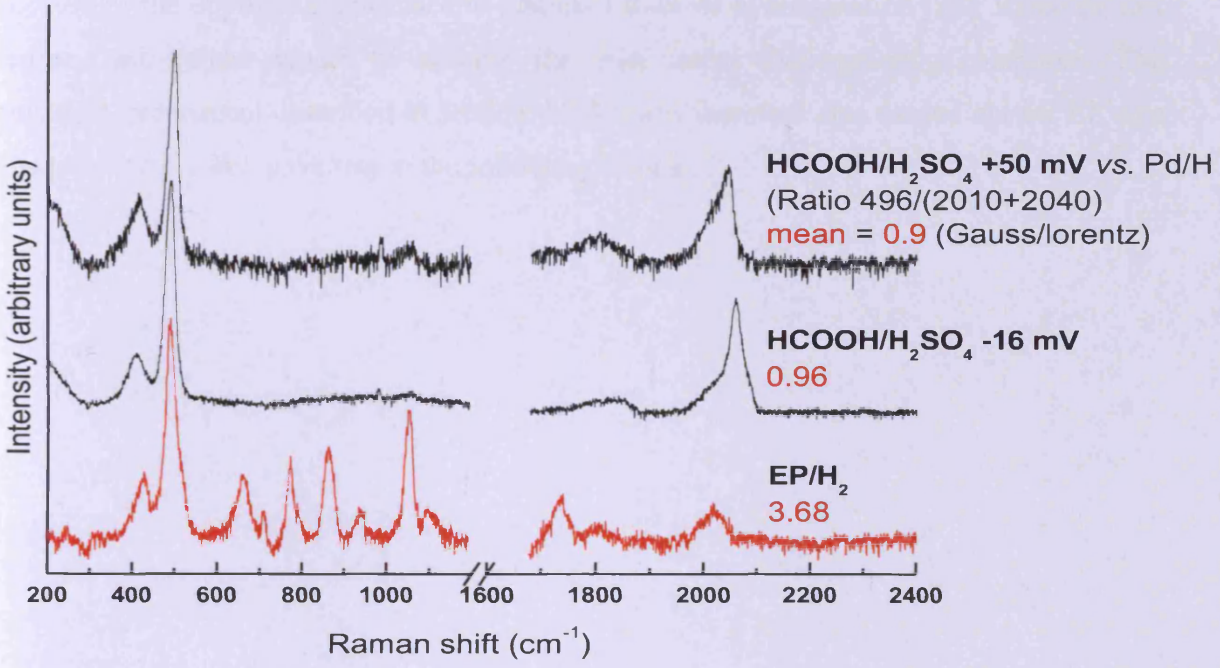

Figure 4.4 Ratio of ν(Pt-C) to ν(C≡O) on Au@Pt CS-NP at a variety of potentials *vs.* Pd/H.

From the SER spectra, two ν(C≡O) stretches were seen at ~2040 and 1995 cm^{-1} corresponding to on-top sites [25]. A bridged site ν(C≡O) was also observed at a lower frequency of ~1820 cm^{-1}. The area of the Pt-C peak was integrated using a Gaussian and Lorentzian combination peak-fitting routine in the proprietary LabSpec® program and was measured against the sum of the integrated areas of the on-top and bridge site peaks. The

values in red in Figure 4.4 were the ratios of the Pt-C area to the total area of $CO_{on\text{-}top}$ + CO_{bridge} normalised to unity. The peak area ratios with formic acid at both potentials gave an average value of 0.93:1. With EP on platinum under hydrogen the ratio was 3.68:1, meaning that more than one vibration was contributing to the peak at 490 cm^{-1}. This was a strong indication that EP was bound to the platinum surface via a Pt-C link under hydrogenating conditions.

4.2.3.2 Ethyl Pyruvate on Au@Pd Core-shell Nanoparticles

Under Orito reaction conditions and using CD as modifier, palladium was known to give rise to the *S*-enantiomer of EL rather than the *R*-enantiomer as seen with platinum upon hydrogenation of EP [26]. The accepted model accounting for this alternation in handedness was the stabilisation of the *enol* tautomer of EP on palladium leading to the hydrogenation of the enolic C=C bond on the surface rather than hydrogenation of a C=O bond and hence the exposure of the opposite enantioface to platinum towards hydrogenation [26]. Based on this premise, one might expect to observe the *enol* under hydrogenating conditions. The equivalent experiment described in section 4.2.3.1 was therefore also carried out for EP on a palladium surface and gave rise to the following results.

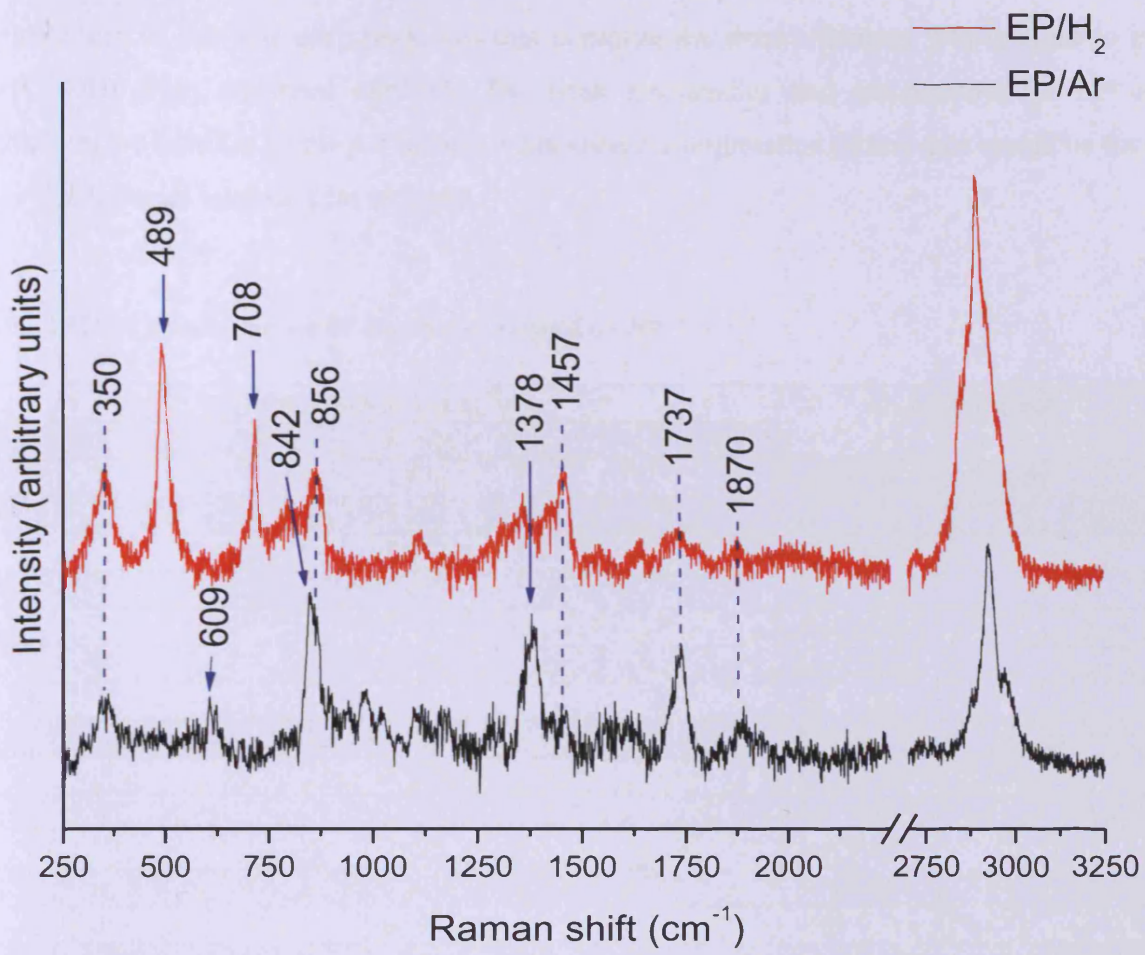

Figure 4.5 SER spectra of gas phase EP on Au@Pd CS-NP in argon and hydrogen atmospheres.

Under an argon atmosphere the two prominent peaks to appear at 1378 and 843 cm^{-1} were identical to those on platinum and therefore were assigned to a carboxylate species. There were also peaks that matched the position and relative intensities of the bulk liquid EP spectrum (1737, 1457, 1106, and 609 cm^{-1}) and were presumed to be derived from a condensed layer of EP.

Under hydrogen, again the spectrum changed dramatically; the carboxylate species was completely removed and was replaced by a species that was carbon bound as signified by the ν(Pd-C) at 489 cm^{-1}. It should be noted that no evidence for a ν(C≡O) of on-top CO could be found. Although, bridge-bonded CO could be observed at 1870 and 350 cm^{-1} [27], it is evident that the 489 cm^{-1} peak cannot be ascribed to adsorbed CO. Similar to EP on platinum, it was apparent that the ν(Pd-CO) peak at 350 cm^{-1} was significantly greater in intensity than

the corresponding ν(PdC≡O) at 1870 cm^{-1} and was again attributed to another vibration contributing to the 350 cm^{-1} peak. On this occasion the extra vibration was thought to be δw(C^2-OH) from adsorbed *enol*-EP. The peak frequencies and assignments for EP on palladium are listed in Table 4.3 below. A consistent interpretation of this data would be for a di-σ bonded *enol* intermediate to form.

Table 4.3 Band assignments for EP adsorbed on Au@Pd CS-NP.

Band Position (cm^{-1})		Assignment
EP/Ar	**EP/H_2**	
1870	1870	ν(PdC≡O) (bridged)
1737	1737	ν(C^1=O)
-	1637	ν(C^3=C^2)
1457	1457	δd(C^5-H_3)
1378	-	νs(C^2OO^-)
-	1330	δw(C^4H_2)
1178	-	ν(C^1-O)
-	1106	δr(C^4-C^5)
-	856	ν(C^4-C^5) / ν(O-C^4)
843	-	δ(C^2OO^-)
-	792	δs(C^4-H_2)
-	708	δr(C^1-O-C^4)
-	489	ν(Pt-C^3) / ν(Pt-C^2)
-	350	δw(C^2-OH) / ν(Pd-CO) (bridged)

4.2.3.3 Discussion of the Gas Phase Dosing Experiments on Core-shell Nanoparticles

On platinum

In a paper by Suh *et al*, three carboxylate species were adsorbed onto SERS active silver surfaces. These workers found that two distinct peaks resolved at 1380 and 843 cm^{-1} assigned to νs(COO^-) and δ(COO^-), respectively [28]. Therefore, the peaks resolved at 1378 and 844 cm^{-1} on an oxidised surface in the present study were also assigned to adsorbed carboxylate. Suh *et al* also suggested that the relative intensity of the νs(COO^-) to the δ(COO^-) peaks increased as the molecular plane tilts away from the surface. However, in this case it was likely that the bulk liquid Raman peak of EP at 857 cm^{-1} was contributing to the intensity rendering such an evaluation subject to error. The adsorption geometry of the carboxylate species will be discussed in section 4.2.4.1.

Under hydrogen, the spectrum changed dramatically and provided evidence of a surface reaction. It also showed that the absence of a surface intermediate using an organic solvent was most likely due to an insufficient quantity of surface hydrogen being available. Initial attempts at assigning the bands indicated that the reactant was adsorbed via an M-C bond (490 cm^{-1}) and possessed an alcohol group (ν(C-OH), 1051 cm^{-1} (also seen in bulk EL and ML)). This suggested that the reactant was converted by adsorbed hydrogen to a half-hydrogenated state (HHS) (Figure 4.16).

The resolution of the Raman peaks from the liquid state of the reactant with an argon overpressure showed that there was a condensed layer over the surface. This was a shortcoming of gas phase operations with the present experimental setup. Although hydrogen did remove some of the condensed layer, it was unclear if the layer was completely removed. In this case it was difficult to differentiate SERS from Raman peaks, such as the peak at 1735 cm^{-1}. A solvent was expected to prevent such a layer from forming.

The method for gas phase dosing of hydrogen on platinum had resulted in a reaction with adsorbed MP and EP in contrast to organic liquid phase conditions where no comparable reaction was observed. To this end, the quantity of hydrogen in contact with the surface had increased to a level where a reaction with the adsorbate was seen. However, observation of the peak for adsorbed hydrogen (ν(Pt-H), ~2085 cm^{-1}) would also be expected, but remained elusive. This could be accounted for by a combination of a saturated coverage by the HHS, site blocking by CO and a condensed layer of EP limiting the access of hydrogen to the surface. Therefore, the rate limiting step for the hydrogenation reaction in this system might be the desorption process for the HHS, CO and EP thereby allowing further hydrogen to adsorb. This could provide a possible explanation for the lower overall rates and lack of rate acceleration, alluded to by Hutchings *et al* in their article on gas phase Orito-type reactions [21].

On palladium

A σ-bound adsorption mode of EP was different to the expected result of a π-bound vinyl group of *enol*-EP based on previous deuterium studies [26]. Using Reflection Absorption Infra-Red Spectroscopy (RAIRS) and low energy electron diffraction (LEED) Tysoe *et al* were able to determine that ethylene was adsorbed in a di-σ configuration on a clean palladium{111} surface [29, 30]. The authors go on to report a π-bound state, but only in the

presence of sub-surface hydrogen. The adsorption geometry was likened to the η^2 configuration (Chapter 1, Figure 1.6 (c)), but in this case the metal-molecule bonds were through C^2 and C^3 as opposed to C^2 and the *keto* oxygen (Figure 4.6). This suggested that an *enol* tautomer of EP might be the precursor involved in the adsorption process on palladium and that the π-bond was susceptible to surface reaction under the present hydrogenation conditions.

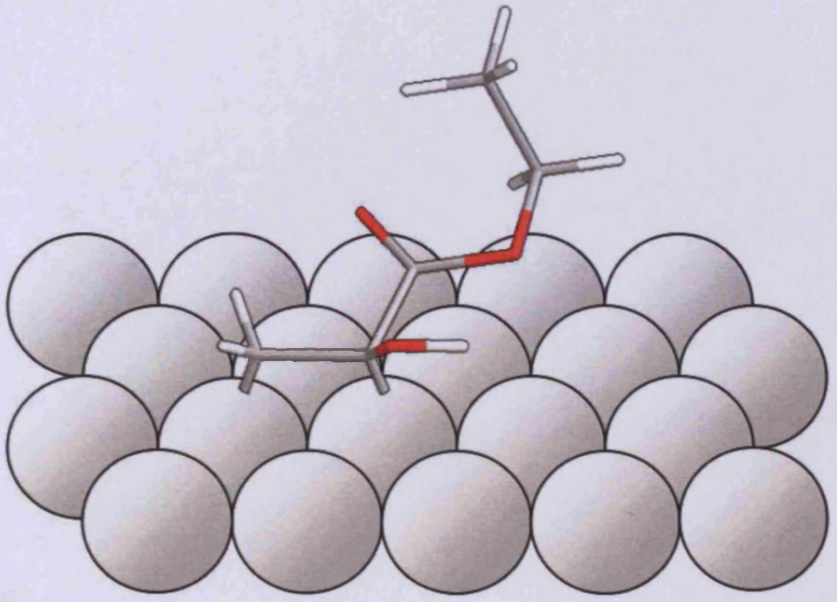

Figure 4.6 The di-σ adsorption geometry of *enol*-EP on Au@Pd CS-NP under gas phase conditions with a hydrogen atmosphere.

For a palladium catalysed hydrogenation of alkenic bonds, the mechanism is widely thought to be of a Langmuir-Hinshelwood type whereby the rate determining step is the addition of hydrogen to the carbon atoms of a π-bound molecule and that desorption is instantaneous [31]. However, similar to the platinum result, a condensed layer may inhibit both desorption of the product and direct access of hydrogen to the surface. Therefore, it is proposed that under gas phase conditions, the initial exposure to hydrogen removed the carboxylate species and reduced the metal surface allowing for EP to adsorb in the enolic state. If the coverage of hydrogen on the palladium surface was low due to a high coverage of EP (which would preferentially react with hydrogen before it could diffuse into the bulk of the metal) then the π-adsorbed state would not be observed [30]. Therefore, the coverage of hydrogen was thought to be similar to that of the "clean" surface under the dynamic conditions of the present dosing experiments, which leads to the formation of the di-σ EP adsorption mode

(Figure 4.6). At this stage, it was predicted that if a higher loading of adsorbed hydrogen could be generated, then π-bound species may become observable.

4.2.4 Liquid Phase Methyl Pyruvate and Ethyl Pyruvate in Sulphuric Acid

It has been shown that by increasing the quantity of hydrogen made available for reaction, a surface intermediate of EP under gas phase conditions was observed. By dissolving the reactant in an aqueous electrolyte, surface hydrogen can be generated by electrolysis. Hence, in order to model liquid phase hydrogenation conditions, such experiments are described in the section that follows.

4.2.4.1 Methyl Pyruvate and Ethyl Pyruvate on Au@Pt Core-shell Nanoparticles

Figure 4.7 shows a polycrystalline platinum voltammogram versus a silver/silver chloride reference electrode. The various potential regions of the voltammogram represent different surface conditions of the electrode, in which it was possible to hold the potential and study the adsorption geometry of the reactant. The main interest was in the regions of hydrogen under potential deposition (H UPD) and hydrogen evolution reaction (HER) where hydrogen was on the surface and therefore in a position to react with MP or EP. By holding the potential further negative into the HER region, the surface hydrogen coverage can be increased to simulate the high pressures used in the real Orito reaction.

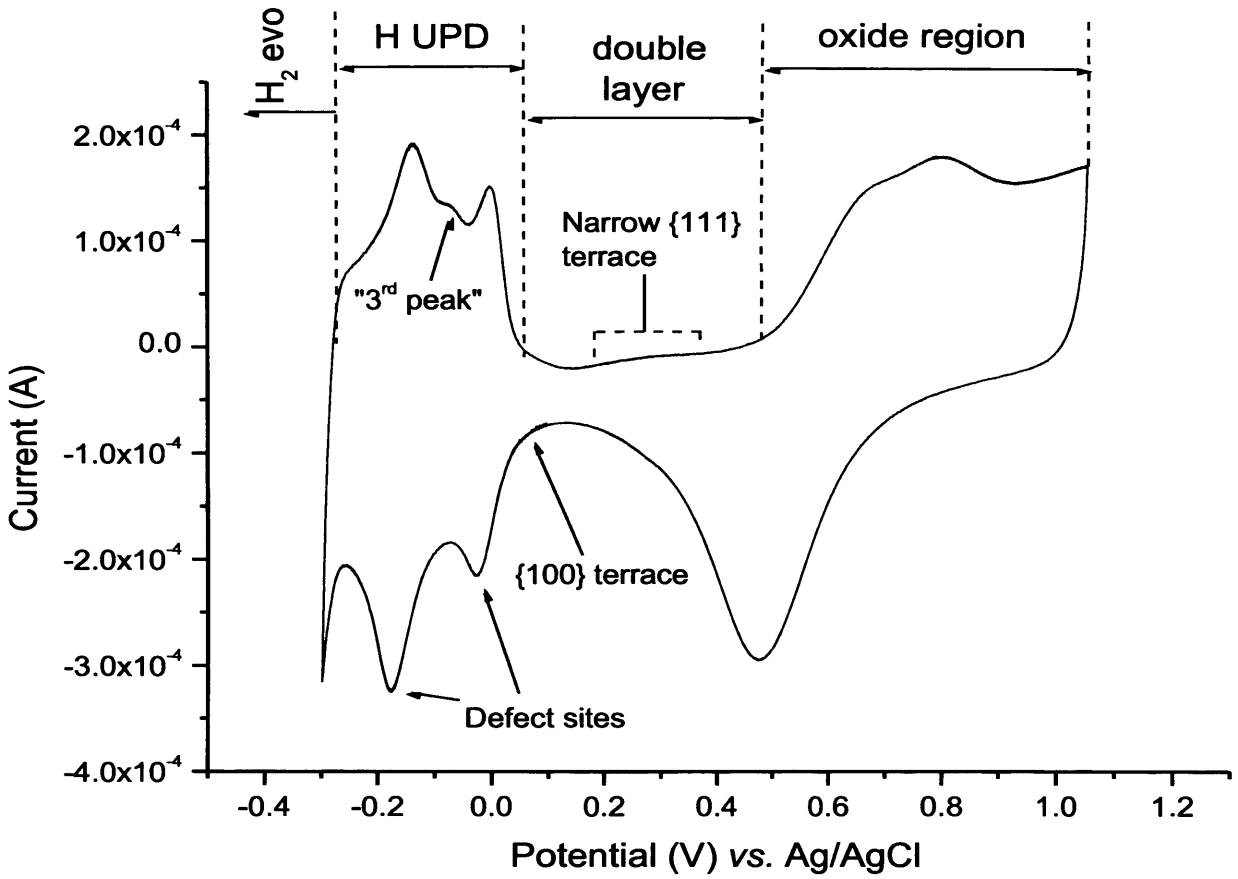

Figure 4.7 Cyclic voltammogram of polycrystalline platinum in 0.1 M H_2SO_4 versus a Ag/AgCl reference at a scan rate of 0.1 V/s.

The SERS active surface was prepared and cleaned in the usual manner as described in chapter 3 section 3.4.1. After the cell was rinsed with ultra-pure water, a solution of 0.1 M EP dissolved in 0.1 M sulphuric acid was introduced into the cell. The potential of the platinum electrode was varied within the different voltammetric regions and the surface was probed for adsorbed EP. Figure 4.8 shows a series of spectra of adsorbed EP at potentials scanning from positive to negative** starting at open circuit potential (OCP), which, after electrochemical cleaning was left oxidised and was measured as approximately 0.5 V versus Ag/AgCl. SER spectra of MP at the extremes of the potential range and a spectrum of gas phase dosed EP are included in Figure 4.8 for comparison.

** The direction of potential scanning was not thought to have a significant effect on the surface conditions when the potential is being held in the absence of an adsorbate, but may influence rate of side reactions and the coverage of their products.

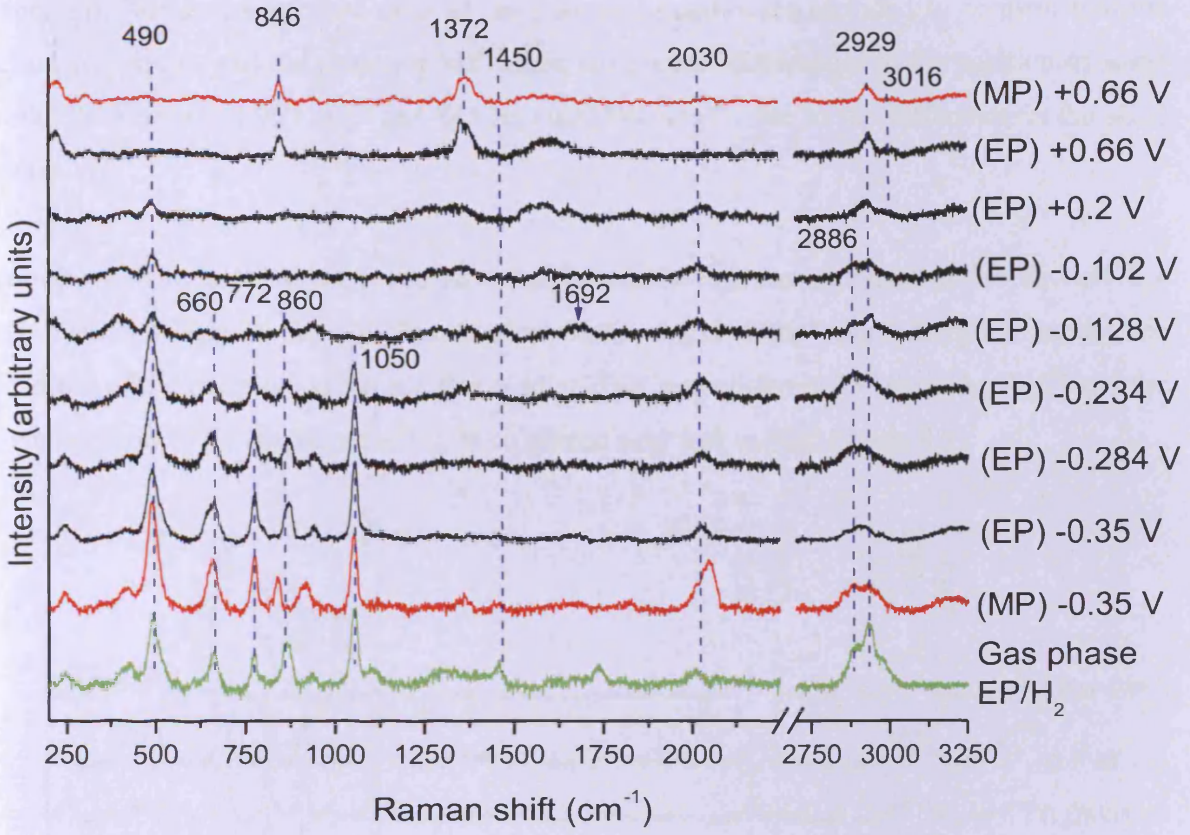

Figure 4.8 SER spectra of 0.1 M MP and EP adsorbed on Au@Pt CS-NP held at different potentials in a negative scanning direction.

At high positive potentials, it can be seen that the SER spectra obtained for MP and EP (Figure 4.8) were identical to that from gas phase dosing on platinum under argon, which was previously identified as an oxygen bound carboxylate species (Figure 4.11). When holding the electrode at potentials corresponding to the double layer region, the peaks from the carboxylate species had reduced in intensity and very little adsorption was seen from other species apart from CO. At potentials corresponding to the H UPD region (-0.128 V, Figure 4.18), a broad feature at 1692 cm^{-1} made a brief appearance before being removed when the potential was scanned more negative. The peaks for the HHS seen on platinum under gas phase hydrogen, began to emerge at -0.234 V as seen by inspection of the green spectrum in Figure 4.8. This shows that the gas phase result was replicated under electrochemical conditions. The main difference was that peaks from the condensed layer found using gas phase dosing were no longer visible (for example ν(C=O) at 1738 cm^{-1}). The intensity of the HHS peaks became progressively more intense as the potential was scanned further negative into the HER region. However, the position of the peaks did not change. In Figure 4.8, the red

spectra of MP at the extreme ends of the potential range were included to confirm that the adsorption mode was the same for MP, again with minor differences to the position of some peaks (915 replaced 937 cm^{-1} and 843 replaced 860 cm^{-1}), due to the difference in the alkyl group.

The above experiment was conducted with a relatively high concentration of the reactant (0.1 M). To determine if the solution concentration would dictate the adsorption mode, the potential of the platinum electrode was held at HER potentials (-0.33 V) *vs.* Ag/AgCl and the concentration of EP dissolved in 0.1 M sulphuric acid was varied (Figure 4.9).

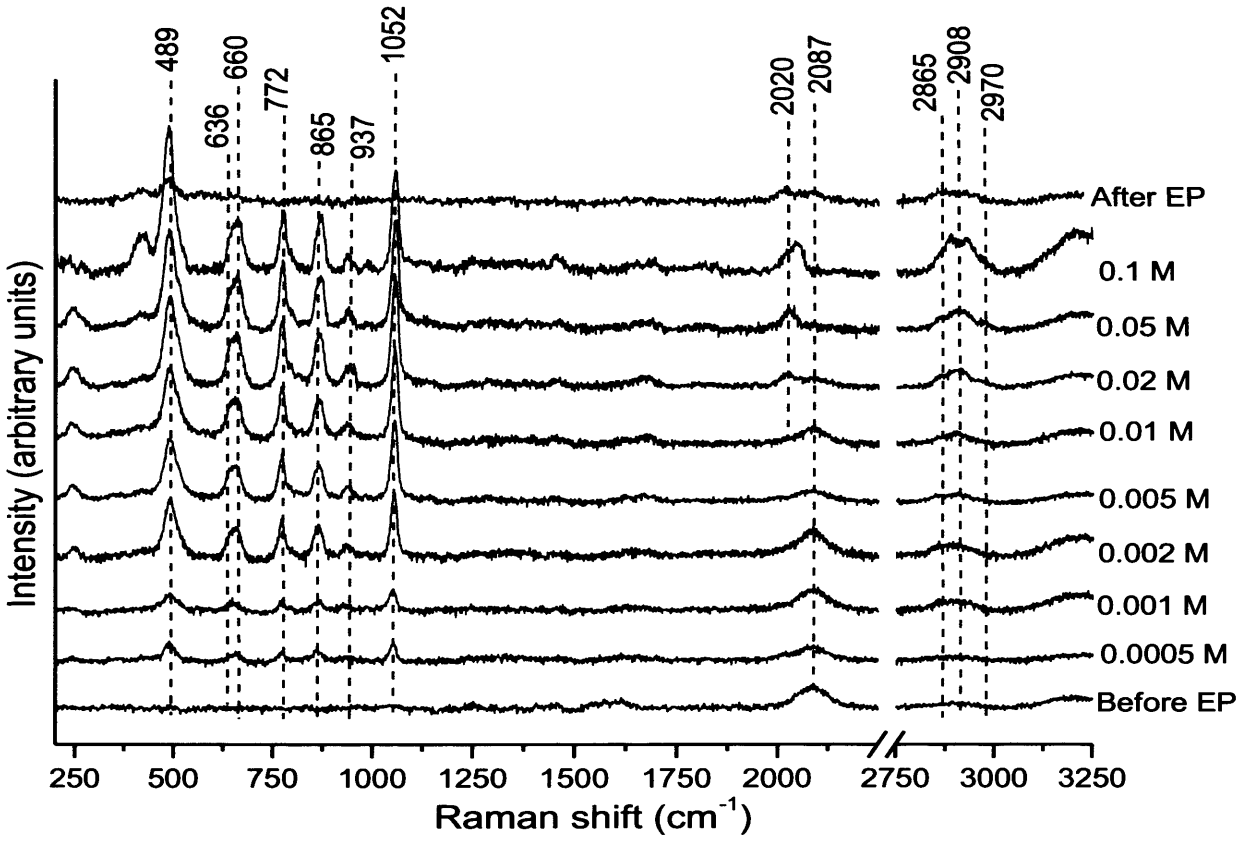

Figure 4.9 Spectra of EP dissolved in 0.1 M H_2SO_4 at varying concentrations held at -0.33 V *vs.* Ag/AgCl.

The intensity of the HHS peaks increased as the solution concentration of EP was varied from 5×10^{-4} M to 1×10^{-1} M but disappeared completely when the solution was switched to pure 0.1 M sulphuric acid. However, the relative intensities of the peaks remained unaffected irrespective of EP concentration. The two main observations from Figure 4.9 were that CO vibrations were clearly resolved at EP concentrations of 2×10^{-2} M and above and that the

surface hydrogen vibration was present up to 2×10^{-2} M EP, but not above this concentration as deduced by the presence of peaks at 2020 (ν(C≡O)) and 2087 cm^{-1} (ν(Pt-H)).

Although the relative intensities of the HHS peaks for EP did not match the analogous peaks of the Raman spectrum of EL, the position of the HHS peaks (except at 660 and 640 cm^{-1}) did match the frequencies exhibited by some of the EL Raman peaks. An equivalent experiment therefore with EL adsorbed on platinum under HER conditions was conducted and did reproduce the SER spectrum of the HHS but at very low intensities (Figure 4.10, dark red spectrum). However, this very low intensity spectrum was thought to arise from the residual 1% EP found in the EL sample using gas chromatography [32] and not from EL itself.

The choice of solvent was well understood to have a significant effect on the Orito reaction [33]. A report by Calvo *et al* had shown that the Orito reaction can be successfully performed electrocatalytically with an aqueous solvent on palladium electrodes [34]. EP was shown to produce the same surface intermediate using the solvent used in Calvo's paper†† (Figure 4.10, red spectrum).

Small amounts of H_2O in the reaction mixture have been shown to be beneficial to the reaction performance (ee and rate) [22]. This was believed to be due to the hydrolysis products of EP stabilising the 'open 3' conformer of the modifier cinchonidine. Even though identical results were obtained with experiments conducted under gas phase conditions where H_2O was excluded, the contribution of possible hydrolysis products needed to be eliminated from all measurements. To test if the products, ethanol (EtOH) and pyruvic acid (PA), were responsible for the observed spectra, both were introduced to the surface under identical conditions to those used to produce the intense SERS peaks below 1100 cm^{-1} for MP and EP (Figure 4.10, green and blue spectra). Although the spectrum of PA (black) did resemble that of the EP spectrum (magenta), close examination revealed that several peaks were at different frequencies including 921 cm^{-1} (936 cm^{-1} (EP)), 812 cm^{-1} (860 cm^{-1} (EP)) and there was an absence to the peak at 660 cm^{-1}. Therefore PA was eliminated as the EP-derived adsorbate under HER conditions.

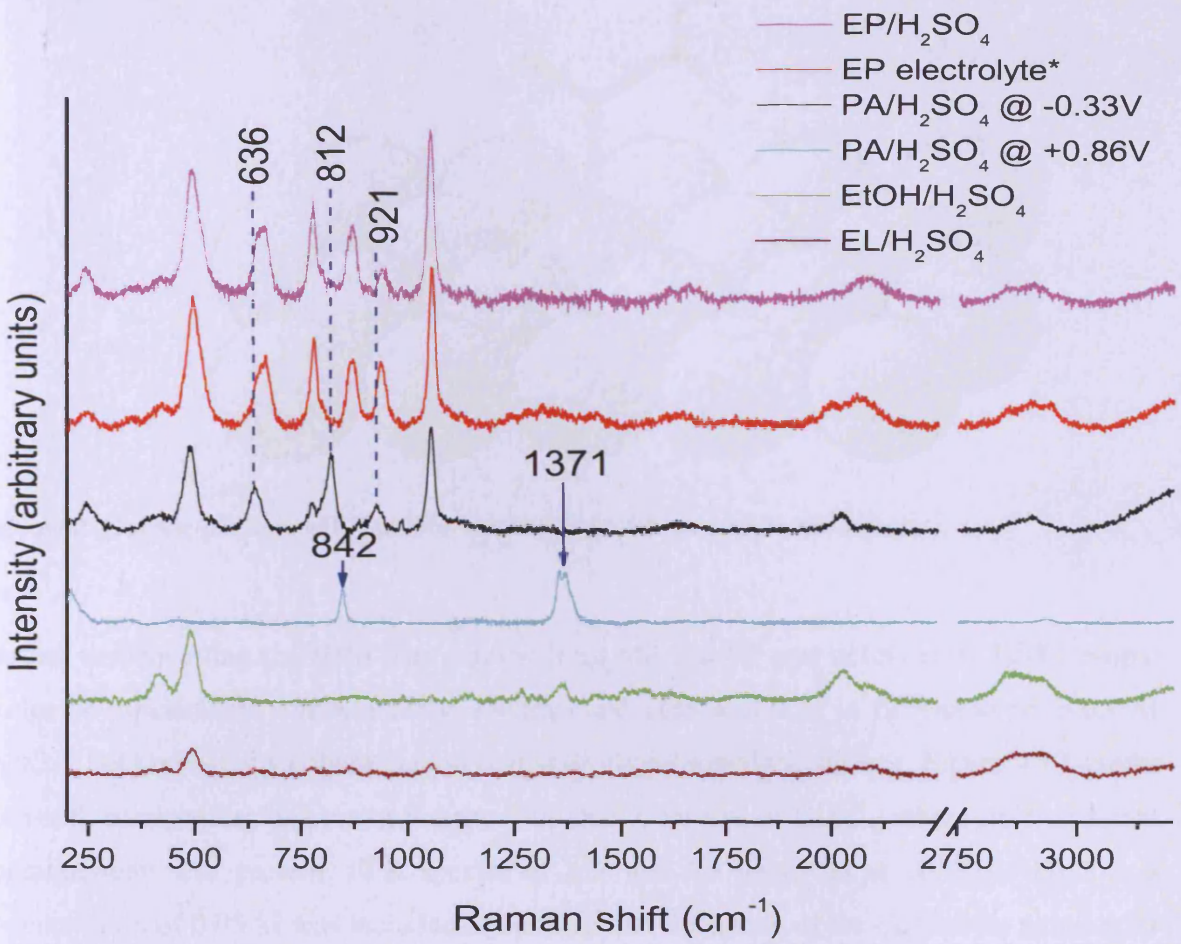

Figure 4.10 Comparison of the SER spectra on Au@Pt CS-NP at -0.33 V of 0.1 M EP dissolved in H_2SO_4 (magenta) and the electrocatalytic solvent used by Calvo *et al* [34][††] (red), 0.1 M PA (black), PA at + 0.86 V (blue), EtOH (green) and 0.1 M EL (dark red).

At potentials corresponding to the oxide region, PA gave the same spectrum as MP and EP with the appearance of peaks at 1371 and 842 cm^{-1}. Therefore these peaks are assigned to vs(COO-) and δ(COO-) of adsorbed PA in a carboxylate state (Figure 4.11). For this adsorption mechanism to occur, both MP and EP must undergo a decomposition reaction on platinum and palladium at oxidising potentials which results in the loss of methanol and ethanol respectively. It is proposed that adsorbed oxide acted as a base to catalyse the saponification of the ester group.

[††] The electrolyte used for the electrocatalytic reaction: 0.3 M $NaClO_4$; 0.2 M CH_3CO_2H and 50 mM CH_3COONa.

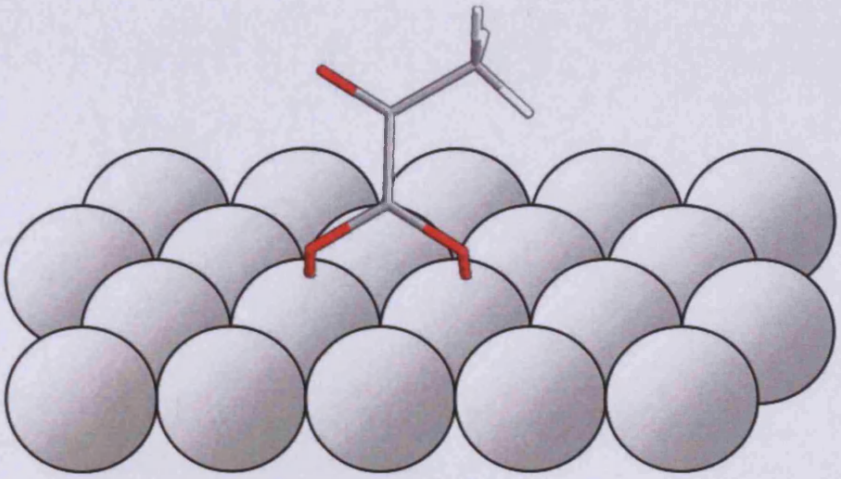

Figure 4.11 Carboxylate form of PA adsorbed on Au@Pt CS-NP under argon atmosphere.

Further evidence that the HHS was derived from MP and EP was obtained by H/D isotopic exchange experiments. Unfortunately, a study conducted with 0.25 M EP dissolved in 0.1 M D_2SO_4 / D_2O revealed a contamination that severely poisoned the surface. Figure 4.12 shows the result of repeating this measurement with $DClO_4$ instead of D_2SO_4, where no significant contamination was present. SER spectra of MP and EP dissolved in $HClO_4$ / H_2O to a concentration of 0.05 M was included to confirm that the nature of the electrolyte anion does not affect the adsorbate.

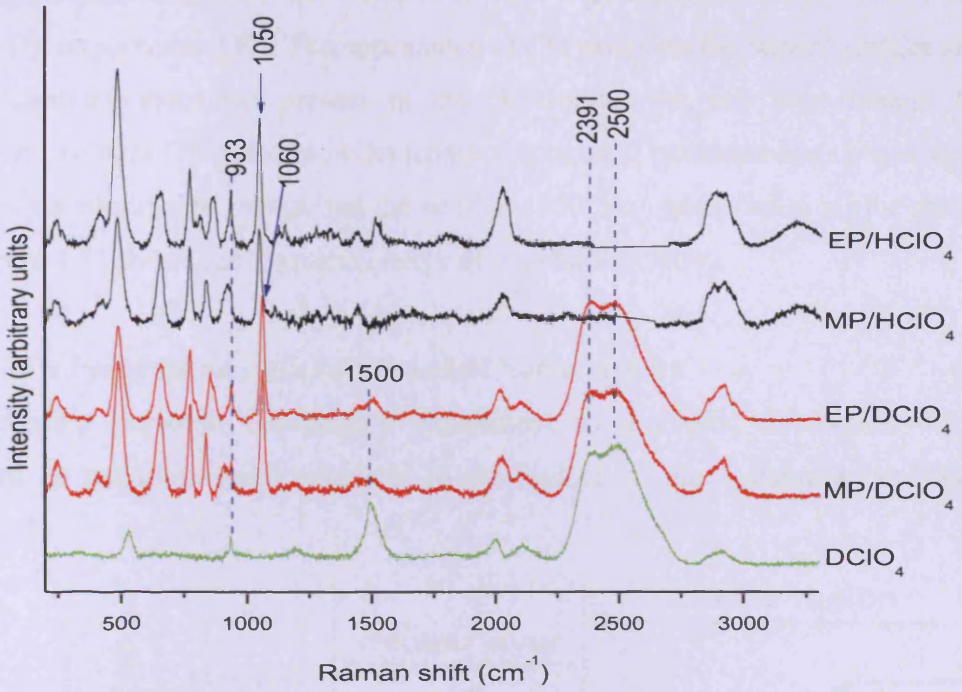

Figure 4.12 SER spectra of 0.1 M $DClO_4/D_2O$ (black), 0.01 M MP and $EP/DClO_4/D_2O$ (red) and 0.05 M MP and $EP/HClO_4/H_2O$ (green) on Au@Pt CS-NP at -0.33 V *vs.* Ag/AgCl.

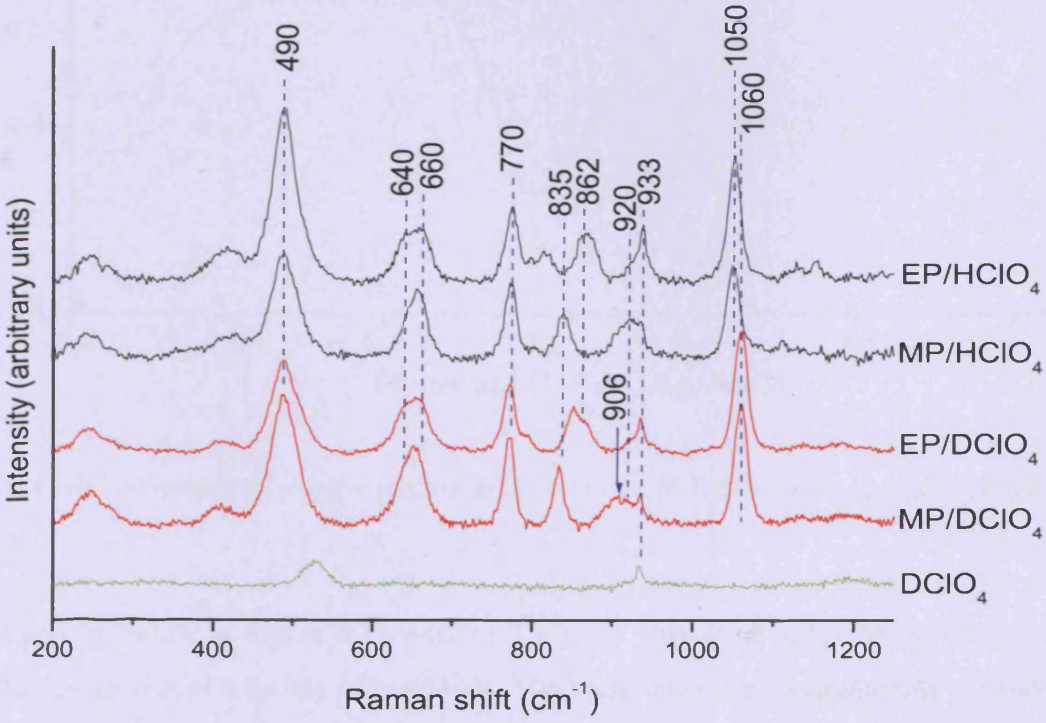

Figure 4.13 Expanded frequency range of Figure 4.12.

The peaks positioned at 2400, 2391 and 1500 cm^{-1} were assigned to va(D-O-D), vs(D-O-D) and v(Pt-D), respectively [40]. The appearance of CO peaks on the 'clean' surface shows that a slight contamination was present in the electrolyte, but this was thought to be an insignificant amount. The spectra in deuteroperchloric acid remained largely unchanged with respect to perchloric acid except that the peak at 1050 cm^{-1} gave rise to a blue shift to 1060 cm^{-1}. Figure 4.13 shows the frequency range of interest for clarity.

4.2.4.2 Ethyl Pyruvate on Au@Pd Core-shell Nanoparticles

The equivalent potential dependency experiment as described in section 4.2.4.1 was performed on palladium with reference to the regions of the voltammogram depicted in Figure 4.14.

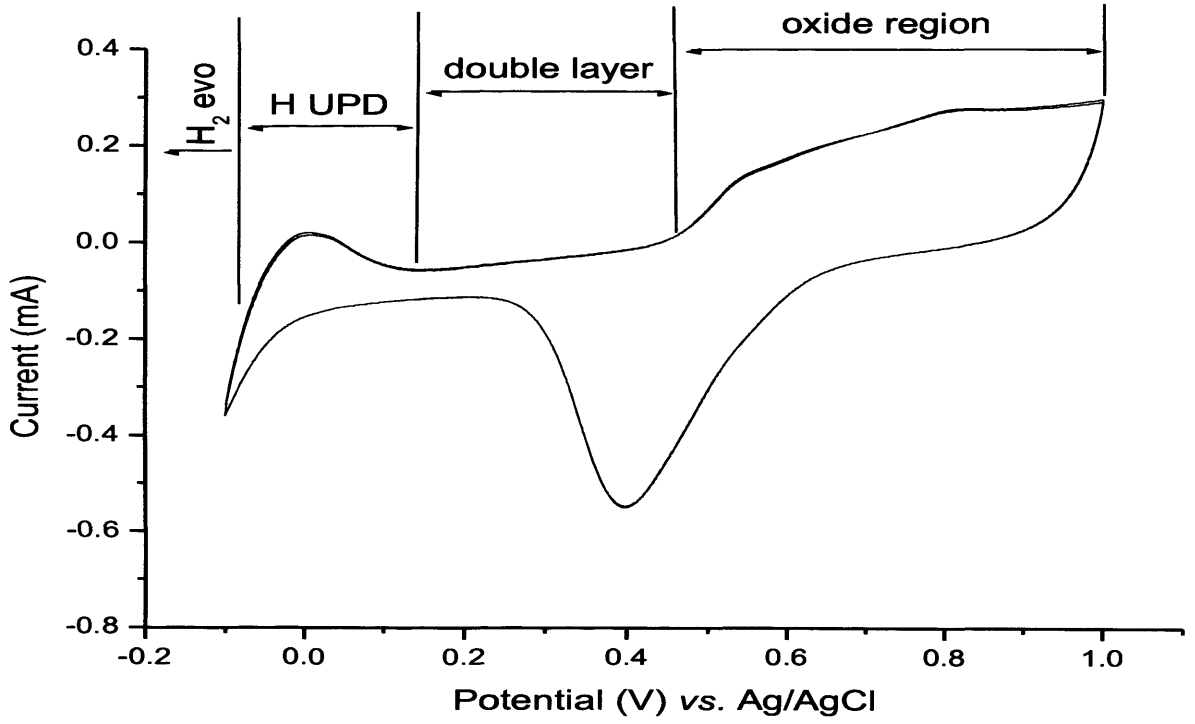

Figure 4.14 Cyclic voltammogram of polycrystalline palladium in 0.1 M H_2SO_4 versus Ag/AgCl reference at 100 mV/s.

The SER spectra below in Figure 4.15 were of 0.1 M EP dissolved in 0.1 M sulphuric acid adsorbed on palladium at a variety of potentials. The vibrational band assignments are shown in Table 4.4.

Table 4.4

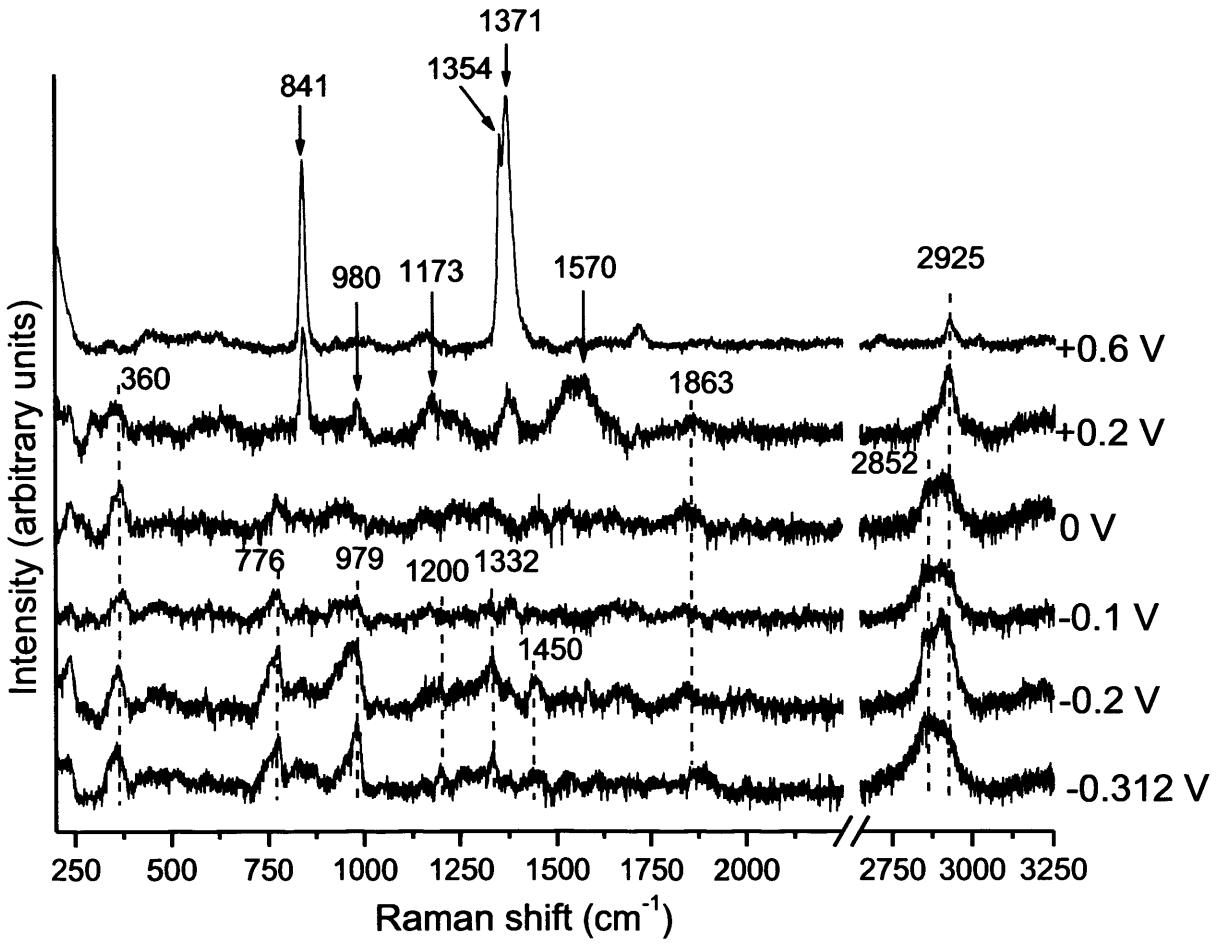

Figure 4.15 SER spectra of EP on Au@Pd CS-NP dissolved in 0.1 M H_2SO_4 at a variety of potentials versus a Ag/AgCl reference electrode.

At positive potentials, where oxygen was adsorbed on the surface, the carboxylate species was again dominant (Figure 4.11). As on platinum, in the double layer region the peaks from the carboxylate species were reduced in intensity. In the H UPD region, very little adsorption can be seen until the potential exceeded -0.1 V in magnitude where an adsorbate emerged that can be tentatively identified as *enol*-EP. Evidence for the vinyl group was observed with out-of-plane $\delta(C^3\text{-}H_2)$ modes at 981 and 770 cm^{-1}. The plane of the ester group was thought to be slightly tilted with respect to the surface as some of the associated frequencies (1450, 1330, 1200 and 860 cm^{-1}) were observed but at low intensity. As with the gas phase results, the peaks at 1863 and 360 cm^{-1} have been assigned to bridge bonded CO [27] with a $\delta w(C^2\text{-}OH)$ vibration from adsorbed *enol*-EP at 360 cm^{-1} aswell.

Table 4.4 Band assignments for liquid phase EP dissolved in 0.1 M H_2SO_4 on Au@Pd CS-NP.

Band Position (cm^{-1})		Assignment
EP / H_2 / H_2SO_4 @ +0.6 V	**EP / H_2 / H_2SO_4 @ -0.312 V**	
1870	1870	ν(PdC≡O) (bridged)
1570	-	ν(C^2=O) (η^1 mode)
-	1450	δd(C^5-H_3)
1371	-	νs(COO^-) (PA)
-	1330	δw(C^4-H_2)
1173	1200	ν(C^4-O)
980	979	δw(C^3H_2) (vinyl)
-	860	ν(H_2C-CH_3)
841	-	δ(COO^-) (PA)
-	770	δt(C^3H_2) (vinyl)
-	360	δw(C^2-OH) / ν(Pd-CO) (bridged)

4.2.4.3 Discussion of the Electrochemical Experiments on Core-shell Nanoparticles

On platinum

Through surface selection rules, an adsorption geometry was extracted for the HHS of both MP and EP, whereby the M-C bond was attached at C^2 and the C-OH bond was directed away from the surface. The absence of a peak around 1735 cm^{-1} (ν(C=O)) suggested that the ester carbonyl was parallel to the surface plane. The peak at 936 cm^{-1} was assigned to an out-of plane deformation of the C-C bond on the ethyl group, the peak at 862 cm^{-1} was assigned to a C-H_3 deformation also on the ethyl group, the peak at 770 cm^{-1} was assigned to out-of-plane C-O-C deformations, and the peak at 660 cm^{-1} was assigned to an out-of-plane δw(C^2=O).

A more accurate vibrational analysis will be discussed in section 4.2.5 where the band assignments will be reported in full. The salient points appropriate to this configuration were that the reactant molecule was adsorbed as a chiral half-hydrogenated intermediate state (HHS) and was anchored to the surface via a Pt-C bond. The plane of the ester group was speculated to be parallel to the surface plane with the ethyl group for EP in the *gauche* configuration such that the C-C bond was at an angle away from the surface (Figure 4.16). It was not clear whether the ester carbonyl was *s-cis* or *s-trans* with respect to the alcohol group at this time. Nor was it clear whether the *keto* or *enol* tautomer was the precursor to the HHS. In the event of the *enol* tautomer being involved, the HHS can be eliminated from the reaction as it has been shown that the reactant is in the *keto* tautomeric form through H/D experiments [35].

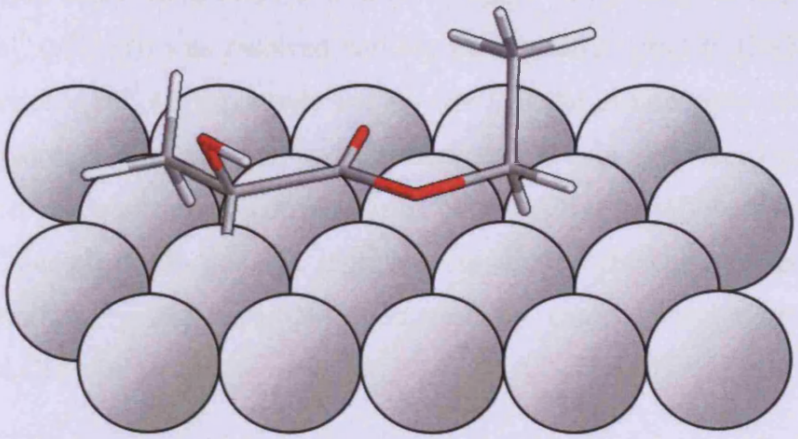

Figure 4.16 Adsorption geometry of the HHS of EP on platinum.

Prior to the formation of the HHS, a broad feature emerged at 1692 cm^{-1}. This was thought to be a ν(C=O) of the ketone in the η^1 adsorption mode of EP before it became hydrogenated. With reference to the regions in the voltammogram, the peaks from the HHS started to emerge at a potential equivalent to H^+ adsorption/desorption on the platinum{110} step site. However, this may be simply a coincidence. Rather, the surface proportion of the HHS appears to be a function of surface hydrogen coverage and not a specific adsorption of EP at particular sites (the commencement of HER is also coincident with {110} step H UPD peak). However, the ratio of peak intensities did not appear to change with potential, leading to the conclusion that the HHS adsorption mode of EP was only generated by the presence of H OPD which overlaps with H UPD [36].

The position and relative intensity of the peaks remained unaffected as the solution concentration of EP was increased (Figure 4.9). Therefore, the adsorption mode was independent of the solution concentration. When the solution was switched to pure 0.1 M sulphuric acid, the HHS was removed from the surface showing that its surface concentration was determined by the balance of the following processes, giving rise to a steady state coverage:

$$EP_{(ads)} + H_{(ads)} \xrightarrow{k_1} HHS_{(ads)} \qquad (4.1)$$

$$HHS_{(ads)} + H_{(ads)} \xrightarrow{k_2} EL_{(l)}$$

The most significant observation was that at concentrations of EP lower than 2×10^{-2} M, the peak at 2087 cm^{-1} (ν(Pt-H)) was resolved and the peak at 2020 cm^{-1} (ν(C≡O)) was hardly seen at all. Above 2×10^{-2} M, this result was reversed. If the decarbonylation reaction was slower than the hydrogenation reaction, then a sufficient coverage of surface hydrogen should prevent the former reaction from occurring (since EP would be rapidly converted to EL). If the coverage of adsorbed EP was too high leaving an insufficient number of sites for hydrogen to adsorb, then the decarbonylation reaction could presumably propagate to produce adsorbed CO.

EtOH and PA were two possible hydrolysis products of EP and have been shown not to produce the same spectrum as EP on platinum under hydrogenating conditions. Furthermore, identical results to EP under HER conditions were obtained when using gas phase dosing and also Calvo's electrolyte [34] where the Orito reaction has been successfully performed. This was evidence that the spectroscopic information was an accurate representation of what occurs on the platinum catalyst during the Orito reaction. It should be noted that Calvo's electrocatalytic reaction was carried out on a palladium electrode [34]. The unique differences in the mechanism for HER on palladium and platinum may prevent the extrapolation of Calvo's results exactly to platinum, but this was thought to be an unlikely scenario.

The deuterium experiment did not produce the expected result of a red shift in frequency of any of the HHS peaks rather; it produced a blue shift of the 1052 cm^{-1} peak to 1060 cm^{-1}. This observation was unexpected and there were very few publications reporting this effect. However, Jensen also observed blue shifts in deuterated hexamethylenetetramine and adamantane [37,38] and ascribed this to an "accidental degeneracy" present in the deuterated molecule.

As will be discussed in section 4.2.5.1, an internal hydrogen bond was present for the HHS molecule. The strength of a hydrogen bond was considered to increase on deuterium exchange [39], therefore this could result in a blue frequency shift, which was referred to by Niaura *et al* in their article on –OH ions on copper electrodes [40].

On palladium

Although there were some clear differences between this result and the spectra obtained under gas phase hydrogen, the interpretation was again of adsorbed *enol*-EP, but with a different configuration for adsorption. In section 4.2.4.2, the adsorbate was believed to be bound by π-bonding via the vinyl group (Figure 4.17). In this situation, the ν(C=C) would vibrate in a direction parallel to the surface and so would be screened by the image dipole in the metal and be SERS inactive. Again, this would be consistent with the theory that enantioinversion of EP to *S*-EL on palladium with CD as modifier was a result of *enol*-EP being the dominant adsorbed tautomer [26]. A further difference to the results on platinum was the absence of any ν(M-H) peak. However, this could merely reflect the well-known properties of hydrogen to absorb into the bulk of palladium. Hence, no surface Raman (or IR) band would be observed due to screening by the substrate electrons.

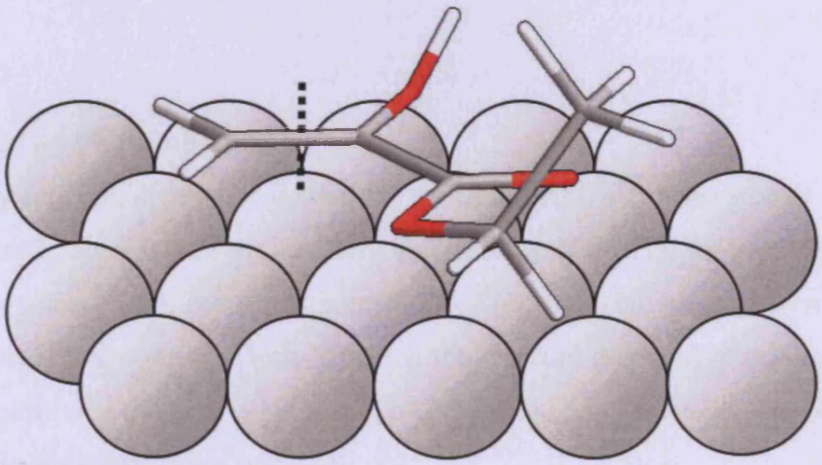

Figure 4.17 π-bound EP on palladium held at potentials corresponding to H OPD.

The interpretation of a π-bound species in the presence of sub-surface hydrogen was also found by Tysoe and colleagues using RAIRS and LEED studies of ethylene adsorbed on palladium{111} [29,30]. This finding also highlighted the difference in the reaction kinetics of hydrogen when dosed under gas phase (section 4.2.3.2) and electrochemical conditions. The formation of the di-σ bonding mode under gas phase conditions indicated that there was an insufficient supply of hydrogen in the bulk of the metal (most likely 'mopped-up' by the physisorbed layer of EP over the surface) in order to stabilise the π-bonded *enol*. Conversely, under electrochemical conditions, the coverage of hydrogen was much higher thereby allowing for electrosorption of hydrogen into the bulk of the palladium and an excess supply of hydrogen to facilitate the reaction towards π-bonded enolic EP. Hence, the prevalence of

the π-bound state of EP under electrochemical conditions would be in agreement with work by Tysoe *et al* on adsorbed ethene [29,30].

4.2.5 Density Functional Theory

The adsorption geometry assigned to the HHS in section 4.2.4.3 involved formation of an M-C bond to C^2, the C-OH bond being at an angle away from the surface plane, the ester carbonyl parallel to the surface plane and the ethyl group rotated to the *gauche* conformation with the C-C bond close to perpendicular to the surface plane. In what follows, density functional theory was commissioned for the assessment of the vibrational and bonding characteristics of such a HHS, of both MP and EP, adsorbed intermediate on a model platinum{100} surface, carried out by Dr David J. Willock of Cardiff University[‡‡]. It should be noted that co-adsorption of hydrogen, other HHS molecules, CO etc were ignored in such calculations.

4.2.5.1 The HHS on Platinum{100}

Periodic density functional theory calculations using the RPBE functional and a planewave basis set were used to investigate the structure and stability of the HHS intermediate adsorbed in an on-top configuration on a platinum{100} surface. The study revealed that the intermediate could have conformations in which the OH and carbonyl groups are *s-cis* or *s-trans* to one another and the ester ethyl group of EP could be in the molecular plane (*anti*) or rotated out of the molecular plane (*gauche*).

Table 4.5 shows that the lowest energy structure for both EP and MP occurred for the *s-cis anti* form with the OH group parallel to the surface and an internal hydrogen bond to the ester carbonyl oxygen atom (Figure 4.18) or to the alkylated ester oxygen atom (for *s-trans*). However, the difference between *s-cis* and *s-trans* forms was quite small. Of greater significance was the internal hydrogen bond which appeared to be strongly favoured, for example in the *s-trans* form rotating the hydroxyl group by 180° and re-optimising gave a conformer 0.37 eV higher in energy.

[‡‡] School of Chemistry, Cardiff University, P.O. Box 912, Cardiff, CF10 3TB. United Kingdom

Table 4.5 Calculated relative energies of the HHS of MP EP on platinum(100), ZPE: zero point energy based on calculated vibrational frequencies in the harmonic approximation.

	relative (eV)	ZPE (eV)	rel. inc. ZPE (eV)
MP			
s-*cis*, methyl *anti*	0.00	2.960	0
s-*trans*, methyl *anti*	0.06	2.980	0.08
s-*trans*, methyl *anti*, no H-bond	0.37	----	----
EP			
s-*cis*, ethyl *anti*	0.00	3.730	0.00
s-*cis*, ethyl *gauche*	0.01	3.742	0.02

Table 4.6 contains the vibrational frequencies and assignments of adsorbed EP on platinum in sulphuric acid under electrochemical conditions of HER and the calculated positions of the peaks derived from the DFT study on the *s-cis anti* conformation of EP.

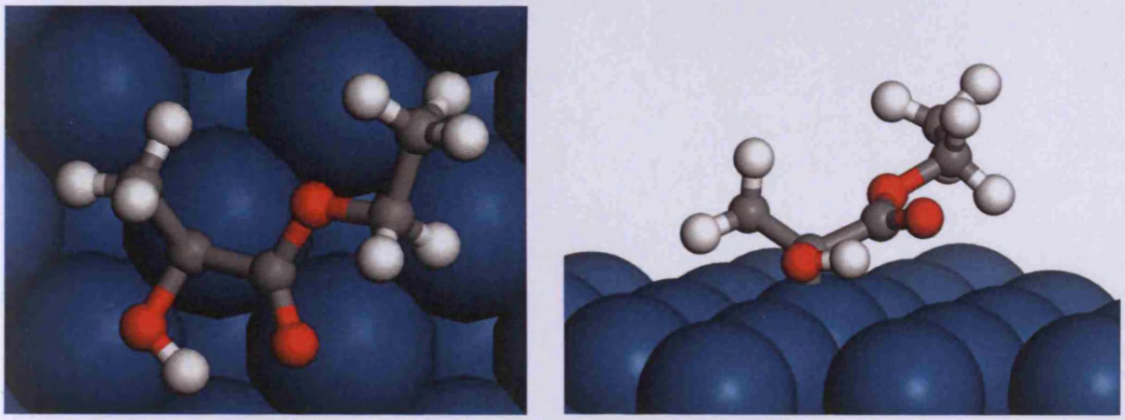

Figure 4.18 Plan view and side view of the HHS of EP on platinum.

Table 4.6 Empirical and calculated band frequency and assignment for EP on platinum.

Band position (cm^{-1})						Assignment
Experimental			**Calculated**			
EP / H_2 / H_2SO_4 @ -0.33 V	**EP / Ar / H_2SO_4 @ +0.66 V**	**EP / $DClO_4$ @ -0.33 V**	**Mode no.**	**EP *anti***	**EP *gauche***	
-	-	2487	-	-	-	va(D-O-D)
-	-	2389	-	-	-	vs(D-O-D)
2040	2015	2021	-	-	-	v(PtC≡O) (on-top site)
-	1990		-	-	-	v(PtC≡O) (bridge site)
-	1600		-	-	-	v(C^2=O)
-	-	1505	-	-	-	v(Pt-D)

-	1378		-	-	-	vs(COO^-) (PA)
1052	-	1060	25	1056	1060	$\nu(C^2\text{-}C^3)$ / $\delta r(C^3\text{-}H_3)$ / δr(O-H)
-	-	-	26	1033	1031	$\delta r(C^3\text{-}H_3)$
985	-	985	27	1002	987	$\nu a(O\text{-}C^4\text{-}C^5)$ / δr ($C^3\text{-}H_3$) / skeletal
937	-	937	28	905	885	$\delta r(C^3\text{-}H_3)$ / $\nu a(O\text{-}C^2\text{-}C^1)$ / $\nu s(O\text{-}C^4\text{-}C^5)$ / skeletal
865	-	865	29	840	828	$\nu s(C^1\text{-}O\text{-}C^4)$ / $\delta r(C^5\text{-}H_3)$ / $\delta r(C^4\text{-}H_2)$
-	844	-	-	-	-	$\delta(COO^-)$ (PA)
-	-	-	31	797	774	$\delta t(C^4H_2)$ / $\delta w(C^5H_3)$
772	-	772	32	736	739	$\delta u(C^3\text{-}C^2(OH)\text{-}C^1)$ about C^2 / $\delta u(C^2\text{-}C^1(O)\text{-}O)$ about C^1 / $\delta r(C^3\text{-}H_3)$
660	-	660	33	685	714	δw(O-H)
636	-	636	34	646	638	δw(O-H) / $\nu(Pt\text{-}C^2)$ / $\delta r(C^3\text{-}H_3)$
-	609	-	-	-	-	$\nu(Pt\text{-}O_x)$
489	489	489	35/36	487/479	496/482	$\nu(Pt\text{-}C^2)$ / ν(Pt-CO)

Those peaks in the gas phase spectra that are not included in Table 4.6 were identified as vibrations from the free molecule in the condensed layer and those assignments can be found in Table 4.2. The equivalent assignments for MP can be found in

Table **4.7** below. The data for MP adsorbed on an oxidised surface was considered to be identical to that of EP and therefore were omitted.

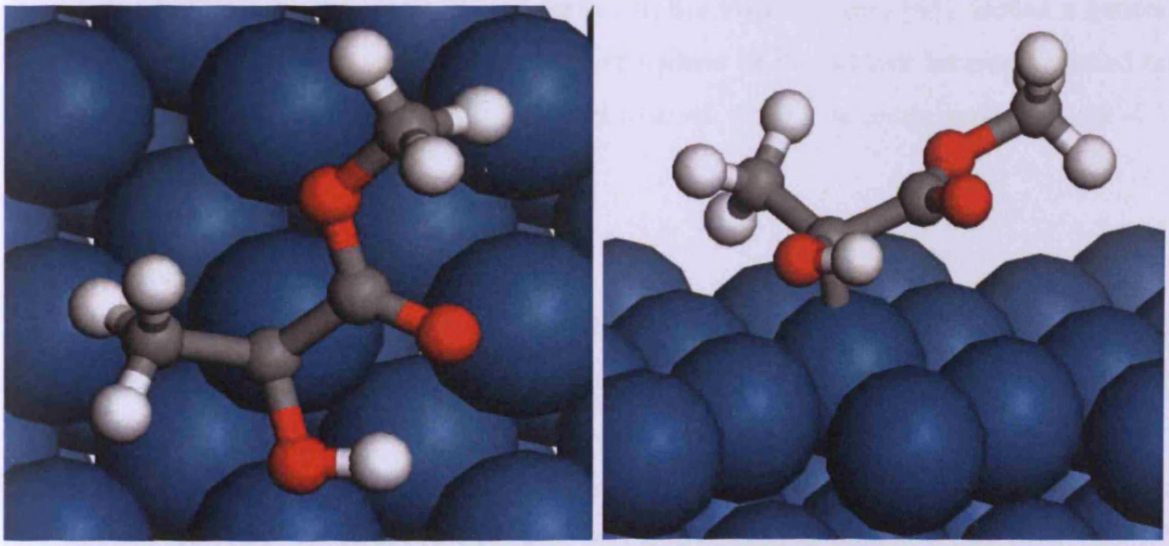

Figure 4.19 Plan view and side view of the HHS of MP on platinum.

Table 4.7 Empirical and calculated band frequency and assignment for MP on platinum.

Band position (cm^{-1})				Assignment
Experimental		Calculated		
MP / H_2 / H_2SO_4 @ -0.33 V	MP / $DClO_4$ @ -0.33 V	Mode no.	MP on Pt{100}	
-	2487	-	-	va(D-O-D)
-	2389	-	-	vs(D-O-D)
2031	2021	-	-	ν(PtC≡O)
-	-		1678	ν(C=O)
-	1505	-	-	ν(Pt-D)
1049	1060	20	1055	$\nu(C^2\text{-}C^3)$ / $\delta r(C^3\text{-}H_3)$ / δ(O-H)
-	-	21	1032	$\delta w(C^3\text{-}H_3)$
985	985	22	964	$\delta r(C^3\text{-}H_3)$ / $\nu(O\text{-}C^4)$ / skeletal
916	905	23	872	$\delta r(C^3\text{-}H_3)$ / va($O\text{-}C^2\text{-}C^1$) / vs($C^1\text{-}O\text{-}C^4$) / skeletal
835	835	24	807	$\nu(C^1\text{-}O)$ / $\delta r(C^4\text{-}H_3)$ / $\nu(C^2\text{-}OH)$ / skeletal
771	771	25	736	umbrella($C^3\text{-}C^2(OH)\text{-}C^1$) about C^2 / $\delta r(C^3\text{-}H_3)$
655	655	26	673	δw(O-H)
641	641	27	638	δw(O-H) / $\nu(Pt\text{-}C^2)$ / $\delta r(C^3\text{-}H_3)$
487	487	28/29	486/472	$\nu(Pt\text{-}C^2)$ / ν(Pt-CO)

DFT analysis on this adsorbate highlighted several conformations, but curiously the C-OH bond was found to lie parallel to the plane of surface. The surface selection rules for SERS applications were not quite as explicit as those for reflection IR applications as the screening of the image dipoles by the metal is less perfect in the visible region [41]. But as a general rule, the intensity increases as the angle from the plane of the surface increases. Based on this, the peak at 1052 cm^{-1} previously assigned to a ν(C-OH) was re-assigned to a $\nu(C^2\text{-}C^3)$ and $\delta r(C^3\text{-}H_3)$ coupled to δ(O-H).

4.2.5.2 Deuterated HHS on Platinum{100}

The calculations alone were also repeated with a deuterium atom on the hydroxyl group of the *s-cis anti* conformation of EP, as opposed to a hydrogen atom. Although the same number of vibrational modes were calculated for the HHS in the presence of hydrogen as in the presence of deuterium, through inspection of animations of the vibrational modes, the mode numbers did not always match. For example, in Table 4.8 mode number 25 for the HHS-H[§§] was matched to mode number 27 of the HHS-D. The modes were matched by comparing the

[§§] The suffix '-D' denotes a deuterated hydroxyl group (C-OD) and for clarity '-H' denotes a hydrogenated hydroxyl group (C-OH).

eigenvectors that represent the set of HHS-H vibrations with the eigenvectors of the HHS-D vibrations. The closest match will have the smallest vector difference. The matched deuterium modes and their vibrational frequencies are shown in Table 4.8 for EP and Table 4.9 for MP with the eigenvector difference. The smaller the difference value, the closer the match. Visual inspection of the matched mode animations also confirmed the calculated matched modes.

Table 4.8 Compared modes for EP-H and EP-D in the *s-cis anti* conformation.

EP-H *s-cis gauche*		**Matched modes of EP-D *s-cis anti***		**Eigenvector difference**
Mode no.	**Frequency (cm^{-1})**	**Mode no.**	**Frequency (cm^{-1})**	
25	1060	27	908	0.779
26	1031	25	1031	0.098
27	987	26	991	0.482
28	885	28	882	0.636
29	828	29	829	0.647
30	815	30	810	0.619
32	739	32	735	0.351
33	714	34	533	0.548
34	638	33	635	0.38
35	496	35	488	0.459
36	482	36	471	0.577

The equivalent calculations were carried out for MP and the results are summarised in Table 4.9 below.

Table 4.9 Compared modes for MP-H and MP-D.

MP-H *s-cis*		**Matched modes of MP-D *s-cis***		**Eigenvector difference**
Mode no.	**Frequency (cm^{-1})**	**Mode no.**	**Frequency (cm^{-1})**	
20	1055	22	911	0.78
21	1031	20	1031	0.073
22	964	21	967	0.178
23	872	23	860	0.437
24	807	24	806	0.072
25	736	25	732	0.128
26	673	27	512	0.754
27	638	26	637	0.427
28	486	28	476	0.628
29	472	29	454	0.655

The resulting matched modes assigned to the peak at 1050 cm^{-1} in the presence of hydrogen (mode 25 for EP and mode 20 for MP) did not blue shift to 1060 cm^{-1} in the presence of deuterium, as seen with the experimental results. In fact, the peak was calculated to red shift by ~150 cm^{-1} (mode 27 (EP) and 22 (MP)).

4.2.5.3 Deuteration of the Free Molecule

To better understand this complex vibrational behaviour, the deuterium experiments were extended to the free product molecule. This was performed experimentally by mixing ML with a small quantity of D_2O and recording the Raman spectrum (**Figure 4.20**).

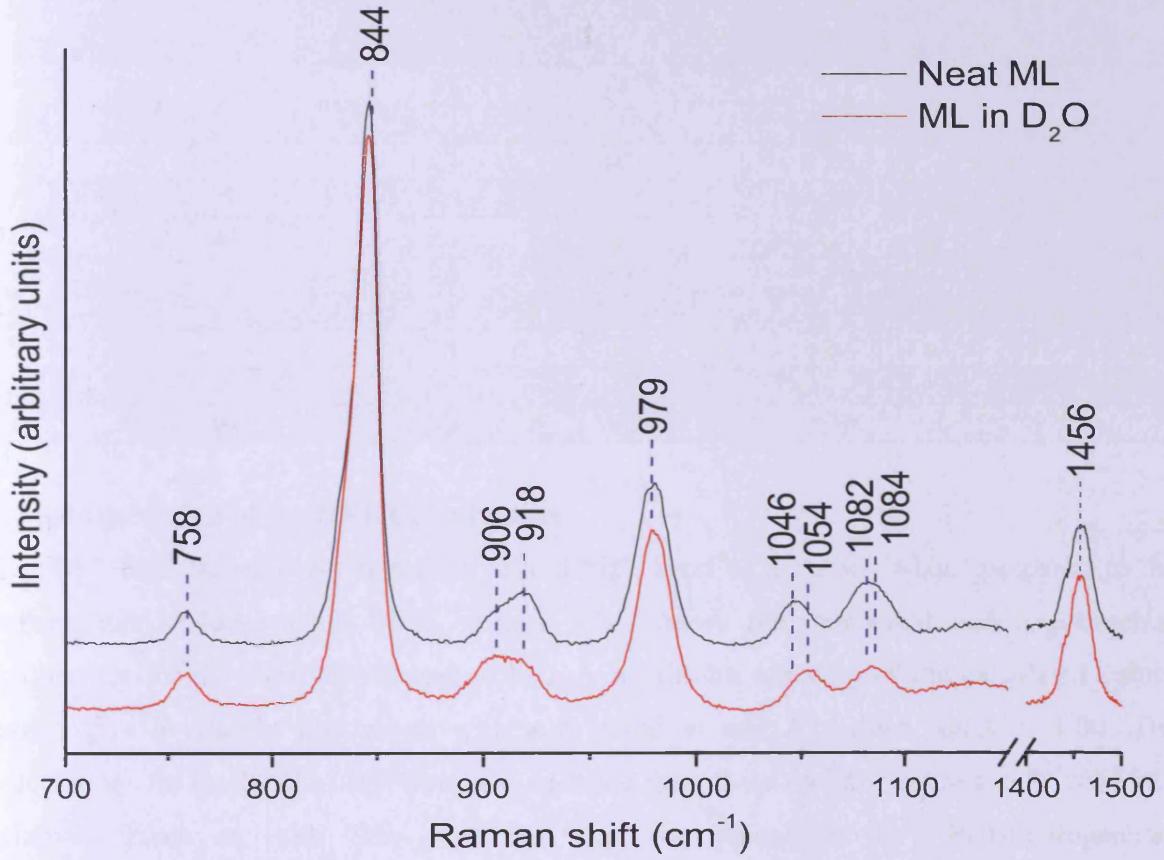

Figure 4.20 Raman spectra of ML and ML in D2O.

In comparison with the neat ML spectrum, a clear blue shift of the peak at 1046 cm^{-1} to 1054 cm^{-1} was seen. A slight blue shift for the peak at 1082 cm^{-1} to 1084 cm^{-1} and a red shift to the peak at 918 cm^{-1} to 906 cm^{-1} was also seen. This latter frequency shift was also seen in the spectrum of the MP-D HHS (Figure 4.13). The calculated frequencies of ML-H and the matched modes of ML-D vibrational modes also showed a blue shift to the corresponding vibrations (Table 4.10, modes 23 and 24 of ML-H).

It should also be noted that no shift was seen for the 1456 cm^{-1} peak, which was assigned to a $\delta d(C\text{-}H_3)$. In this case, the deuterium can be identified as having been added to the ketone to form a deutero-alcohol group as would be expected if the *keto*-EP was involved as opposed to being added to the adjacent methyl group, for which a shift of the 1456 cm^{-1} peak would be expected and have implicated the *enol*-EP as the precursor to the HHS.

Table 4.10 Experimental and calculated frequencies of the ML-H and ML-D free molecules.

Experimental		**Calculations**			
ML-H (cm^{-1})	**ML-D (cm^{-1})**	**ML-H**		**ML-D**	
		Mode no.	**(cm^{-1})**	**Matched Mode no.**	**(cm^{-1})**
1456	1456	11	1458.5	11	1458.5
1082	1084	23	1074	22	1114
1046	1054	24	1011	23	1042
979	979	25	963	24	964
917	906	26	907	25	933
		26	907	26	888
845	845	27	823	27	822
756	756	28	742	28	735
585/532	585/532	29	591	29	586
494	494	30	462	30	456

4.2.5.4 Discussion of the DFT Calculations

The DFT calculations were found to have a high level of accuracy when compared to the experimental values of the HHS. Figure 4.21 shows the calculated and experimental frequencies for the HHS of MP and of ML. A maximum accuracy of the calculated values would give a straight line graph with a gradient m and R^2 values equal to 1.00. The calculations for the HHS of MP were less accurate than those for ML, but m and R^2 were still relatively close to 1.00. This confirmed that the adsorption of a half-hydrogenated intermediate state of MP and EP on the surface at high coverages of surface hydrogen is consistent with model calculations of such a species adsorbed on platinum{100}.

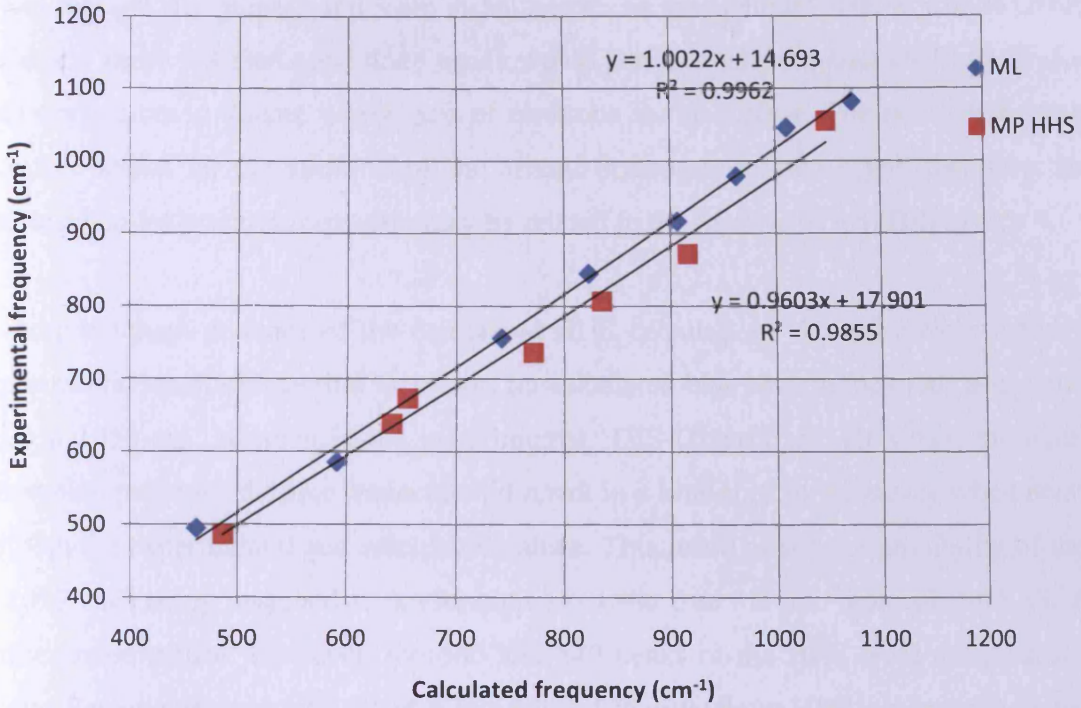

Figure 4.21 Accuracy of the calculated vibrational frequencies for the HHS of MP to the experimental values (red squares) in comparison with the calculated and experimental values for ML (blue diamonds).

Clearly, the mechanism that resulted in the formation of the HHS must involve an initial hydrogen addition to the keto oxygen followed by the formation of a surface Pt-C bond as described by Rauls *et al* [42]. In the absence of a chiral modifier, the racemic reaction mechanism may be described by the following steps:

1. Diffusion of the reactant to the metal surface.
2. The reactant molecule initially adsorbs in an end-on η^1 configuration possibly via the oxygen lone pair of electrons from the ketone.
3. Surface hydrogen is then transferred onto the keto oxygen to form an alcohol.
4. The platinum atom from where the hydrogen had just been removed being negatively charged facilitates a nucleophilic attack on the alcohol carbon to form a Pt-C surface bond and the HHS.
5. A second hydrogen from an adjacent platinum atom is transferred to the alcohol carbon to form the product.
6. The product can then diffuse away into the reaction medium.

It was thought that steps 2 and 3 are instantaneous as the platinum surface will be covered in hydrogen under reaction conditions which would preferentially form an O-H bond before the keto oxygen could donate a lone pair of electrons to the surface. The rate determining step therefore might be the addition of the second hydrogen in step 5 and therefore the rate limiting step for product formation may be related to the lifetime of the HHS in step 4.

A more thorough analysis of the deuterated HHS calculations showed a close match to the experimental result except that there was no calculated blue shift in the mode assigned to the peak at 1050 cm^{-1} as seen in the experimental HHS-D spectrum. However, the equivalent vibrational mode for the free molecule did result in a blue shift in frequency when deuterated for both the experimental and calculated values. This result raised the possibility of the peak at 1050 cm^{-1} being assigned to a vibration from the free ML/EL molecule and not from a surface intermediate. However, the 660 and 640 peaks of the HHS were not present in the lactate Raman spectrum, the relative intensity of the matching HHS peaks were different to those in the lactate Raman spectrum and EL was shown not to adsorb on platinum (Figure 4.10). Therefore, the HHS SER spectrum was from a surface intermediate. However, calculations and theory suggested that the HHS contained more character of the free molecule than that of an isolated HHS molecule. Two shortcomings of the DFT analysis are the absence of surface hydrogen (known to be in abundance at HER potentials) and the absence of adjacent HHS molecules. A nucleophilic interaction by surface hydrogen on C^2 of the HHS could possibly have given rise to this 'extra lactate character', i.e. a weakening of the Pt-C bond and a potential formation of a C-H bond instead.

The strength of the hydrogen bond was not altered in the DFT calculations when hydrogen was substituted for deuterium. Hence, the blue shift could also be assigned to an "accidental degeneracy" rather than a difference in the bond strength.

Due to the fact that the modelling of the HHS models was of a single adsorbate, the hydrogen bond was exclusively internal. However, under experimental conditions, adjacent HHS adsorbates would provide other donators and acceptors for hydrogen bonds. Hence intermolecular hydrogen bonding could be thought of as a more likely scenario. In this situation, the intermolecular interactions could create islands of the HHS on the surface and occupy adjacent platinum atoms that may be required for the second addition of hydrogen in step 5 of the racemic reaction mechanism.

4.2.6 Ethyl Benzoylformate

Hydrogenation of ethyl benzoylformate (EBF) to the product ethyl mandelate (EMD) on CD modified platinum was selective towards the *R*-enantiomer and a report by Bartok *et al* reported an optical yield of 98% [43]. The reaction rate was slow and the phenomenon of rate acceleration after modification was minimal or not observed at all in this reaction. This was thought to be due to poor product desorption depending on the solvent used [44]. EBF differed in structure from EP containing as it does an aromatic ring in the α-position to the ketone instead of a methyl group, which means that EBF is non-enolisable as there is no proton at $C^{1'}$ with which to exchange. However, the carbonyl groups in EBF were able to rotate about the C^1-C^2 bond and C^3-C^4 to form *s-cis* / *s-trans* and *anti* /*gauche* isomers. The plane of the large phenyl ring should also aid in determining the adsorption geometry in SERS measurements.

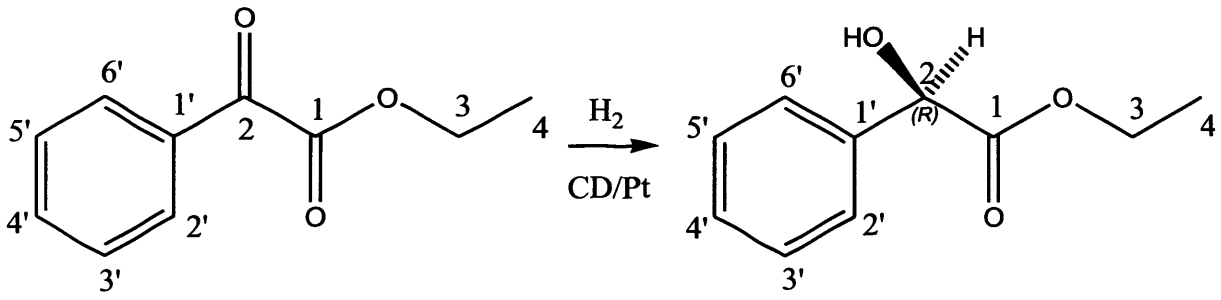

The normal Raman spectra of EBF and the product EMD have been included to identify and discuss the features that may be expected in the SER spectra (Figure 4.22).

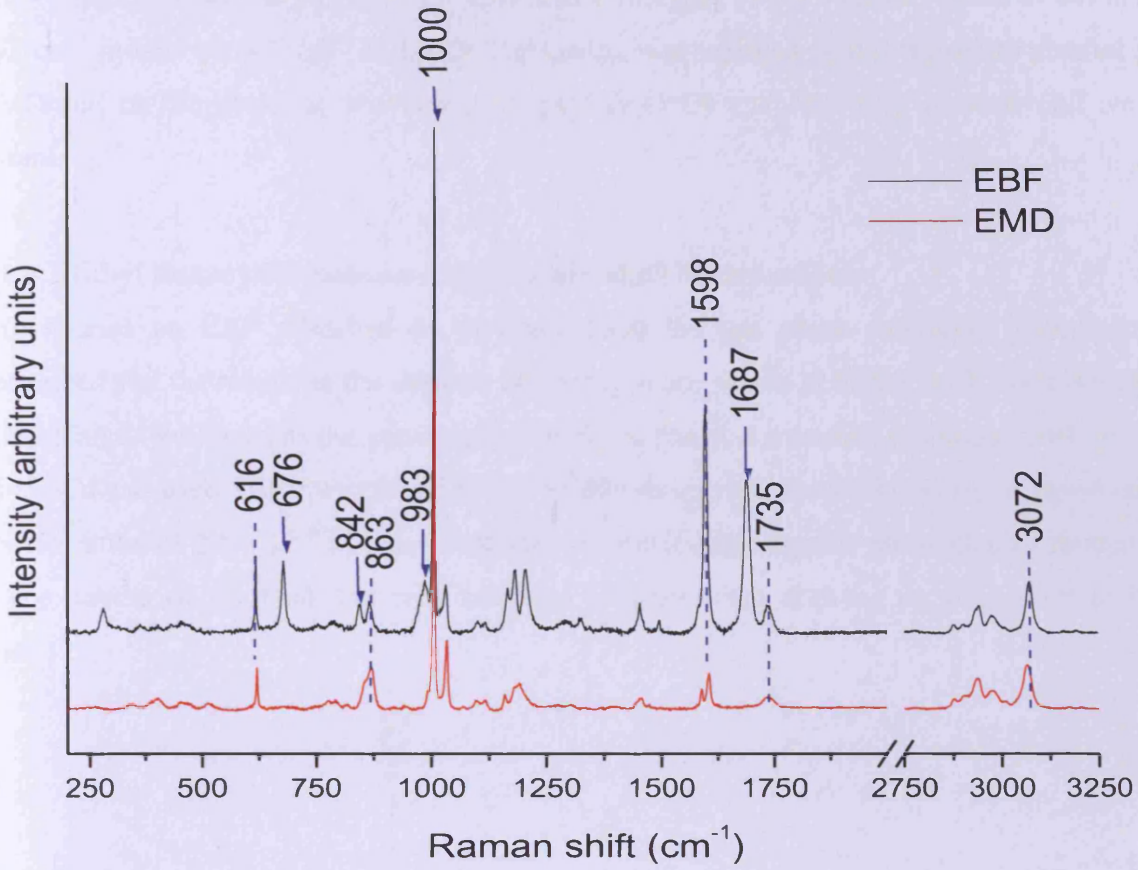

Figure 4.22 Raman spectra of liquid EBF and EMD.

There were some notable features in the spectrum from the aromatic ring which included the peak at 3072 cm^{-1} (aromatic ν(C-H)), the peak at 1598 cm^{-1} (aromatic ν(C=C)), the peak at 1000 cm^{-1} (aromatic ν(ring)) and the peaks at 863 and 842 cm^{-1} (aromatic δw(C-H)). Differences between EBF and EMD could be seen in the peak at 1598 cm^{-1} from conjugation of the aromatic ring with the ketone. For linear unsaturated molecules, conjugation will cause the frequency of ν(C=C) and ν(C=O) vibrations to red shift due to delocalisation of the π-electrons, but will also cause an increase in the polarisability of the molecule and hence lead to an increase in the Raman scattering intensity [45]. For EBF, the position of the keto ν(C=O) vibration was indeed red shifted from 1735 to 1687 cm^{-1} and was 5–6× more intense than the ν(C=O) of the ester carbonyl. The intensity of the ν(C=C) vibration of the aromatic ring was also 5–6× stronger for EBF than for EMD and there was a notable split to this peak in EMD into two weaker peaks at 1604 and 1588 cm^{-1}. However, the position of this peak(s) was not notably shifted, possibly because the π-electrons were already delocalised in the aromatic ring. The effects of conjugation were also seen for the ν(ring) vibration with a more

pronounced shoulder at 983 cm^{-1} for EBF and a merging of the δw(C-H) peaks at 842 and 863 cm^{-1} in EBF to 867 cm^{-1} in EMD. The ketone was replaced with a secondary alcohol in EMD and so the peaks at 1687 and 676 cm^{-1} (ν(C=O) and δw(C=O), respectively) were absent.

4.2.6.1 Ethyl Benzoylformate on Au@Pt Core-shell Nanoparticles

Experiments on EBF adsorbed on platinum from the gas phase and liquid phase were performed and the results in the absence of hydrogen are shown in Figure 4.23. For gas phase dosing, argon was used as the carrier gas. For liquid phase, a saturated solution of EBF in 0.1 M H_2SO_4 was used. (EBF was found not to readily dissolve in the selected electrolyte when a concentration of 2.5×10^{-3} M was attempted. An immiscible organic phase globule remained at the bottom of the flask but was carefully avoided when drawing up solution from the flask.)

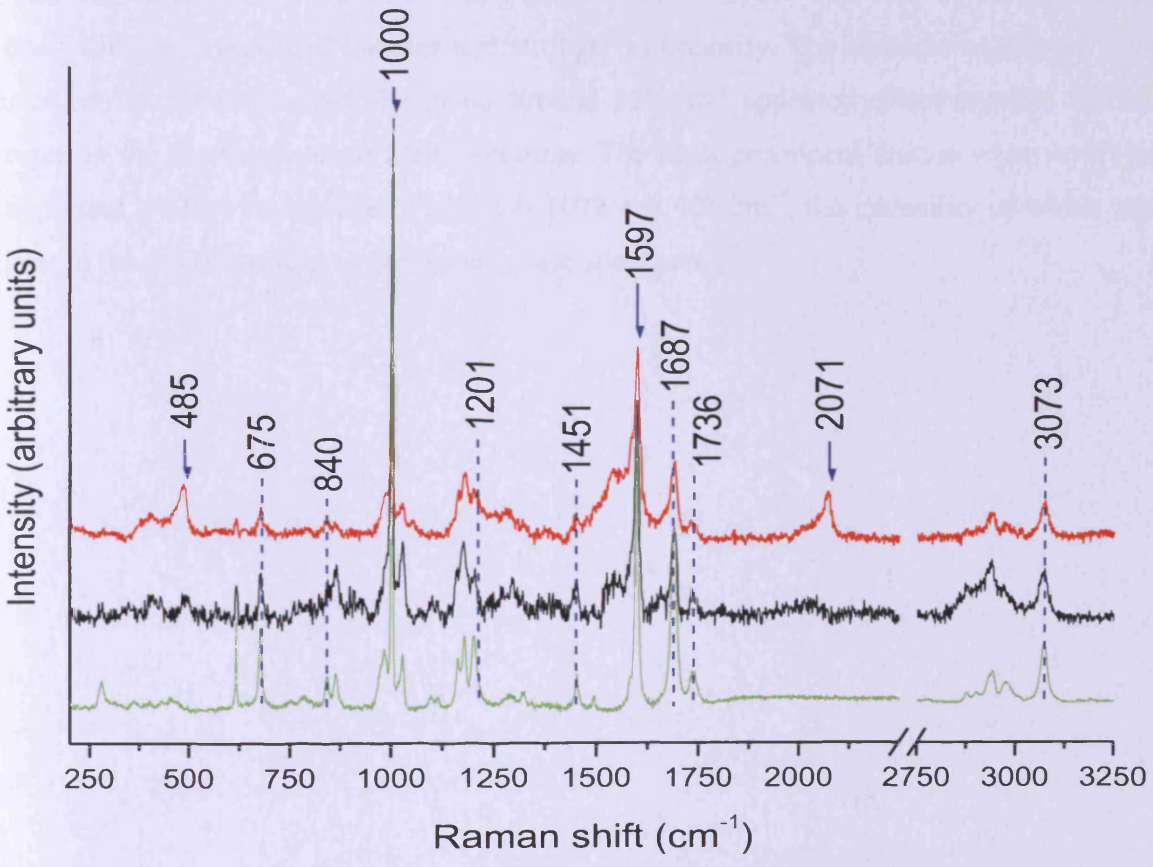

Figure 4.23 Raman and SER spectra of bulk EBF (green), EBF/Ar (black) and EBF/H_2SO_4 on Au@Pt CS-NP at +0.1 V *vs.* Ag/AgCl (red).

In the absence of hydrogen, EBF produced a very similar spectrum to gas phase dosing with an over pressure of argon (Figure 4.23, black) and to the electrochemical conditions in sulphuric acid at +0.1 V (Figure 4.23, red). One minor difference between these SER spectra was that the quantity of CO under electrochemical conditions was much greater than under gas phase conditions. Besides this, both SER spectra were closely similar to the bulk liquid spectrum of the reactant EBF (Figure 4.23, green).

In the presence of surface hydrogen, EBF produced the red and green SER spectra under a gas phase hydrogen atmosphere and in sulphuric acid at -0.33 V, respectively (Figure 4.24). Again, the only notable difference between the SER spectra was the higher quantity of CO in the aqueous solution than compared to the gas phase. When compared with the spectra of neat EBF and EMD, the surface spectral features were better matched with those of EMD. Although the peak at 1690 cm^{-1} was still resolved (assigned to $\nu(C^2=O)$), albeit much reduced in intensity relative to when EBF was adsorbed under argon. The ν(C=C) aromatic peaks around 1587 cm^{-1} appeared broader and stronger in intensity. The shoulder at 983 cm^{-1} was narrower. The aromatic δw(C-H) peaks around 851 cm^{-1} appeared closer together and had merged in the electrochemical SER spectrum. The most prominent feature when hydrogen was present was the emergence of peaks at 1072 and 428 cm^{-1}, the intensities of which were higher in the gas phase than in the liquid phase spectrum.

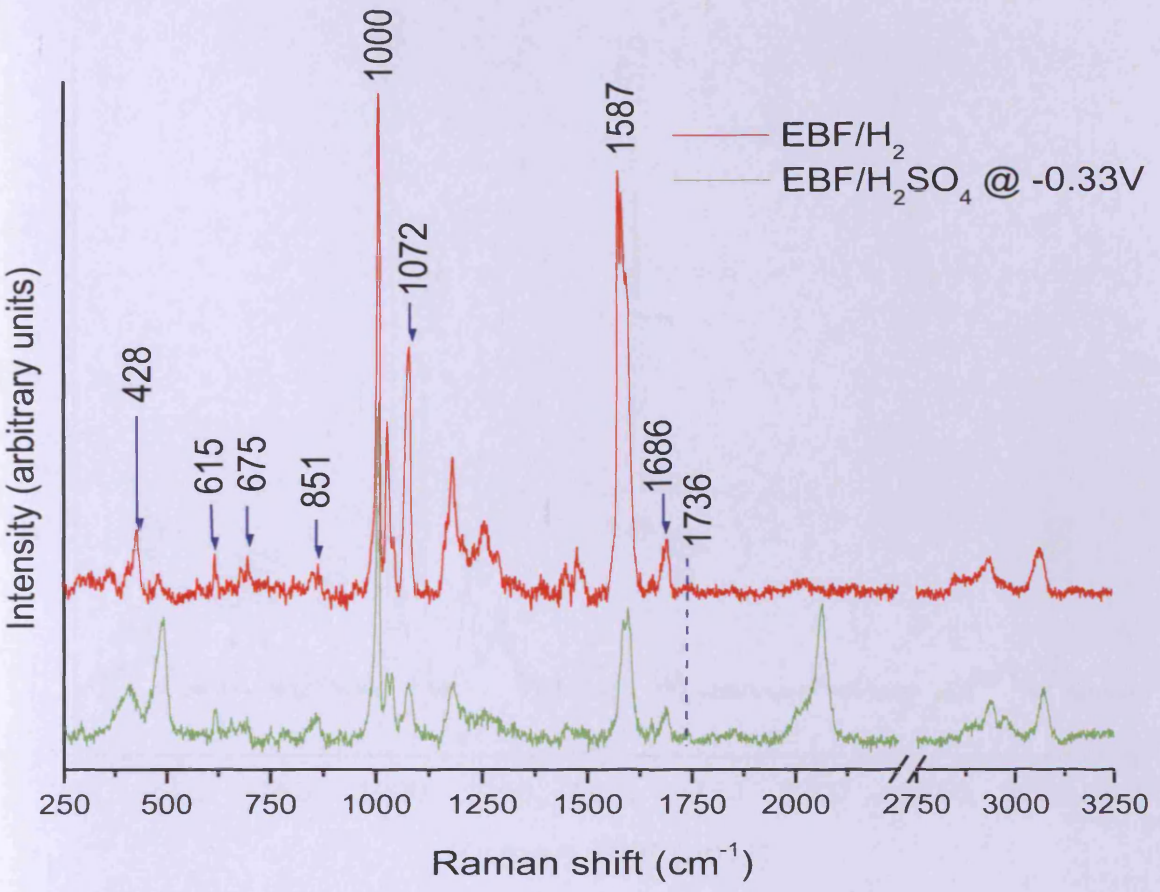

Figure 4.24 SER spectra of EBF on Au@Pt CS-NP in 0.1 M H_2SO_4 (green) and a hydrogen atmosphere (red).

The presence of the peaks at 1686 and 675 cm^{-1} was evidence that EBF was still on the surface under both gas and liquid phase. It was presumed to be from a physisorbed layer condensed from the gas phase and as an organic partition of EBF under the aqueous phase for electrochemical conditions. By subtracting the neat liquid Raman spectrum of EBF from the SER spectrum, the contribution of chemisorbed EBF could be seen more clearly. Figure 4.25 shows the SER spectrum of EBF under hydrogen after subtraction of a Raman spectrum of liquid EBF normalised to the peak at 1686 cm^{-1}.

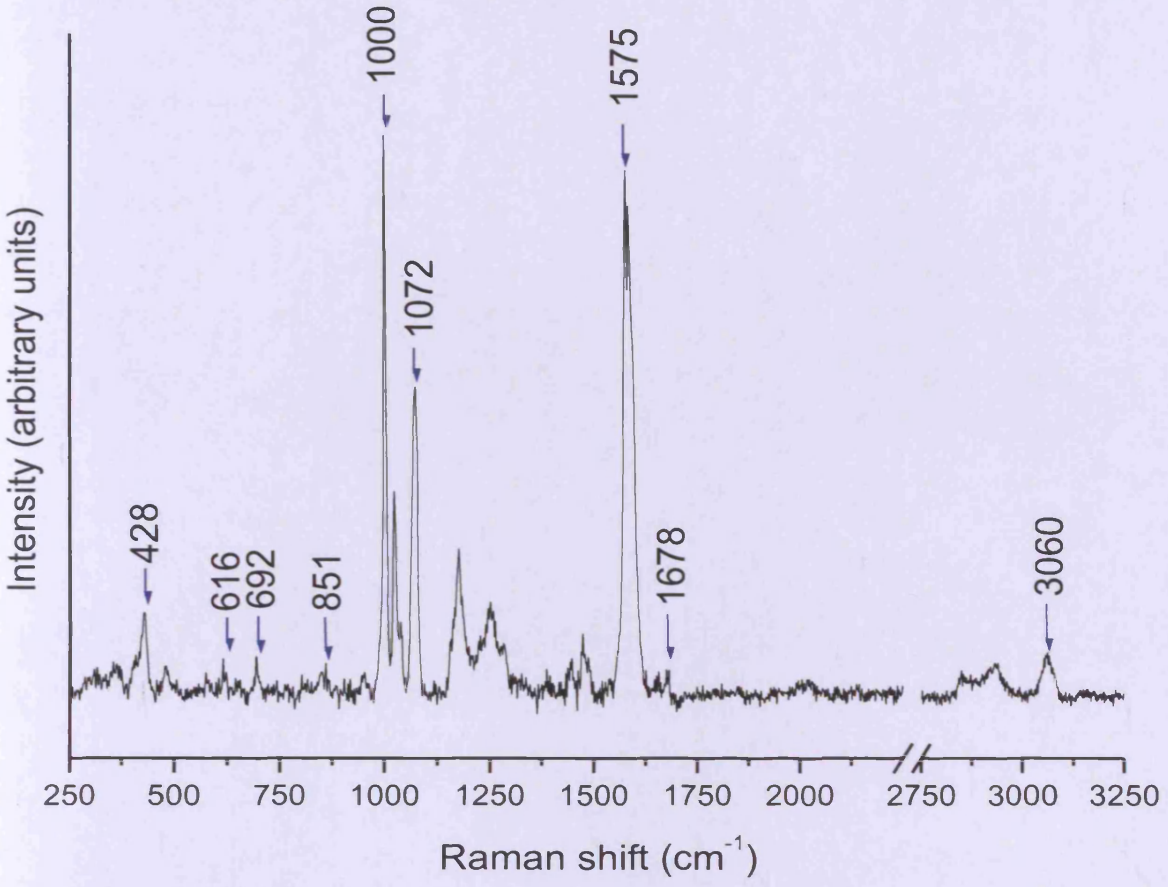

Figure 4.25 SER spectrum of EBF on Au@Pt CS-NP in gas phase hydrogen subtracted by liquid EBF spectrum.

The lower frequency peaks at 851, 692 and 616 cm^{-1} were still resolved (from either an imperfect superposition of the liquid EBF Raman spectrum or originating from contributions of the chemisorbed molecule). It is interesting to note the remaining feature at 1678 cm^{-1}, which could be from a hydrogen-bonded or surface adsorbed carbonyl. Also, the most intense features for the phenyl group were from in-plane vibrations including the peaks at 3060, 1575 and 1000 cm^{-1}, indicating that the plane of the aromatic ring was orthogonal to the plane of the surface. The main features were the two peaks at 1072 and 428cm^{-1} which were reminiscent of the spectral features of the HHS for EP and MP at 1050 and 489 cm^{-1} under these conditions.

The proposal that the product EMD was difficult to remove and was responsible for the relatively slow reaction rate, was tested by introduction of EMD under gas phase hydrogen

conditions and from a saturated solution of sulphuric acid under HER conditions (Figure 4.26). Peaks from the product could be seen, which did add credence to the speculation of slow product desorption relative to EL, but were very low in intensity and became even lower when EMD was removed from the flowing medium. The surprising result was that the peaks at 1070 and 428 cm^{-1} were not resolved. This signified that the SER spectra of EBF with hydrogen was not of the product EMD prior to desorption, but like EP and MP was a half-hydrogenated intermediate state.

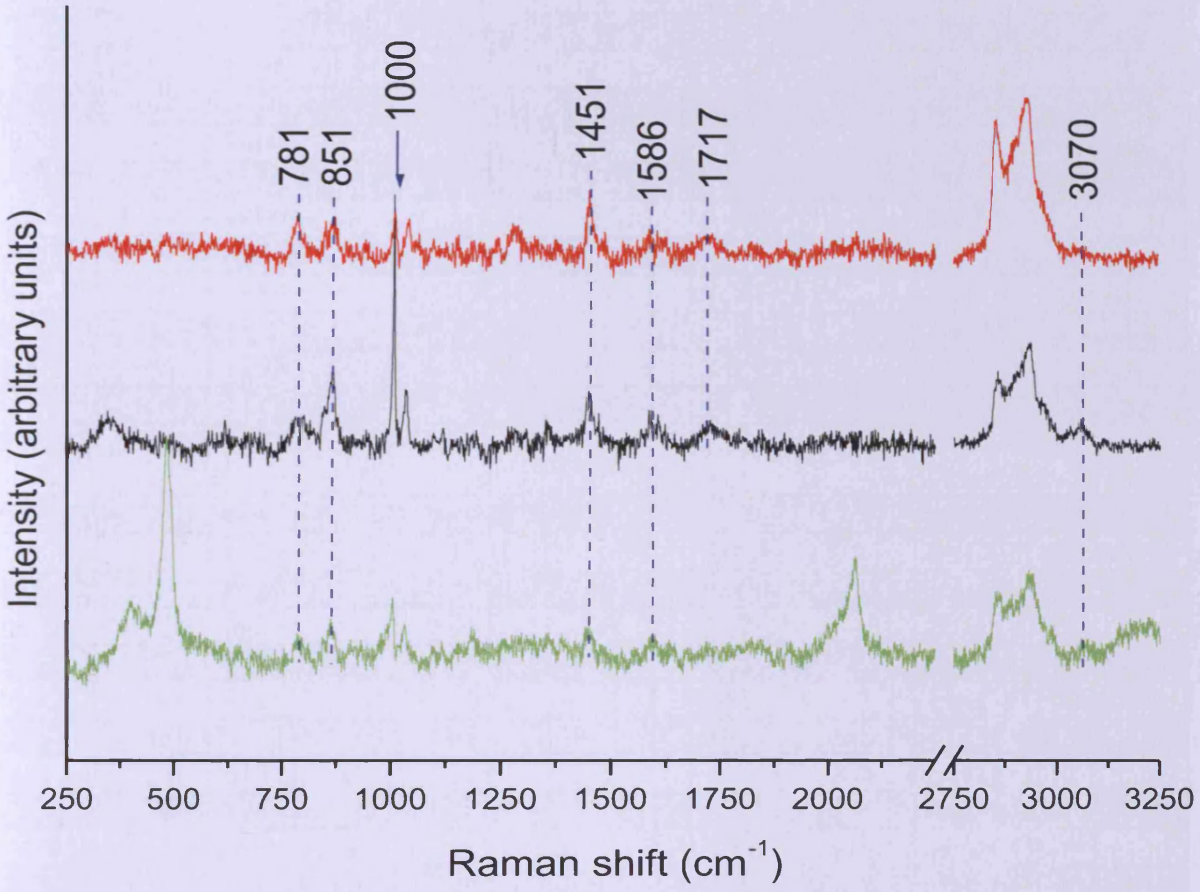

Figure 4.26 SER spectra of EMD/H_2SO_4 on Au@Pt CS-NP at -0.33 V (green), EMD/H_2 on Au@Pt CS-NP (black) and H_2 on Au@Pt CS-NP after EMD (red).

Table 4.11 Band assignments for EBF.

Band Position (cm^{-1})				Assignment
Bulk EBF	**Bulk EMD**	**EBF on Pt / H_2SO_4 @ -0.33 V**	**EBF on Pt / H_2SO_4 @ +0.10 V**	
3073	3065	3073	3073	ν(C-H) aromatic
2975	2975	2975	2975	$\nu a(C^5\text{-}H_3)$
2938	2938	2938	2938	$\nu a(C^4\text{-}H_2)$
2898	2898	2898	2898	$\nu s(C^5\text{-}H_3)$
2876	2876	2876	2876	$\nu s(C^4\text{-}H_2)$
-	-	2064	2071	$\nu(PtC{\equiv}O)$
1736	1736	1736	1736	$\nu(C^1{=}O)$
1687	-	1687	1690	$\nu(C^2{=}O)$
1597	1604	1595	1596	ν(C=C) aromatic
1582	1587	1583	1583	ν(C=C) aromatic
1494	1470	-	1470	$\delta(C^3\text{-}H_2)$
1451	1457	1451	1451	$\delta d(C^5\text{-}H_3)$
1201	1189	1201	1201	δr(C-H) aromatic
1177	1177	1177	1177	ν(C-O-C) *gauche*
1163	1157	1159	1162	ν(C-O-C) *anti*
1111	1111	-	-	$\delta r(C^4\text{-}C^5H_3)$ *anti*
1097	1097	-	-	$\delta r(C^4\text{-}C^5H_3)$ *gauche*
-	1067	1070	-	$\nu(C^2\text{-}C^1)$ / δr(O-H)
1028	1031	1031	1023 + 1036	δr(C-H) aromatic
1000	1000	1000	1000	ν(ring)
972	992	983	972	$\delta r(OC\text{-}C'H_3)$
863	867		863	δw(C-H) aromatic
840	851	859	841	δw(C-H) aromatic
675	-	-	675	$\delta w(C^2{=}O)$
616	619	617	617	$\delta w(C^1{=}O)$
-	511	-	-	$\delta r(C^2\text{-}OH)$
-	-	491	485	ν(Pt-CO)
-	-	428		$\nu(Pt\text{-}C^2)$

4.2.6.2 Ethyl Benzoylformate on Au@Pd Core-shell Nanoparticles

Stereo-inversion of EP on palladium was thought to be due to the preferential existence of EP in the enolic form on the surface [26]. Being a non-enolisable species, EBF should not undergo stereo-inversion on palladium, unless the stereo-inversion is associated with the modifier, but this reaction has yet to be reported in the literature. Therefore, a non-enolisable molecule like EBF, should adsorb in the same geometry on palladium as on platinum.

Substantial decarbonylation occurred with EBF on platinum when an aqueous solvent was used and masked the resolution of the peak at 428 cm^{-1}. The experiment was repeated on palladium using gas phase dosing and the resulting spectra are reported in Figure 4.27.

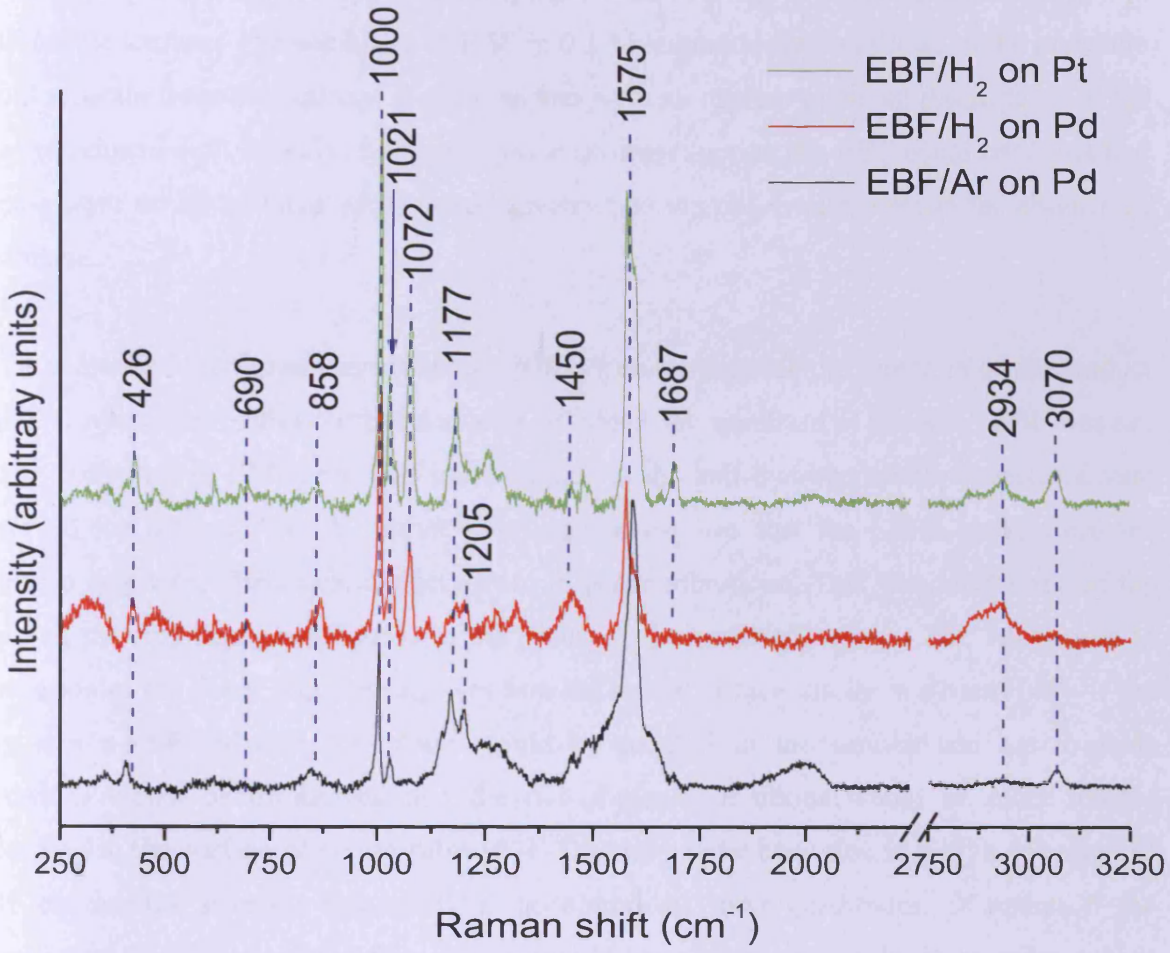

Figure 4.27 SER spectra of gas phase EBF on Au@Pd CS-NP in argon (black) and hydrogen (red) atmospheres compared to EBF on Au@Pt CS-NP in hydrogen (green).

Under argon, there was significant broadening of the bands around 1575 and 1250 cm^{-1} and this is likely to be due to multiple adsorption modes. When hydrogen was introduced, apart from a few minor differences such as the weak intensity of the peak at 1687 cm^{-1} and stronger intensity of the 858 cm^{-1} peak, the spectra on palladium were very similar to those on platinum and hence, EBF was assumed to adopt the same adsorption geometry under these conditions.

4.2.6.3 Discussion of the SERS Experiments with Ethyl Benzoylformate on Core-shell Nanoparticles

In the absence of hydrogen on platinum, the SER spectra of EBF matched that of the Raman spectrum of the neat liquid. This was symptomatic of a weakly interacting adsorbed layer of EBF on the surface. The solubility of EBF in 0.1 M sulphuric acid was low, so the molecule could separate from the aqueous electrolyte and form an organic phase on the surfaces of the electrochemical cell. Equally, in the gas phase dosing experiments, EBF could condense and form a layer on all surfaces which could give rise to the observed spectra in the absence of hydrogen.

In the presence of hydrogen on platinum, EBF began to resemble the spectrum of the product EMD. However, through adsorption studies of EMD, the spectrum of adsorbed EBF was not totally converted to EMD, but was more similar to the half-hydrogenated intermediate state observed for EP and MP. A further point of interest was that the SERS peaks from the aromatic ring were almost exclusively from in-plane vibrations. This was interpreted as the plane of the ring being orthogonal to the plane of the surface (Figure 4.28), which was in opposition to the belief that the ring was bonded to the surface via its' π system [46]. If the ring was π-adsorbed then the plane would be parallel to the surface and the in-plane vibrations would be disallowed and the out-of-plane vibrations would be more intense according to the surface selection rules [47]. This may have been due to a high coverage of EBF causing the aromatic ring to tilt to accommodate more adsorbates. Of course if the phenyl ring of EBF was lying flat, then it should have been open to hydrogenation, which was not reported for this reaction [44]. In addition, very few peaks were seen from the ethyl ester group suggesting that it was either positioned away from the surface (no SERS) or it was lying parallel to the surface. A saponification reaction in the presence of water would remove the ethyl group to form ethanol and would also account for the lack of peaks from this group. However, water was not present under gas phase conditions which produced identical results to the electrochemical conditions. Therefore saponification was not thought to be occurring.

The similarities seen with EBF on platinum and palladium leads to the conclusion that the same adsorption geometry occurs on both metals. This augmented the theory that for stereo-inversion to occur the molecule should be adsorbed in an enolic state [26] and predicts that

non-enolisable reactants will form the same enantiomer on palladium as on platinum, for a given modifier, if the reaction proceeds at all.

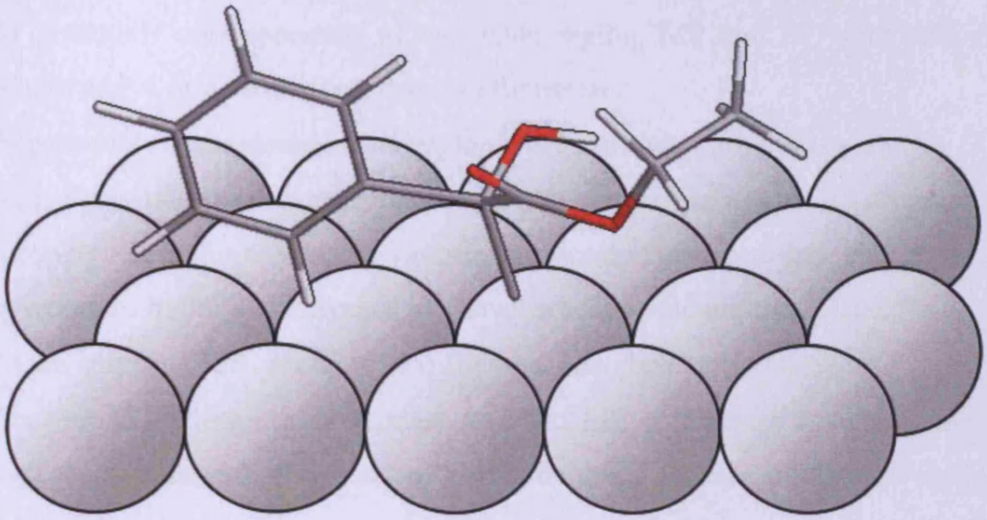

Figure 4.28. Adsorption geometry of EBF on Au@Pt and Au@Pd CS-NP.

4.2.7 Summary of the Vibrational Analyses

SERS of MP and EP on Au@Pt CS-NP under gas phase conditions gave rise to the following features:

- On an oxidised surface, both MP and EP were adsorbed in a carboxylate type configuration, which was later discovered to be PA formed from a saponification reaction involving the loss of an alcohol.
- On a reduced surface, both MP and EP were found to be adsorbed as a half-hydrogenated intermediate state (HHS).
- The absence of a solvent allowed for the reactant to condense from the gas phase and form a physisorbed layer on all surfaces.

SERS of EP on Au@Pd CS-NP under gas phase conditions afforded the following notable features:

- On an oxidised surface, again EP underwent saponification to form PA and was adsorbed in a carboxylate type configuration.
- On a reduced surface, EP was found to be tethered via a di-σ bond from C^2 and C^3 as a result of an *enol* precursory state.

SERS of MP and EP on Au@Pt CS-NP under electrochemical conditions produced the following features:

- At potentials corresponding to the oxide region, MP and EP were both found to adsorb as PA in a carboxylate type configuration.
- At potentials in the double layer region, very little adsorption was seen.
- As the potential was scanned into the H UPD region, an η^1 type adsorption geometry, probably through a keto oxygen-metal bond, was recorded before the surface coverage of hydrogen increased to a level where a reaction took place.
- At the onset of HER, both MP and EP were adsorbed as the HHS.
- Concentration dependency studies revealed that at reactant coverages too high for hydrogen to adsorb, the reactant could undergo a decarbonylation reaction which produced adsorbed CO.
- Deuteration of the HHS resulted in a blue-shift of the peak at 1050 to 1060 cm^{-1}.

SERS of EP on Au@Pd CS-NP under electrochemical conditions may be summarised as follows:

- At potentials corresponding to the oxide region, MP and EP were both found to adsorb as PA in a carboxylate type configuration.
- At the onset of HER, EP was found to adsorb via π-bonding in the enolic form as depicted in Figure 4.17.
- The presence of sub-surface hydrogen in the bulk of the palladium is speculated as preventing the formation of the di-σ configuration seen in the gas phase. The physisorbed layer of EP under gas phase conditions was thought to 'mop-up' the hydrogen and prevent it accessing the bulk of the palladium substrate.

EP and MP on platinum{100} using DFT produced the following insights:

- The calculated frequencies of the HHS vibrational modes were well matched with the experimental frequencies.
- When deuterated, the calculated shifts in frequency of the surface species were different to those seen in the experimental deuteration studies.
- However, deuteration of the free product molecule reproduced the frequency shifts of the HHS both experimentally and theoretically.

SERS of EBF on Au@Pt and Au@Pd CS-NP under hydrogen saturated gas phase and electrochemical HER conditions gave rise to the following observations:

- EBF was adsorbed as a half-hydrogenated state on both platinum and palladium.
- Decarbonylation reactions also led to the formation of adsorbed CO on platinum and appeared to be most apparent when a high EBF coverage was observed.

4.3 Conclusion

4.3.1 Ethyl Pyruvate on Palladium

On an oxidised surface, the majority of EP was found to adsorb in the form of a carboxylate species (Figure 4.11). This carboxylate was demonstrated to be adsorbed PA formed from a saponification reaction of the ethyl group resulting in the loss of ethanol. The introduction of hydrogen removed the carboxylate state. Using the gas phase dosing method, the surface was thought to be saturated by EP on account of condensation. In the presence of hydrogen, the ubiquitous EP would react with all the available hydrogen and prevent hydrogen diffusion into the bulk of the electrode. In the absence of sub-surface hydrogen, EP was found to adsorb in a di-σ configuration via C^2 and C^3 (Figure 4.6). Under electrochemical conditions, the EP coverage was much lower and at HER potentials, hydrogen was electrosorbed into the bulk of the electrode. In the presence of sub-surface hydrogen, EP was found to adsorb via π-bonding (Figure 4.17). Under both conditions, EP was found to adsorb in the *enol* tautomeric form. This was evidence for the observed enantioinversion being a consequence of the stabilisation of the *enol* tautomer [26].

4.3.2 Methyl Pyruvate and Ethyl Pyruvate on Platinum

On an oxidised platinum surface, the same carboxylate spectrum seen on palladium was resolved for both MP and EP and was again assigned to the formation of PA.

The well documented decarbonylation side reaction of the alkyl pyruvate on platinum that results in the formation of adsorbed CO was also found to occur using the techniques described in this chapter. If surface hydrogen was present in sufficient quantities, the hydrogenation reaction to produce the alkyl lactate proceeded at a faster rate than the decarbonylation reaction. Hence, the formation of CO can be maintained at a minimum level

by controlling the concentration of the alkyl pyruvate to ensure that the catalytic surface is not blocked. Therefore the number of active sites for hydrogenation can be maximised and the rate of the hydrogenation reaction would be optimal. At HER potentials, adsorbed EP was found to be removed.

The most significant finding of these experiments was the transformation of MP, EP and EBF into a half-hydrogenated intermediate state on platinum in the presence of hydrogen generated in both gas phase and aqueous liquid phase. Voltammetric tests on EP showed the HHS to be generated at the onset of HER. The coverage of the HHS increased as the potential was scanned more negative corresponding to an increase also in the hydrogen coverage. The key feature of this adsorption pathway would be that the HHS was already chiral. *Therefore, in the absence of a chiral modifier, the HHS would be an intermediate for the racemic reaction.* The mechanism for the racemic reaction is outlined in section 4.2.5.4 and involved the addition of the first hydrogen atom to the keto oxygen to form an alcohol group. Subsequently, the keto/alcohol carbon formed a bond with the surface metal atom to produce the chiral HHS (possibly with the same metal atom as this would be briefly hydrogen deficient and in close proximity to the reactant intermediate). The rate determining step for EL formation was thought to be the addition of the second hydrogen to the metal-carbon bond of the HHS, which would require a free surface site adjacent to the HHS allowing for hydrogen to adsorb. At high HHS surface coverages, intermolecular hydrogen bonding would create islands of the HHS, which would occupy platinum atoms adjacent to most HHS molecules except those on the perimeter of the island. The occupation of an HHS molecule at a platinum atom would prevent the adsorption of hydrogen and hence the completion of the second and final hydrogenation step. It was thought in this situation that the decarbonylation side reaction could occur leading to irreversibly adsorbed CO, which would further block the adsorption of hydrogen. The extent to which the decarbonylation reaction occurred would depend on the lifetime of the HHS. Hence, the decarbonylation reaction was thought to be a secondary effect in blocking catalytic sites. Therefore, the HHS and to a lesser extent CO, would effectively inhibit the hydrogenation reaction if the reactant surface coverage was not carefully controlled. If the mechanism for the enantioselective reaction is the same as the racemic reaction, then chiral induction must occur prior to the formation of the M-C bond of the HHS intermediate.

4.4 References

[1] Y. Orito, S. Imai, S. Niwa, *J. Chem. Soc. Jpn.*, **1979**, 8, 1118.

[2] X. Li, R.P.K. Wells, P.B. Wells, G.J. Hutchings, *J. Catal.*, 221 **(2004)** 653–656.

[3] J.M. Bonello, E.C.H. Sykes, R. Lindsay, F.J. Williams, A.K. Santra, R.M. Lambert, *Surf. Sci.*, 482-485 **(2001)** 207-214.

[4] S. Lavoie, M-A. Laliberte, G. Mahieu, V. Demers-Carpentier, P. McBreen, *J. Am. Chem. Soc.*, **2007**, 129, 11668-11669.

[5] J.M. Bonello, E.C.H. Sykes, R. Lindsay, F.J. Williams, A.K. Santra, R.M Lambert, *J. Phys. Chem. B,* **2000,** 104, 9696-9703.

[6] T. Burgi, F. Atamny, A. Knop-Gericke, M. Havecker, T. Schedel-Niedrig, R. Schlogl, A. Baiker, *Catal. Lett.*, 66 **(2000)** 109-112.

[7] T. Burgi, F. Atamny, R. Schlogl, A. Baiker, *J. Phys. Chem. B,* **2000,** 104, 5953-5960.

[8] S. Lavoie, M-A. Laliberte, P.H. McBreen, *J. Am. Chem. Soc.* **2003**, 125, 15756-15757.

[9] A. Vargas, T. Burgi, A. Baiker, *J. Catal.*, 222 **(2004)** 439–449.

[10] E.L. Jeffery, R.K. Mann, G.J. Hutchings, S.H. Taylor, D.J. Willock, *Catal. Today* 105 **(2005)** 85–92.

[11] Socrates, G. Infrared & Raman Characteristic Group Frequencies. (3rd Edn) John Wiley: Chichester, UK, 2004.

[12] http://www.chem.uni-potsdam.de/

[13] S. Lavoie, M-A. Laliberte, P.H. McBreen, J. Am. Chem. Soc. 2003, 125, 15756-15757.

[14] M. Castonguay, J.-R. Roy, S. Lavoie, M-A. Laliberte′, and P. H. McBreen, J. Phys. Chem. B 2004, 108, 4134-4140.

[15] Y. Mido, H. Shiomi, H. Matsuura, M-A. Raso, M. Victoria Garcia, J. Morcillo, J. Mol. Struct., 176 (1988) 253-277.

[16] S.F. Tayyari, F. Milani-nejad, Spectrochim. Acta Part A, 56 (2000) 2679–2691.

[17] J. Wang, M. Castonguay, J.-R. Roy, E. Zahidi, P. H. McBreen, J. Phys. Chem. B, Vol. 103, No. 21, 1999.

[18] W.J. Ray, J.E. Katon, D.B. Phillips, J. Mol. Struct., 74 (1981) 75-84.

[19] X. Yang, Z.H. He, X.J. Zhou, S.H. Xu, K.T. Leung, App. Surf. Sci. 252 (2006) 3647–3657.

[20] D.J. Jenkins, A.M.S. Alabdulrahman, G.A. Attard, K.G. Griffin, P. Johnston, P.B. Wells, J. Cat*al.*, 234 (2005) 230–239.

[21] M. von Arx, N. Dummer, D. J. Willock, S. H. Taylor, R. P. K. Wells, P. B. Wells, G. J. Hutchings, *Chem. Commun.* , **2003**, 1926–1927.

[22] R. P. K. Wells, N. R. McGuire, X. Li, R. L. Jenkins, P. J. Collier, R. Whyman, G. J. Hutchings, *Phys. Chem. Chem. Phys.*, **2002**, 4, 2839–2845.

[23] D. Ferri, T. Burgi, A Baiker J. Phys. Chem. B, 2004, 108, 14384-14391.

[24] S. C. Dahlberg, G. A. Fisk, R. R. Rye, *J. Catal.*, 36, 2, **1975**, 224-234.

[25] Y. Zhang, M.J. Weaver, *J. Electroanal. Chem.*, 354 (**1993**) 173-188.

[26] T.J. Hall, P. Johnston, W.A.H. Vermeer, S.R. Watson, P.B. Wells, *Stud. Surf. Sci. Catal.*, 101 (**1996**) 221.

[27] S. Zou, M.J. Weaver, *Anal. Chem.*, **1998**, 70, 2387-2395.

[28] J. S. Suh, J. Kim, *J. Raman Spectrosc.*, 29, 143-148 (**1998**).

[29] D. Stacchiola, L. Burkholder, W.T. Tysoe, *Surf. Sci.*, 511 (**2002**) 215–228.

[30] D. Stacchiola, F. Calaza, T. Zheng, Wilfred T. Tysoe, *J. Mol. Cat. A: Chem.*, 228 (**2005**) 35–45.

[31] L. Brandão, D. Fritsch, A.M. Mendes, L.M. Madeira, *Ind. Eng. Chem. Res.*, **2007**, 46 (2), pp 377–384.

[32] G. Attard, M. Aban, R. Taylor, unpublished work.

[33] Z. Ma, F. Zaera, *J. Phys. Chem. B* **2005**, 109, 406-414.

[34] M. Vago, F. J. Williams, E. J. Calvo, *Electrochemistry Communications* 9 (**2007**) 2725–2728.

[35] A. Solladie-Cavallo, F. Hoernel, M. Schmitt, F. Garin, Tetrahedron Lett., 43 (**2002**) 2671–2673.

[36] B.E. Conway, B.V. Tilak, *Electrochimica Acta* 47 (**2002**) 3571.

[37] J.O. Jensen, *Spectrochim. Acta A* 60 (**2004**) 1895–1905.

[38] J.O. Jensen, *Spectrochim. Acta* A 58 (**2002**) 1347.

[39] A. K. Soper, C. J. Benmore, *Phys. Rev. Lett.* **101** (**2008**) 065502.

[40] G. Niaura, *Electrochim. Acta* 45 (**2000**) 3507–3519.

[41] A. Campion, *Ann, Rev. Phys, Chem.* **1985**, 36: 549-72.

[42] E. Rauls, B. Hammer, *Catal. Lett.*, 106, **2006**, 3–4.

[43] M. Sutyinszki, K. Szori, K. Felfoldi, M. Bartok, *Catal. Commun.*, 3 (**2002**) 125–127.

[44] E. Toukoniitty, P. Maki-Arvela, N. Kumar, T. Salmi, D. Yu. Murzin, Catal. Lett., 95, 3–4, 2004.

[45] Y.S. Bobovich, V.V. Perekalin, *J. Struct. Chem.*, 1, 3 (**1961**), 288-293.

[46] Y. Zhao, F. Gao, L. Chen, M. Garland, *J. Catal.*, 221 (**2004**) 274–287.

[47] M. Moskovits, *J. Chem. Phys.*, 77 (**1982**) 9.

Chapter 5
Adsorption of Ethyl Pyruvate on Well Defined Platinum and Palladium Surfaces

5.1 Introduction

The Orito reaction itself is usually conducted on metallic nanoparticles which are intrinsically multi-facetted and hence possess numerous sites onto which the substrates may adsorb and undergo reaction. Catalyst pre-treatment methods such as sintering [1], sonication [2] and use of inert adatoms [3] have been used to promote or eliminate specific surface sites during reaction studies. These results were amongst many reports associated with topographical studies in heterogeneous catalysis [4] and ultimately suggest that there was a specificity to one or more surface sites with a preference for high ee at high co-ordination site such as steps and defects.

Thus far, the studies performed on the adsorption of Ethyl Pyruvate (EP) on platinum and palladium had been on nanoparticulate, polycrystalline surfaces with no clarity concerning site specificity. In this section, the adsorption of EP and the effect of hydrogenation were investigated on platinum single crystal surfaces, palladium films epitaxially grown on platinum single crystals and a platinum catalyst supported on carbon using cyclic voltammetry (CV).

5.2 Results

The experiments began with a cyclic voltammogram of the clean surface. EP was then introduced by immersing the crystal in a volume of distilled EP for a fixed length of time. Excess EP was then removed by immersing the crystal in a volume of ultra-pure water (degassed by nitrogen) before being returned into the electrochemical cell.

The percentage values quoted in parentheses indicate the residual amount of free platinum sites relative to the clean CV i.e. "(33%)" equates to a 67% reduction in the charge of the hydrogen underpotential deposition (H UPD) region. These values were obtained by integrating the area of the H UPD region on the forward scan using the trapezoidal rule integration function in OriginPro® 8 and are summarised in Table 5.12.

5.2.1 Ethyl Pyruvate on Low Miller Index Platinum Surfaces

5.2.1.1 Platinum{100}

Figure 5.1 displays the CVs on platinum{100}, before and after adsorption of EP. The clean CV showed two characteristic peaks at 0.225 and 0.325 V representing {100}×{111} step sites and (1×1) – platinum{100} long range order terrace sites, respectively [5].

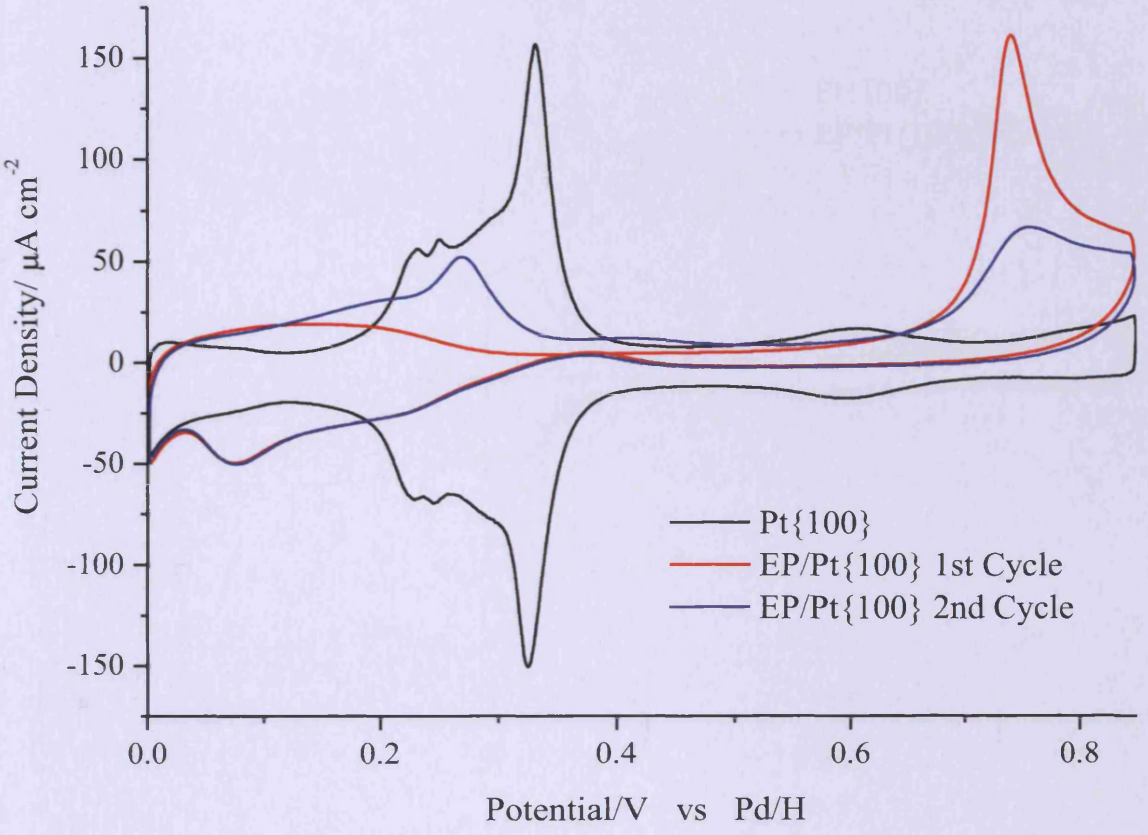

Figure 5.1 CVs of platinum{100} before and after adsorption of EP. Both first and second cycles recorded following adsorption are shown for comparison. Electrolyte = 0.1M H_2SO_4, sweep = 50mV s^{-1}.

After the first exposure to CVs of platinum{100} before and after adsorption of EP. Both first and second cycles recorded following adsorption are shown for comparison. Electrolyte = 0.1M H_2SO_4, sweep = 50mV s^{-1}.EP, several new electrosorption features were observed. The first sweep indicated a large reduction in the current associated with the H UPD region (potential range from 0.0 to 0.35 V) as vacant surface sites became blocked after exposure to EP (33%). This sweep also revealed a large peak at 0.74 V, which could be ascribed to the electrooxidation of CO [6], a known decomposition product of EP on platinum [7]. In the second sweep, some of the H UPD area returned (65%), which also led to a reduction in the

CO peak intensity. In order to establish the potential range in which adsorbed CO was formed, a series of potential window opening experiments were performed. After EP adsorption, a potential sweep from 0 V to 0.85 V was performed to reproduce the CO electrooxidation peak. The potential was then swept from the upper potential to increasingly more negative potentials followed by sweeping positive again to observe whether or not adsorbed CO had formed (Figure 5.2).

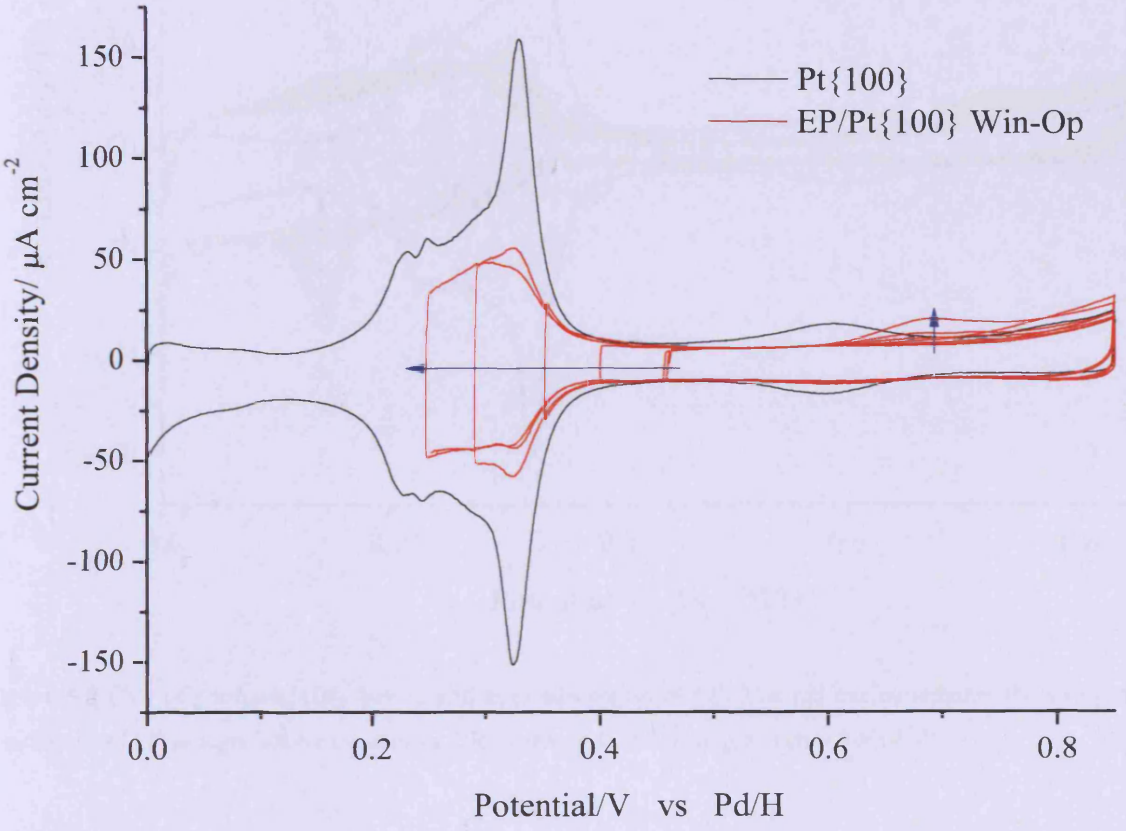

Figure 5.2 CVs of platinum{100} before and after adsorption of EP. The red cycles indicate a window opening experiment (Win-Op) in the direction of the horizontal arrow. Electrolyte = 0.1M H_2SO_4, sweep = 50mV s^{-1}.

It was found that so long as the negative-going potential sweep did not reach in to the H UPD region, no CO electrooxidation would be observed on the subsequent positive sweep. However, when the potential was swept into the H UPD region and subsequently swept towards positive potentials, a CO electrooxidation peak would be observed.

Figure 5.3 shows the CV of platinum{100} obtained without rinsing off excess EP with water.

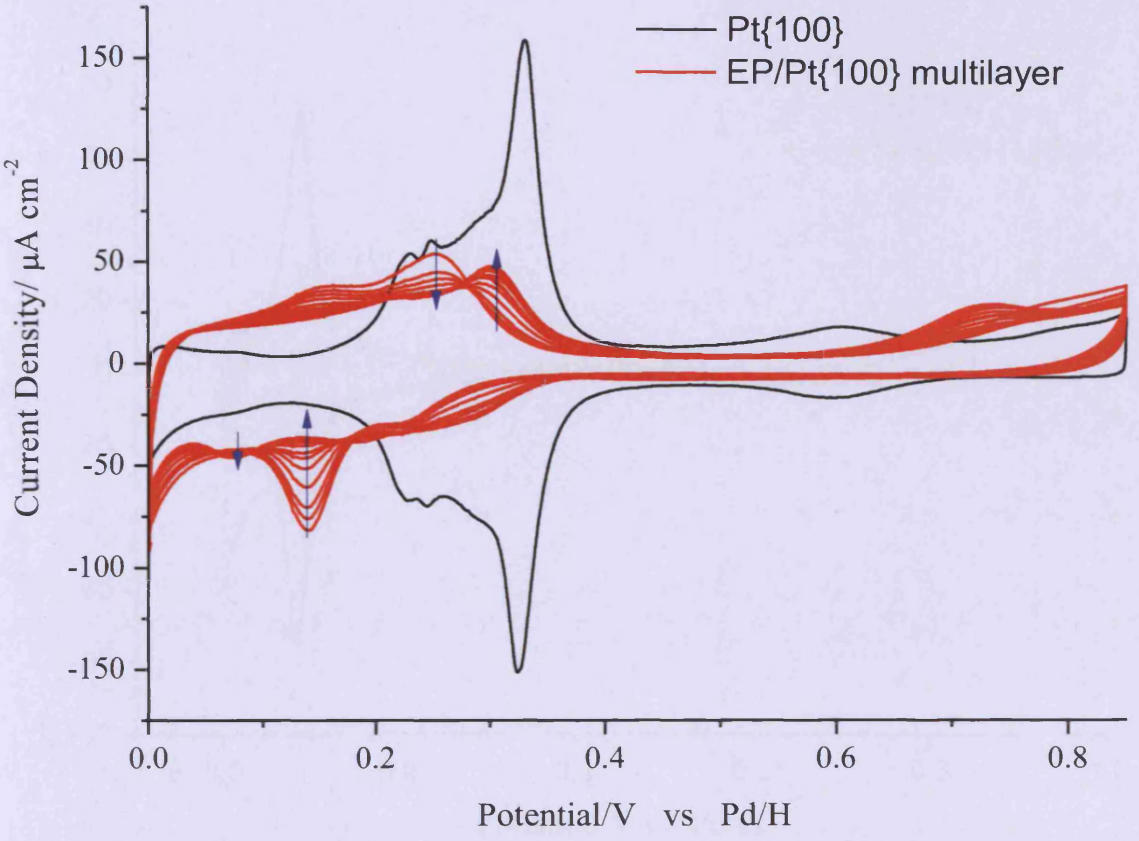

Figure 5.3 CVs of platinum{100} before and after adsorption of EP. The red cycles indicate the stripping of multilayers of EP as signified by the arrows. Electrolyte = 0.1M H_2SO_4, sweep = 50mV s^{-1}.

In Figure 5.3, the first positive going sweep from 0 V gave rise in this instance to a large voltammetric peak at 0.25 V which was ascribed to the electrochemical stripping of EP multilayers from the surface. After repetitive potential cycles, both this peak and its' related adsorption peaks at 0.14 V and 0.07 V were seen to decrease in magnitude. The peak at most negative potentials on the negative going sweep (0.07 V) only emerged after all of the 0.14 V and 0.25 V peak intensities have been dissipated (presumably due to diffusion of excess EP away from the stationary electrode surface into the electrolyte).

5.2.1.2 Platinum{110}

The CVs in Figure 5.4 are of platinum{110} before and after five seconds of exposure to EP.

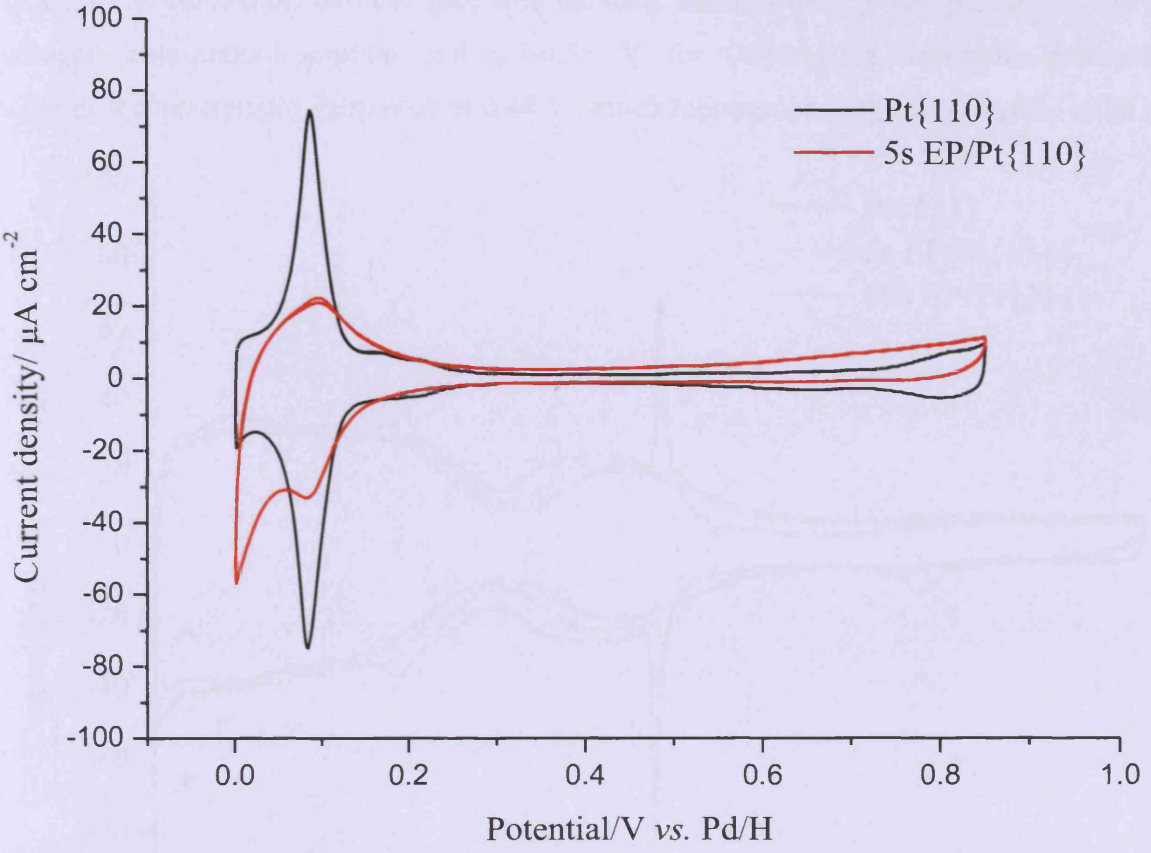

Figure 5.4 CVs of platinum{110} before and after adsorption of EP. Electrolyte = 0.1M H_2SO_4, sweep rate = 50mV s^{-1}.

The intense peak observed in the clean CV at 0.086 V resulting from H UPD on platinum{110} terraces was attenuated markedly after the surface became blocked by EP (61%). Only a very weak, broad signal arising from the electrooxidation of CO could be observed from the EP/platinum{110} CV. Hence, in contrast to the data shown in Figure 5.1, platinum{110} appeared to exhibit a much lower propensity towards decarbonylation of adsorbed EP in comparison with platinum{100}. However, similarly to what was found for platinum{100}, incomplete blocking of all H UPD sites by EP was observed with approximately 39% of these sites being occupied by adsorbed EP. The onset of a significant reduction current at potentials more negative than 0.05 V when EP was adsorbed was ascribed to hydrogenation of adsorbed EP.

5.2.1.3 Platinum{111}

The CVs displayed in Figure 5.5, show the effect of adsorbed EP on platinum{111}. The black CV represented the clean surface with the main features having emerged at 0-0.3 V for hydrogen adsorption/desorption and 0.3-0.55 V for (bi)sulphate adsorption/desorption including a characteristic sharp peak at 0.44 V, which represented long range surface order.

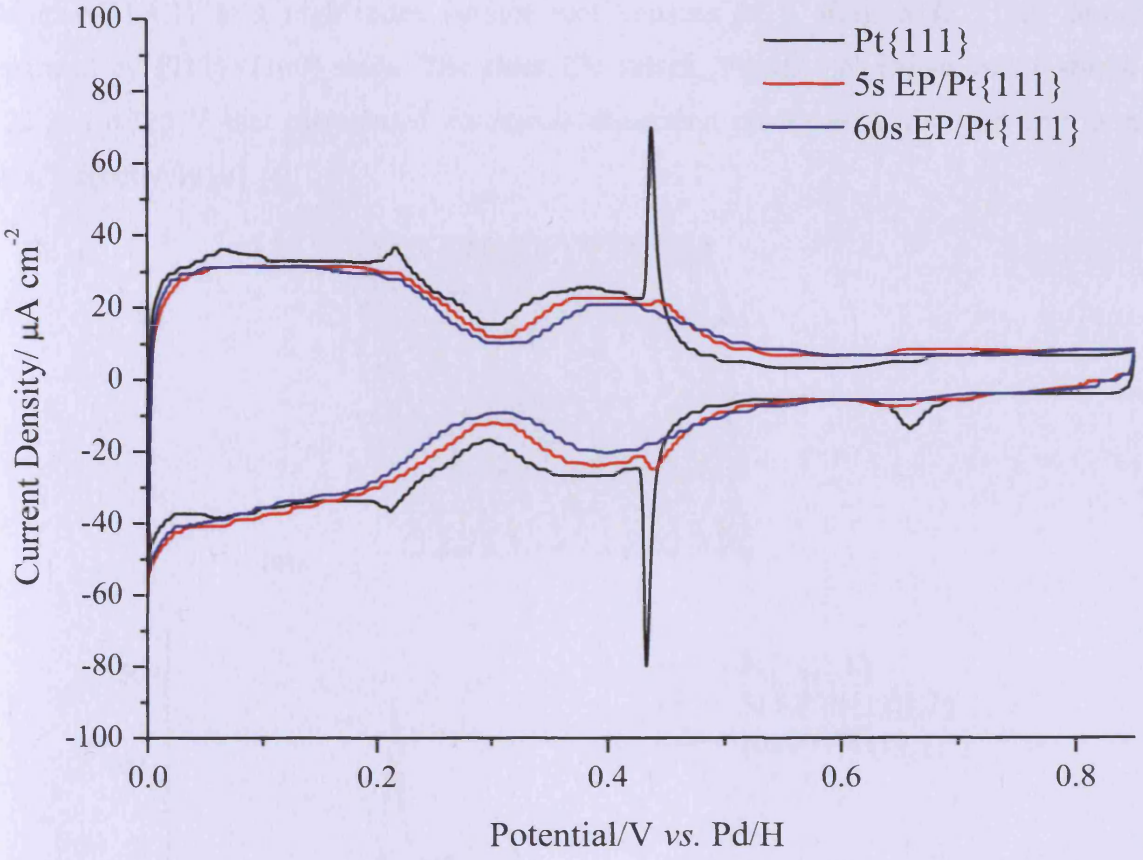

Figure 5.5 CVs of platinum{111} before and after adsorption of EP. Legend indicates the length of time EP was allowed to adsorb onto the electrode surface. Electrolyte = 0.1M H_2SO_4, sweep = 50mV s^{-1}.

The CV taken after EP exposure for five seconds showed a small reduction in the H UPD current (90%) with a further similar decrease after sixty seconds. The sharp spike characteristic of well-ordered platinum{111} electrodes in sulphuric acid at 0.44V was heavily attenuated in both of the EP dosed CVs. In contrast to Figure 5.1 however, CV indicated that even after sixty seconds of exposure to EP, only a small proportion of the platinum{111} surface became blocked by EP (86%). It was evident that the majority of the {111} surface remained free of adsorbed EP. Furthermore, no oxidation or reduction peaks corresponding to EP decomposition products were observed.

5.2.2 Ethyl Pyruvate on High Miller Index Platinum Surfaces

The possibility of site selective adsorption by EP was explored further using stepped platinum electrodes.

5.2.2.1 Platinum{11,1,1}

Platinum{11,1,1} is a high index surface that consists of 6 atom wide {100} terraces separated by {111}×{100} steps. The clean CV (black, Figure 5.6) shows two features at 0.22 and 0.325 V that represented adsorption/desorption processes at the step and terrace sites, respectively [8].

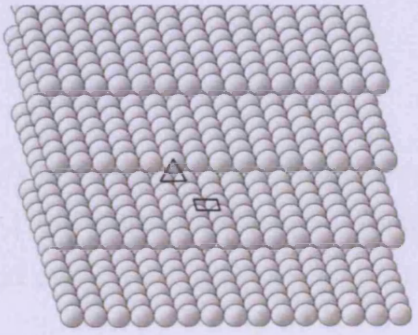

(a)

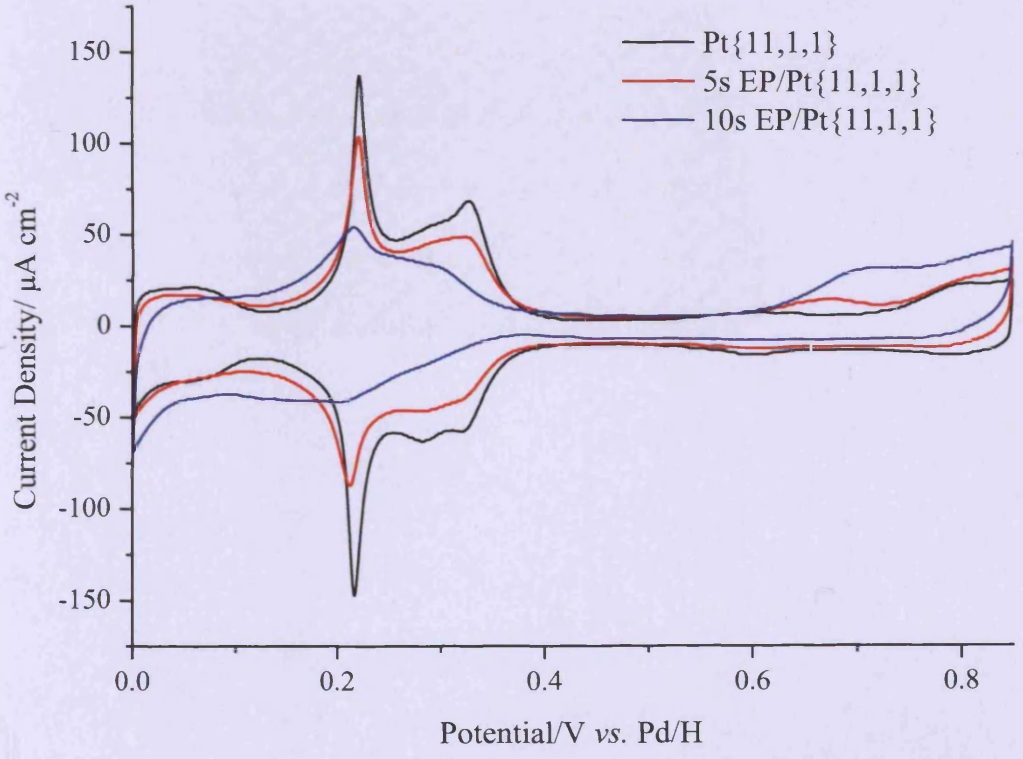

(b)

Figure 5.6 (a) An fcc {11,1,1} surface. (b) Cyclic voltammograms of platinum{11,1,1} before and after adsorption of EP. Electrolyte = 0.1M H_2SO_4, sweep = 50mV s^{-1}.

The sweep after five seconds of EP exposure revealed a significant attenuation in both the 0.33 and 0.22 V peaks (89%). After ten seconds exposure, there was a further decrease in the current to both features with almost complete blockage of the {100} terraces, whereas some of the {100} × {111} step sites remained vacant (74%). As the {100} terraces on the platinum{11,1,1} surface became increasingly filled with EP (from 5s – 10s exposure time) there was a corresponding increase in the magnitude of the signal between 0.60-0.75V caused by the electrooxidation of decarbonylation products formed at the platinum{100} terrace sites (Figure 5.1). The size of the CO electrooxidation peak was significantly decreased in relation to that observed in Figure 5.1, which was ascribed to a reduction in the surface density of platinum{100} terrace sites in stepped platinum{11,1,1} relative to platinum{100}.

5.2.2.2 Platinum{533}

Platinum{533} is another stepped surface, but this time consisting of 4 atom wide {111} terraces separated by {111}×{100} steps. The clean CV (black, Figure 5.7) shows features at 0.215 and 0.5 V of the step site and terrace processes, respectively.

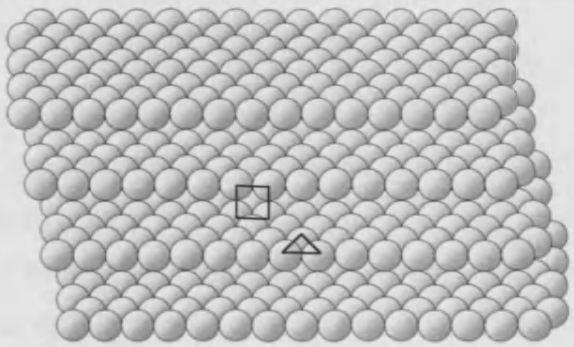

(a)

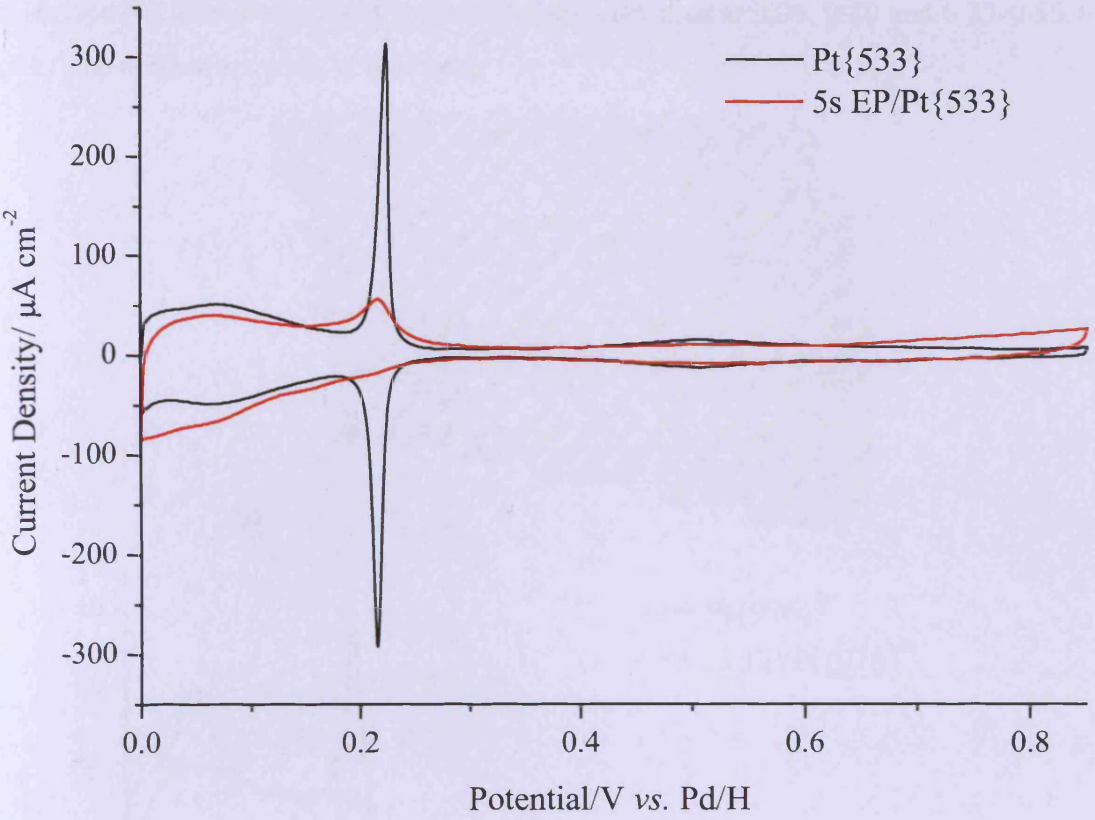

(b)

Figure 5.7 (a) An fcc {533} surface. (b) Cyclic voltammograms of platinum{533} before and after adsorption of EP. Electrolyte = 0.1M H_2SO_4, sweep = 50mV s^{-1}.

From five seconds exposure to EP, the step site at 0.22 V had decreased substantially in current density (although some free sites remained (71%)) whereas the weak terrace signal between 0.45-0.55 V remained unchanged. The attenuation of the signal at 0.22 V was caused by selective blocking of step sites by EP and the absence of a change in the signal between 0.45-0.55 V suggested that the {111} terraces remained largely unoccupied. In addition, the absence of platinum{100} terraces appeared to afford negligible adsorbed CO as signified by the presence of only a weak, broad electrooxidation feature at 0.7 V.

5.2.2.3 Platinum{976}^{R}

Platinum{976}^{R} is a chiral surface with a 6 atom wide {111} terrace with a 3 atom long {100} and 1 atom deep {110} right handed kink (Figure 5.8a). The chirality is determined by the density of atoms of the respective surfaces and their arrangement in space. In this case the surface atomic density at the kink site increases in a clockwise fashion giving a right handed

chiral surface [9]. The clean CV (Figure 5.8) shows features at 0.06, 0.20 and 0.33-0.55 V of the kink, step and terrace sites, respectively.

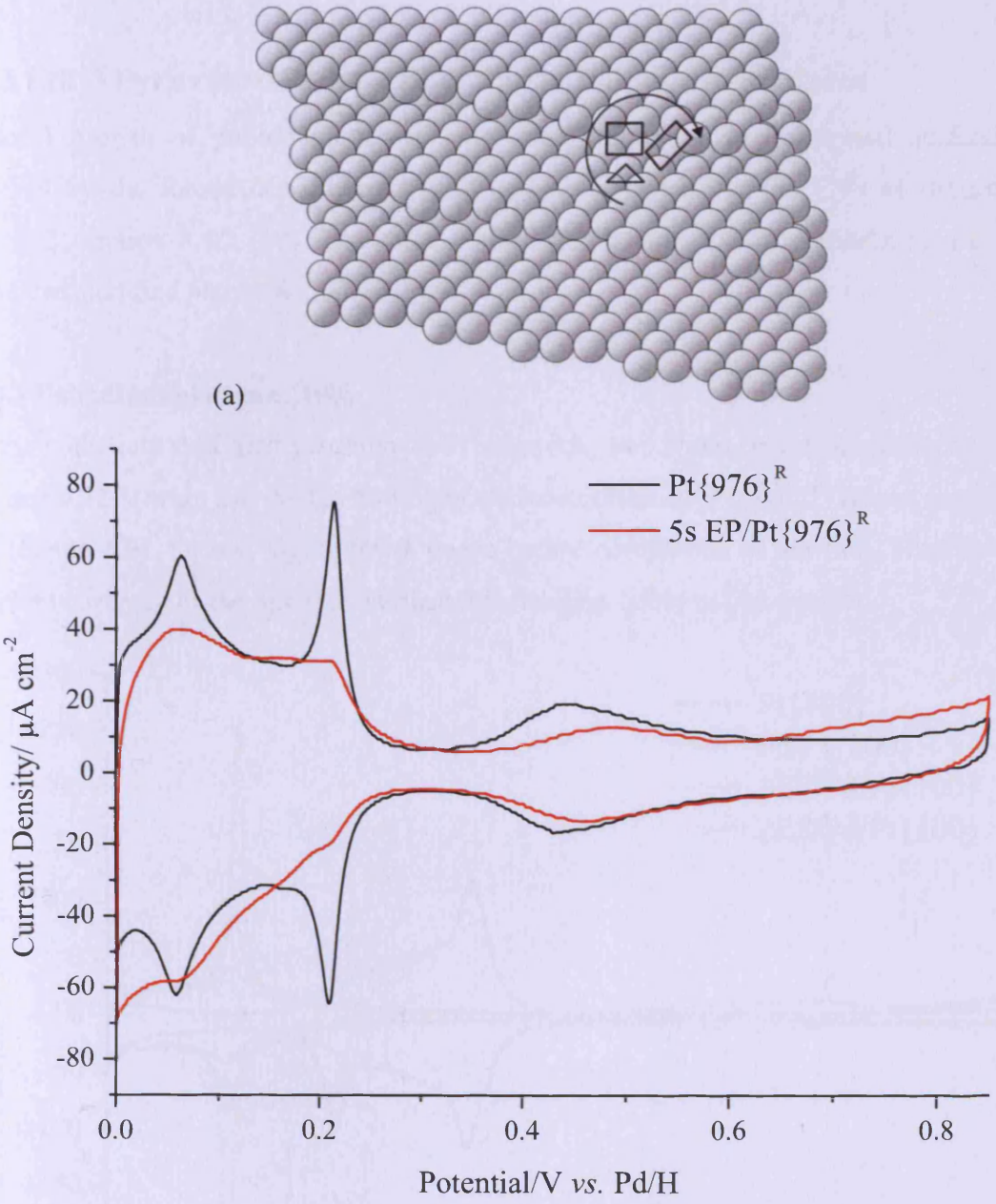

Figure 5.8 (a) An fcc $\{976\}^R$ surface. Cyclic voltammograms of platinum$\{976\}^R$ before and after adsorption of EP. Electrolyte = 0.1M H_2SO_4, sweep = 50mV s^{-1}.

A large decrease in the current signal from the kink and step site features was observed after initial EP exposure as these sites became blocked (71%). Only a slight decrease in the current signal from the {111} terraces showed that these sites were only partially occupied by EP. In fact after stripping of the small amount of adsorbed CO formed on the positive going sweep, the reverse sweep indicated an increase in charge in the platinum{111} terrace anion peak.

Hence the small amount of blocking observed initially for {111} terrace sites may be ascribed almost entirely to adsorbed CO, not EP.

5.2.3 Ethyl Pyruvate on Low Miller Index Palladium Surfaces

Epitaxial growth of palladium adlayers on basal platinum single crystal surfaces was achieved by the forced deposition method and characterised in the CVs as described in chapter 3, section 3.4.2 [10]. The same method for dosing EP on platinum was used for palladium modified platinum {*hkl*}.

5.2.3.1 Palladium/platinum{100}

For the palladium modified platinum{100} electrode, two sharp reversible peaks centred at 0.12 and 0.22 V were ascribed to hydrogen electrosorption on 1st and 2nd layers, respectively [11] (Figure 5.9). Second layer growth began before completion of the first. Thus to ensure complete coverage of the platinum surface this situation could not be avoided.

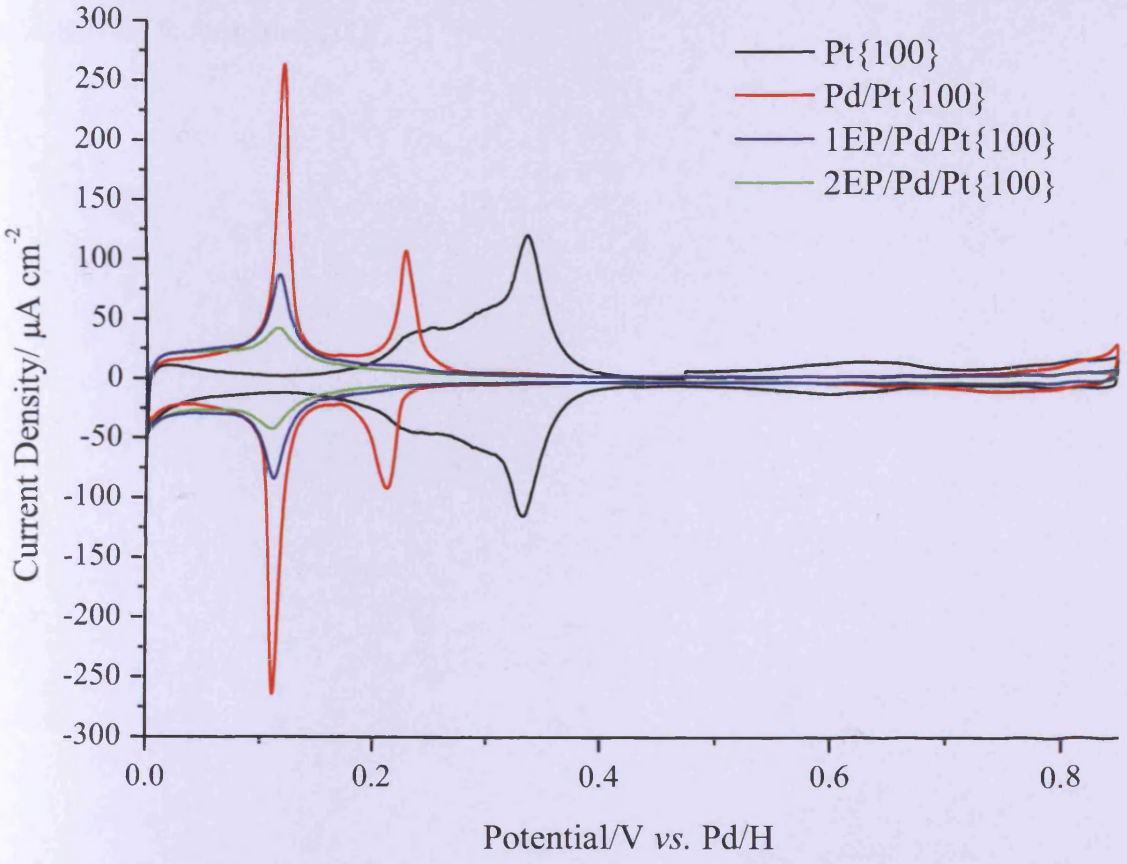

Figure 5.9 CVs of epitaxial palladium adlayers supported on platinum{100} recorded before and after adsorption of EP. Electrolyte = 0.1M H_2SO_4, sweep = 50mV s^{-1}.

The CV after the first EP exposure (blue CV) resulted in a significant reduction in the H UPD current as the palladium{100} surface became heavily blocked with EP (61%). In particular, the second layer palladium sites were heavily attenuated, whereas those sites corresponding to the first palladium adlayer were less affected. Further reduction in the first layer features was seen after the second exposure of EP (green CV) (45%) as more vacant sites in the first palladium monolayer became occupied, leading to 55% coverage. In contrast to Figure 5.1, signals resulting from the oxidation of CO and/or other EP decomposition products were not observed in the palladium/platinum{100} CV though EP was clearly present on the surface. The absence of this signal suggested that EP does not undergo decarbonylation/degradation on palladium{100} (as it does on platinum{100}). This indicated that the decarbonylation reaction of EP was both structure sensitive and metal sensitive.

5.2.3.2 Palladium/platinum{110}

For palladium/platinum{110}, a broad peak was seen between 0.02-0.3 V which corresponded to H UPD on multilayer palladium along with a signal at 0.79 V indicative of palladium oxide formation [11].

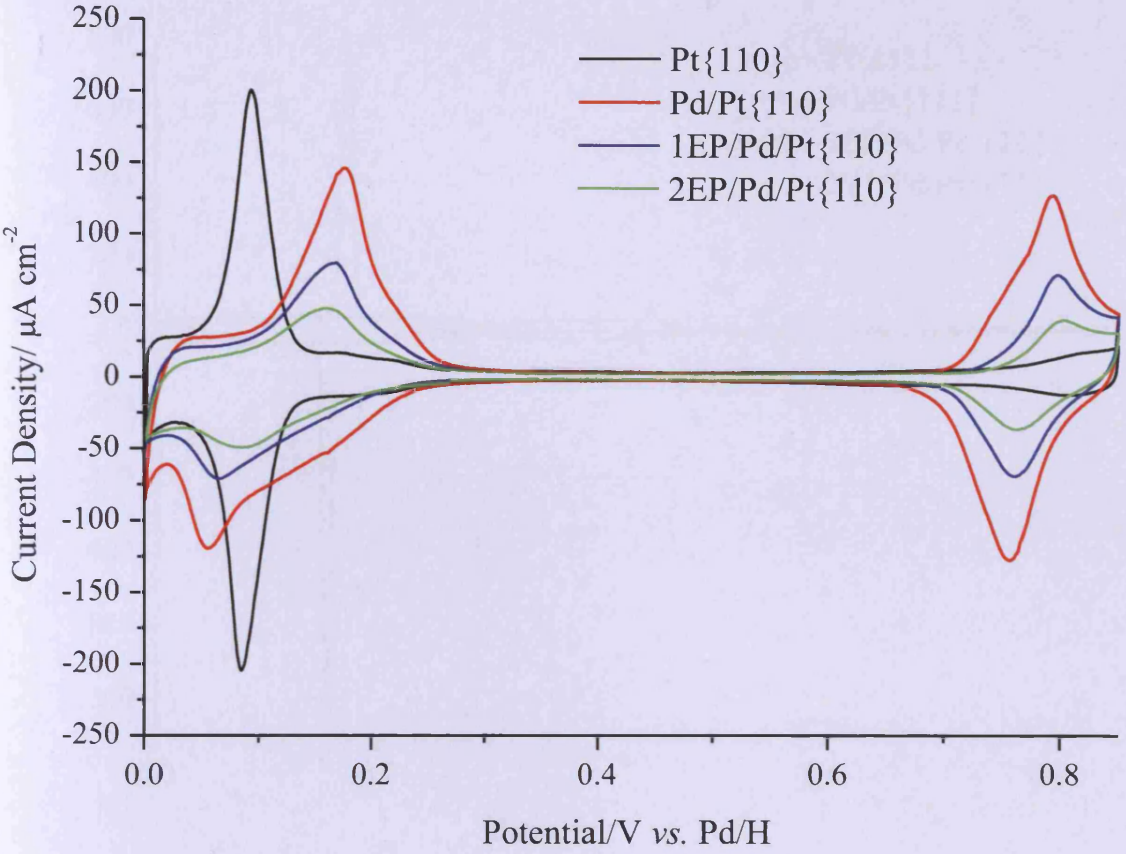

Figure 5.10 CVs of epitaxial palladium adlayers supported on platinum {110} recorded before and after adsorption of EP. Electrolyte = 0.1M H_2SO_4, sweep = 50mV s^{-1}.

Similar to palladium/platinum{100}, the voltammetric features decreased in intensity with increasing EP coverage to a maximum coverage of 60% after the second exposure (Figure 5.10). In addition, no evidence of EP decomposition to form adsorbed CO on palladium could be observed using CV.

5.2.3.3 Palladium/platinum{111}

Palladium/platinum{111} exhibited two hydrogen electrosorption features centred at approximately 0.16 and 0.2 V, which corresponded with 1st and 2nd layer palladium [11] (Figure 5.11).

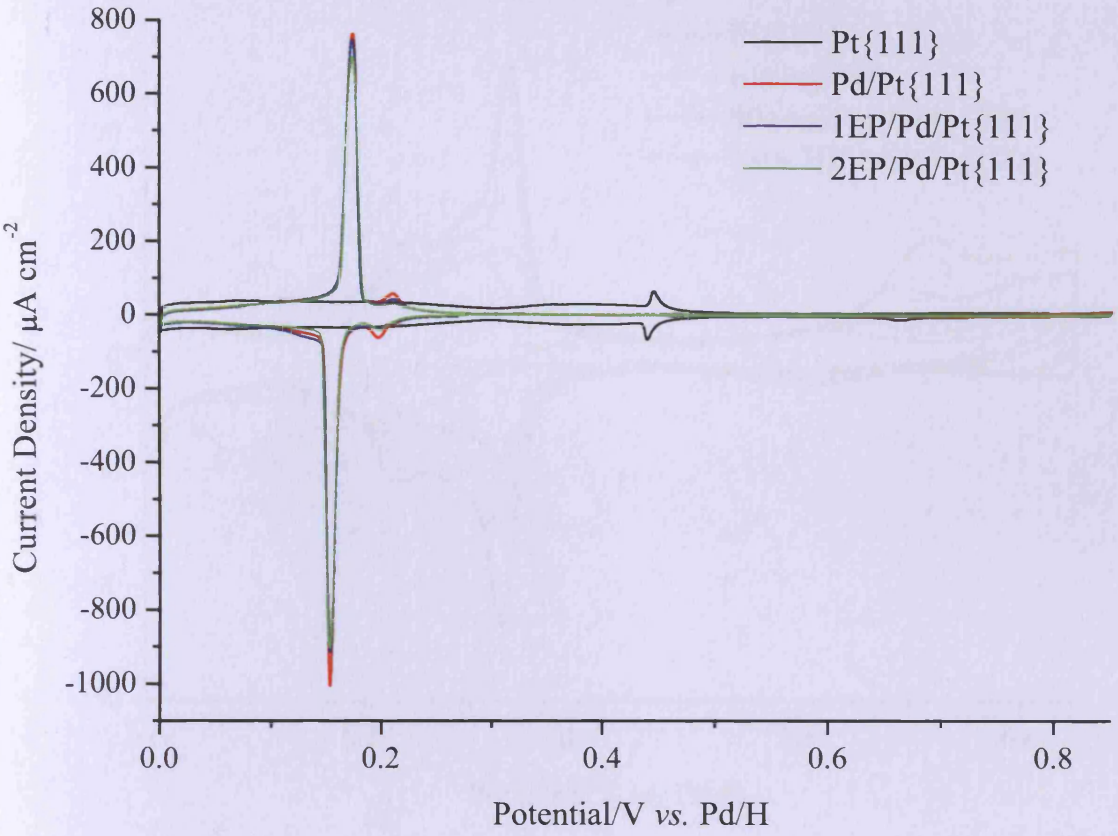

Figure 5.11 CVs of epitaxial palladium adlayers supported platinum {111} recorded before and after adsorption of EP. Electrolyte = 0.1M H_2SO_4, sweep = 50mV s^{-1}.

By comparison of the green and blue with the red voltammogram(s) in Figure 5.11, very little attenuation of the voltammetric features was observed even after the second dose of EP (96%).

5.2.4 Hydrogen Induced Ethyl Pyruvate Desorption

In this section, the stability of adsorbed EP on platinum was studied in the presence of hydrogen generated by holding the working electrode potential in the hydrogen evolution region (HER (-0.1 V *vs.* Pd/H)) for various lengths of time.

5.2.4.1 Platinum{100}

Figure 5.12 illustrates the clean platinum{100} surface (black), the surface after EP adsorption (red) and the effect of evolving hydrogen for increasing lengths of time (blue and green, respectively).

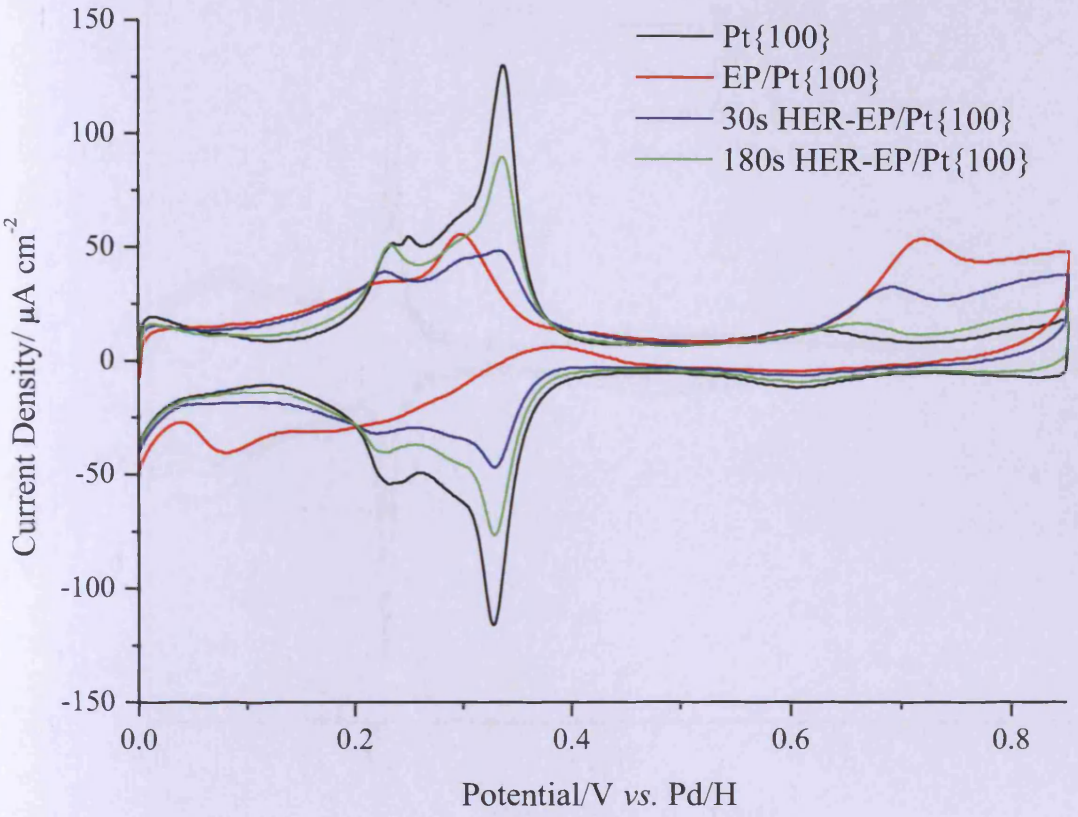

Figure 5.12 CVs showing the change in EP coverage on platinum{100} after holding the potential at -0.1V (Pd/H) for different lengths of time. Electrolyte = 0.1M H_2SO_4, sweep = 50mV s^{-1}.

As a result of hydrogenation, the profile of the CV was noted to return towards that of the clean surface with the recovery of the hydrogen anion adsorption/desorption peaks at 0.1-0.38 V. Also, the irreversible peak at 0.7 V on the positive scan and the oxidation peak at 0.39 V on the negative scan were seen to return to the clean profile including a shift of the peak at 0.7 V to a more negative potential, which was evidence for desorption of CO to a lower coverage [12].

5.2.4.2 Platinum{755}

Platinum{755} consisted of 6 atom wide {111} terraces separated by {100}×{111} step sites. It was the step site feature in the CV (0.21 V) that was shown to decrease the most with EP adsorption, relative to the {111} terrace peak (Figure 5.13, 0.3-0.5 V). The {111} terrace peak was also seen to shift to more positive potentials.

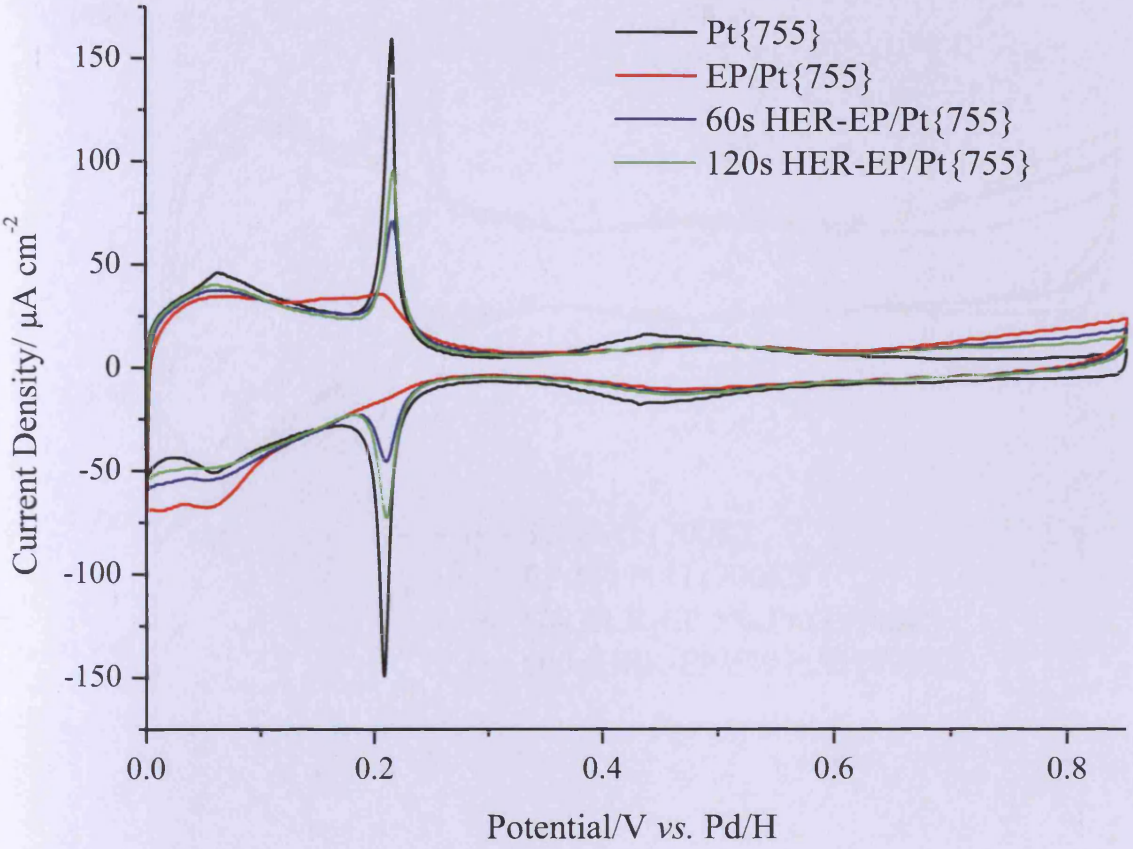

Figure 5.13 CVs showing the change in EP coverage on platinum{755} after holding the potential at -0.1V (Pd/H) for different lengths of time. Electrolyte = 0.1M H_2SO_4, sweep = 50mV s^{-1}.

Upon hydrogenation, the step site area recovered on successive periods at hydrogen evolution, but the terrace sites appeared largely unperturbed although there was a subtle shift to more negative potentials associated with "larger" {111} terraces free of EP.

5.2.4.3 Platinum/Graphite Catalyst

Platinum nanoparticles supported on graphite possessed all three platinum basal planes (and defects). The peaks in the CV at 0.1 V and 0.24 V (positive scan) corresponded to {110} and {100}×{111} step sites respectively and were seen to decrease upon EP adsorption (Figure 5.14).

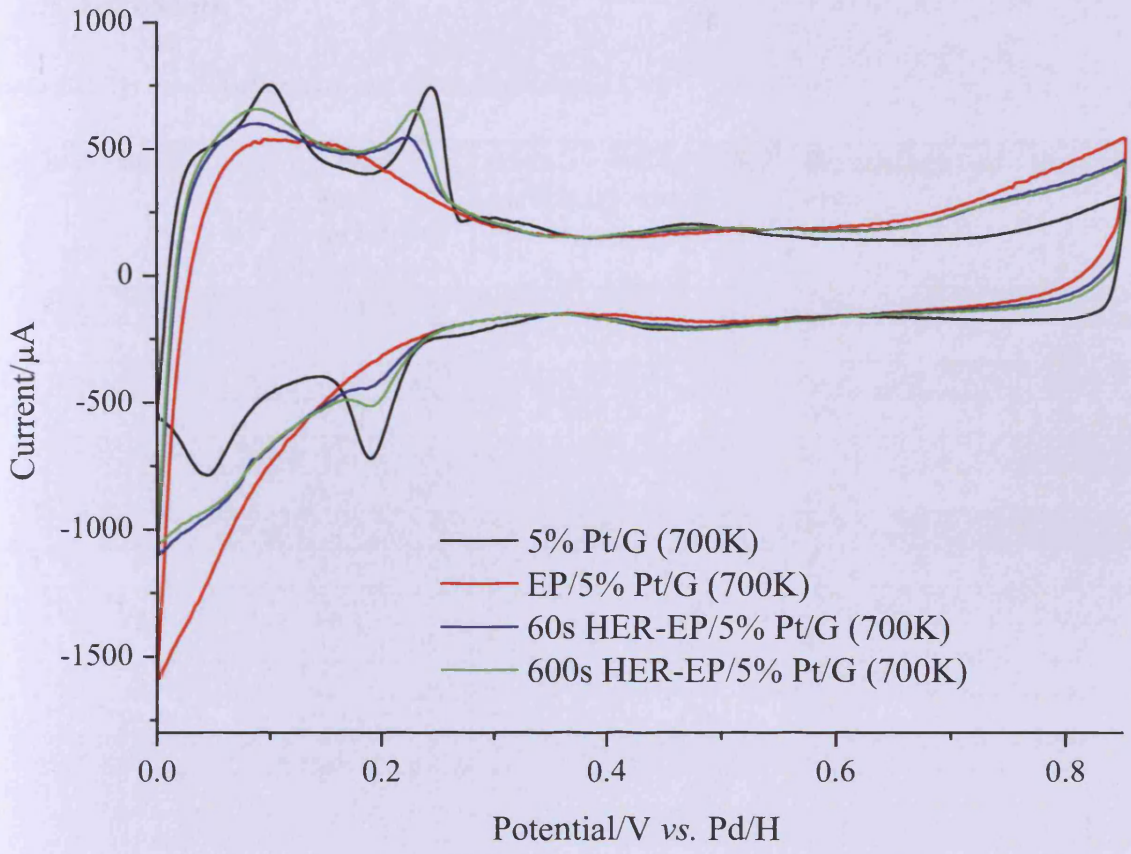

Figure 5.14 CVs showing the change in EP coverage on 5% platinum/graphite catalyst after holding the potential at -0.1V (Pd/H) for different lengths of time. Electrolyte = 0.1M H_2SO_4, sweep = 50mV s^{-1}.

The step site peaks were seen to begin recovery to the formerly clean state after hydrogenation, but the recovery was not complete. The {111} terrace peak (0.3-0.59 V) was again shifted to a more negative potential after hydrogention, but remained largely unperturbed throughout the experiment. In accordance with previous figures this was attributed to the selective blocking of {110} and {100} surface sites whilst {111} sites remained largely unoccupied.

5.2.5 Discussion

Table 5.12 The relative changes in area of the single crystal CVs.

Single crystal	Clean area (arbitrary units)	Area with EP (arbitrary units)	Percentage of the clean area
Pt{100}	1.43×10^{-5}	4.77×10^{-6} (1st cycle)	33%
		9.42×10^{-6} (2nd cycle)	65%
Pt{110}	1.12×10^{-5}	6.79×10^{-6}	61%
Pt{111}	1.33×10^{-5}	1.2×10^{-5} (5s)	90%
		1.14×10^{-5} (60s)	86%
Pt{11,1,1}	1.31×10^{-5}	1.17×10^{-5} (5s)	89%
		9.69×10^{-6} (60s)	74%
Pt{533}	1.19×10^{-5}	8.54×10^{-6} (5s)	71%
Pt{976}^{R}	8.96×10^{-6}	6.45×10^{-6} (5s)	71%
Pd/Pt{100}	1.09×10^{-5}	6.64×10^{-6} (1st dip)	61%
		5×10^{-6} (2nd dip)	45%
Pd/Pt{110}	1.43×10^{-5}	8.97×10^{-6} (1st dip)	63%
		5.74×10^{-6} (2nd dip)	40%
Pd/Pt{111}	1.55×10^{-5}	1.51×10^{-5} (1st dip)	97%
		1.49×10^{-5} (2nd dip)	96%
Pt{100} HER	1.36×10^{-5}	1.09×10^{-5} (EP dip)	80%
		1.11×10^{-5} (HER 30s)	82%
		1.23×10^{-5} (HER 180s)	90%
Pt{755} HER	1.22×10^{-5}	1.04×10^{-5} (EP dip)	85%
		1.06×10^{-5} (HER 30s)	87%
		1.09×10^{-5} (HER 120s)	89%
Pt/graphite catalyst HER	1.92×10^{-4}	1.58×10^{-4} (EP dip)	82%
		1.79×10^{-4} (HER 60s)	93%
		1.9×10^{-4} (HER 600s)	99%

EP was shown to adsorb on all basal planes, step and kink sites on platinum and palladium with coverages descending in the order {100}>{110}>{111}. The most notable observation of these adsorption studies was the emergence of an irreversible peak at 0.7 V in the positive scan whenever a platinum{100} site was available and to a much lesser degree with {110} sites. This peak corresponded to oxidation of adsorbed CO and was ascribed to a decarbonylation reaction of EP on platinum. Decarbonylation of EP on platinum is a well documented side reaction [23] and was found to occur the fastest on {100} followed by

{110}, but did not occur on {111}, which was a similar trend reported by Clavilier and co-workers on the oxidation of formic acid on the equivalent surfaces [13].

Window opening experiments on the platinum{100} surface (Figure 5.2) indicated that the decarbonylation reaction required either the adsorption of H UPD or the desorption of anions (which also takes place in this potential range [14]) thus freeing up platinum sites for EP decomposition. It was also apparent that the magnitude of the CO electrooxidation peak was also sensitive to the number of available platinum sites, i.e., the first potential sweep following exposure of the clean platinum electrode always gave rise to the largest CO electrooxidation peak (Figure 5.1). As platinum sites became more and more occupied by chemisorbed EP, it was found that the CO peak would decrease in magnitude. This suggested that the decomposition of EP on platinum{100} to form adsorbed CO required an ensemble of platinum sites sufficiently large to allow formation of the necessary transition state facilitating decomposition.

The highest coverage of EP on a basal plane was seen for platinum{100}. Evidently, the decomposition reaction of EP on platinum must have also produced other fragments and intermediates which would have been present on the surface. These may have contributed to the blocking of H UPD features in the CV or indeed to the features at 0.07, 0.14 and 0.25 V in Figure 5.1. However, these features were noted to occur when the excess, neat EP liquid had not been rinsed off prior to insertion in the electrochemical cell. Therefore it was tentatively suggested that these features corresponded to adsorption/desorption of multilayers of molecular EP attached to the chemisorbed EP layer. The adsorption peak at 0.07 V would then have corresponded to a very low amount of adsorbed EP, perhaps contained in the first layer of EP attached to the chemisorbed EP layer. Multilayer pyruvate adsorption was not seen in the equivalent Surface Enhanced Raman Scattering (SERS) experiments. However, the mechanism for dosing the analyte in those experiments was via a flowing solution as opposed to immersion of the electrode in a neat liquid EP sample followed by voltammetric measurements in a static solution as in the present experiments. It was surmised that the flow of the solution would have prevented a localised area of highly concentrated EP around the electrode and diffusion of EP towards and away from the electrode surface. In the absence of excess EP, it is emphasised that all multilayer peaks have vanished from the CV and only site blocking by chemisorbed EP was observed (Figure 5.1).

Adsorbed CO was wholly absent on palladium. Whilst there was evidence of some CO on palladium from with the SERS results on Pd@Au core-shell nanoparticles (section 4.2.4.2), this indicated that the decarbonylation reaction of EP was both structure sensitive and metal sensitive.

In all cases, EP was found to desorb when the electrode was held at a potential in the HER region as shown by the recovery of voltammetric features of all surfaces examined by CV. This was also in accord with the findings made from the spectroscopic experiments outlined in Chapter 4. Attempts were made to fully recover the entire area of the electrodes by evolving hydrogen for extended periods, but could not be achieved. However, this could be accounted for by the need to use fresh, electrolyte after desorption, otherwise re-adsorption of EP could occur.

5.3 Conclusion

EP adsorption was found to be highly dependant on surface morphology. The present voltammetric studies found that EP adsorbed preferentially on {100} and {110} sites on both platinum and palladium often leading to high coverages of surface intermediates. The study also found that EP readily decomposed on platinum{100} producing adsorbed CO and other (unknown) fragments on the surface, which are oxidised at more positive potentials. Adsorption of EP was disfavoured on {111} terraces of both platinum and palladium.

The present study clearly demonstrates the dependency of EP adsorption and its stability on surface morphology and has implications concerning catalyst design methodologies. It can be postulated that increasing the number of active {100} and {110} sites on the catalyst surface would increase the amount of EP adsorbed. However, it may be that increasing the number of {100} terraces on the catalyst would also facilitate more EP decomposition towards adsorbed CO.

5.4 References

[1] G.A. Attard, K.G. Griffin, D.J. Jenkins, P. Johnston, P.B. Wells, *Catal. Today* 114 (**2006**) 346.

[2] B. Torok, K. Felfo1di, G. Szakonyi, M, Bartok, *Ultrason. Sonochem.* 4 (**1997**) 301.

[3] D.J. Jenkins, A.M.S. Alabdulrahman, G.A. Attard, K.G. Griffin, P. Johnston, P.B. Wells, *J. Catal.*, 234 (**2005**) 230–239.

[4] P.W. Jacobs, G. Somorjai, *J. Mol. Catal. A-Chem.* 131 (**1998**) 5.

[5] O.A. Hazzazi, G.A. Attard, P.B. Wells, F.J. Vidal-Iglesias, M. Casadesus, *J. Electroanal. Chem.*, 625 (**2009**) 123–130.

[6] E. Herrero, A. Rodes, J.M. Perez, J.M. Feliu, A. Aldaz, *J. Electroanal. Chem.*, 393 (**1995**) 87-96.

[7] D. Ferri, T. Burgi, A Baiker *J. Phys. Chem. B*, **2004**, 108, 14384-14391.

[8] A. Rodes, K. El-Achi, M.A. Zamakhchari, J. Clavilier, *J. Electroanal. Chem.*, 284 (**1990**) 245.

[9] G.A. Attard, *J. Phys. Chem. B*, 105 (**2001**) 3158.

[10] M.J. Llorca, J.M. Feliu, A. Aldaz, J. Clavilier, *J. Electroanal. Chem.* 351 (**1993**) 299.

[11] F.J. Vidal-Iglesias, A. Al-Akl, D.J. Watson, G.A. Attard, *Electrochem. Comm.* 8 (**2006**) 1147–1150.

[12] D. Ferri, T. Burgi, A. Baiker, *J. Phys. Chem. B*, **2001**, 105, 3187-3195.

[13] J. Clavilier, R. Parsons, R. Durand, C. Lamy, J.M. Leger, *J. Electroanal. Chem.*, 124 (**1981**) 321-326.

[14] G.A. Attard, C. Harris, E. Herrero, J. Feliu, *Faraday Discuss.*, **2002**, 121, 253–266.

Chapter 6
Adsorption of Cinchona Alkaloids on Platinum Surfaces

6.1 Introduction

Hydrogenation of an activated ketone to a chiral secondary alcohol can be catalysed heterogeneously using a high surface area platinum catalyst. Unmodified, the result is a racemic product i.e. no discrimination between production of one enantiomer over the other. The cinchona alkaloid series are naturally occurring chiral molecules that have been successfully used to modify supported platinum catalysts to be enantioselective in the hydrogenation of methyl pyruvate (MP) and ethyl pyruvate (EP) to the corresponding lactates to an enantiomeric excess (ee) above 90% (when optimised), commonly referred to as the Orito reaction [1]. Not only was the selectivity considered high for a heterogeneously catalysed chiral reaction, but also the rate of the modified reaction was noted to increase over the unmodified racemic reaction.

Understanding the role of the chiral modifier in the Orito reaction represents a major challenge faced by surface scientists. A wide range of surface science and heterogeneous catalytic techniques have been used to address this topic including XPS [2], STM [3], CV [4], calorimetry [5], derivitisation [6], NEXAFS [7], ATR-IR [8], RAIRS [9], LEED [2], SERS [10], NMR [11] and DFT [12]. It has been established that cinchonidine (CD) adsorbs onto the platinum surface via the quinoline ring parallel to the plane of the surface in a "flat" orientation at low concentrations. The mechanism for adsorption in this case was thought to be via the aromatic π states [9] (Figure 6.1 (a)). At a higher concentration, the quinoline ring becomes tilted with respect to the surface plane and adsorbs through the nitrogen lone pair of electrons and the carbon in the α-position (hydrogen abstracted) to the nitrogen of the quinoline ring, referred to as α-quinolyl [8] (Figure 6.1 (b)). Other adsorption modes were understood to exist, but the flat and α-quinolyl modes were dominant.

Under a nitrogen atmosphere, random assortments of different adsorption geometries were seen on a platinum{111} surface using STM [3]. When hydrogen was admitted, most CD molecules were adjudged to be converted to the flat mode and became less mobile across the surface. An equivalent study using SERS had also shown the CD molecules to be converted to the flat lying adsorption mode in the presence of hydrogen [10].

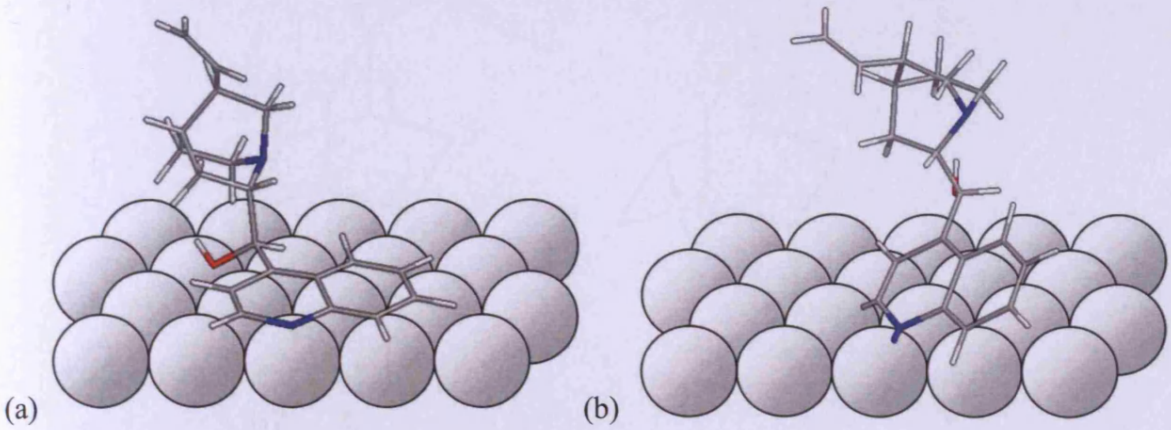

Figure 6.1 Adsorption geometries for CD on platinum in the (a) "flat" orientation and (b) α-quinolyl as determined in reference [8].

The highly sensitive nature of the surface science techniques listed above required exclusion of contaminating species that would confuse or mask the true result, particularly those that utilise the X-ray sources where high vacuum conditions were required. This is far from ideal, as it is at high ambient pressure conditions that the reactions of interest occur. The inability to run an experiment under real reaction conditions using electron based spectroscopies often sparked a question of legitimacy concerning the results. Creating a truly *in situ* technique continues to be a challenge for instrumental design.

This chapter is focussed on the adsorption behaviour of the cinchona alkaloid cinchonidine (CD), its near enantiomer cinchonine (CN) and two other derivatives in the form of quinine (QNE) and hydroquinine-4-chlorobenzoate (HQnClB) (Figure 6.2) on polycrystalline SERS active platinum surfaces. Using a dedicated spectro-electrochemical flowcell, further light was shed on Williams' original SERS study of CD on platinum and the effects of hydrogen [13].

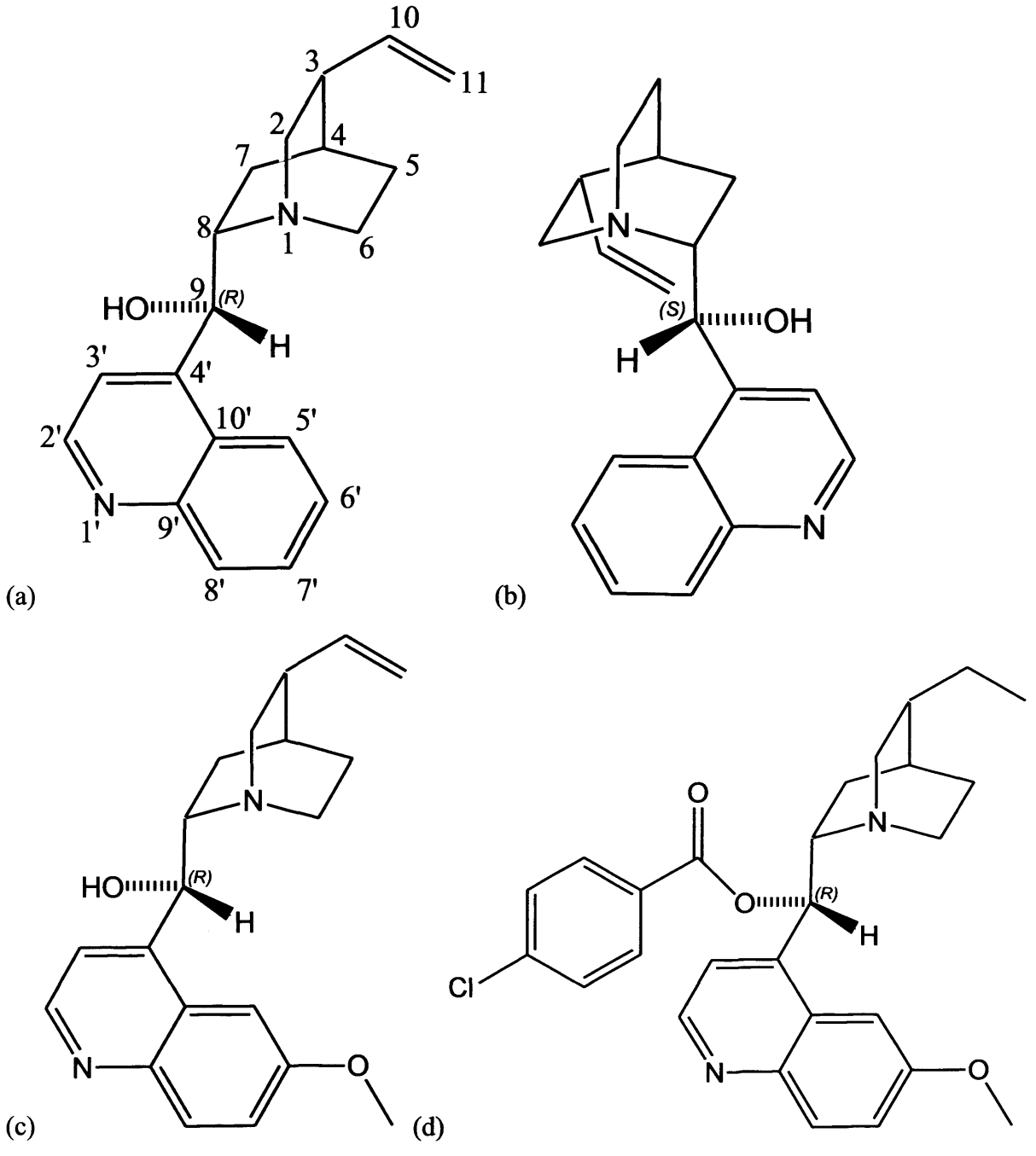

Figure 6.2 Structures (a) CD, (b) CN, (c) QNE and (d) HQnClB.

6.2 Results

6.2.1 Raman Spectra of the Alkaloids

The Raman spectra of the pure species are included to show the spectroscopic differences between the modifiers and identify the groups that may help ascertain adsorption geometries. Table 6.13 shows the frequency of the peaks of interest and their vibrational assignment using standard references [8, 9, 13, 14, 15, 16].

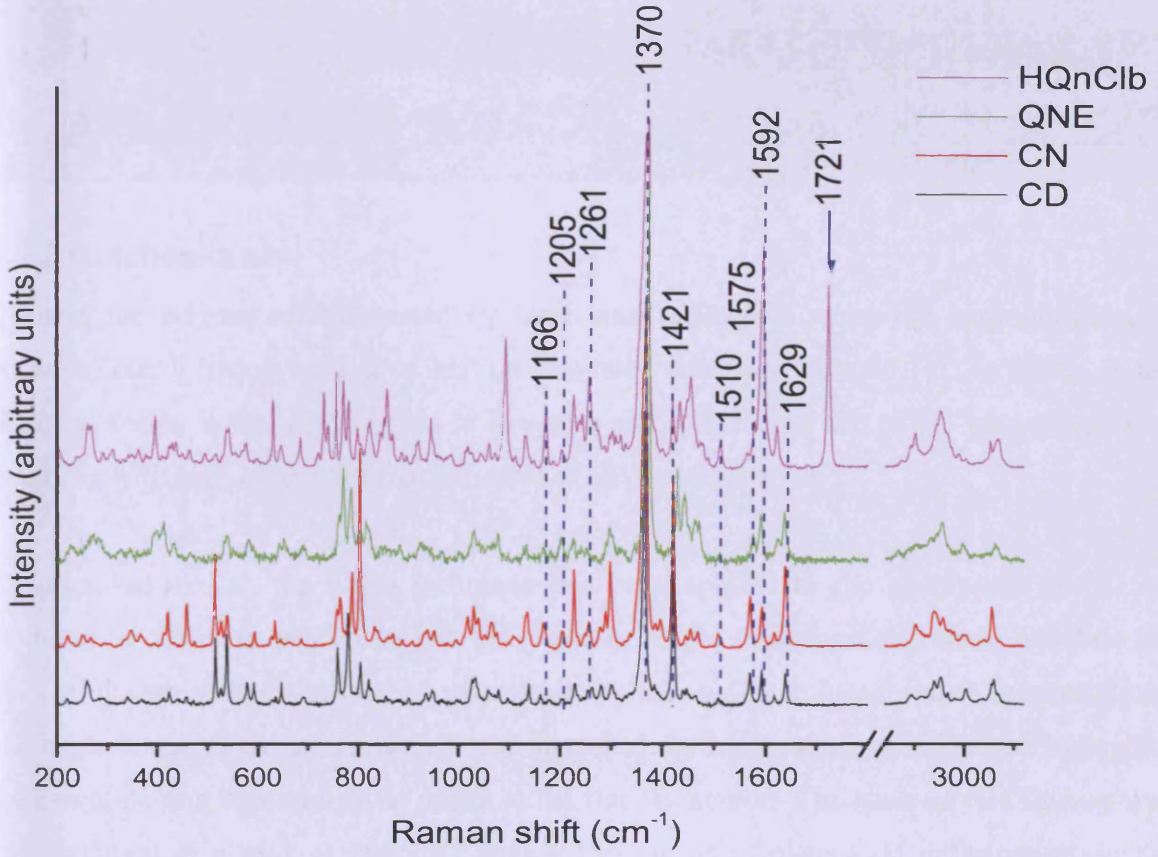

Figure 6.3 Raman spectra of the pure solid cinchona species.

Table 6.13 Band assignments for the pure species [9].

Band Position (cm^{-1})						Assignment
CD	**CN**	**QNE**	**HQnClB**	**Q**	**QN**	
3060	3060	3060	3060	3060	-	ν(C-H)
-	-	-	1721	-	-	ν(C=O)
1638	1638	1636	-	-	-	ν(C=C) (vinyl)
1592	1592	1590	1590 + 1592 i.p. ν(C=C) (ph ring)	-	-	ν(C=C) (Q ring) short axis
1570	1570	1576	1578	1570	-	ν(C=C) (Q ring) short axis
1508	1508	1510	1510	1502	-	i.p. δ(Q ring) / ν(C=C) long axis
1450	1452	1447	1453	-	1453	δt(C-H) (QN ring)
1421	1421	1429	1433	1432	-	δ(C-H) (Q ring)
1365	1367	1377	1370	1372	-	i.p. ν(Q ring)
1263	1257	1261	1261	-	1273	ν(C^9-OH) / δ(C^9-H) / δ(C-H) (QN ring)
1205	1206	1203	1203	-	1205	δt($C-H_2$) (QN ring)
-	-	1182	1186	-	-	i.p. δ(C-H) (QB ring)
1140	1137	1134	1134	1141	-	δw(C-H) (Q ring)
-	-	-	1093	-	-	ν(C-Cl) / ν(ring) (phenyl)
1033	1039	1030	1028	1030	-	ring breath
1058	1052	1061	1061	-	1054	ν(C-N) (QN ring)

900	908	897	884	-	-	i.p. $\delta(C^{4'}\text{-}C^{9}\text{-}C^{8})$
803	803	803	803	-	803	ν(C-C) (QN skeletal)
758	763	762	755	760	-	δw(C-H) (Q ring)
538	539	539	542	-	542	ν(C-C) (QN skeletal)
516	516	-	-	521	-	o.o.p. δ(Q ring)

6.2.2 Cinchonidine

CD was the original modifier used by Orito and colleagues when the hydrogenation of enantioselective hydrogenation of MP on platinum was first reported [1]. In terms of the cinchona series, it was the simplest in structure and remains as one of the best performing modifiers with high ee and fast reaction rates of EP hydrogenation.

As discussed earlier, the SERS technique has been applied to the adsorption of CD on platinum by Williams and colleagues [13]. The principal finding of this study was that the plane of the aromatic quinoline ring was parallel to the surface at low solution concentrations and began to tilt as the concentration was increased. In the presence of dissolved hydrogen, the quinoline ring was thought to return to the flat orientation. The basis of this finding was the resolution of a peak at 784 cm^{-1} assigned to an out-of-plane C-H deformation on the quinoline ring (Figure 6.4).

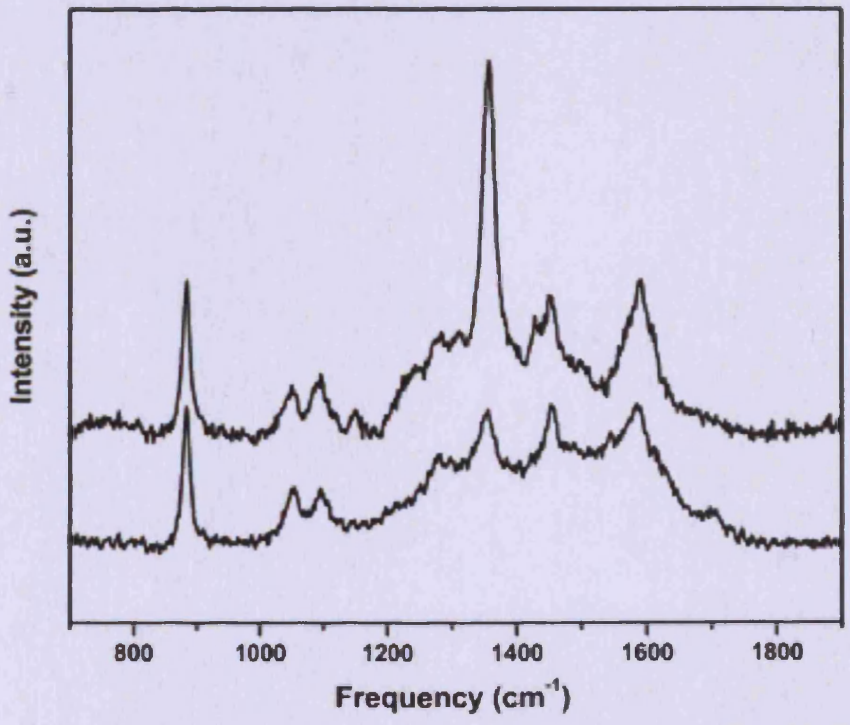

Figure 6.4 Typical *in situ* SER spectra obtained for platinum in a 0.120mM CD in ethanol solution before (bottom) and after (top) introduction of solution-phase H_2. Reprinted from [13].

6.2.2.1 Cinchonidine in Dichloromethane on Au@Pt Core-shell Nanoparticles

Williams' results displayed a broad peak with a shoulder at 2080 cm^{-1} and they ascribed this to adsorbed hydrogen from the dissociation of ethanol (the solvent used by Williams) [13]. Although the position was not disputed with regard to ν(Pt-H), based on the shape of the peak(s) and prior knowledge of ethanol decomposition on platinum, this was more likely to be adsorbed carbon monoxide (CO), which as a co-adsorbate could interfere with the target analyte. An analogous study was performed using DCM as solvent, which was less prone to forming CO on platinum.

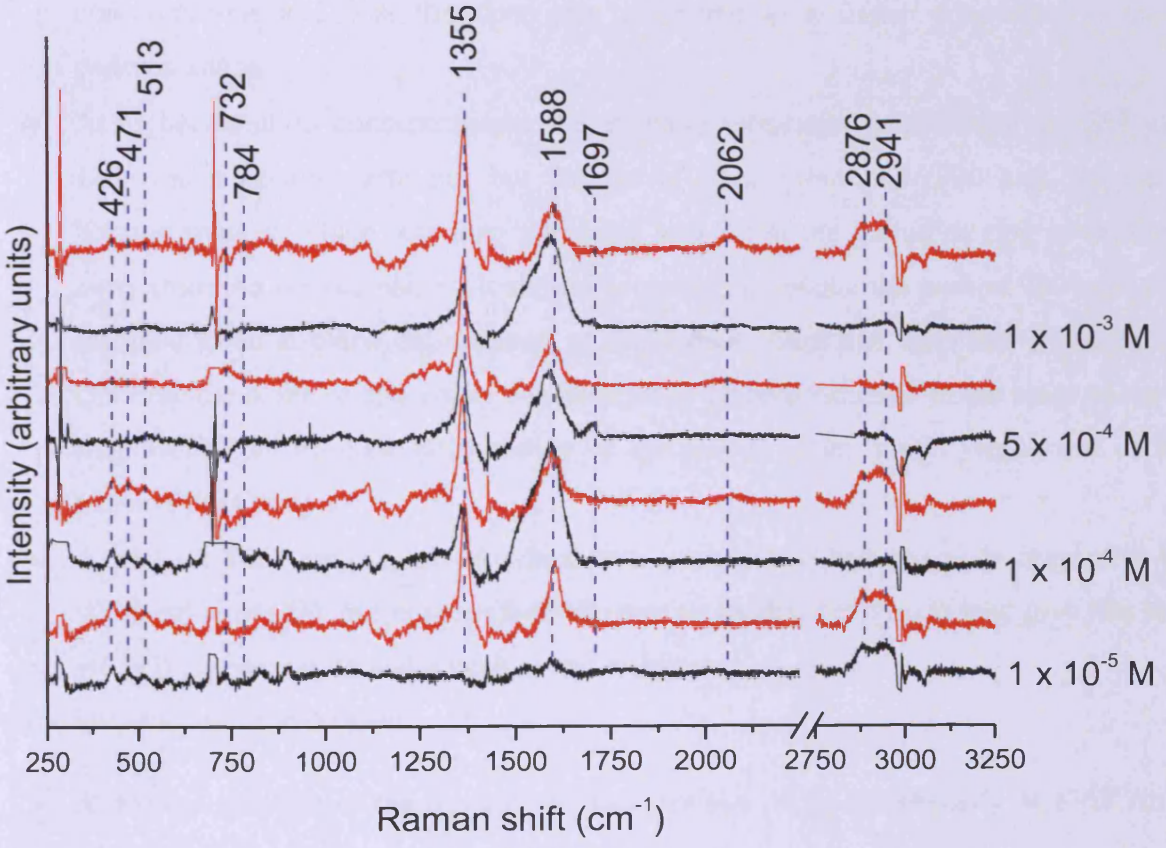

Figure 6.5 SER spectra of CD dissolved in DCM to varying concentrations adsorbed on Au@Pt Core-shell Nanoparticles (CS-NP) (black) then sparged with hydrogen until saturated (red). The SER spectrum of pure DCM on Au@Pt CS-NP has been subtracted from each of the spectra above to highlight the SERS features of CD.

In the paper by Williams *et al* the frequency range reported for the SER spectra did not extend below 700 cm^{-1}. However, three peaks were clearly resolved at 513, 471 and 428 cm^{-1} in the present study. From Table 6.13 it can be seen that the Raman spectrum of quinoline

(Q) produced a peak at 516 cm^{-1}, which was assigned to an out-of-plane deformation of the ring and was assigned as such in the SER spectrum. The peaks at 471 and 428 cm^{-1} were in the frequency range for ν(Pt-C) and ν(Pt-N) [14, 17] and were tentatively assigned to these vibrations, respectively. Despite this, the same behaviour reported by Williams *et al* was also seen in this experiment:

- The peak intensity increased with solution concentration.
- The general resolution of peaks below 1000 cm^{-1} (mostly from vibrations of the QN ring and out-of-plane vibrations of the Q ring) was seen to be stronger at lower concentrations and was therefore also attributed to a flatter orientation at these concentrations.
- At higher solution concentrations, the in-plane vibrations (particularly at 1588 and 1355 cm^{-1}) became stronger, but the out-of-plane vibrations (900 and 516 cm^{-1}) became weaker, which was also attributed to a tilt of the quinoline ring at an angle away from the surface plane. (It should be noted that whilst the peak at 900 cm^{-1} was assigned to an in-plane deformation of the carbon chain that links the Q ring to the QN ring, the plane of this group was thought to be perpendicular to the plane of the Q ring. Hence, an in-plane deformation of the carbon chain would vibrate out of the plane of the Q ring.)
- A peak at 1697 cm^{-1} resolved which was assigned to carbonaceous impurities by Williams *et al* [13], but is proposed here that an oxidised fragment may give rise to a ν(C=O) type vibration and a peak at this frequency.

On the introduction of hydrogen:

- A marked increase of the intensity of the in-plane peaks (particularly at 1355 cm^{-1}, which was also noted to remain relatively narrow).
- The peak at 1697 cm^{-1} was noted to disappear. This behaviour could be ascribed to a removal of oxidised species on introduction of hydrogen.
- A weak and broad peak at 2060 cm^{-1} assigned to ν(Pt-H) was resolved.
- The peak at 1588 cm^{-1} was also noted to become narrower.

What was not obvious was the increase in the out-of-plane peaks from the introduction of hydrogen as reported by Williams *et al*. Neither was their interpretation: "The increase in the SERS intensity of the 1357 cm^{-1} band can thus be attributed in large part to increased π-bonding of the aromatic ring with the Pt surface" [13]. Although the increased interaction

would satisfy the charge transfer (CT) theory for SERS, the changing polarisability of in-plane vibrations should be screened by the image charge in the metal when in a vector parallel to the surface plane. Therefore, the interpretation of a return to the flat orientation in the presence of hydrogen could not be confirmed under the present conditions.

Using RAIRS, Zaera and colleagues were able to assign the peaks around 1500-1600 cm^{-1} to aromatic ν(C=C) representing the long and short axes of the quinoline ring [9]. In the absence of hydrogen, the peak at 1588 cm^{-1} was noted by Zaera to be broad. This was attributed to an assortment of different adsorption geometries of CD that gave rise to ν(C=C) at slightly different frequencies. The mixture of different adsorption modes was analogous to the interpretation of an STM study under similar conditions [3]. It was proposed that not all of the adsorption geometries present in the absence of hydrogen gave rise to the peak from the Q ring stretching mode at 1355 cm^{-1}. However, if the adsorption geometries that remained upon exposure to hydrogen did give rise to the 1355 cm^{-1} peak, then this would account for the increased intensity of this peak relative to the broader 1588 cm^{-1} peak. Hence, the narrowing of the peak at 1588 cm^{-1} and increased intensity to the peak at 1355 cm^{-1} in the presence of hydrogen was ascribed to a conversion of the multiple different adsorption geometries to just one or two different modes, for which the in-plane ring stretching mode was angled in a vector away from the surface and therefore was SERS active.

6.2.2.2 Cinchonidine on Au@Pt Core-shell Nanoparticles under Gas Phase Conditions

The choice of solvent in the Orito reaction can have significant effects on the overall catalyst performance [18]. Hutchings and co-workers have performed the reaction in the gas phase over a pre-modified catalyst [19], proving that an organic liquid medium was not intrinsic to the propagation of the reaction. For spectroscopic purposes, identifying the peaks resolved from the target analyte was easier in the absence of interfering bulk liquid Raman scattering from an organic solvent. In this experiment, the SERS active Au@Pt core-shell nanoparticles were pre-modified by dipping the electrode in a solution of 1×10^{-4} M CD dissolved in DCM. The DCM was removed by the argon gas flow upon insertion of the electrode into the cell. After the spectrum was taken, argon was replaced by hydrogen and another spectrum was collected.

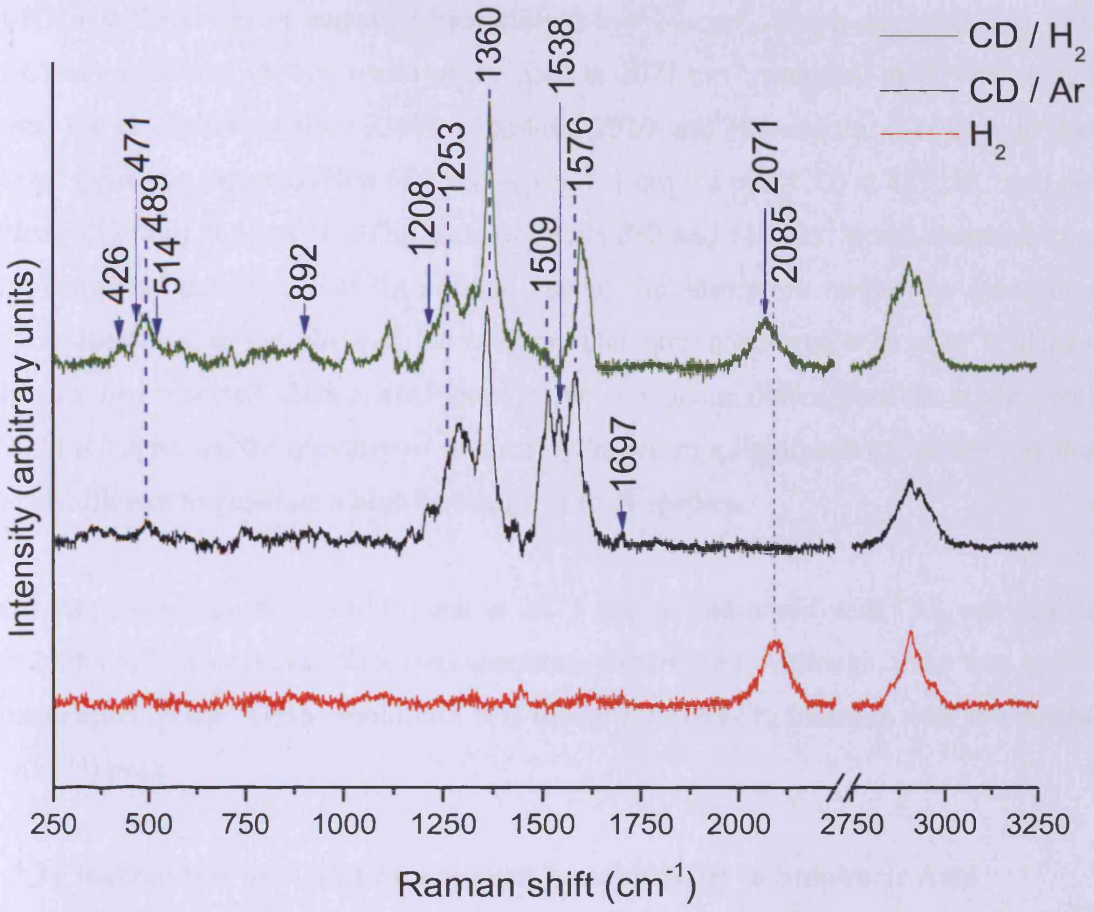

Figure 6.6 SER spectra of the clean platinum surface under hydrogen (red), CD on Au@Pt CS-NP under argon (black) and hydrogen (green) overpressures.

Under gas phase conditions, the definition of the peaks was much improved compared to the results obtained in DCM. Under argon, the location on the electrode where the laser spot was focussed had a marked effect on the relative intensity of the peaks in the spectrum, particularly between 1500 and 1600 cm^{-1}. This was again assigned to multiple adsorption modes and a variation in the relative numbers of the different adsorption modes at different surface locations.

The effects of hydrogen were also seen more clearly. The multiple peaks between 1500-1600 cm^{-1} transformed into a single peak at 1591 cm^{-1} and was consistently observed irrespective of surface position. The shape of this peak was noted to be asymmetric. Therefore, at least two vibrations were contributing to this peak. Also, the relative intensity of the peak at 1360 to the peak(s) at 1591 cm^{-1} increased, which again showed that fewer distinguishable

adsorption modes existed. The peaks at 489 and 426 cm^{-1} were again assigned to ν(Pt-C) and ν(Pt-N). The former peak appeared blue shifted by ~20 cm^{-1}, which does coincide with the ν(Pt-C) of adsorbed CO. The width of the peak at 2071 cm^{-1}, assigned to ν(Pt-H), may have masked the resolution of the ν(C≡O) at around 2020 cm^{-1}. Therefore, it is thought that the 489 cm^{-1} peak is a superposition of a ν(Pt-C) at 471 cm^{-1}, a ν(Pt-CO) at 489 cm^{-1} and an out-of-plane δ(Q ring) at 514 cm^{-1}. The increase in the 892 and 514 cm^{-1} peaks assigned to out of plane vibrations indicated that for at least one of the adsorption modes the quinoline ring began to tilt closer to the plane of the surface. This now concurred with what Williams and colleagues had reported. Hence, analogous to the conclusion drawn from the studies with EP in DCM (Chapter 4), the quantity of surface hydrogen in a liquid solvent phase was thought to be insufficient to generate a high coverage of Pt-H species.

It was also found that the ν(Pt-H) peak at 2071 cm^{-1} co-adsorbed with CD, was red shifted from 2085 cm^{-1} on a clean surface (red spectrum, Figure 6.6). Although, there was some mild contamination on the 'clean' spectrum, it is thought unlikely to interfere with the position of the ν(Pt-H) peak.

6.2.2.3 Cinchonidine on Au@Pt Core-shell Nanoparticles in Sulphuric Acid

A disadvantage to studying this system under a gas phase environment was that desorption of the modifier was no longer facilitated by a solvent and fresh modifier was not available to refresh the active sites. Using sulphuric acid, a surface-liquid dynamic equilibrium could be maintained. There were no interfering peaks from the bulk of the liquid and electrochemical control could be used to model certain surface environments particularly at hydrogen evolution reaction (HER) potentials where the hydrogen surface coverage was similar to that at high hydrogen overpressures. The reaction was not usually carried out in aqueous solvents, but Calvo *et al* have successfully performed the reaction on palladium using an aqueous electrolyte and electrochemical control [20].

Figure 6.7 illustrates the adsorption behaviour of CD under different surface conditions. A fixed concentration of 5×10^{-5} M of the modifier dissolved in 0.1 M sulphuric acid was drawn through the cell and the potential of the platinum electrode was varied[***].

[***] The direction of potential scanning was not thought to have a significant effect on the surface conditions when the potential is being held.

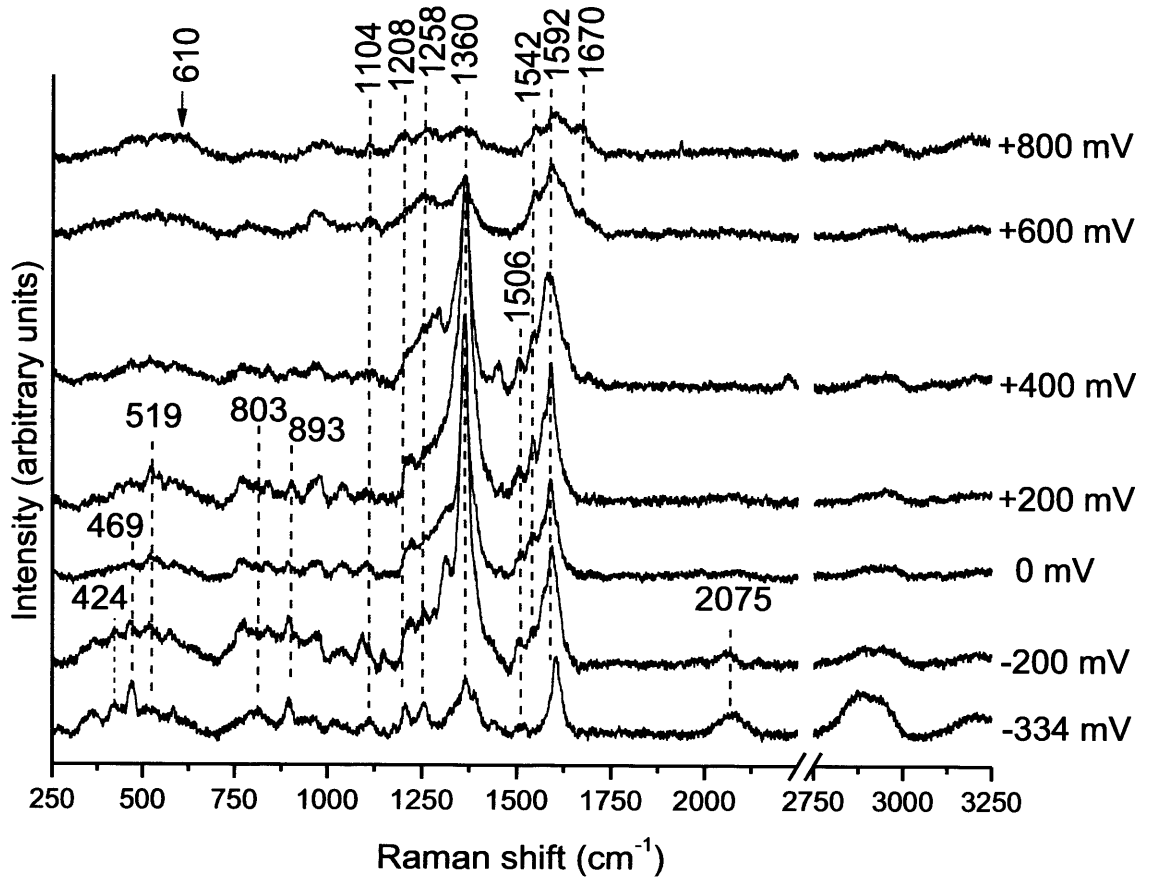

Figure 6.7 SER spectra of 5×10^{-5} M CD dissolved in 0.1 M H_2SO_4 adsorbed on Au@Pt CS-NP and held at a variety of potentials *vs.* Ag/AgCl in a negative scanning direction.

At +0.8 V, the platinum surface was in an oxidised state (as seen from the Pt-O_x peak at ~590 cm^{-1}). The peaks of adsorbed CD were low in intensity and broad in shape. Like the results of CD on platinum in DCM and under gas phase argon, this was ascribed to the existence of several adsorption modes. Also, the low intensity of the peaks was consistent with previous results of strongly adsorbed anionic species inhibiting the uptake of CD [21]. As the potential was scanned more negative, all peak intensities increased and the peak shapes became more defined. In particular, the peak at 1360 cm^{-1} was markedly increased in intensity. This trend continued through to potentials corresponding to the electrical double layer and into the H UPD region. These were the same observations made in DCM and under gas phase conditions when hydrogen was introduced. The peak at 1670 cm^{-1} present at high positive potentials was noted to disappear as the potential was scanned negative. This behaviour was similar to the peak at 1697 cm^{-1} observed using DCM as solvent and under gas phase conditions as hydrogen was introduced and was again assigned to an oxidised species.

Clearly, stripping off the oxide allowed for more CD adsorption sites to become available and hence the increase in intensity of the CD peaks in the double layer region.

At potentials corresponding to HER, the trend of a steady increase in the intensity of the peak at 1360 cm^{-1} as the potential was scanned more negative was reversed as the intensity reduced to a level similar to the peak at 1592 cm^{-1}. The peak at 1592 cm^{-1} was no longer asymmetric in shape, which indicated that only one adsorption mode existed under these surface conditions. The peaks resolved at 900 and 519 cm^{-1} showed that the Q ring in this adsorption mode was close to being flat against the surface, but was not parallel as the in-plane peaks were still quite intense. The surface peaks at 469 and 424 cm^{-1} were also resolved. In addition, peaks from the QN ring were clearly resolved including at 1208 and 803 cm^{-1}.

The surface coverage of hydrogen on platinum at HER potentials (-0.33 V versus Ag/AgCl) was thought to be similar to that at the hydrogen pressures used to run the Orito reaction and therefore the spectra should provide a good approximation of the adsorption behaviour of CD under catalytic reaction conditions. The potential of the platinum electrode was held in the HER region and the solution concentration of CD was varied. Figure 6.8 shows the spectra of adsorbed CD at HER potentials and the surface behaviour at increasing concentrations.

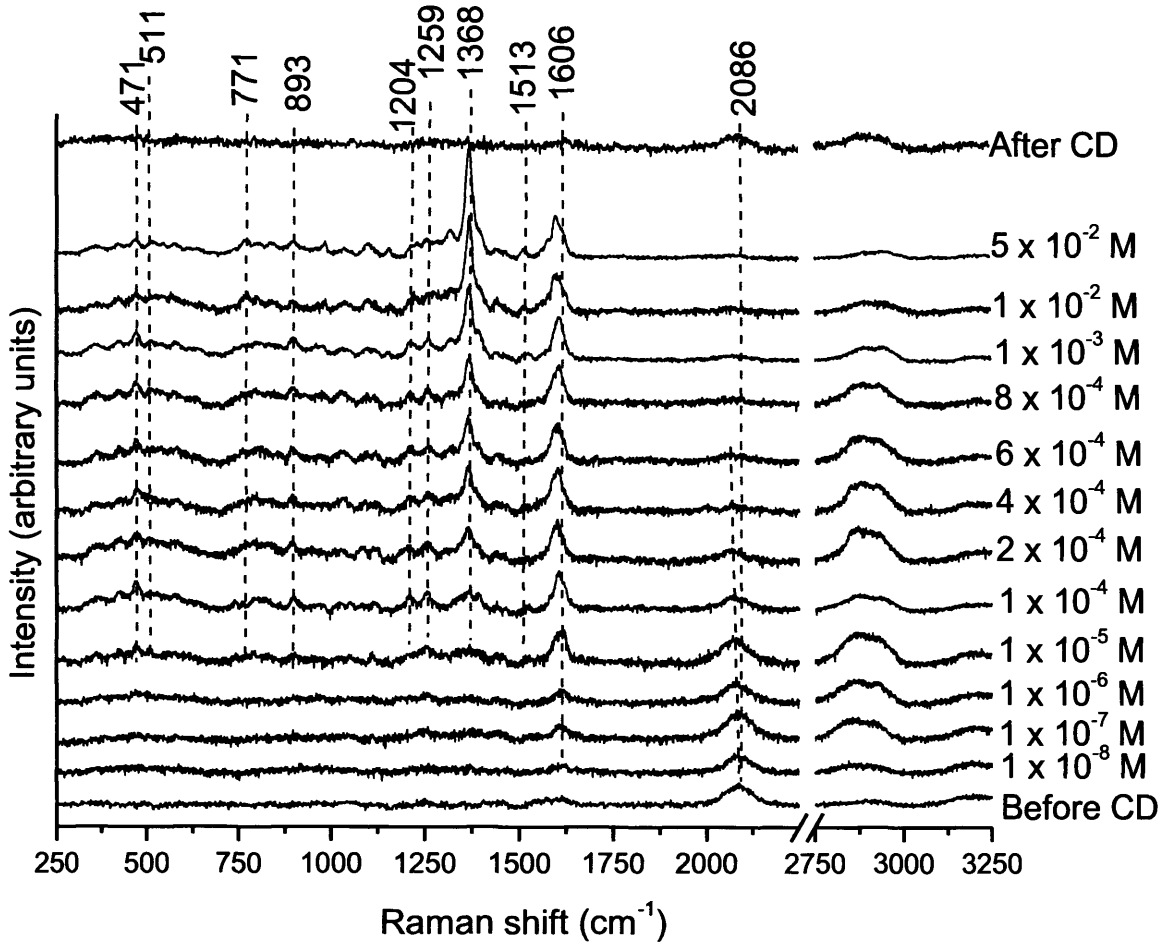

Figure 6.8 SER spectra of varying concentrations of CD dissolved in 0.1 M H_2SO_4 on Au@Pt CS-NP held at -0.33 V *vs.* Ag/AgCl.

At the lowest concentration of CD, the spectrum was similar to that of the clean surface ("Before CD"), which included the peak at 2086 cm^{-1} corresponding to ν(Pt-H). Increasing the concentration resulted in a decrease in the peak from the Pt-H stretch and an increase in all the peak intensities from adsorbed CD including the emergence of a new band at 1592 cm^{-1} at concentrations above 2×10^{-4} M. In addition, the growth in intensity of the peak at 1368 cm^{-1} was again more pronounced relative to the rest of the peaks from CD. The intensity of the out-of-plane peaks, appeared to decrease with increasing concentration, but the effect only appeared to be significant at the two highest solution concentrations. The same effect was noted in the concentration ranges used in DCM (section 6.2.2.1) and by Williams and colleagues who used ethanol as a solvent [13]. This was interpreted as a re-orientation of the modifier to a more tilted configuration that promoted the in-plane quinoline peak at 1368 cm^{-1}, but curiously not the other in-plane peak at 1606 cm^{-1}. When the incoming solution was switched back to pure 0.1 M sulphuric acid ("After CD"), the peaks from adsorbed CD

disappeared showing that under HER conditions the modifier is not irreversibly held to the surface.

The position of the ν(Pt-H) peak was found to shift down by 10 cm^{-1} to 2075 cm^{-1} as the concentration of CD increased up to 6×10^{-4} M as indicated by the red dashed line in Figure 6.8. Above this concentration, the intensity of the peak was too small to judge the position due to an overwhelming coverage of CD.

6.2.2.4 Cinchonidine on Au@Pt Core-shell Nanoparticles in Deuteroperchloric Acid

It was found that the vinyl and the alcohol groups of CD were both hydrogenated on platinum during Orito type reactions through deuteration experiments [22]. Figure 6.9 shows the results of a similar experiment made with CD dissolved in a 0.1 M solution of $DClO_4$ in D_2O held in the hydrogen evolution region on platinum (unfortunately considerable contamination was observed when using D_2SO_4 (see section 4.2.4.1)).

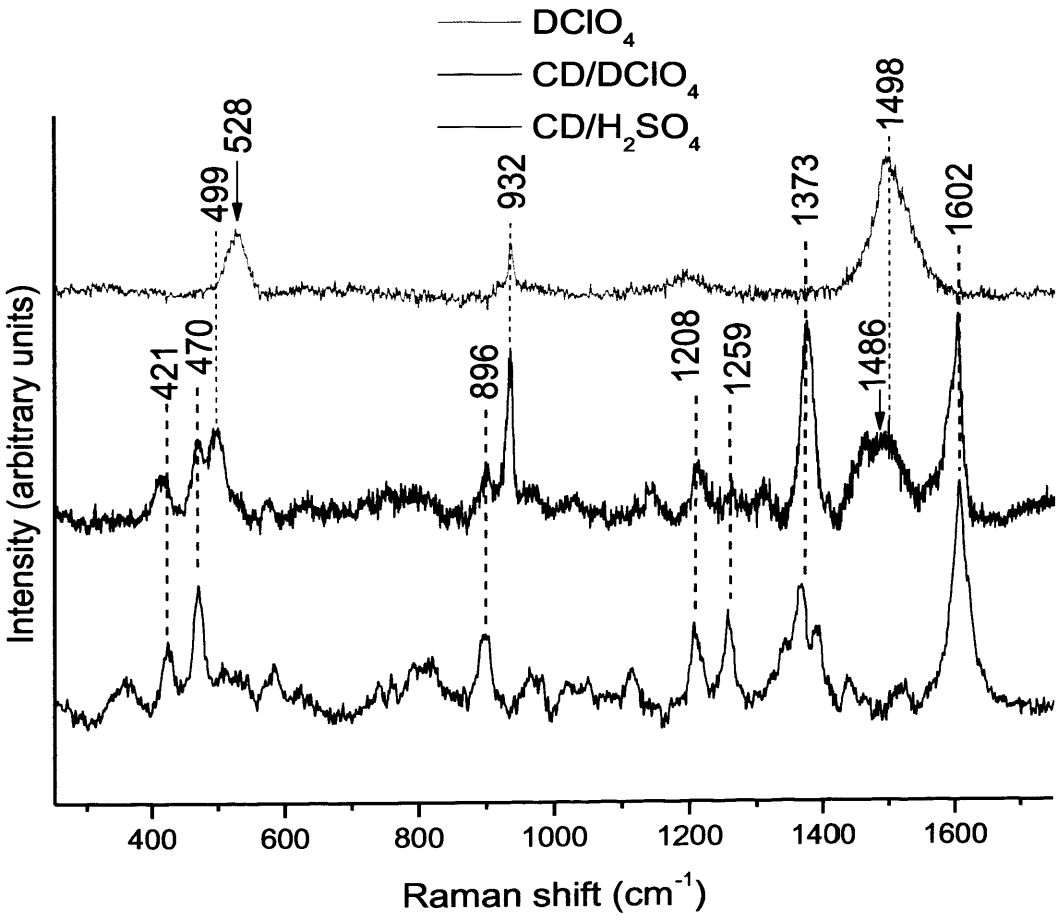

Figure 6.9 SER spectra of 5×10^{-5} M CD in 0.1 M $DClO_4$ on Au@Pt CS-NP at -0.33 V compared to 5×10^{-5} M CD in H_2SO_4.

The peaks at 1498 and 932 cm^{-1} arose from ν(Pt-D) and ν(Cl-O) of the liquid phase ClO_4- anion respectively. The resolution of a peak at 499 cm^{-1} was thought to be from a minor contamination of the $DClO_4$ solution which produced adsorbed CO (This peak was curiously higher in frequency when CD was not present (528 cm^{-1}, green spectrum) but did correspond to a peak at 2005 cm^{-1} assigned to ν(PtC≡O) (see section 4.2.4.1)). The major differences between the spectra included a merging of the peaks around 1373 cm^{-1} into one intense peak and the peaks at 1259 and 896 cm^{-1} being significantly reduced in intensity from partial hydrogen-deuterium exchange on the alcoholic carbon chain in $DClO_4$. Like the ν(Pt-H) peak in sulphuric acid, a subtle, but discernable red shift to the equivalent peak in $DClO_4$ (ν(Pt-D)) from 1498 to 1486 cm^{-1} was seen.

6.2.2.5 Quinoline and Quinuclidine

As discussed earlier, CD consisted of the aromatic quinoline (Q) ring and the aliphatic quinuclidine (QN) ring system joined together by a chiral alcoholic carbon chain. Both types of rings are heterocyclic with a tertiary nitrogen from which a lone pair of electrons could be donated. Q and QN were each dissolved in 0.1 M sulphuric acid and introduced into the spectro-electrochemical flowcell to help estimate the surface contribution and orientation of both moieties.

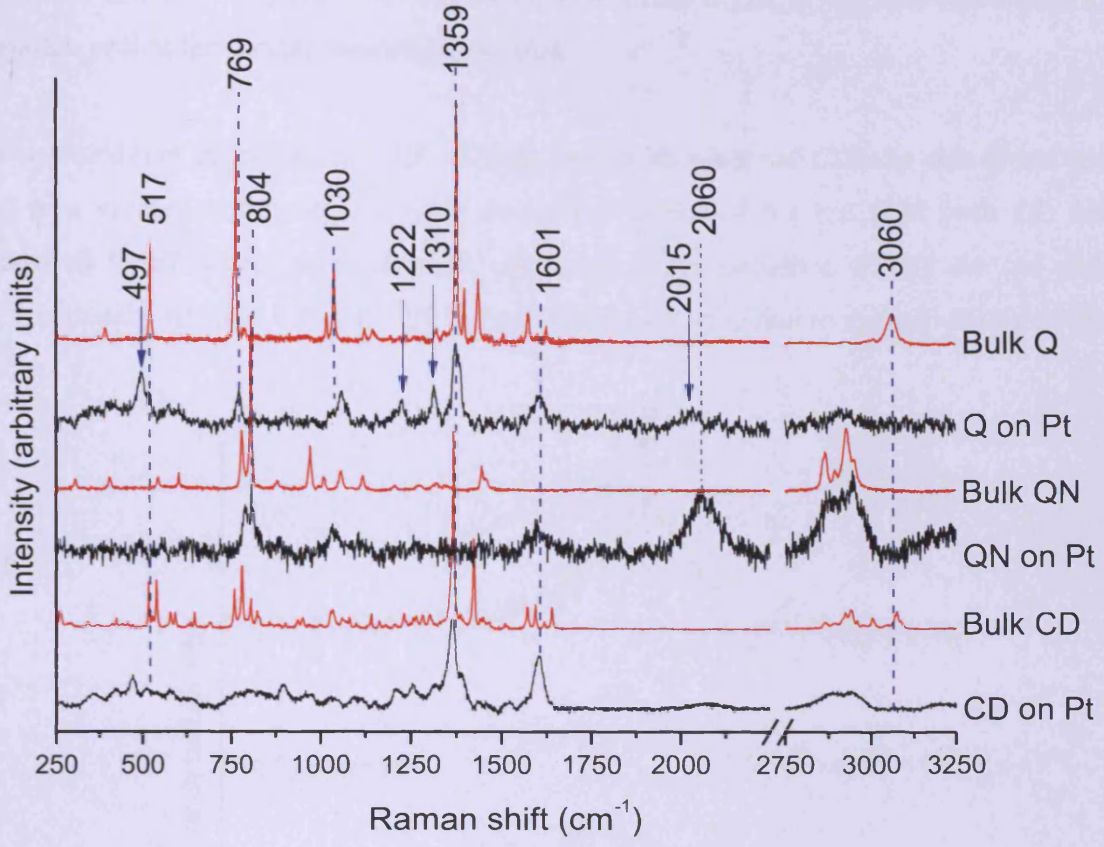

Figure 6.10 SER and Raman spectra of 50 mM QN and 5 mM Q dissolved in 0.1 M H_2SO_4 on Au@Pt CS-NP held at -0.33 V *vs.* Ag/AgCl (black) against the bulk spectra (red) compared to the corresponding CD spectra.

From electrochemical studies (not shown here), QN was found to only weakly adsorb on platinum and was the reason for the relatively high concentration (50 mM) used in this study. In the Raman spectrum of solid QN, two peaks at 787 and 807 cm^{-1} were assigned to skeletal C-C vibrations and the peak at 1030 cm^{-1} was assigned to ν(C-N), which may have contributed to the broad features centred at 1031 and 797cm^{-1} for adsorbed CD. The spectrum of adsorbed Q also showed peaks resolved at 1030 and 769 cm^{-1} from a ring breathing mode and out-of-plane C-H deformations, which also could have contributed to the broad features at 1030 and 797 cm^{-1} in the SER spectrum of CD. The Q SER spectrum also showed a mixture of in-plane and out-of-plane vibrations, which was evidence of an adsorption geometry tilted with respect to the surface. The same peaks were resolved in the SER spectrum of CD including 1601, 1359, 1310, 769 and 516 cm^{-1}, which was also indicative of the modifier adsorbed in a tilted geometry. The peaks at 2015 and 497 cm^{-1} were assigned to

ν(PtC≡O) and ν(Pt-CO) from adsorbed CO. This showed that Q was less stable than QN on platinum or that the sample was contaminated.

It was noted that the red shift to the ν(Pt-H) peak with adsorbed CD was also found with QN and to a greater extent. Figure 6.11 shows the extent of the red shift with CD and QN compared to EP where no such shift occurred. In the presence of CD the red shift was approximately 10 cm^{-1}, but with QN the red shift nearly doubled to approximately 20 cm^{-1}.

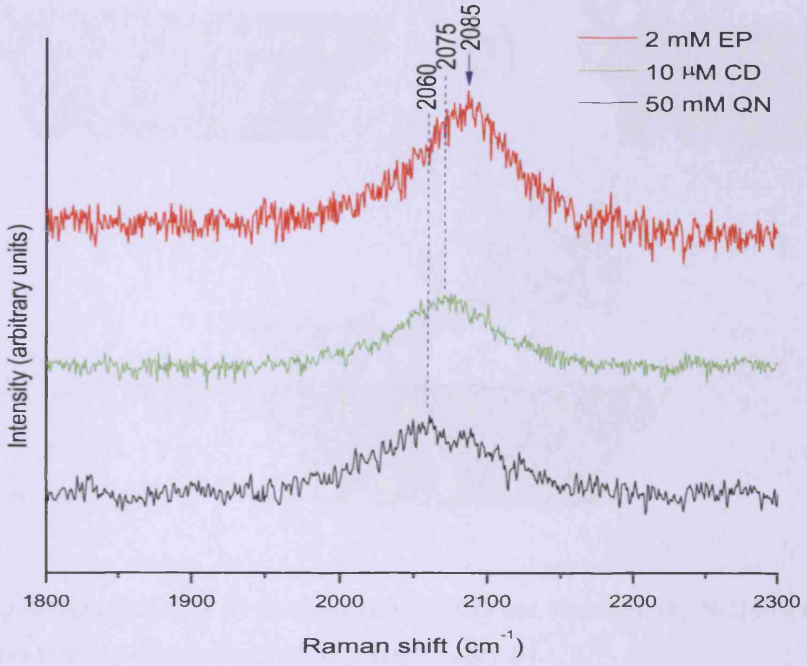

Figure 6.11 SER spectra of 2×10^{-3} M EP in 0.1 M H_2SO_4 (red), CD in gas phase under H2 (green) and 5×10^{-2} M QN in 0.1 M H_2SO_4 (black) on Au@Pt CS-NP.

This red shift may be interpreted as an interaction between the tertiary nitrogen of QN and surface hydrogen, weakening the Pt-H bond and hence the ν(Pt-H) vibration was lower in frequency. Theoretical calculations on CD co-adsorbed with hydrogen found that such interactions could occur [23]. In reference 23, it was shown that the QN ring of CD could be protonated to form an ammonium ion when dissolved in an aprotic solvent. The mechanism of protonation involved an intermediate state where the hydrogen atom was "suspended" between the two nucleophiles (N and Pt) (Figure 6.12 b). The Pt-H bond length was calculated to increase from 1.58 to 1.83 Å. It is proposed here that the red shift in frequency is due to the increased length of the Pt-H bond of the intermediate when interacting with the

tertiary N of CD. This interaction may also be the mechanism for adsorption of QN as π-bonding to the platinum surface would be impossible with this non-aromatic molecule. There was no evidence either to show formation of a Pt-C or a Pt-N bond, which would give bands in range 550-430 cm^{-1}.

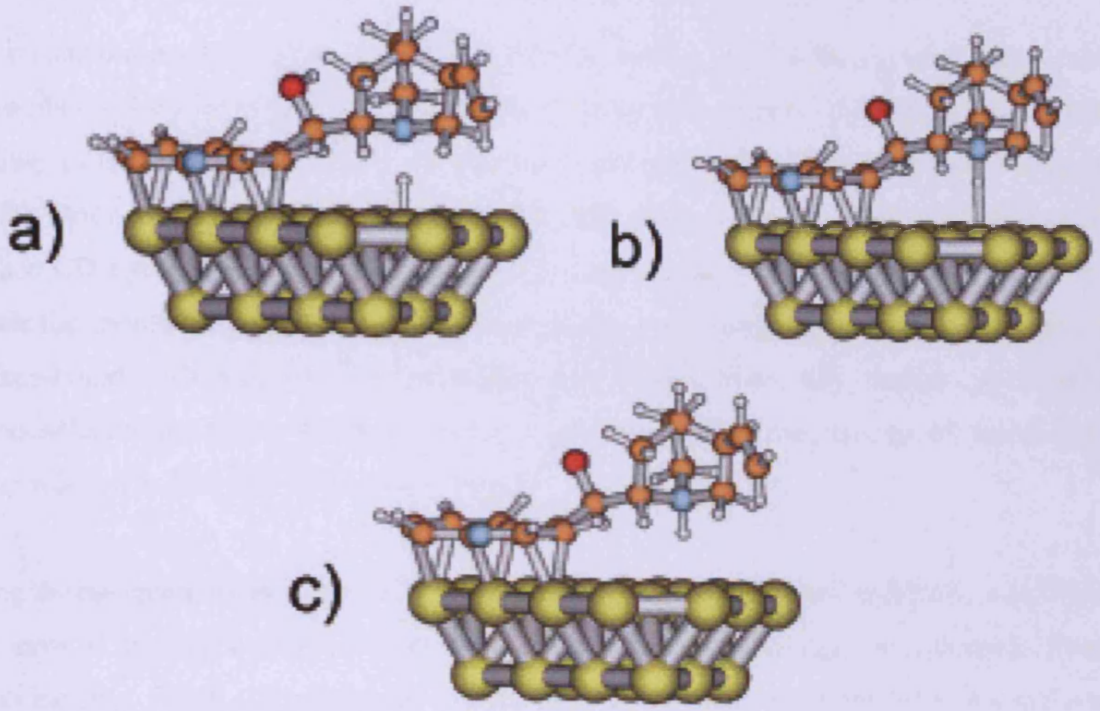

Figure 6.12 Adsorption geometries of a) Co-adsorption of CD and hydrogen, b) N-H-Pt intermediate and c) protonated nitrogen to form the ammonium ion. Reprinted from [23].

6.2.2.6 Discussion of the Cinchonidine Results

The band assignments for the SER spectra of adsorbed CD are summarised in Table 6.14 below.

Table 6.14 Band assignments for SER spectra of CD on Au@Pt CS-NP.

Band Position (cm^{-1})	Assignment	Band Position (cm^{-1})	Assignment
CD		**CD**	
1670	ν(C=C)/ν(C=N) oxide species	1140	δw(C-H) (Q ring)
1592	ν(C=C) (Q ring) short axis	900	i.p. $\delta(C^{4'}\text{-}C^{9}\text{-}C^{8})$
1570	ν(C=C) (Q ring) short axis	803	ν(C-C) (QN skeletal)
1508	ν(C=C) (Q ring) long axis	758	δw(C-H) (Q ring)
1450	δt(C-H) (QN ring)	550-600	$\nu(Pt\text{-}O_x)$

1421	δ(C-H) (Q ring)	516	o.o.p. δ(Q ring)
1365	ν(Q ring)	475	ν(Pt-C)
1263	ν(C^9-OH) / δ(C^9-H) / δ(C-H) (QN ring)	421	ν(Pt-N)
1205	δt($C-H_2$) (QN ring)		

The results obtained from adsorbed CD in $DCM_{(l)}$, $Ar/H_{2(g)}$ and $H_2SO_{4(aq)}$ were comparable to those obtained by Williams and co-workers [13]. In this respect, the results confirmed the findings of Hutchings and co-workers that an organic solvent was not a necessary component for the Orito reaction to work [19]. However, there was a limited level of control over the surface CD coverage in the gas phase dosing method and a lack of a soluble medium into which the modifier could desorb and from which could possibly re-adsorb. Absence of a surface-liquid dynamic of the modifier may have been the reason for mediocre enantioselectivities (51% *R*-methyl lactate) and no rate acceleration seen by the Hutchings group relative to the racemic reaction [19].

Using the assignments in Table 6.14 and according to the principles of SERS, it can be seen that most of the peaks observed with adsorbed CD could be assigned to vibrations from the quinoline ring, which augmented the theory that the modifier was tethered to the surface via this moiety. The broad shape to the peak at 1588 cm^{-1} was indicative of multiple sites in the adsorption geometry giving rise to ν(C=C) vibrations at slightly different frequencies. This finding was analogous to the interpretation formed from an STM study of CD on platinum{111} [3]. When hydrogen was added by sparging the solution with $H_{2(g)}$, the spectrum changed due to removal of oxidised fragments competing with CD as signified by the loss of the peak at 1697 cm^{-1} and a re-orientation of the CD molecules, a fact also noted in the paper by Williams [13]. The re-orientation could be a direct result of a close packing arrangement of the adsorbates caused by an increase in coverage. This could also explain the apparent conformity to the adsorption geometry of the CD molecules in the presence of hydrogen. The mechanism for adsorption was proposed by Burgi *et al* [8] to be through the nitrogen lone pair of electrons donated to the surface and a carbon in the α-position to the nitrogen ($C^{2'}$ (hydrogen abstracted)) and denoted as the α-quinolyl adsorption mode (Figure 6.1 b).

Under HER conditions, the reduction of the intensities of all bands was attributed to a removal of an undefined amount of adsorbed CD by hydrogenation of the Q ring, which was

known to occur under Orito reaction conditions [24]. It was thought that this then enabled subsequent adsorbing CD molecules to adopt a flatter orientation, which accounted for the increase in the out-of-plane peak intensities. Peaks from the QN ring were also seen to be resolved in this configuration, which suggested that this moiety was closer to the surface and this was thought to be advantageous for the enantiodifferentiation step. The re-orientation and removal of the modifier could also play a role in the initial transient period observed in the early stages of Orito type reactions [25]. During this time, the catalytic system was thought to be in a process of optimisation. Achieving the ideal coverage and adsorption geometry of the modifier may be a factor contributing to this latent effect.

The red shift of the ν(Pt-H) vibration for both QN and CD seen in the present study was indicative of an interaction between these adsorbates and chemisorbed hydrogen, which weakened the strength of the Pt-H bond. Acidic/protic solvents should protonate the QN nitrogen of the modifier and hence open the possibility of hydrogen bonding between the N-H and C=O of the reactant [26]. In aprotic solvents, the modifier is thought to abstract a hydrogen atom from the surface, thus restoring this N^{+}-H···O=C interaction [23]. The interaction between surface hydrogen and QN was manifested in this system by a red shift in frequency of the ν(Pt-H) vibration from 2085 to 2060 cm^{-1}. However, the red shift was less pronounced when CD was adsorbed (~10 cm^{-1}). A possible explanation could be based on an assumption that the QN ring on CD would be fixed at a position further away from the surface compared to free QN. The increased distance from the surface to the QN ring on CD would therefore lead to a weaker interaction with surface hydrogen and a less pronounced red shift of the ν(Pt-H) peak. Hence, it is proposed that under hydrogenating conditions, the QN ring of the modifier interacts with surface hydrogen causing the length of the Pt-H bond to increase and the strength of the bond to decrease. A weakened Pt-H bond may be thought of as advantageous for the rate of the Orito reaction and may explain the increase in rate seen from addition of achiral tertiary amines like QN to the reaction slurry [27]. However, a red shift from 2085 to 2060 cm^{-1} corresponds to only a 2% decrease in the frequency. Therefore, the change in force constant and hence strength of the bond was thought to be negligible. The theoretical calculations also show the hydrogen atom to become more positively charged at increased distances from the surface towards the tertiary nitrogen of CD [23]. Such a scenario would provide an increased electrostatic attraction towards nucleophiles (such as an activated ketone oxygen) causing a migration to the chiral pocket of the modified site via such electrostatic interactions.

A further observation from the concentration dependency studies was the attenuation of the ν(Pt-H) peak at 2075 cm^{-1} as the CD concentration increased. This was likely to be from CD blocking the surface at higher loadings, which was to be expected, but may have consequences for the reaction performance at these modifier coverages since chemisorbed hydrogen is obviously a key reaction intermediate.

6.2.3 Cinchonine

CN is the near enantiomer of CD and was used to produce the opposite enantiomer (e.g. *S*-methyl lactate in the hydrogenation of methyl pyruvate) during a platinum catalysed hydrogenation reaction [28]. The reaction performance with CN was slightly lower than when using CD and this has been interpreted as a slight difference in the adsorption geometries, caused as a consequence of the different position of the vinyl group [29]. On CD, the vinyl group is at C^3 on the QN ring, but is on C^5 with CN and this may have an effect on either the adsorption geometry or restriction of the rotation about the C8-C9 bond to form the 'open-3' conformer [97].

6.2.3.1 Cinchonine on Au@Pt Core-shell Nanoparticles in Sulphuric Acid

A study analogous to the experiments using CD was performed with CN in an attempt to observe a difference in the adsorption geometry between the two modifiers. Figure 6.13 shows the results from the potential dependency study of CN dissolved in 0.1 M sulphuric acid to a concentration of 5×10^{-5} M, adsorbed on platinum.

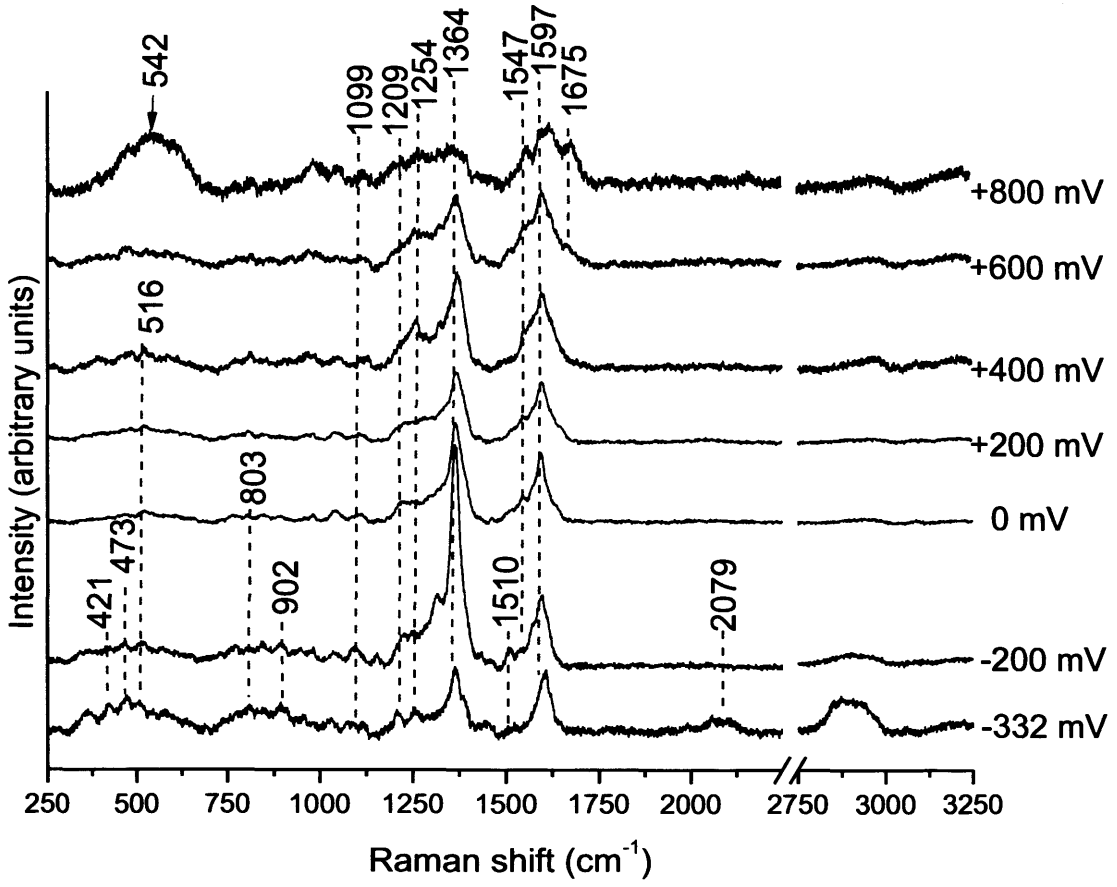

Figure 6.13 SER spectra of 5×10^{-5} M CN dissolved in 0.1 M H_2SO_4 adsorbed on Au@Pt CS-NP and held at a variety of potentials *vs.* Ag/AgCl in a negative scanning direction.

The same concentration of modifier in sulphuric acid and the same potentials at which the surface was probed were used for CN as for CD. The results showed the same broad features resolved at positive potentials including the presence of platinum oxide and the oxidised fragment at 1675 cm^{-1}, as found with CD. As the potential was scanned negative, the definition and intensity of all peaks improved and again was most pronounced for the peak corresponding to the stretch of the Q ring at 1364 cm^{-1}. In the HER potential region, this peak was again seen to decrease and out-of-plane peaks increased in intensity such as those at 900 and 516 cm^{-1}. The peaks assigned to ν(Pt-C) and ν(Pt-N) at 473 and 421 cm^{-1} of the α-quinolyl mode were again observed, as was the red shift to the peak from ν(Pt-H) 2079 cm^{-1}.

Figure 6.14 shows the results from the concentration dependency study of CN in 0.1 M sulphuric acid adsorbed on platinum. The same concentration increments were used as for the

CD experiments (except a concentration of 5×10^{-2} M was not used) and all samples were held at the same potential of -0.33 V.

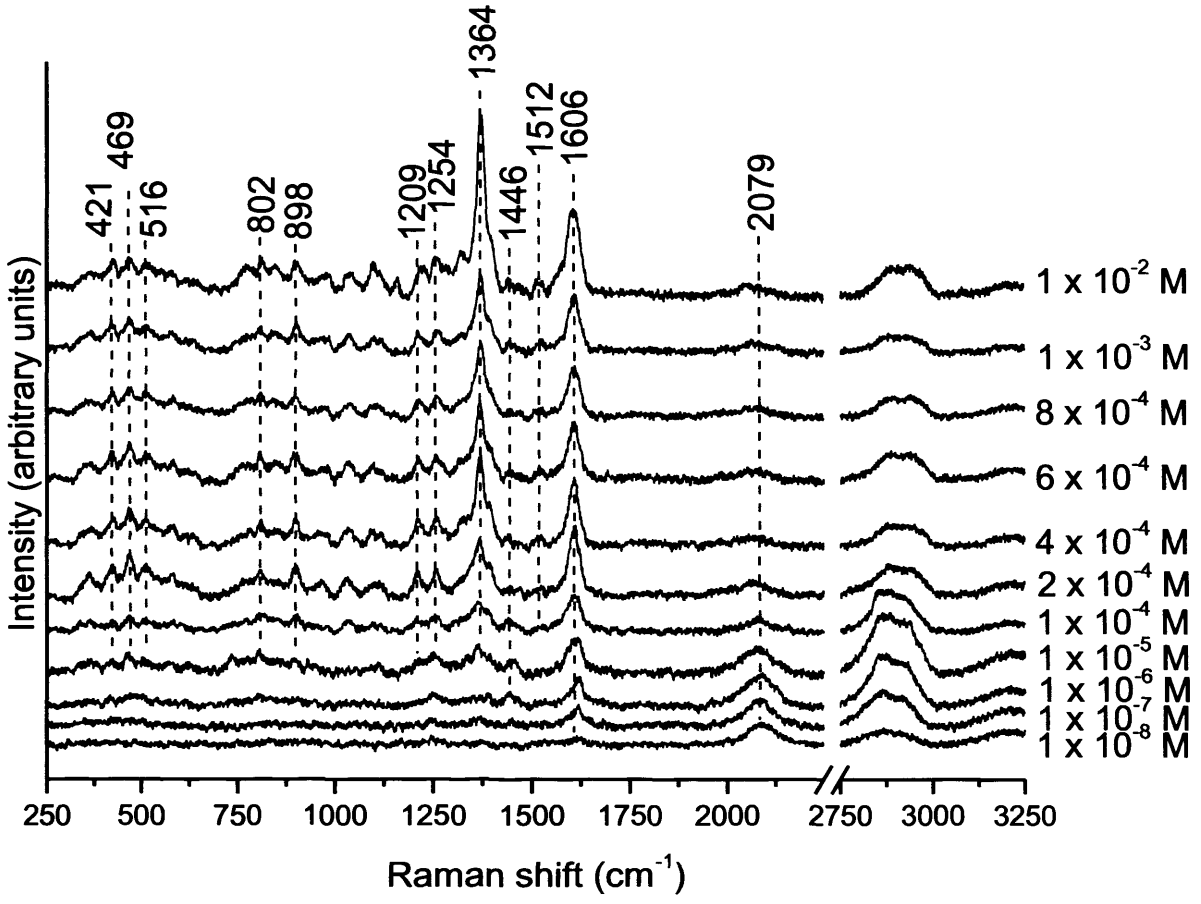

Figure 6.14 SER spectra of varying concentrations of CN dissolved in 0.1 M H_2SO_4 on Au@Pt CS-NP held at -0.33 V *vs.* Ag/AgCl.

The peak from the ν(C=C) short axis vibration at 1606 cm^{-1} was present at the lowest concentration. All in-plane peaks increased in intensity relative to the out-of-plane peaks with concentration, in particular the peak at 1364 cm^{-1}, which increased the most relative to the other in-plane peaks. The surface coverage of hydrogen was inversely proportional to the CN concentration.

6.2.3.2 Discussion of the Cinchonine Results

There were no clear differences between the SER spectra of CN and CD and so the adsorption geometry and band assignments were also assumed to be the same. This result was not in accord with the theory of a difference in the surface geometry between the two modifiers [97].

6.2.4 Quinine

Quinine (QNE) like CN has a very similar reaction performance to CD [30], but differs structurally with a methoxy group at $C^{6'}$. This subtle difference can be seen in the Raman spectrum with the absence of a peak at 516 cm^{-1} from the out-of-plane Q ring deformation, but may provide other features in the SER spectrum.

6.2.4.1 Quinine on Au@Pt Core-shell Nanoparticles in Sulphuric Acid

Figure 6.15 shows the results from the potential dependency study using the same parameters as the previous CD and CN experiments in sections 6.2.2.3 and 6.2.3.1, respectively.

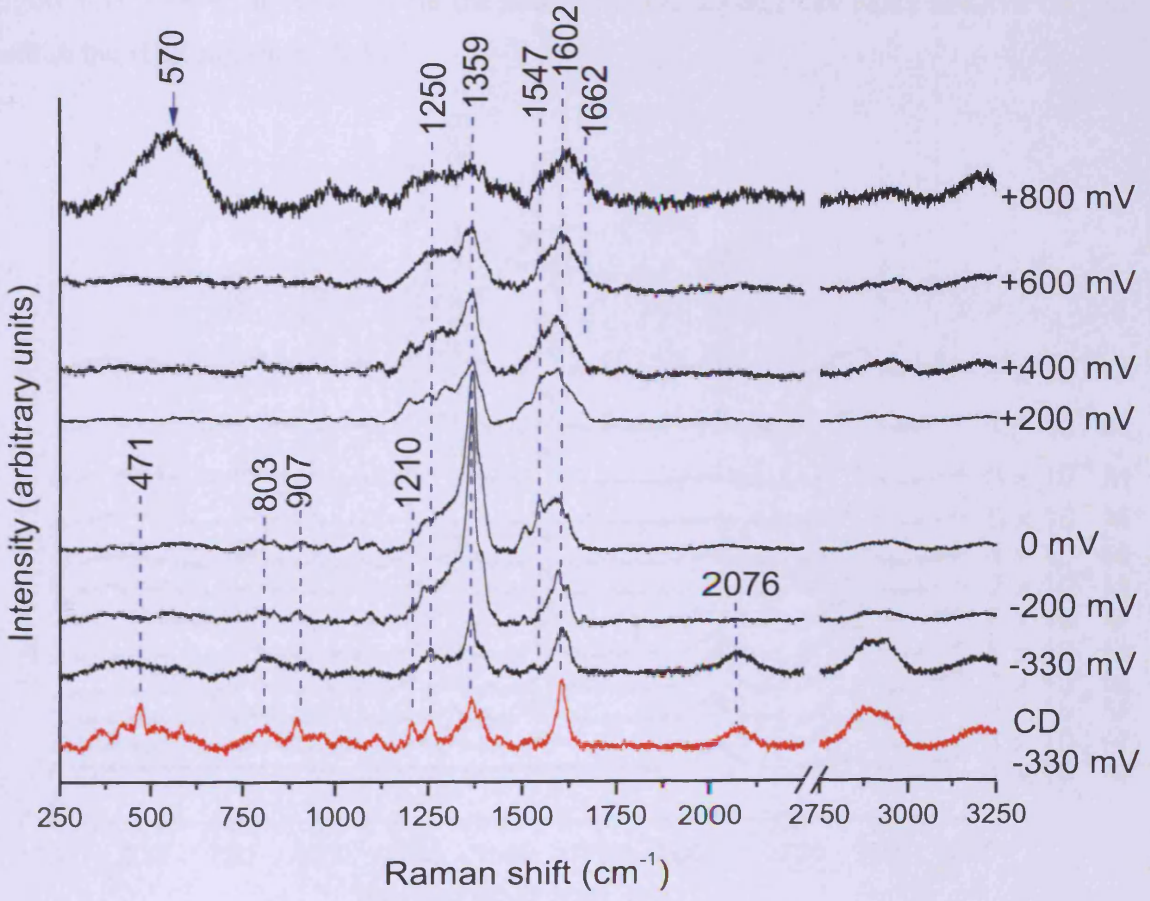

Figure 6.15 SER spectra of 5×10^{-5} M QNE dissolved in 0.1 M H_2SO_4 adsorbed on Au@Pt CS-NP and held at a variety of potentials *vs.* Ag/AgCl in a negative scanning direction.

The effect on the SER spectra at positive potentials was the same for QNE as for CD and CN with respect to the breadth, intensity and ratio of intensities of the peaks and the presence of platinum oxide. As the potential was scanned negative, the peaks became narrow and more intense. However, there was a notable decrease in the quality of some of the peaks resolved in

the QNE spectra compared to CD and CN. The peaks at 907 and 1210 cm^{-1} were poorly resolved and the three peaks around 500 cm^{-1} assigned to an out-of-plane Q ring deformation, ν(Pt-C) and ν(Pt-N) for CD and CN appeared absent altogether. It was unclear as to why the peaks below 1000 cm^{-1} were poorly defined, but this was attributed to the methoxy group at $C^{6'}$. Nonetheless, it could be seen that the broad features around 900 and 800 cm^{-1} did increase in intensity as the potential was scanned into the HER region. Like CD and CN, this was ascribed to a more flat adsorption geometry. The ν(Pt-H) peak was again red shifted by nearly 10 cm^{-1}.

Figure 6.16 shows the results from the concentration dependency study of QNE on platinum held in the HER region at -0.33 V.

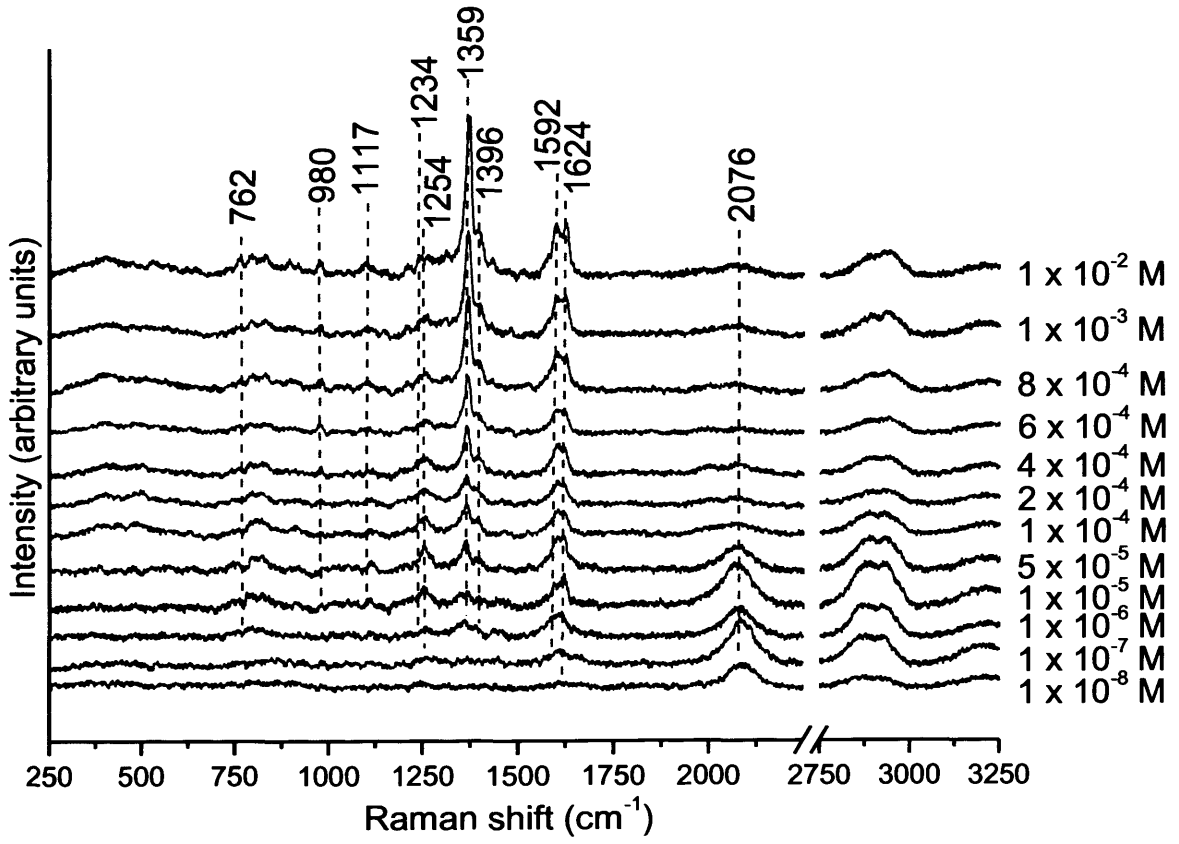

Figure 6.16 SER spectra of varying concentrations of QNE dissolved in 0.1 M H_2SO_4 on Au@Pt CS-NP held at -0.33 V *vs.* Ag/AgCl.

As expected the 1359 cm^{-1} band from the quinoline ring stretch was absent at first and then grew in intensity to dominate the spectrum. Also, the intensity of the 2076 cm^{-1} band from the Pt-H stretch was reduced as the modifier coverage was increased. The out-of-plane peaks

including 1117 and 762 cm^{-1} again appeared to be more pronounced at lower concentrations than at high concentrations. But, the out-of-plane ring deformation and the two surface peaks below 500 cm^{-1} were still not present. The resolution of the ν(C=C) band at the higher frequency of 1624 cm^{-1} was likely to be an effect of the methoxy group at $C^{6'}$ on the Q ring.

6.2.4.2 Discussion of the Quinine Results

Given that the only significant difference between CD and QNE was the methoxy group, it was unlikely to have a different mode for adsorption. Like many of the peaks for adsorbed QNE, the definition was poor and this was thought to be due to other peaks associated with the methoxy group occurring at similar frequencies which would appear to broaden the observed peak. The frequency range between 300 and 650 cm^{-1} did appear very broad. Therefore, the resolution of the surface peaks in this region could be masked by this behaviour. Alternatively, the electronic effects of the methoxy group may inhibit the abstraction of a hydrogen atom from the carbon in the α-position to the Q ring nitrogen and hence prevent the formation of the α-quinolyl mode.

6.2.5 Hydroquinine-4-chlorobenzoate

HQnClB like QNE has a methoxy group at $C^{6'}$, but differs structurally in two other ways with a protonated vinyl group and a chlorobenzoate group substituting the hydroxyl group at C^{9}. More interestingly, inversion of enantioselectivity has been observed when the concentration of this modifier was high [31]. The study concluded that an ester linkage at C^{9} was a structural requirement for the modifier in order to observe inversion and because the reactions were carried out in the gas phase, the phenomenon was independent of solvent effects. The reason for the inversion of enantioselectivity was speculated as being a dominant occupation of the modifier at high energy defect surface sites at low concentrations which produced the expected enantiomer. At high concentrations the modifier spilled over onto the low energy terrace sites which were responsible for the different enantiodiscrimination (so long as an ester linkage at C^{9} on the modifier remained intact [31]). Due to either a faster rate or a greater number of sites on the terraces, the opposite enantiomer was produced at quantities over and above the expected enantiomer being generated at the high energy defect sites. This theory does not take into account the re-orientation of the modifier when the concentration was high as demonstrated here and in previous publications for CD. This section aims to address this possibility with an investigation of HQnClB dissolved in

sulphuric acid and introduced to the platinum electrode at different potentials and concentrations.

6.2.5.1 Hydroquinine-4-chlorobenzoate on Au@Pt Core-shell Nanoparticles in Sulphuric Acid

Figure 6.17 shows the results from the potential dependency study performed on HQnClB dissolved to a concentration of 5×10^{-5} M in sulphuric acid using the same parameters as the previous potential dependency studies outlined in section 6.2.2.3.

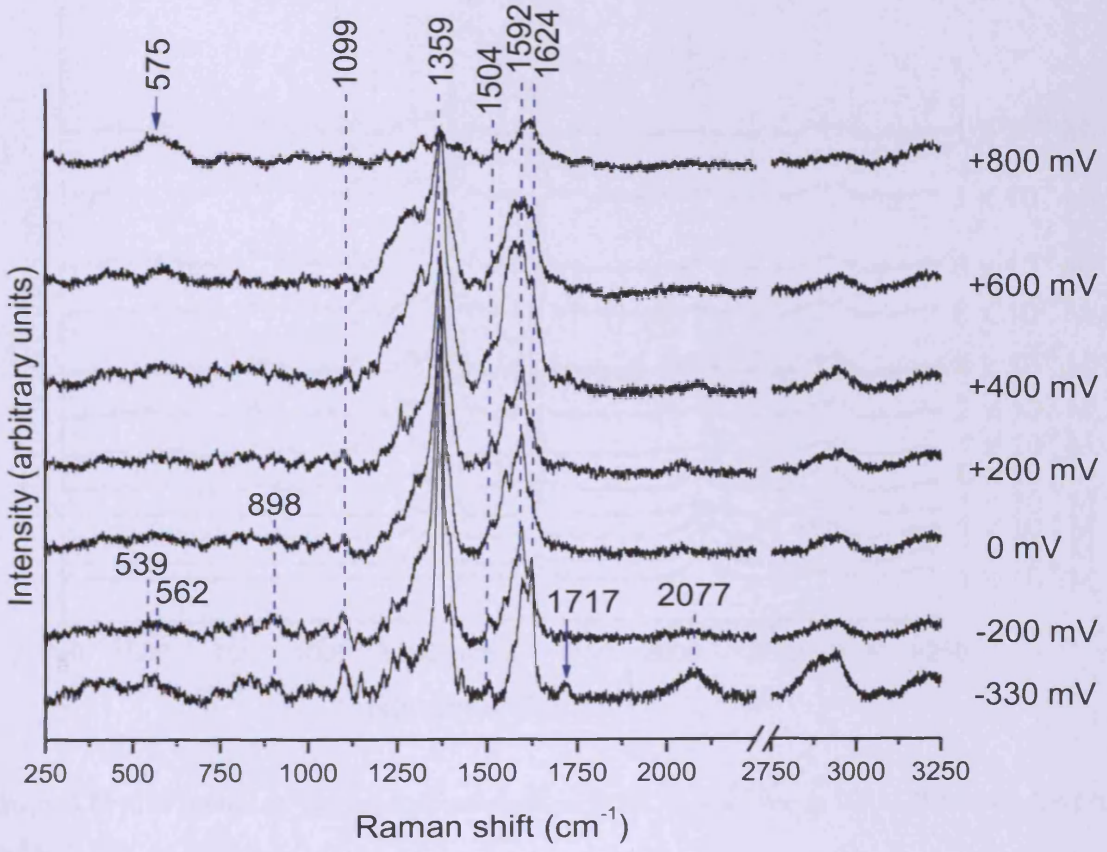

Figure 6.17 SER spectra of 5×10^{-5} M HQnClB dissolved in 0.1 M H_2SO_4 adsorbed on Au@Pt CS-NP and held at a variety of potentials *vs.* Ag/AgCl in a negative scanning direction.

As the potential was made more negative, the same effects as seen with the other modifiers of narrowing of SERS peaks to give improved definition were seen. Like QNE, the peaks below 1000 cm^{-1} were broad and poorly resolved, but did increase in intensity when the potential was set in the HER region. Compared to QNE, extra peaks were clearly resolved including 1099 and 1721 cm^{-1} which were all associated with the chlorobenzoate group and were

particularly prominent when the potential was in the HER region. But other similarities did exist like the peak 1624 cm^{-1} from ν(C=C) proximal to the methoxy group at C6′ and a red shift of the ν(Pt-H) peak to 2077 cm^{-1}.

Figure 6.18 shows the results obtained from a concentration dependency study of HQnClB on platinum held in the HER region at -0.33 V.

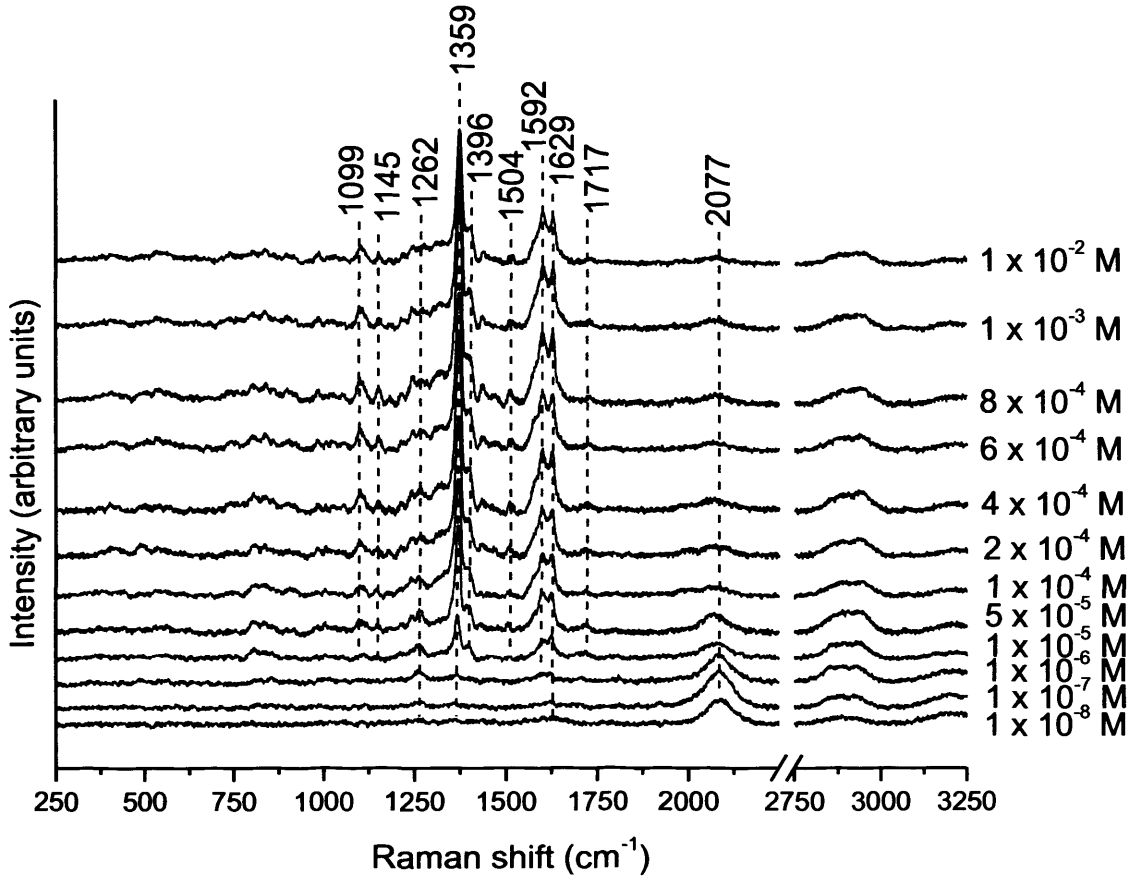

Figure 6.18 SER spectra of varying concentrations of HQnClB dissolved in 0.1 M H_2SO_4 on Au@Pt CS-NP held at -0.33 V *vs.* Ag/AgCl.

Like for the other modifiers, the in-plane peaks (e.g. 1592 cm^{-1}) of HQnClB increased in intensity relative to the out-of-plane peaks (e.g. 1145 cm^{-1}) as the concentration increased and was most pronounced for the peak at 1359 cm^{-1}. Again, the quantity of adsorbed hydrogen decreased with increasing concentration.

The peaks at 1717 and 1099 cm^{-1} were both assigned to in-plane peaks of the chlorobenzoate group. As such, this group was considered to be tilted with respect to the surface plane at these surface coverages.

6.2.5.2 Discussion of the Hydroquinine-4-chlorobenzoate Results

The band assignments for adsorbed HQnClB are summarised in Table 6.15 below.

Table 6.15 Band assignments for SER spectra of HQnClB on Au@Pt CS-NP.

Band Position HQnClB	Assignment	Band Position HQnClB	Assignment
2077	ν(Pt-H)	1210	δt(C-H_2) (QN ring)
1717	ν(C=O)	1144	δw(C-H) (Q ring)
1629	ν(C=C) conjugated to methoxy group (Q ring) / (phenyl)	1099	ν(C-Cl) / ν(ring) (benzoyl)
1596	ν(C=C) (Q ring, short axis)	898	δw(C-H) (Q ring) / δ(QN)
1569	ν(C=C) (Q ring, short axis)	803	ν(C-C) (QN skeletal)
1504	ν(C=C) (Q ring, long axis)	758	δw(C-H) (Q ring)
1460	δt(C-H) (QN ring)	575	ν(Pt-O_x)
1428	δ(C-H) (Q ring)	562	ν(C-Cl)
1365	ν(Q ring)	539	o.o.p. δ(Q ring)
1263	ν(C^9-OH) / δ(C^9-H) / δ(C-H) (QN ring)		

Previous work by Hutchings *et al* showed that solvent interaction was not responsible for the inversion of enantioselectivity using HQnClB [31]. However, the solubility of the modifier in a solvent is likely to have an effect on the concentrations required to observe the inversion. In their article, Hutchings quoted two concentrations of 0.85 and 8.5 mM g_{cat}^{-1} to premodify the catalyst [31]. In the concentrations used in the present study, very little change was observed in 0.1 M sulphuric acid.

6.2.6 Discussion of Modifier Adsorption Geometry

As the coverage of oxide decreased, the coverage of the modifier increased. As the coverage of the modifier increased, the plane of the Q ring tilts away from the surface to allow for a closely packed arrangement. However, at HER potentials where the surface coverage of hydrogen was high, the Q ring moiety of each of the modifiers tested was shown to tilt closer to the surface plane, in a flatter adsorption geometry such as that required for the "open 3" conformation thought to be involved in the enantiodifferentiation step [35]. This indicated

that the modifier coverage had reduced and allowed space for the plane of the Q ring to return to a flat arrangement. However, at the concentrations used in this study, the Q ring was not completely flat as proposed by several authors [2-12]. As the solution concentration of the modifier increased, so did the tilt of the Q ring away from the surface and this phenomenon was again attributed to a close packing arrangement (Figure 6.19).

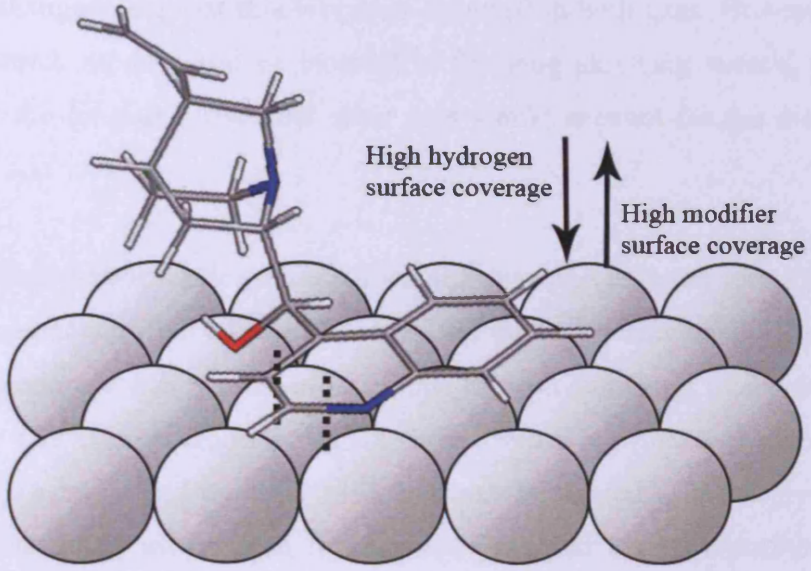

Figure 6.19 Adsorption geometry via the π-states of the cinchona modifier. Arrows indicate tendency for the Q ring to tilt towards or away from the surface.

Although for CD and CN two peaks did resolve at 471 and 428 cm^{-1}, which were assigned to ν(Pt-C) and ν(Pt-N) vibrations characteristic of the α-quinolyl adsorption mode (Figure 6.1 b). These peaks were not seen for QNE or HQnClB under similar conditions. It is suggested here that the methoxy group at $C^{6'}$ either possessed SERS active vibrations at similar frequencies thereby causing the peak shape to broaden and become indiscernible, or that electronic effects prevented the formation of the metal-molecule bonds ascribable to an "α-quinolyl" species. In the latter case, the mechanism for adsorption was thought to be through the aromatic π-system associated with the flat adsorption mode. However, due to the tilt of the Q ring, the π-bonding was thought to be localised between N-$C^{2'}$-$C^{3'}$ (Figure 6.19). Deuterium experiments by Solladie-Cavallo and co-workers, found that deuterium exchange occurred the most for $C^{2'}$ and $C^{3'}$ [22], which would suggest a greater interaction with the surface for these atoms and would support a tilted angle hinged at these atoms. This would be consistent with either the α-quinolyl mode or the "localised π-states" mode [8].

It was unclear as to why the peak at 1355 cm^{-1} increased in intensity over and above the other in-plane peaks around 1588 cm^{-1} in the presence of hydrogen. Zaera and colleagues had identified a long axis ν(C=C) vibration of the quinoline ring at 1516 cm^{-1} [9], which did appear to increase relative to the 1606 cm^{-1} band with concentration. The principle stretching axis of the ring stretching mode that gave rise to the peak at 1362 cm^{-1} was not commented on by Zaera *et al* suggesting that this vibration occurred in both axes. However, if the peak from the ring stretch mode could be isolated to the long axis ring stretch, then a greater degree of tilt of the long axis over the short axis would account for the different relative intensities.

In terms of reaction performance, the enantioselectivity and reaction rate increased as the modifier solution concentration increased and passed through a maximum [32]. The decrease in ee after the maximum was presumed to be due to an overloading of the modifier on the catalyst surface. The concentration at which these events occurred was dependant on the choice of solvent, catalyst and modifier [33], but may be related to the degree at which the quinoline ring was tilted away from the surface [34] and also the surface coverage of hydrogen being influenced by the tertiary nitrogen of the QN group.

6.3 Conclusion

The adsorption behaviour of cinchona modifiers on platinum has been studied by SERS in several environments including organic and aqueous solvents and in the gas phase. In the absence of hydrogen, several configurations of the modifier were adsorbed in a number of different configurations in line with the observations made by Baiker *et al* in their STM study of CD on platinum{111} [3]. In the presence of hydrogen, the modifier coverage increased initially due to the desorption of oxide which blocks the uptake of CD. In addition, the range of different adsorption modes decreased. Due to a close packing arrangement of the modifier at high coverage, the Q ring tilts away from the surface. At high hydrogen coverage (analogous to reaction conditions), some of the adsorbed modifier was removed due to the hydrogenation of the Q ring [24]. The removal of the modifier from the surface was thought to be a factor in allowing the remaining adsorbed and newly adsorbing modifier species to adopt a flatter geometry to the surface plane approaching the "open 3" configuration [35]. Achieving the optimal coverage and adsorption geometry of the modifier may be the reason for the initial transient period observed during the early stages of Orito type reactions.

The surface coverage of hydrogen was noted to decrease at higher modifier loading and this too may be causing a drop in reaction rate as the surface becomes overloaded with modifier [36]. Furthermore, it was noticed that the ν(Pt-H) vibration, which normally appeared at 2085 cm^{-1} was found to resolve at ~2075 cm^{-1} in the presence of a modifier and at 2060 cm^{-1} in the presence of QN. This red shift may be attributed to an interaction between the lone pair on the nitrogen of QN and the surface hydrogen, which caused a lengthening and a weakening of the Pt-H bond. The addition of QN to the reaction mixture was found to be beneficial to the rate (i.e. the rate increased by a factor of 6.5 compared to the racemic reaction in the absence of CD [37] and by a factor of ~5 in the enantioselective reaction [38] in the presence of CD). A weaker Pt-H bond would be consistent with an increase in rate and it is proposed here that it may be a factor in QN's ability to enhance the rate. In terms of the rate enhancement phenomenon, a weakened Pt-H bond would lower the activation energy for hydrogen transfer to the reactant ketone in a similar mechanism described for the "Ligand Acceleration" theory [39]. However, it is again stressed that the vibrational shift of the ν(Pt-H) was only minor and so this feature is likely to have only a minor effect on the rate. The charge of the hydrogen atom on the surface has previously been reported to become more positive as the bond length increased [23]. It is therefore speculated that the force of an electrostatic attraction between the nucleophilic, activated ketone oxygen of the α-ketoester and the more electrophilic surface hydrogen in the chiral pocket could attract the ketone towards the chiral pocket.

6.4 References

[1] Y. Orito, S. Imai, S. Niwa, *J. Chem. Soc. Jpn.*, **1979**, 8, 1118.

[2] A.F. Carley, M.K. Rajumon, M.W. Roberts, P.B. Wells, *J. Chem. Soc. Faraday Trans.*, **1995**, 91, 2167-2172.

[3] M. von Arx, M. Wahl, T. A. Jung, A Baiker, *Phys . Chem. Chem. Phys.*, **2005**, 7 , 273–277.

[4] G.A. Attard, J.E. Gillies, C.A. Harris, D.J. Jenkins, P. Johnston, M.A. Price, D.J. Watson, P.B. Wells, *Appl. Catal. A: General*, 222 (**2001**) 393–405.

[5] Y. Sun, J. Wang, C. LeBlond, R.N. Landau, D. G. Blackmond, *J. Catal.*, 161, 759–765 (**1996**).

[6] E. Orglmeister, T. Mallat, A. Baiker, *J. Catal.*, 233 (**2005**) 333–341.

[7] T. Evans, A.P. Woodhead, A. Gutierrez-Soza, G. Thornton, T.J. Hall, A.A. Davis, N.A. Young, P.B. Wells, R.J. Oldman, O. Plashkevych, O. Vahtras, H. Agren, V. Carravetta, *Surf. Sci.*, **1999**, 436, L691-L696.

[8] D. Ferri, T. Burgi, *J. Am. Chem. Soc.*, **2001**, 123, 12074-12084.

[9] Z. Ma, I. Lee, F. Zaera, *J. Am. Chem. Soc.*, **2007**, 129, 16083-16090.

[10] R. J. LeBlanc, C. T. Williams, *J. Mol. Catal. A: Chem.*, 220 (**2004**) 207–214.

[11] T. A. Martineka, T. Varga, F. Fülöp, M. Bartók, *J. Catal.* 246 (**2007**) 266–276

[12] A. Vargas, A. Baiker, *J. Catal.* 239 (**2006**) 220–226.

[13] R.J. LeBlanc, W. Chu, C.T. Williams, *J. Mol. Catal. A: Chem.* 212 (**2004**) 277–289.

[14] Socrates, G. Infrared & Raman Characteristic Group Frequencies. (3rd Edn) John Wiley: Chichester, UK, 2004.

[15] http://www.chem.uni-potsdam.de/

[16] W. Chu, R.J. LeBlanc, C.T. Williams, J. Kubota, F. Zaera, *J. Phys. Chem. B* **2003**, 107, 14365-14373.

[17] J.R. Durig, D.W. Wertz, *Appl. Spectrosc.* 22, 6, (**1968**) , 627-633.

[18] Z. Ma, F. Zaera, *J. Phys. Chem. B*, **2005**, 109, 406-414.

[19] M. von Arx, N. Dummer, D.J. Willock, S.H. Taylor, R.P.K. Wells, P.B. Wells, G.J. Hutchings, *Chem. Commun.*, **2003**, 1926–1927.

[20] M. Vago, F. J. Williams, E. J. Calvo, *Electrochem. Commun.*, 9 (**2007**) 2725–2728.

[21] G.A. Attard, C. Harris, E. Herrero, J Feliu, *Faraday Discuss.*, **2002**, 121, 253–266.

[22] A. Solladie-Cavallo, F. Hoernel, M. Schmitt, F. Garin, *Tetrahedron Lett.*, 43 (**2002**) 2671–2673.

[23] A. Vargas, D. Ferri, A. Baiker, J. Catal., 236 (2005) 1–8.

[24] K. Balázsik, M. Bartók, *J. Catal.*, 224 (**2004**) 463–472.

[25] J. Wang, Y. Sun, C. LeBlond, R.N. Landau, D.G. Blackmond, *J. Catal.*, 161, 752–758 (**1996**).

[26] K.E. Simons, G. Wang, T. Heinz, T. Giger, T. Mallat, A. Pfaltz and A. Baiker, Tetrahedron Asymm., 6 (1995) 505.

[27] J.L. Margitfalvi, E. Talas, M. Hegedus, *Chem. Commun.* (**1999**) 645.

[28] D.M. Meier, D. Ferri, T. Mallat, A. Baiker, *J. Catal.*, 248 (**2007**) 68–76.

[29] M. Bartok, M Sutyinszki, K. Balazsik, G. Szollsi, *Catal. Lett.*, 100, 3–4, **2005**.

[30] H. U. Blaser, H. P. Jalett, W. Lottenbach, M. Studer, *J. Am. Chem. Soc.*, **2000**, 122 (51), 12675-12682

[31] N. Dummer, R. Jenkins, X. Li, S. Bawaked, P. McMorn, A. Burrows, C. Kiely, R. Wells, D. Willock, G. Hutchings, *J. Catal.*, 243 (**2006**) 165–170.

[32] L. Xing, F. Dub, J-J. Liang, Y-S. Chenb, Q-L. Zhou, *J. Mol. Catal. A: Chem.*, 276 (**2007**) 191–196.

[33] H-U. Blaser, M. Studer, *Acc. Chem. Res.*, 40, 12 (**2007**) 1348-1356.

[34] J. Kubota, F. Zaera, *J. Am. Chem. Soc.*, **2001**, 123, 11115-11116.

[35] A. Vargas, T. Bürgi, A. Baiker, *J. Catal.*, 226 (**2004**) 69–82.

[36] H.U. Blaser, M. Garland, H.P. Jalett, *J. Catal.*, 144 (**1993**) 569.

[37] G. Bond, P.A. Meheux, A. Ibbotson, P.B. Wells, *Catal. Today*, 10 (**1991**) 371.

[38] J.L. Margitfalvi, E. Talas, M. Hegedus, *Chem. Commun.*, **1999**, 645–646.

[39] T. Burgi, A. Baiker, *Acc. Chem. Res.*, **2004**, 37, 909-917.

Chapter 7
Co-adsorption of α-Ketoesters with Cinchona Modifiers on Platinum Surfaces

7.1 Introduction

Since Orito's discovery in 1979 [1], several hypotheses on the origin of the enantioselectivity have emerged (see chapter 1, section 1.3.9). Currently, the most widely accepted model is that of Baiker *et al* who proposed a 1:1 interaction between the modifier and reactant on the catalyst surface [2]. Within this model, the adsorbed modifier creates a chiral pocket into which the reactant can dock with the modifier by one or more hydrogen bond(s). However, the exact mechanism for enantiodiscrimination is not yet thoroughly understood and unequivocal evidence to support this theory is yet to be reported.

Similarly, the rate enhancement commonly seen with modified catalysts over unmodified catalysts is not totally understood. As discussed in chapter 1, section 1.3.10, two main theories for the rate enhancement have been developed. These are a "suppression of catalyst deactivation" by the modifier and "ligand acceleration". The former theory addressed the issue of side reactions such as aldol condensation, which would produce polymeric species of α-ketoesters and a decarbonylation reaction that would produce carbon monoxide (CO) and other adsorbed fragments [3,4]. These products could feasibly block reaction sites and if the modifier prevented the formation or removed such products, then the rate would be accelerated. The ligand acceleration theory suggested that a specific interaction with the activated ketone would further destabilise this substituent and make it more susceptible to hydrogenation. Therefore, the reaction at a modified site would be faster than at an unmodified site [5].

This chapter aims to address these two key areas of the Orito reaction with SER spectra of cinchona modifiers co-adsorbed on Au@Pt core-shell nanoparticles with the prochiral carbonyl reactants. Most experiments were conducted in the liquid phase using an aqueous electrolyte and holding the potential of the SERS active working electrode at -0.33 V (versus a silver/silver-chloride reference electrode) to simulate high pressure hydrogenation reaction conditions.

7.2 Ethyl Pyruvate Co-adsorbed with Cinchonidine

Cinchonidine (CD) was structurally the simplest of the cinchona alkaloid family extracted from cinchona bark. When used to chirally modify a platinum catalyst in the hydrogenation of α-ketoesters, the *R*-hydroxyester was produced in excess of the *S*-enantiomer [1]. Methyl pyruvate (MP) and ethyl pyruvate (EP) are two of the simplest forms of α-ketoesters and have been used in archetypal reaction studies of Orito-type chemistry including the one presented here.

From the studies conducted in chapter 4, no vibration from a carbonyl group was observed from SER spectra of the reactant. This was rationalised by the formation of the half-hydrogenated state (HHS), which involved a conversion of the ketone to an alcohol and the ν(C=O) mode of the ester carbonyl vibrating in a vector parallel to the surface plane, therefore becoming SERS inactive. Hence, the interactions between modifier and reactant described by Baiker [2] and McBreen [6], which involved carbonyl groups, may not be seen under the present conditions since the chiral outcome has already been set once the HHS has formed.

7.2.1 Ethyl Pyruvate and Cinchonidine on Au@Pt Core-shell Nanoparticles in Sulphuric Acid

Two methods of dosing were used to study the co-adsorption behaviour on Au@Pt Core-shell Nanoparticles (CS-NP). The first involved the introduction of both reactant and modifier dissolved in the same solution ('co-adsorbed') and the second involved pre-modification of the surface followed by the introduction of the reactant ('pre-modified'). Figure 7.1 shows the spectra obtained for EP co-adsorbed with CD and for EP on a surface pre-modified with CD. The corresponding band assignments are presented in Table 7.16. SER spectra of singly adsorbed EP and CD are both included for comparison.

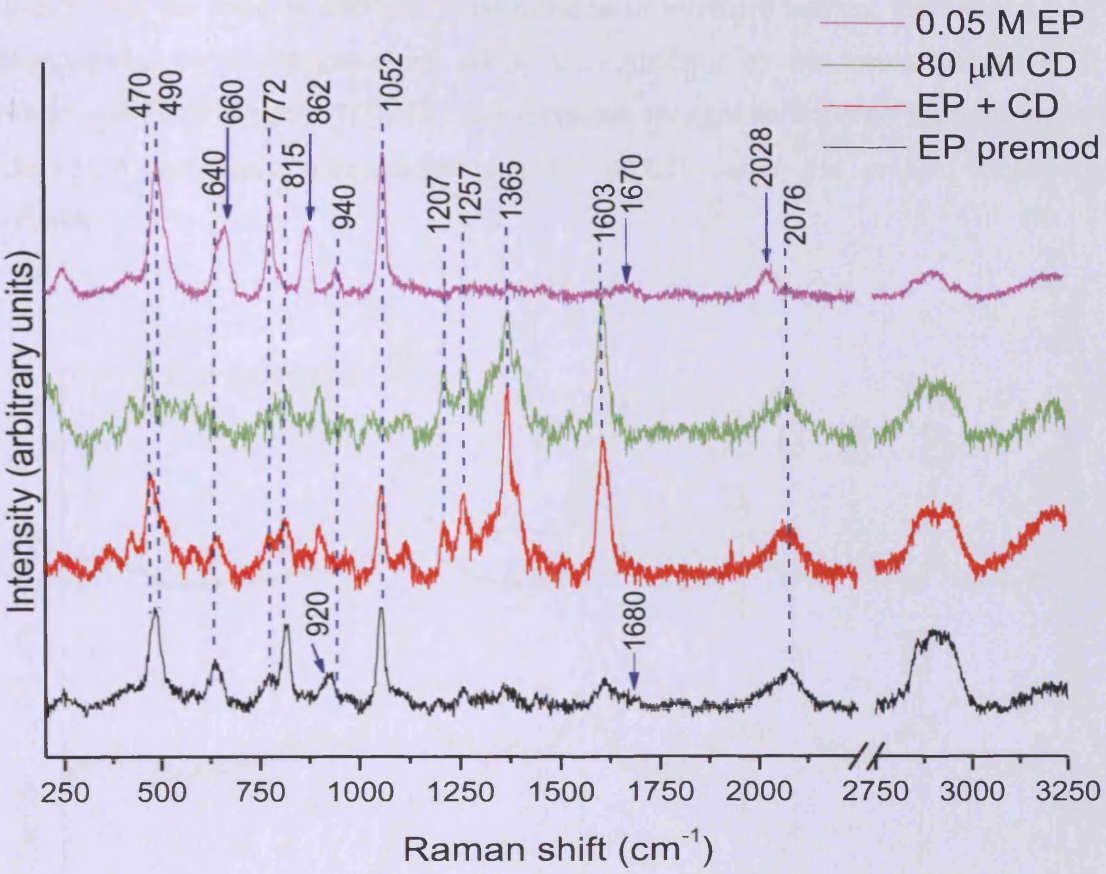

Figure 7.1 SER spectra of EP, CD, EP + CD co-adsorbed and EP pre-modified with CD on Au@Pt CS-NP at -0.33 V *vs.* Ag/AgCl.

Upon comparing the green and red spectra, the peaks from adsorbed CD remained largely unaffected by the presence of the HHS of EP. The ν(Pt-H) peak was also noted to remain at a position red shifted by ~10 cm^{-1} to 2076 cm^{-1}, a feature noted in chapter 6 with adsorption of cinchona modifiers. No peaks that corresponded to carbonyl vibrational modes were seen to emerge except for a broad and weak feature at 1680 cm^{-1} observed with EP adsorbed on a pre-modified surface (black spectrum). This could be assigned to a ν(C=O) vibration red shifted by a hydrogen bonding interaction with the adsorbed modifier. However, it was difficult to discern when EP was co-adsorbed with the modifier (red spectrum) and it may be confused with the normal Raman peak at 1670 cm^{-1} from a δs(H-O-H) vibration of water seen in the singly adsorbed EP (magenta) spectrum.

There were also some notable changes in the spectrum of the HHS of EP when co-adsorbed with CD. These were best seen when CD was used to pre-modify the platinum surface. The peak at 937 cm^{-1} was downshifted to 920 cm^{-1}, the peak at 865 cm^{-1} was replaced by a peak at

820 cm^{-1} and the peak at 660 cm^{-1} was reduced in intensity leaving the band at 636 cm^{-1}. Unfortunately, these changes could all be accounted for by the formation of the HHS of pyruvic acid (PA) (Figure 7.2). EP was therefore thought to undergo saponification in the presence of the basic quinuclidine moiety of CD under the present electrochemical conditions.

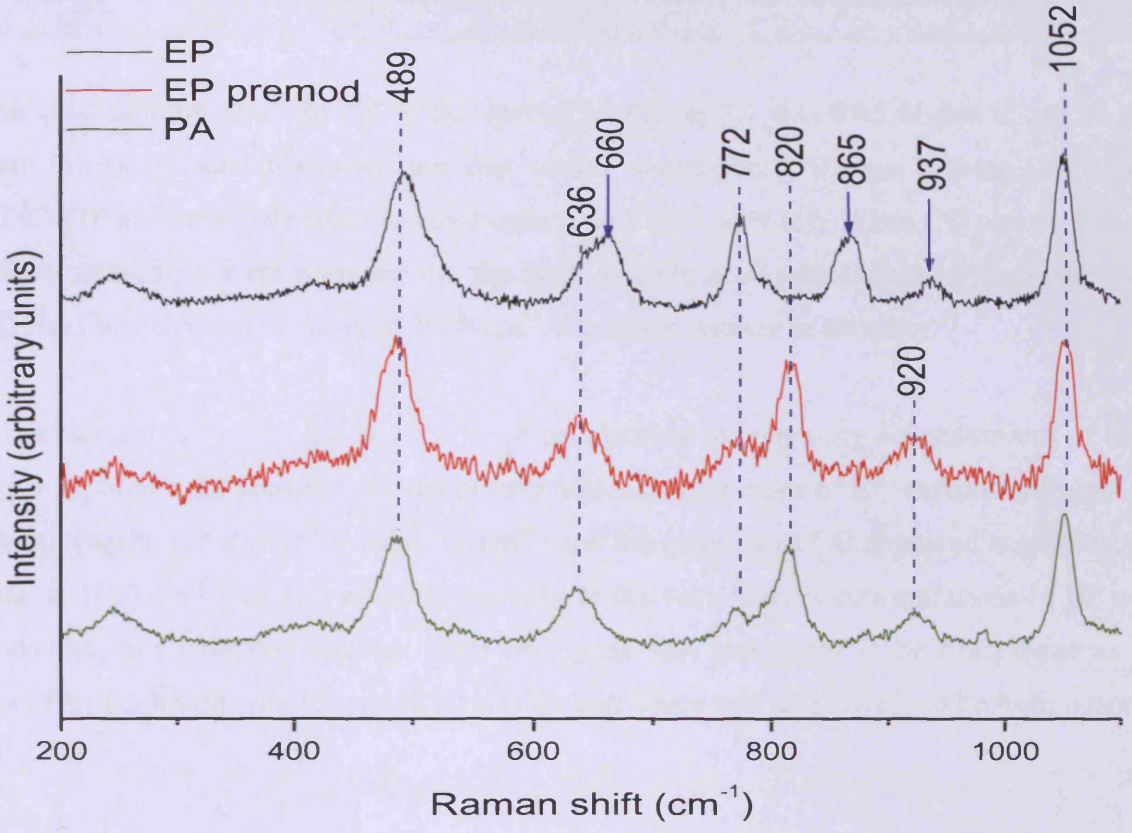

Figure 7.2 SER spectra of EP on Au@Pt CS-NP (black) and EP on Au@Pt CS-NP pre-modified with CD (red) and PA (green) on Au@Pt CS-NP at -0.33 V *vs.* Ag/AgCl.

Table 7.16 Band assignments.

Band position (cm^{-1})				Assignment
EP	**CD**	**EP + CD**	**EP premod**	
	2076	2076	2076	ν(Pt-H)
2028	-	-	-	ν(PtC≡O)
-	1603	1603	1603	ν(C=C) (Q ring) short axis
-	1365	1365	1365	i.p. ν(Q ring)
-	1257	1257	1257	ν(C^9-OH) / δ(C^9-H) / δ(C-H) (QN ring)
-	1207	1207	1207	δt(C-H_2) (QN ring)
1052	-	1052	1052	ν(C^2-C^3H_3) / δr(C^3-H_3) / δr(O-H)
937	-	-	-	δr(C^3-H_3) / va(O-C^2-C^1) / vs(O-C^4-C^5) / skeletal

-	-	-	915	va(O-C^4-C^5) / skeletal (PA)
	900			i.p. δ(C^4-C^9-C^8)
862	-	-	-	vs(C^1-O-C^4) / δr(C^5-H_3) / v(C^2-OH)
-	-	815	815	v(C^1-OH) / v(C^2-OH) (PA)
772	-	772	772	umbrella(C^3-C^2(OH)-C^1) about C^2 / δr(C^3-H_3)
660	-	-	-	δw(O-H)
640	-	640	640	δw(O-H) / v(Pt-C^2) / δr(C^3-H_3)
490	-	490	490	v(Pt-C^2) (EP) / v(Pt-CO)
-	470	470	470	v(Pt-C) (CD)

The concentration used for EP in the spectra in Figure 7.1 was 0.05 M and it can be seen from the singly adsorbed spectrum that carbon monoxide (CO) was present (2028 cm^{-1}, v(PtC≡O)) and very little adsorbed hydrogen (2086 cm^{-1}, v(Pt-H)). When CD was present, the relative intensities were reversed i.e. the peak at 2076 cm^{-1} (red shifted by the presence of CD) was stronger and the peak at 2028 cm^{-1} was much weaker in intensity.

To further test this effect, EP and CD were co-adsorbed at increasing concentrations of EP up to 0.1 M. Figure 7.3 shows that even at very high concentrations of EP, surface hydrogen was present (again, red shifted by some 10 cm^{-1}) and the quantity of CO appeared negligible. The peak at 1680 cm^{-1} was also present, but only at the very highest concentrations of EP used. Therefore, this indicated that the 1680 cm^{-1} peak was less likely to be from water as this would be a constant feature seen in all spectra and hence was more likely to be from adsorbed EP.

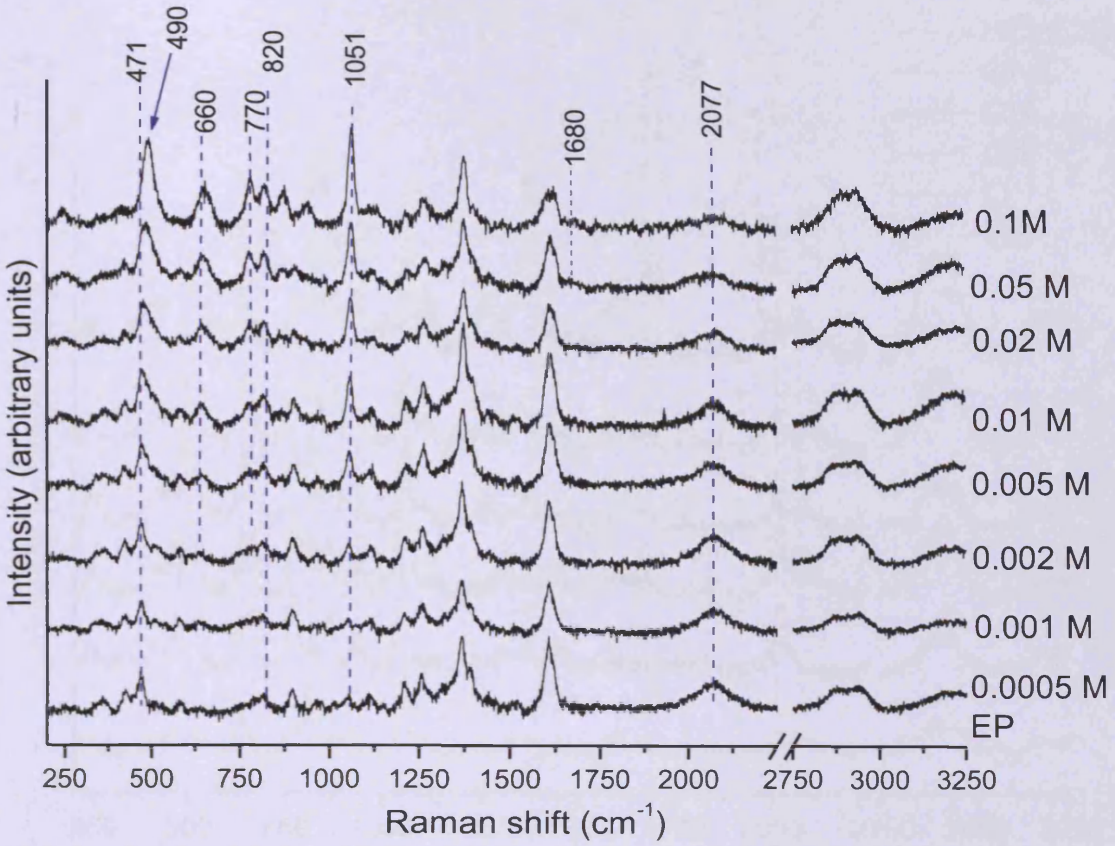

Figure 7.3 SER spectra of CD co-adsorbed with different concentrations of EP on Au@Pt CS-NP @ -0.33 V *vs.* Ag/AgCl.

7.2.2 Ethyl Pyruvate Co-adsorbed with Other Modifiers on Au@Pt Core-shell Nanoparticles

Other modifiers of the cinchona family have been used with measured success for the enantioselective hydrogenation of EP on platinum. Four of these modifiers, including CD, were investigated in Chapter 6 and were re-examined here for their interactions with EP. These included cinchonine (CN), quinine (QNE) and hydroquinine 4-chlorobenzoate (HQnClB).

Pre-modified surfaces were used to study co-adsorption between EP and the respective modifier as the changes to the EP spectrum were more pronounced when the surface was pre-modified with CD. Figure 7.4 shows the spectra of EP adsorbed on pre-modified surfaces, including the cinchona substituent ring systems; quinuclidine (QN) and quinoline (Q), at potentials corresponding to HER.

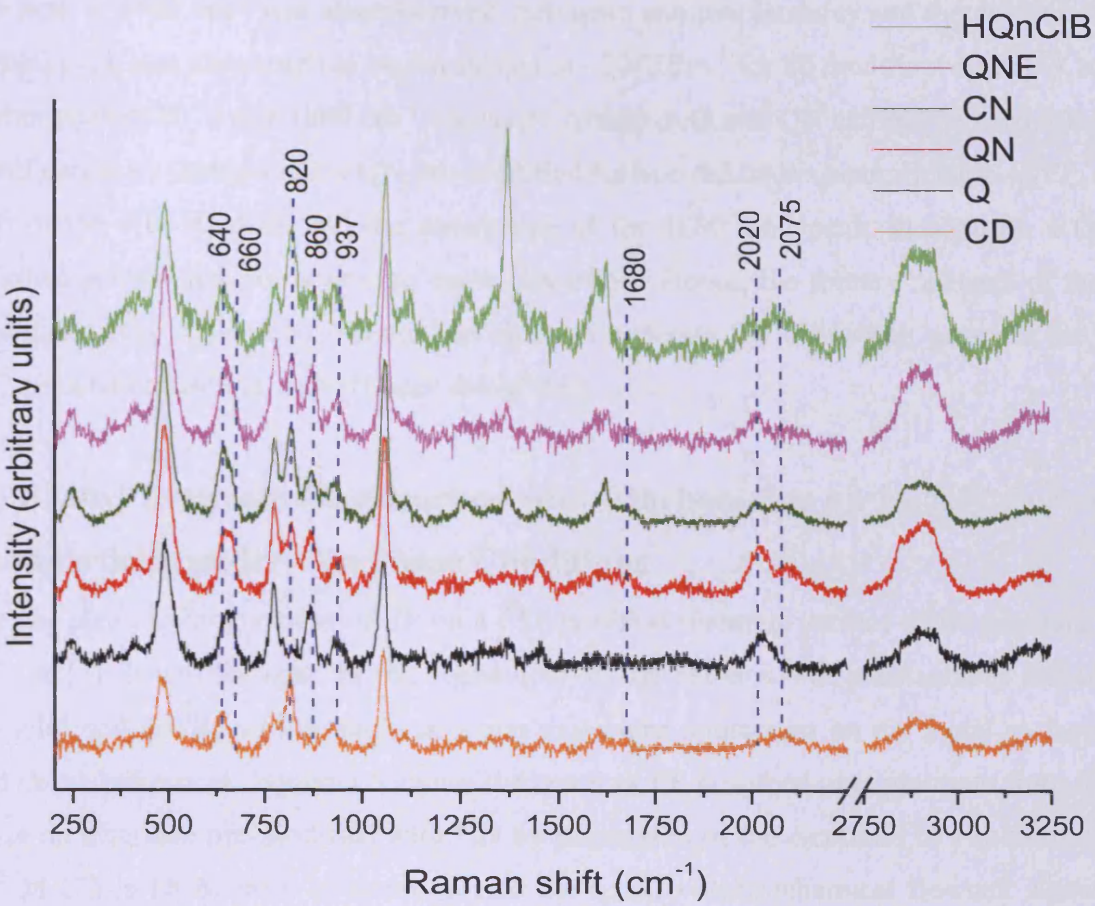

Figure 7.4 SER spectra of 0.1 M EP adsorbed on Au@Pt CS-NP pre-modified using ~7 × 10^{-5} M modifier solution @ -0.33 V *vs.* Ag/AgCl using various modifiers.

As observed with CD, the formation of the HHS of PA was also seen after pre-adsorption with all other modifiers (except Q), which gave rise to the spectral changes to the HHS of EP (937 cm^{-1} was red shifted, 862 cm^{-1} was lower in intensity, 820 cm^{-1} was newly emerged and 660 cm^{-1} was red shifted/lower in intensity). But, unlike with CD, the saponification reaction did not occur throughout all adsorbed HHS intermediates i.e. there were some features of the EP-HHS (937 cm^{-1} was not shifted as much, 862 cm^{-1} was still resolved albeit lower in intensity as was the 660 cm^{-1}). Also, the degree to which the changes occurred was different for each modifier. Interestingly, the intensity of the peaks for adsorbed HQnClB remained relatively strong, which indicated that the coverage of this modifier was high compared to the other modifiers under the same conditions and may have been a factor in the comparatively high level of saponification caused by this modifier.

The peak at 1680 cm^{-1} was also observed, but again at a low intensity and the position of the ν(Pt-H) peak was also noted to be red shifted to ~2075 cm^{-1} for all modifiers except Q, where neither peak at 2075 nor 1680 cm^{-1} was seen. Although Q and QN can not be used for chiral modification by themselves, a QN pre-modified surface did cause saponification of EP, a red shift of the ν(Pt-H) peak and the emergence of the 1680 cm^{-1} peak. In contrast, a Q pre-modified surface did not appear to cause any effect. Hence, the tertiary nitrogen of the QN substituent was considered essential in order to generate PA formation, generate the 1680 cm^{-1} peak and cause the ν(Pt-H) peak to red shift.

7.2.3 Ethyl Pyruvate Co-adsorbed with Cinchonidine on Au@Pt Core-shell Nanoparticles under Gas Phase Conditions

The gas phase hydrogenation of EP on a CD modified platinum surface could generate up to 51% ee [7]. It was thought that the behaviour of the reaction was substantially different at gas/solid and gas/liquid interfaces and that molecular interaction on the metal surface may also show differences. Figure 7.5 shows the result of EP adsorbed onto platinum from the gas phase on a surface pre-modified with CD by immersion of the electrode in a solution of 2×10^{-5} M CD in DCM prior to insertion into the spectro-electrochemical flowcell. Spectra of singly adsorbed CD and EP are included for comparison.

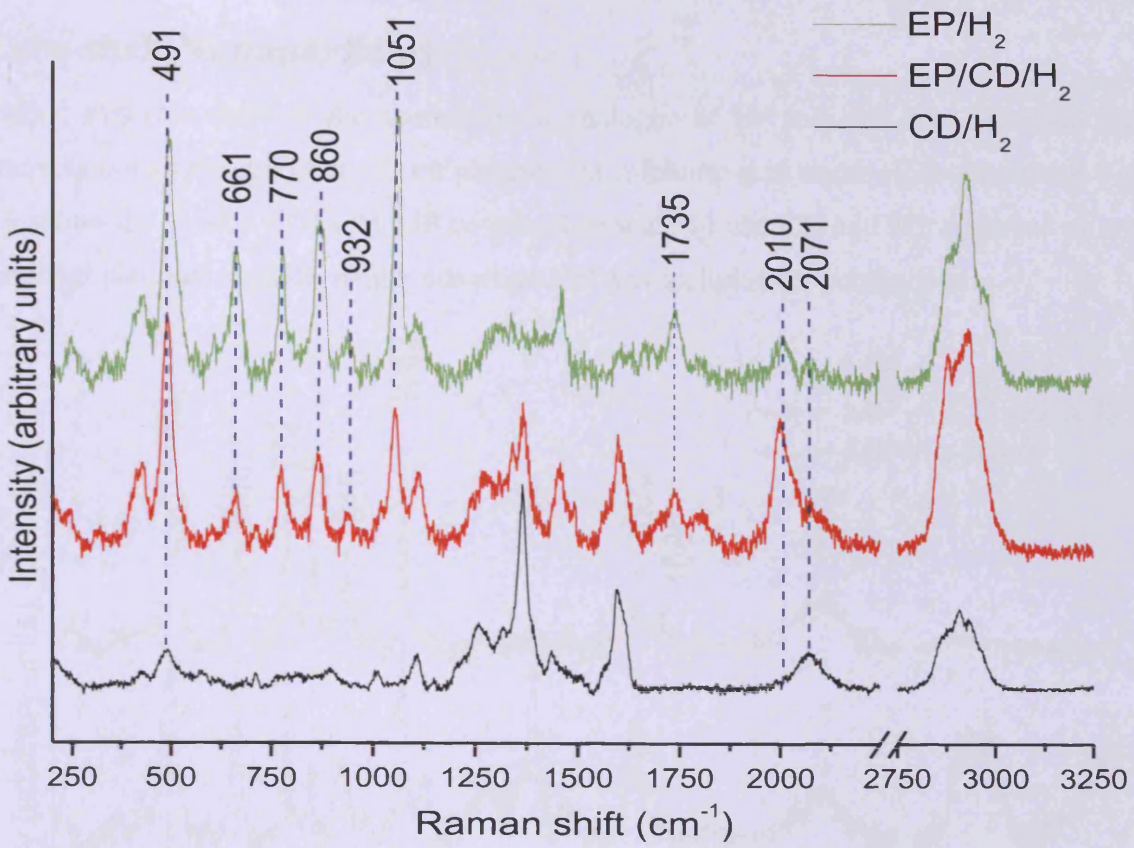

Figure 7.5 SER spectra of gas phase EP co-adsorbed with CD on Au@Pt CS-NP under H_2.

The spectrum of EP co-adsorbed with CD did not show the spectral changes seen in the equivalent experiment under electrochemical HER conditions. The absence of the PA peaks indicated that the saponification side reaction did not occur when EP was dosed in the gas phase. The peak at 1735 cm^{-1} was assigned to a ν(C=O) vibration. However, in chapter 4, this was shown to be from a condensed layer of physisorbed species formed under gas phase conditions. There was no shift to the 1735 cm^{-1} peak and it was difficult to discern a peak at 1680 cm^{-1} observed under electrochemical conditions, so an interaction with the modifier could not be determined. Also, the peak from adsorbed CO was seen to prevail even with CD present. Nonetheless, adsorbed hydrogen was also seen from the shoulder at 2071 cm^{-1}.

7.3 Methyl Pyruvate Co-adsorbed with Cinchonidine on Au@Pt Core-shell Nanoparticles

Methyl pyruvate (MP) is the shorter chain analogue of EP and was also examined for an interaction with the modifier CD on platinum in sulphuric acid under HER conditions. Figure 7.6 shows the spectra of 0.1 M MP co-adsorbed with 80 μM CD and MP adsorbed on a pre-modified platinum surface, singly adsorbed MP was included for comparison.

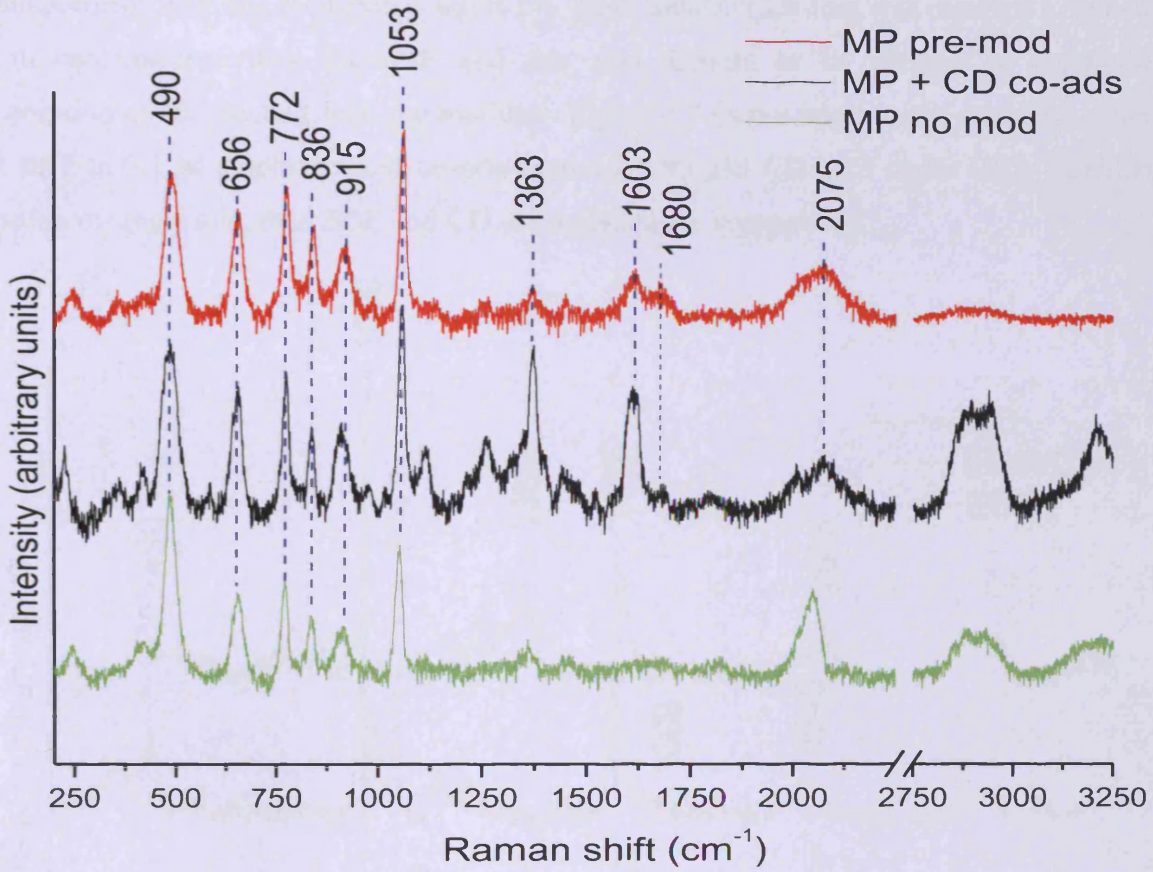

Figure 7.6 SER spectra of 0.1 M MP co-adsorbed with 80 μM CD on Au@Pt CS-NP @ -0.33 V *vs.* Ag/AgCl.

Unexpectedly, the saponification reaction seen with the HHS of EP when co-adsorbed with CD under electrochemical conditions, was not seen with the HHS of MP. Analogous to the EP results at high pyruvate concentrations, the presence of surface hydrogen when CD was co-adsorbed was detected, but not when MP was singly adsorbed. The position of the ν(Pt-H) peak was again red shifted to 2075 cm^{-1}. The weak and broad peak seen at 1680 cm^{-1} for EP co-adsorbed with modifiers was also observed for MP co-adsorbed with CD and on a pre-modified surface.

7.4 Ethyl Benzoylformate Co-adsorbed with Cinchonidine on Au@Pt Core-shell Nanoparticles

Similar to the results with EP, ethyl benzoylformate (EBF) was found to form a half-hydrogenated state on platinum in the presence of hydrogen (Chapter 4 section 4.2.6). Very high enantioselectivities have been reported (98% *R*-ethyl mandelate [8]), but at a slow reaction rate relative to EP with, depending on the solvent used, minimal or no observed rate enhancement from the modified catalyst [9]. High modifier loading was required to generate high enantioselectivities for EBF and this was thought to be because of competitive adsorption of the reactant with the modifier. Figure 7.7 shows spectra of a saturated solution of EBF in 0.1 M sulphuric acid co-adsorbed with 80 μM CD held under HER conditions, spectra of singly adsorbed EBF and CD are included for comparison.

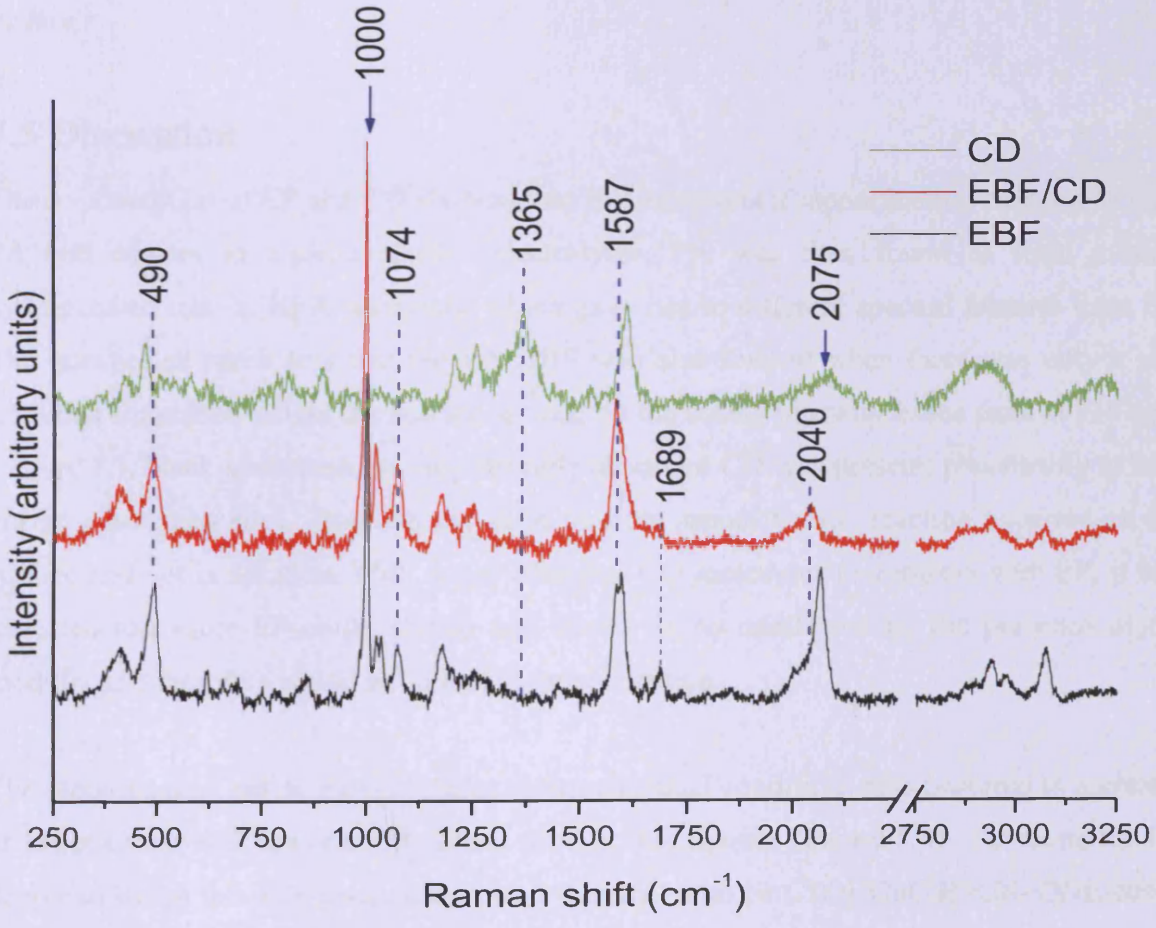

Figure 7.7 SER spectra of EBF co-adsorbed with CD on Au@Pt CS-NP @ -0.33 V *vs.* Ag/AgCl.

From the spectrum of co-adsorbed EBF and CD, the intensity of the CD peaks was significantly reduced, showing that very little CD was on the surface. As reported from the studies on enantioselective hydrogenation of EBF, the reactant could have competed for surface sites with CD [8,44] and this explanation may be responsible for the weak spectral features from CD. This was believed to be exacerbated in this system by the low solubility of EBF in 0.1 M sulphuric acid, which could have led to an organic/aqueous partition of EBF on the surface. The peak at 1689 cm^{-1} was assigned to a ν(C=O) of the neat liquid Raman spectrum and confirmed the presence of a physisorbed state. The high coverage and competitive adsorption of EBF could have led to a small amount of surface CD being stable. The most significant finding was the ν(PtC≡O) (2040 cm^{-1}) peak from adsorbed CO was much lower with CD present, but no peaks from adsorbed hydrogen were resolved. Like for MP, no spectral changes to adsorbed EBF were seen when co-adsorbed with CD on the surface.

7.5 Discussion

The co-adsorption of EP and CD showed that EP underwent a saponification reaction to form PA and ethanol in aqueous acidic electrolytes. PA was then found to form a half-hydrogenated state at HER potentials, which gave rise to different spectral features from EP. The unexpected result was that the PA-HHS was also formed when there was only a pre-adsorbed amount of CD on the surface as seen by the strong intensity in the peak at 815 cm^{-1} (Figure 7.1, black spectrum) i.e. only strongly adsorbed CD was present, presumably at high energy adsorption sites. This was evidence that the saponification reaction occurred on the surface and not in solution. With fewer adsorbed CD molecules to compete with EP, it was expected that more EP could adsorb and would do so unaffected by the presence of the modifier and therefore would not undergo saponification.

The saponification reaction of EP under electrochemical conditions also occurred to a greater or lesser extent with the other modifiers used in this chapter (Figure 7.4). The trend for the degree to which this side reaction occurred was shown to be CD≥HQnClB>CN≥QNE based on the relative intensity of the 860 cm^{-1} peak of EP-HHS to the 815 cm^{-1} peak of PA-HHS. The reason for this trend was unclear and would require further experimentation. However, from experiments on the non-linear effect (NLE) it was found that the adsorption strength of three of the modifiers on platinum descended in the order CD>CN>QNE in toluene, but in

acetic acid the order descended CD>QNE>CN [10,11]. No report of the relative adsorption strength of HQnClB could be found in the literature. However, the intensity of the HQnClB peaks after pre-modification was noted to be high. Therefore, the degree of saponification of EP could be related to the quantity of the adsorbed modifier that remained after modification at HER potentials. Interestingly, saponification was not recorded for MP under electrochemical conditions (Figure 7.6) or for EP under gas phase conditions (Figure 7.5). Therefore, it was evidently caused by the presence of an aqueous acidic phase and a longer alkyl chain. The absence of PA when EP is co-adsorbed with Q also suggested that the tertiary nitrogen of the QN ring was crucial to this transformation.

From the co-adsorption studies of CD with varying concentrations of EP, it can be seen that adsorbed hydrogen was always present, but most notably, was still present at high concentrations of EP where previously it was absent (chapter 4, Figure 4.17). The same effect was noted to occur with other modifiers and for high coverages of the HHS of MP co-adsorbed with CD. In addition, the amount of adsorbed CO was much less in these co-adsorption measurements. Hence, the decarbonylation reaction was able to occur, but was significantly curtailed by CD. This could be explained if the hydrogenation reaction was faster than the decarbonylation reaction. By increasing the coverage of hydrogen, as seen in the presence of CD, the hydrogenation reaction pathway would be promoted and the decarbonylation reaction pathway would be suppressed. Conversely, if hydrogen was blocked from adsorbing on the surface by a high coverage of HHS, as seen in the absence of CD, the hydrogenation reaction pathway would be suppressed, which would direct adsorbates down the decarbonylation pathway. Therefore the rate of the hydrogenation reaction appears to be dependent on the coverage of hydrogen, which at high concentrations of EP is directly related to the coverage and lifetime of the HHS.

This situation was more pronounced with EBF (Figure 7.7) and with gas phase dosing of EP (Figure 7.5) where a high coverage of CO and a low coverage of hydrogen was observed. Due to the low solubility of EBF in sulphuric acid and a condensed layer of EP in the gas phase dosing experiment, the coverage of these two adsorbates was considered to be high. The result of the high coverage of the EBF and gas phase EP HHS was that hydrogen was

inhibited towards adsorbing on the surface[†††]. Therefore the decarbonylation reaction could proliferate and adsorbed CO would be present in relatively high quantities. Clearly, CO would also block hydrogen from adsorbing and further impede the hydrogenation reaction. This concurs with the lack of rate enhancement observed for the reaction of EBF [44] and of EP under gas phase conditions [7].

The peak at 1680 cm^{-1} observed for EP/MP co-adsorbed with a modifier could be assigned to a ν(C=O) vibration red shifted from a hydrogen bonding interaction between a carbonyl group and the modifier. If it is considered that the peak is from a vibration of the HHS, then it must be from the ester carbonyl group. The peak was not seen for EP on a surface pre-modified with Q, but it was present when pre-modified with QN. Hence, the hydrogen bond formation was considered to occur between the ester carbonyl and a protonated nitrogen (ammonium ion) on the QN ring as described by McBreen *et al* in their 2-point hydrogen bond complex [6] (see section 1.3.10.3). Alternatively, the hydrogen bond could form between the ammonium ion and the keto carbonyl prior to the formation of the HHS as described by Baiker *et al* [12]. However, the intensity of this peak is weak and does not appear when the coverage of the modifier is high. Also, EP was shown to form the HHS of PA in the presence of a modifier, which would be hydrogenated to form lactic acid and not the expected product; ethyl lactate. Therefore, further investigation into this feature is required in order to draw a sound conclusion for its appearance.

It is universally accepted that the cinchona modifiers chemisorb via the Q moiety and that the QN ring is implicated in the interaction with the reactant possibly to produce rate enhancement and enantioselectivity [13]. From the results presented in Figure 7.4, this view could be supported in the present study as there were clear interactions with QN but not with Q. It was interesting to note that QN also promoted adsorbed hydrogen at high EP concentrations and did so without possessing an aromatic ring with which to bind to the surface. Conversely, the ν(Pt-H) peak was not seen with Q, which was wholly aromatic. Hence the donation of charge to the platinum surface hydrogen via the lone-pair of electrons from the nitrogen of the tertiary amine appeared to promote adsorption of hydrogen even at

[†††] Surface hydrogen formation under gas phase conditions was also inhibited by the extra energy required to dissociate the H-H bond compared to electrochemical conditions where H atoms were formed from protons in the electrolyte.

high EP coverages, analogous to the action of a chiral modifier. This feature was thought to be the source of QN's ability to enhance the rate [14].

7.6 Conclusion

Surface hydrogen is a commonly overlooked and poorly understood reaction intermediate in Orito type reactions. By assuming the reaction order for surface hydrogen is greater than zero, it can be expected that by increasing the availability of surface hydrogen results in an increase in the reaction rate.

The observed increase in surface hydrogen coverage on platinum with a high coverage of either MP or EP adsorbed in the presence of a modifier is thought to result in an increase in the rate of reaction. This is compared to a platinum surface with a high coverage of MP/EP, but in the absence of a modifier where surface hydrogen coverage was found to be negligible. Based on this observation it is clear that the modifier promotes adsorption of hydrogen under the experimental conditions used in this study and is thought to contribute significantly to the rate enhancement phenomenon.

7.7 References

[1] Y. Orito, S. Imai, S.J. Niwa, *Chem. Soc. Jpn.*, **1979**, 8, 1118.

[2] H.U. Blaser, H.P. Jalett, D.M. Monti, A. Baiker, J.T. Wehrli, *Stud. Surf. Sci. Catal.* 67 **(1991)** 147.

[3] D. Ferri, T. Burgi, A. Baiker, *J. Phys. Chem. B*, **2004**, 108, 14384-14391.

[4] D.J. Jenkins, A.M.S. Alabdulrahman, G.A. Attard, K.G. Griffin, P. Johnston, P.B. Wells, *J. Catal.*, 234 **(2005)** 230–239.

[5] M. Garland, H.U. Blaser, *J. Am. Chem. Soc.*, **1990**, 112, 7048.

[6] S. Lavoie, M-A. Laliberte, I. Temprano, P.H. McBreen, *J. Am. Chem. Soc.* **2006**, 128, 7588-7593.

[7] M. von Arx, N. Dummer, D.J. Willock, S.H. Taylor, R.P.K. Wells, P.B. Wells, G.J. Hutchings, *Chem. Commun.*, **2003**, 1926–1927.

[8] M. Sutyinszki, K. Szori, K. Felfoldi, M. Bartok, *Catal. Commun.* 3 **(2002)** 125–127.

[9] E. Toukoniitty, P. Maki-Arvela, N. Kumar, T. Salmi, D. Yu. Murzin, *Catal. Lett.*, 95, 3–4, **2004**.

[10] M. Bartok, M Sutyinszki, K. Balazsik, G. Szollsi, *Catal. Lett.*, 100, 3–4, **2005**.

[11] D.M. Meier, D. Ferri, T. Mallat, A. Baiker, *J. Catal.* 248 (**2007**) 68–76.

[12] T. Burgi, A. Baiker, *Acc. Chem. Res.* **2004**, 37, 909-917.

[13] H-U. Blaser, M. Studer, *Acc. Chem. Res.*, 40, 12 (**2007**) 1348-1356.

[14] J.L. Margitfalvi, E. Talas, M. Hegedus, *Chem. Commun.* (**1999**) 645.

Chapter 8
Conclusion

8.1 The Study

Two crucial questions faced by the scientific community involved in the study of the Orito reaction may be summarised as follows:

1. How does the chiral modifier discriminate between the formation of one enantiomer and the other to an enantiomeric excess (ee) > 90%?
2. Why is the rate accelerated on a cinchona-modified surface compared to an unmodified surface?

To address these two questions Surface Enhanced Raman Scattering, Density Functional Theory and Cyclic Voltammetry have been used to study the surface behaviour of reactants and modifiers used in the Orito reaction. These surface science techniques have led to the extraction of molecular adsorption information of the reaction components on nanoparticulate and well defined platinum and palladium surfaces at simulated reaction conditions. The following chapter aims to summarise the key conclusions drawn from this study and the implications they present to the concepts currently understood about the Orito reaction.

8.2 Rate Enhancement and the Initial Transient Period

As discussed in chapter 1, section 1.3.10 the rate enhancement phenomenon is the increased rate of hydrogenation on a modified surface compared to an unmodified surface [1] and the initial transient period is the time taken from the beginning of a reaction for the performance to reach maximum rate and enantioselectivity [2]. The two theories that address these features are summarised below.

8.2.1 Suppression of Catalyst Deactivation

Suppression of catalyst deactivation is based on side reactions that produce catalytic poisons in the racemic reaction. The addition of a modifier was thought to prevent such side reactions from occurring and/or remove the products leading to an increase in catalytic sites [3,4]. These side reactions would include decarbonylation of the pyruvate ester on platinum to form

adsorbed CO and oligomerisation of the pyruvate ester to produce high molecular mass products (HMMP) catalysed by the basic amine-type modifiers in solution [5]. It was thought that on the surface, the modifier cinchonidine (CD) could prevent such reactions [3]. Murzin *et al* found that at low concentrations of the reactant ethyl pyruvate (EP), the rate of the racemic reaction was similar to that of the enantioselective reaction, viz, no enhancement [6]. The ee for the enantioselective reaction at low EP concentration was noted to be >80%, which indicated that the enantiodifferentiation interaction did occur, but without a ligand-type acceleration. The authors predicted that it was due to catalyst deactivation at high reactant concentrations.

8.2.2 Ligand Acceleration

Ligand acceleration is based on a specific interaction between the reactant and modifier that is responsible for rate enhancement, similar to that seen in homogeneous catalytic reactions [1]. If oligomerisation and decarbonylation reactions were occurring to an appreciable extent that would cause rate enhancement in the enantioselective reaction, then it was presumed that in the racemic reaction the catalyst surface would become progressively more blocked leading to an observable attenuation of the rate of hydrogenation [7]. This was shown to be case when the reaction was carried out in aprotic solvents [8]. However, when acetic acid was used, no such catalyst deactivation could be observed, yet the rate was still enhanced in the enantioselective reaction [9]. The formation of HMMPs was also eliminated by Margitfalvi *et al* who conducted reactions by introducing the reactant via an injector at the last possible moment to minimise contact with solution phase modifier which could cause oligomerisation [10]. In fact, these authors found the best rates were achieved when injection was not performed i.e. there was the opportunity for the oligomerisation reaction and if it had occurred then it certainly was not detrimental to the rate. Both Margitfalvi [10] and Baiker [7] had no direct evidence of a ligand type interaction that would cause the rate to enhance, but were able to eliminate the products of side reactions and their suppression by a modifier as being the cause for rate acceleration.

Experiments with different modifiers in a continuous flow reactor revealed a slower rate of the EP hydrogenation reaction with cinchonine (CN) than with quinine (QNE) when the modifier solution was switched from the latter to the former [11]. It was also found that the rate would return to a high value when the solution was switched back to QNE. The authors

found that the rate changed reliably with the modifier and that such regularity cannot be associated with catalyst deactivation. Furthermore, this non-linear effect (NLE) was reversed for the hydrogenation of ketopantolactone, i.e. rate and enantioselectivity improved when the modifier was switched from QNE to CN [12]. Therefore the difference in rate was more likely to be from a kinetic effect such as a difference in a ligand-type interaction.

8.3 The 'Hydrogen Availability' Model

Neither of the two models described above were independently able to fully account for all the empirical findings concerning the rate enhancement phenomenon. In the following section the results of this study are summarised and evaluated in the context of a new model proposal dubbed the 'Hydrogen Availability' model. This model was developed from a hybridisation of components of both the Ligand Acceleration and Catalyst Deactivation theories in an attempt to explain a wider range of experimental observations concerning the rate enhancement phenomenon.

From chapter 4; the rate determining step of the racemic reaction was thought to be the addition of the second hydrogen to the alcohol carbon, which was directly proportional to the lifetime of the half-hydrogenated state (HHS). It was recognised that the HHS had an internal hydrogen bond through Density Functional Theory (DFT) analysis, but it was thought more likely that the hydrogen bond was intermolecular and that islands of HHS were forming on the surface. In the absence of a modifier, a high coverage of the HHS islands would block the platinum surface and prevent hydrogen from adsorbing. As discussed in section 7.5, in the absence of surface hydrogen the decarbonylation side reaction could proceed to form adsorbed CO since the fast hydrogenation step to form the product would be inhibited. The adsorbed CO in turn would further block the platinum sites and again prevent hydrogen from adsorbing. It can be expected that with low quantities of surface hydrogen, the rate of the hydrogenation reaction would be slow. The results from chapter 5 also suggest that platinum sites containing {100} character are most prolific at catalysing the decarbonylation reaction. This may lead to a reduction in {100} sites in future catalyst design in an attempt to reduce this debilitating side reaction.

From chapter 6; it was found that when the modifier coverage increased it adopted a more tilted geometry to accommodate still more modifier. At high hydrogen coverages, the

coverage of the modifier was found to decrease on account of hydrogenation of the quinoline (Q) ring [13] and as a consequence, the adsorption mode was found to conform to a "flatter" geometry. The frequency of the ν(Pt-H) vibration was also found to be red shifted from 2086 to ~2076 cm^{-1} in the presence of a modifier corresponding to 1-2% weakening in the force constant of the bond. This was consistent with a lengthening [14] and a weakening of the Pt-H bond. This was thought to be advantageous to the rate of enantioselective hydrogenation, as it would activate the surface hydrogen in the chiral pocket for transfer onto the reactant ketone.

From chapter 7; even at the highest reactant concentrations of methyl pyruvate (MP) or EP, hydrogen was found to be present on the surface when a modifier was adsorbed and the ν(Pt-H) vibration was again red shifted by ~10 cm^{-1}. This could be interpreted as a break-up of the extended HHS islands and formation of free platinum sites onto which hydrogen could adsorb and possibly be activated for reaction. Both EP and MP and adsorbed hydrogen are now in a position to react and therefore the rate of hydrogenation would be expected to increase. Hence, the rate enhancement on modified surfaces is proposed to be from an increased coverage of hydrogen that may also be slightly activated (possess a weaker bond to the platinum surface) towards hydrogenation by the interaction with the modifier.

The initial transient period may also be interpreted in terms of an increase in surface hydrogen coverage. At a low coverage of hydrogen, such as that achieved during catalyst pre-treatment [15] or at reaction start-up (gas-liquid, liquid-solid and pore diffusion limitations can be minimised but not eliminated and is a well recognised factor in achieving high reaction performances [16]), the racemic HHS islands could form and cover a large portion of reaction sites. In addition, the modifier is at a 'high' coverage and in a tilted adsorption geometry. It is proposed here that the initial transient period is the time required for the coverage of both the HHS and the modifier to reduce to allow adsorption of hydrogen and for the modifier to adopt the flat adsorption geometry where it can interact with surface hydrogen and activate it for hydrogenation of the reactant ketone.

This 'hydrogen availability' model can be considered as a hybrid of the ligand acceleration and the suppression of catalyst deactivation models. Unfortunately, the ketone reactant was already converted to an alcohol under these conditions, so no evidence of the keto-modifier interaction that was proposed to be the source of the ligand acceleration and indeed chiral

induction [5] could be observed in the present study. However, there was evidence of surface hydrogen activation and of competitive adsorption (with regard to the spectra of ethyl benzoylformate (EBF) co-adsorbed with CD), which would satisfy the kinetic effect in the explanation for ligand acceleration [10]. The presence of adsorbed HMMPs could not be supported by this study and whilst adsorbed CO was recorded, it was thought to play only a secondary role in catalyst deactivation. However, the formation of the HHS islands was found to deactivate the catalyst by blocking surface hydrogen adsorption. Hence, the emphasis for catalyst restoration in the presence of a modifier, is on the generation of surface hydrogen that can remove the self-blocking HHS islands.

This model also fits with some of the observations made concerning this phenomenon that were previously unexplained by one model or the other. For example, the absence of rate enhancement at low concentrations of EP observed by Murzin *et al* [6] may now be attributed to a low coverage of the HHS islands, leaving free platinum sites for hydrogen to adsorb. This was confirmed by the resolution of the ν(Pt-H) on platinum at low EP concentrations in chapter 4 (Figure 4.9). The surface coverage of hydrogen would be sufficiently high to maintain maximum turnover frequency. This model could also be transferred to the observations made in the gas phase by Hutchings and colleagues who found no rate acceleration in gas phase hydrogenations (but did attain an ee of 51%) [17], if the equilibrium coverage of EP under gas phase conditions did not lead to the complete blocking of all Pt-H adsorption sites. The hydrogenation of EBF on CD modified platinum catalysts was also found not to be rate accelerated in the presence of CD [18], yet 98% ee was generated [19]. From the studies performed here, it was shown that EBF competitively adsorbed with CD (Figure 7.7). Hence, CD could not facilitate the removal of EBF and could not promote adsorption of hydrogen. The steady state conditions attained for the racemic reaction in acetic acid, was evidence that catalyst deactivation by irreversible adsorption of HMMPs and CO was not occurring [9]. However, HHS islands would not be irreversibly adsorbed but would have an extended lifetime, therefore steady state conditions could be achieved. The non-linear effect with EP, ketopantolactone, CN and QNE seen by Bartok and co-workers could not be fully explained as a function of modifier adsorption strength but was "also due to the nature of the complexes formed by EP and the chiral modifier adsorbed on the surface of the catalyst" [11,12]. Although the authors could not specify what the nature of the complex was, it is proposed here that competitive adsorption may play a role. This can be explained as a difference in competitive adsorption of the two modifiers with the HHS of EP compared to

competitive adsorption of the two modifiers with the surface intermediate of ketopantolactone, i.e. QNE can remove the HHS of EP more effectively than CN, but CN can remove the surface intermediate of ketopantolactone more effectively than QNE. Although it was recognised that the adsorption of the HHS of EBF could compete more strongly with CD than the HHS of EP, no such studies have been performed with ketopantolactone co-adsorbed with CN or QNE. Therefore, the proposal of competitive adsorption being responsible for the non-linear effect seen in Bartok's publication remains at present only a speculation.

8.4 Enantiodifferentiation

The current models for enantiodifferentiation are based on a 1:1 hydrogen bond interaction between the reactant and the modifier on the platinum surface [20]. Methylation of the quinuclidine (QN) nitrogen led to a complete loss of enantioselectivity [21], hence a crucial hydrogen bond was thought to be formed between the QN nitrogen and the reactant.

8.4.1 Baiker's Model

The model from Baiker *et al* [22] was based on the assumption that the QN nitrogen was protonated in acidic media [23] or from surface hydrogen in aprotic solvents [14]. The authors proposed that a hydrogen bond could exist between the keto oxygen lone pair of electrons and the N-H of the QN ammonium ion. They also suggested that protonation of the keto oxygen is more energetically favoured from an ammonium ion compared to Pt-H leading to a possible rate enhancement [23]. The mechanism for reaction would be an initial hydrogen addition to the keto oxygen from the ammonium ion, followed by a second hydrogen addition to the carbon from the surface.

There is still no clear evidence to distinguish between the formation of the ammonium ion on CD in protic solvents or from surface hydrogen. However, molecular modelling calculations did show that the "open 3" conformer of CD (which was thought to be the enantioselective conformation [24]) was more stable when the QN ring was protonated [25]. Also, a spectroscopic study on the interaction between ketopantolactone and CD did show a peak that was assigned to a red shifted ν(C=O) to 1725 cm^{-1} and a broad feature around 2580 cm^{-1} that was assigned to a red shifted ν(N-H) [26]. Conversely, when the experiment was repeated with *N*-methyl CD (no enantioselectivity with this modifier was seen [21]), the aforementioned peaks could not be resolved. This was evidence of a hydrogen bond acting on

a carbonyl group of ketopantolactone. However, the authors were unable to determine which of the carbonyls (ester or keto) of ketopantolactone were hydrogen bonded.

For this interaction to be enantioselective, the reactant must be orientated on the approach to the modified surface site. A systematic study of variation in the 'bulkiness' of the keto and ester ends of the reactant revealed that increased bulk of the group in the α-position to the ketone (e.g. the methyl group in EP) had a deleterious effect on both rate and ee but the effects were minimal when the bulkiness of the ester was altered [27,28]. The purpose of these studies was to discover if the orientation of the reactant on approach to the modified site was controlled by steric factors. The "open 3" conformer of CD was not only L-shaped, but also helical. Hence, steric repulsion on the bulkiest end of the reactant would force the reactant to rotate in solution until the steric repulsion was minimised. This would give rise to a consistent orientation of the reactant in the chiral pocket at the modified site and hence the same enantioface would be hydrogenated. However, it was concluded that steric repulsion was not the only effect that caused the orientation change as aromatic rings on the keto end (which had more bulk than the ethyl ester side) still gave rise to the *R*-enantiomer with CD, as did EP where the ester side had the bulkiest group.

8.4.2 McBreen's Model

McBreen and colleagues proposed that the hydrogen bonded carbonyl seen in the spectroscopic study of ketopantolactone and CD [26] was directed at the ester carbonyl and not the keto carbonyl [29]. This model was based on the prediction that the ester carbonyl had a higher proton affinity than the keto carbonyl [30]. A second hydrogen bond was also proposed to occur between the keto carbonyl and the aromatic C-H of the Q ring, which were rendered more acidic by a redistribution of electrons in the C-H bond via a surface interaction [31]. No steric repulsion was required in this model as the two-point hydrogen bond system would fix the reactant in the correct position for hydrogenation rather than directing the reactant to the correct position on approach to the chiral pocket. The mechanism for hydrogenation could be a simultaneous addition to both the oxygen and carbon of the ketone group from the surface. In this case, the ketone would adsorb in an η^2 type configuration, which was recognised by the authors as being a hindrance to the interaction of the ketone and aromatic C-H [29]. Therefore, the mechanism was thought more likely to be a stepwise

addition of a hydrogen atom to the carbonyl oxygen followed by a final addition of hydrogen to the carbon in analogy to the mechanism that forms the HHS.

The McBreen model does not fit well with all forms of reactant such as pyruvaldehyde dimethyl acetal which possesses two ether groups in the α-position to the ketone. The lone pairs of electrons on the ether group(s) could form a hydrogen bond, but it was thought that the lone pair on the ketone would have a higher proton affinity and therefore would preferentially form a hydrogen bond to the ammonium ion. In a two-point hydrogen bond mechanism, this would produce the *S*-enantiomer with CD, but the product is actually the *R*-enantiomer [32]. Furthermore, the model cannot be extended to reactants that do not possess a second group with which to form a hydrogen bond, such as acetophenones, which also form the *R*-enantiomer with CD [29]. The authors conceded that this reactant is an exception for which the Baiker model would fit.

8.4.3 Wells' model

Initially, Wells *et al* considered that a hydrogen bond could exist between the alcohol group of a half-hydrogenated state of the reactant and the QN nitrogen lone pair [33]. The enantiodifferentiation step, in the case of the HHS, would be the direction from where the donator of the hydrogen bond occurred on the formation of the alcohol, prior to the formation of the surface bond. The presence of a HHS of the reactant was initially proposed in conjunction with the "template model" [34]. This model was based on an ordered formation of CD molecules adsorbed on the platinum surface which exposed a chiral ensemble of platinum atoms on which the reactant would be enantioselectively hydrogenated. This model soon became disfavoured on account of surface science studies that reported no such supra-molecular order of CD on platinum [35]. Research into this model was later dropped by the scientific community as was the proposition that the reactant was adsorbed in a HHS, most probably because the high reaction performance in acetic acid was proposed to be from a protonation of the QN nitrogen to form an ammonium ion [23], which was subsequently thought to form a hydrogen bond to the activated ketone, but not the alcohol of a HHS.

8.4.4 Observations from the Present Results

Apart from the subtle and ambiguous feature at 1680 cm^{-1} for EP/MP on a pre-modified surface, no further interaction was observed experimentally between the adsorbed modifier

and the HHS in the spectroscopic results presented here. The reason for this is unclear, however three possibilities are suggested:

1. Such an interaction took place before the formation of the HHS, which suggests that the mechanism for hydrogenation is the same for both racemic and enantioselective hydrogenation.
2. The enantioselective surface intermediate was not SERS enhanced on account of no direct charge transfer between the metal and the reactant (only between the reactant and surface hydrogen). In this case the racemic and enantioselective mechanisms for hydrogenation could be different. However, this suggestion does not satisfy the electromagnetic (EM) theory for SERS (see chapter 2, section 2.3.6.1).
3. The reaction was not enantioselective under the conditions used to take SERS measurements.

Based on the lack of interaction between the two adsorbates, any comment made on the enantiodifferentiation step from these results should be treated with caution. However, one point of contention is the assumption made that the nitrogen on the QN ring on surface CD will be protonated from either an acidic/protic solvent or from surface hydrogen in aprotic solvents. The electrolyte used to carry out the electrochemical SERS measurements in this study was sulphuric acid, which should have protonated the QN ring to form the ammonium ion according to Baiker and colleagues [23]. However, the red shift of the ν(Pt-H) suggested that the nitrogen lone pair was still available for interaction with the surface hydrogen (it should be noted that the ammonium ion could be deprotonated by the surface, which would also give rise to this effect). The magnitude of the red shift may be related to the length and strength of the Pt-H bond, which was stretched by the interaction with the modifier. When QN was singly adsorbed the red shift was 26 cm^{-1} to a position of 2060 cm^{-1}. It is possible that this state corresponds to the intermediate Pt-H before the hydrogen is transferred to QN as proposed by Baiker *et al* [14]. The red shift with the adsorbed cinchona modifier was only ~10 cm^{-1} to a position of ~2076 cm^{-1}. Therefore, it is less likely that the hydrogen had transferred to the QN ring of the modifier. Hence, the modifier is thought to lengthen and weaken the Pt-H bond but not break it. The molecular modelling to show how CD could take up a surface hydrogen atom also showed that the charge on the hydrogen atom became more positive the further it was from the surface [14]. Hence, the nucleophilic keto oxygen would be more attracted to the Pt-H in the modified site than the more negatively charged Pt-H in unmodified sites. In this case, the ketone could actually be attracted to the chiral pocket

where it can undergo enantioselective hydrogenation based on the formation of a hydrogen bond between the newly formed alcohol of the HHS and the nitrogen lone pair of electrons (Figure 8.1).

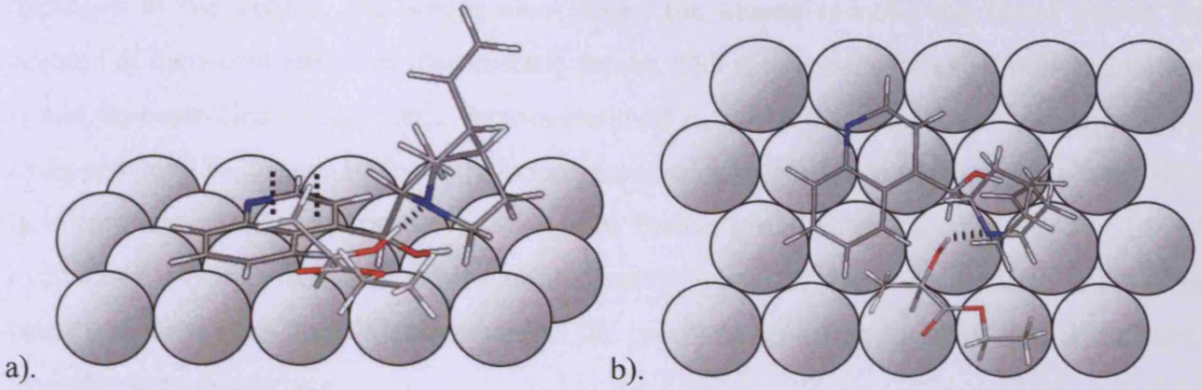

Figure 8.1 Co-adsorption geometry of EP and CD a). side view b). plan view.

This mechanism is similar to what Rauls *et al* had proposed through theoretical calculations [36].

8.5 Conclusion

Based on the presence of surface hydrogen at high reactant coverage and a red shift of the ν(Pt-H) vibration in the presence of an adsorbed modifier, it is proposed that the rate enhancement observed on modified catalysts could be accounted for by the 'hydrogen availability' model, which can be summarised as follows:

1. Promotion of surface hydrogen formation by the adsorbed modifier.
2. Suppression of the decarbonylation side reaction through availability of surface hydrogen.
3. Activation of the surface hydrogen towards hydrogenation of the reactant ketone.
4. Competitive adsorption with the HHS.

The model for enantiodifferentiation and hence the mechanism for the enantioselective hydrogenation reaction may be resolved by unequivocal evidence of the presence or absence of the QN ammonium ion on the surface under reaction conditions.

In the event of the absence of the ammonium ion on the surface, a model is hereby proposed that involves the activation of the surface hydrogen in the chiral pocket towards the hydrogenation reaction. The "activation" step would not only facilitate the transfer of hydrogen to the ketone, but would also attract the ketone towards the chiral pocket on account of increased attractive electrostatic forces. The mechanism for enantiodifferentiation would be controlled by the steric factors outlined in Baiker's model and a formation of a hydrogen bond to the newly formed alcohol group of a half-hydrogenated intermediate state. It is emphasised that this model differs from Baiker's model in only the location of the hydrogen atom that would be added to the keto oxygen. In the present study, rather than being delivered from the QN substituent of the cinchona modifier, the hydrogen is delivered from the platinum surface.

8.6 Future Work

The present work was conducted using only three different types of reactant; EP, MP and EBF and four different types of modifier; CD, CN, QNE and hydroquinine-4-chlorobenzoate (HQnClB). However, many other successful Orito type reactions using different reactants and/or modifiers have been reported in the literature, which could also be studied using this system. Ketopantolactone is one such reactant and is a particularly useful molecule to conduct studies on because the product *R*-pantolactone can be generated to an ee of 91.6% [37] and is used to synthesise pantothenate (vitamin B5) [38]. Structurally, ketopantolactone has few conformational isomers. There is no hydrogen in the alpha position to the ketone, so it is non-enolisable and the ring structure prevents an *s-trans* isomer across the C^1-C^2 bond. However, there is a torsional angle between the ring members that distorts the plane of the ring known as the 'half-boat' or 'twist'. Therefore the rigid structure removes uncertainties about which conformer is involved in the reaction as it can only be the *s-cis keto* form.

Chiral fluorinated alcohols are of particular value in the pharmaceutical and agrochemical industries as building blocks in the synthesis of antileukemic drugs [39] and pesticides [40]. Ethyl trifluoropyruvate is similar in structure to EP, but contains a trifluoromethyl group in the α-position to the ketone and the product of hydrogenation, ethyl trifluorolactate, is one such fluorinated alcohol that has been found as a useful component for ferroelectric liquid crystal compositions [41]. The trifluoromethyl group further activates the ketone by electron withdrawal as dictated by a large positive Hammett constant (σ) compared to the methyl

group of EP [42]. Electron withdrawing groups in this position are reported as being beneficial to rate and enantioselectivity [43]. Although ethyl trifluoropyruvate itself has a very poor reaction performance [44], a surface science investigation on this molecule is yet to be attempted.

The Orito type reaction shows further diversity with the successful hydrogenation of the α-ketoacetal pyruvaldehyde dimethyl acetal to the chiral lactaldehyde dimethyl acetal [45], which is frequently used in synthetic organic chemistry as a chiral precursor to valuable synthons [46,32]. The reaction performance is comparable to that achieved with EP with an increased rate over the modified surface and enantiomeric excesses over 90% [32]. Similar to EP and MP, pyruvaldehyde dimethyl acetal has enolisable hydrogens in the α-position and no cyclic structures or groups inducing extra electronic effects. It is therefore expected that pyruvaldehyde dimethyl acetal will have similar behaviour to EP and MP on the surface in the presence of hydrogen and that it too will form the half-hydrogenated intermediate state.

The concentration transient study on EP co-adsorbed with CD (Figure 7.3) showed that the ν(Pt-H) peak remained clearly visible even at high concentrations of EP. However, it was recognised that the HHS in this case was of pyruvic acid (PA) due to a saponification reaction of EP in the presence of the tertiary nitrogen on the QN group. Therefore, it would be prudent to repeat the concentration range using singly adsorbed MP and MP co-adsorbed with CD where no saponification was found to occur.

The peak seen at 1680 cm^{-1} when EP/MP was adsorbed on a surface pre-modified with a cinchona alkaloid was poorly resolved and often difficult to discern from other peaks of similar frequency. However, the peak could be evidence of the interaction between the reactant and modifier and therefore its appearance should be pursued. *N*-methyl CD is known not to be enantioselective when used to modify a platinum catalyst in the hydrogen of EP and was attributed to a blocking of the interaction between the alkaloid and reactant [21]. The expected result of using this modifier for a co-adsorption experiment in this system would be an absence of the 1680 cm^{-1} peak. It was interesting to note that the appearance of the 1680 cm^{-1} peak was less frequent when the modifier was at a high coverage. This could be due to a slightly more tilted arrangement of the modifier, known to occur at high coverage, which has forced the QN ring away from the surface and the HHS leading to a weaker interaction. To test this hypothesis, MP and CD could be co-adsorbed at increasing concentrations of CD.

As discussed in Chapter 3, section 3.3.2, the core-shell nanoparticles used in the present study were 50-60 nm in diameter, which was approximately 40 nm smaller than the ideal size of 100 nm for generating SERS activity using gold. Therefore to increase the signal to noise ratio and improve the resolution of the SERS peaks, the nanoparticle preparation method could be developed by increasing the size of the gold seed. However, the metal film deposition procedure would also need to be adjusted to maintain the integrity of the shell. The nanoparticles used in the present study for SERS measurements were spherical and multi-facetted with poorly defined surface morphology. Recently, cubic, cuboctahedral and octahedral platinum nanoparticles were prepared using the Ahmadi method [47] to vary the ratio in area of {111}/{100} facets [48]. It may be possible to use a similar approach to produce SERS active nanoparticles and conduct structure sensitive experiments on the components of the Orito reaction using this system.

The SERS technique inherently requires the surface to have a rough topography, which may be made more ordered by controlling the shape of SERS active nanoparticles as described above. For more concise surface structure dependency studies, other surface science techniques may be used. As described in section 2.3.5.4, Tip Enhanced Raman Scattering (TERS) is one such technique that enables the enhancement of adsorbates on well defined single crystal surfaces. Alternatively, Reflection Absorption Infra-Red Spectroscopy (RAIRS) may also be used to identify adsorbates on well defined surfaces. Using RAIRS, may also be complementary to the data collected using SERS. However, generating surface hydrogen at hydrogen evolution reaction (HER) potentials may be problematic in traditional Internal Reflection Elements used for RAIRS studies.

The spectro-electrochemical flowcell and the gas/liquid phase system was designed and built in-house to meet the needs of the present study. The development of this system has been ongoing, but may be improved further by reducing the volume of the channel in the flowcell and replacing the platinum/palladium working electrode with a glassy carbon electrode of larger area. These two changes would be beneficial in three ways:

1) Lower sample volumes passing in the cell and faster flow rates should ensure a faster transition between different solutions/gases.

2) The glassy carbon electrode would provide a standard support material for the nanoparticles and would not contribute voltammetric features when running a CV to determine the integrity of the nanoparticle shell.
3) A larger surface area on the working electrode would generate more product in a hydrogenation reaction, which together with lower sample volumes, may enable product sampling for chiral analysis.

In order to prevent the oxidation of the working electrode products before exiting the flowcell, the counter electrode may need to be placed in a separate volume of electrolyte. The circuit would then be maintained using a salt bridge connected to the flowcell.

8.7 References

[1] M. Garland, H.U. Blaser, *J. Am. Chem. Soc.*, **1990**, 112, 7048.

[2] J. Wang, Y. Sun, C. LeBlond, R.N. Landau, D.G. Blackmond, *J. Catal.*, 161, 752–758 (**1996**).

[3] D. Ferri, T. Burgi, A. Baiker, *J. Phys. Chem. B*, **2004**, 108, 14384-14391.

[4] D.J. Jenkins, A.M.S. Alabdulrahman, G.A. Attard, K.G. Griffin, P. Johnston, P.B. Wells, *J. Catal.*, 234 (**2005**) 230–239.

[5] D. Ferri, T. Bürgi, K. Borszéky, T. Mallat, A. Baiker, *J. Catal.*, 193 (**2000**) 139.

[6] E. Toukoniitty, D.Yu. Murzin, *J. Catal.*, 241 (**2006**) 96–102.

[7] D.M. Meier, D. Ferri, T. Mallat, A. Baiker, *J. Catal.*, 248 (**2007**) 68–76.

[8] U. Böhmer, F. Franke, K. Morgenschweis, T. Bieber, W. Reschetilowski, *Catal. Today*, 60 (**2000**) 167.

[9] A. Kraynov, R. Richards, *Appl. Catal. A Gen.*, 314 (**2006**) 1.

[10] J.L. Margitfalvi, E. Talas, E. Tfirst, *Top. Catal.*, 39 (**2006**) 77.

[11] G. Szollosi, S. Cserenyi, K. Balazsik, F. Fulop, M. Bartok, *J. Mol. Catal. A: Chemical*, 305, 1-2, (**2009**), 155-160.

[12] K. Balazsik, S. Cserenyi, G. Szollosi, F. Fulop, M. Bartok, *Catal. Lett.*, (**2008**) 125:401–407.

[13] K. Balázsik, M. Bartók, *J. Catal.*, 224 (**2004**) 463–472.

[14] A. Vargas, D. Ferri, A. Baiker, *J. Catal.*, 236 (**2005**) 1–8.

[15] T. Mallat, Z. Bodnar, B. Minder, K. Borszeky, A. Baiker, J. Catal., 168, 183–193 (**1997**).

[16] Y. Sun, R.N. Landau, J. Wang, C. LeBlond, D.G. Blackmond, *J. Am. Chem. Soc.*, **1996**, 118, 1348-1353.

[17] M. von Arx, N. Dummer, D.J. Willock, S.H. Taylor, R.P.K. Wells, P.B. Wells, G.J. Hutchings, *Chem. Commun.*, **2003**, 1926–1927.

[18] E. Toukoniitty, P. Maki-Arvela, N. Kumar, T. Salmi, D.Yu. Murzin, *Catal. Lett.*, 95, 3-4, **2004**.

[19] M. Sutyinszki, K. Szori, K. Felfoldi, M. Bartok, *Catal. Commun.* 3 (**2002**) 125–127.

[20] T. Mallat, E. Orglmeister, A. Baiker, *Chem. Rev.*, **2007**, 107 (11), pp 4863–4890.

[21] H.U. Blaser, H.P. Jalett, D.M. Monti, A. Baiker, J.T. Wehrli, *Stud. Surf. Sci. Catal.* 67 (**1991**) 147.

[22] T. Burgi, A. Baiker, *Acc. Chem. Res.* **2004**, 37, 909-917.

[23] K.E. Simons, G. Wang, T. Heinz, T. Giger, T. Mallat, A. Pfaltz and A. Baiker, *Tetrahedron Asymm.*, 6 (**1995**) 505.

[24] G.D.H. Dijkstra, R.M. Kellogg, H. Wynberg, *J. Org. Chem.*, 55 (**1990**) 6121.

[25] T. Burgi, A. Baiker, *J. Am. Chem. Soc.*, 120 (**1998**) 12920.

[26] N. Bonalumi, T. Burgi, A. Baiker, *J. Am. Chem. Soc.*, **2003**, 125, 13342-13343.

[27] S. Diezi, S. Reimann, N. Bonalumi, T. Mallat, A. Baiker, *J. Catal.*, 239 (**2006**) 255–262.

[28] K. Szöri, M. Sutyinszki, K. Felföldi, M. Bartók, *App. Catal. A: Gen.*, 237 (**2002**) 275–280.

[29] S. Lavoie, M-A. Laliberte, I. Temprano, P.H. McBreen, *J. Am. Chem. Soc.* **2006**, 128, 7588-7593.

[30] A. Taskinen, V. Nieminen, E. Toukoniitty, E.; M.D. Y., M Hotokka, *Tetrahedron*, **2005**, 61, 8109-8119.

[31] S. Lavoie, P.H. McBreen, *J. Phys. Chem. B*, **2005**, 109, 11986-11990.

[32] B. Torok, K. Felfoldi, K. Balazsik, M. Bartok, *Chem. Commun.*, **1999**, 1725–1726.

[33] G. Webb, P.B. Wells, *Catal. Today*, 12, 319 (**1992**).

[34] G. Bond, P.A. Meheux, A. Ibbotson, P.B. Wells, *Catal. Today*, 10, 371 (**1991**).

[35] A.F. Carley, M.K. Rajumon, M. W. Roberts, P.B. Wells, *J. Chem. Soc. Faraday Trans.*, **1995**, 91(14), 2167-2172.

[36] E. Rauls, B. Hammer, *Catal. Lett.*, 106, **2006**, 3–4.

[37] M. Schurch, N. Kunzle, T. Mallat, A. Baiker, *J. Catal.*, 176, 569–571 (**1998**).

[38] http://biocyc.org/META/NEW-IMAGE?type=COMPOUND&object=PANTOTHENATE

[39] Y. Yoshimura, K. Saitoh, N. Ashida, S. Sakata, T. Sasaki, A. Matsuda, *Nucleic Acids Symp Ser.*, **1993**;(29):33-4.

[40] K. Naumann, *Pesticide Science*, 52, 1, **1999**, 3-20.

[41] http://www.freepatentsonline.com/EP0592669.html

[42] http://www.wiredchemist.com/chemistry/data/hammett_sigma_constants.html

[43] M. von Arx, T. Mallat, A. Baiker, *Tetrahedron: asymmetry.*, 12 (**2001**) 3089–3094.

[44] M. von Arx, T. Mallat, A. Baiker, *J. Catal.*, 193, 161–164 (**2000**).

[45] M. Studer, S. Burkhardt, H-U. Blaser, *Chem. Commun.*, **1999**, 1727–1728.

[46] R. S. Atkinson, *Stereoselective Synthesis*, Wiley, Chichester, **1995**.

[47] T.S. Ahmadi, Z.L. Wang, T.C. Green, A. Henglein, M.A. El-Sayed, *Science*, **1996**, 272, 5270, 1924–1926.

[48] E. Schmidt, A. Vargas, T. Mallat, A. Baiker, *J. Am. Chem. Soc.*, **2009**, 131, 12358–12367.

CARDIFF UNIVERSITY
PRIFYSGOL CAERDYDD